

Numerical reactive transport modeling of soluble mineral and fluid interactions in the
subsurface and application to sedimentary geothermal systems

by
Kayla Moore

A Thesis submitted to the Faculty of Graduate Studies of
The University of Manitoba
In partial fulfillment of the requirements of the degree of

Doctor of Philosophy

Department of Civil Engineering
University of Manitoba
Winnipeg

Copyright © 2020 by Kayla Moore

Abstract

Economics of deep geothermal systems for power production can be improved by targeting warm thermal anomalies. Anomalies can occur near minerals with high thermal conductivity such as halite and dolomite. However, the solubility of these formations may contribute to technical problems associated with geochemistry. In order to evaluate the feasibility and potential benefits of a deep, low-temperature geothermal system targeting thermal anomalies caused by high thermal conductivity minerals, this research investigated the application of thermal, hydraulic and chemical numerical models to problems of high ionic strength mineral and fluid interaction in subsurface flow. Numerical model performance for problems of mineral dissolution flow and transport were studied using laboratory measurements, characterizing sensitivities and accuracy. Field-scale simulations of sinkhole development validated the predictive capability at the field scale. These validations of model performance for fluid-mineral interactions confirmed the validity of numerical models for large-scale geothermal simulations. The geothermal models were binary, doublet systems based in the Williston Basin, Saskatchewan, Canada. A geochemical investigation of produced fluids from a well targeting the halite Prairie Evaporite with 120°C at depth and 60°C at surface, resulted in 0.37 mol L⁻¹ of halite precipitation. Halite precipitation could be inhibited by introducing MgCl₂ into the heat exchange fluid and through pressure controls. A second scenario investigated a horizontal production well in the dolomite Dawson Bay formation, including the conversion of an oil and gas well in the Bakken formation for injection. A 6°C temperature anomaly resulted from 371 m of underlying halite and dolomite, increasing power production by 1.5 MW. Produced temperatures ranged from 112°C to 103°C over 30 years. At a flow rate of 0.2 m³s⁻¹ and injection temperature from 60 – 80°C the system produced 6.8 – 10.9 MW. The geochemical analysis indicated the potential for lithium production. Numerical models provided valuable information on produced geochemistry in deep geothermal wells, which can be used to study scale inhibition. Geothermal wells targeting formation above thick high thermal conductivity formations benefit from warm thermal anomalies, reducing drilling costs.

Acknowledgments

I would like to thank my advisors Dr. Hartmut Holländer and Dr. Allan Woodbury for their guidance, support, and encouragement through my study and research. I would also like to acknowledge my advisory committee, Dr. Jörg Stetefeld and Dr. Beata Gorczyca for contributing their valuable time to help improve my work. Thanks to Kerry Lynch and Victor Wang for answering my question in the lab and helping me find everything I needed. I will be forever grateful for all of my colleagues in the Geotech office and in the groundwater research group. I also appreciated the opportunity to collect field data from Shawn Gurke and the Alonsa Conservation district and to Mundzir Basri and Stantec for partnering on the research.

I am grateful for the scholarships which supported my studies, the University of Manitoba Graduate Fellowship and Manitoba Graduate Scholarship programs, as well as the Vanier Canada Graduate Scholarship program. I would also like to acknowledge funding from the National Ground Water Association, the Neil Burgess Memorial Scholarship Fund, and Edward R. Toporeck Graduate Fellowship program.

Thank you to all of my neighbours, teammates, friends, and family for helping me to keep life balanced, and my 4-legged ‘co-worker’ Otter for reminding me to take breaks and enjoy life. I would not be here without my parents, who taught me to work hard and encouraged me to pursue my education. Finally, to Owen for supporting this endeavor and providing love, support, and encouragement.

Contributions of Authors

1. Chapter 3: Moore, K.R., Holländer, H.M., Woodbury, A.D., 2019.

In preparation.

- i. Moore, K.R.: Project conceptualization, methodology development, data acquisition, laboratory measurements, and modeling simulations, original draft and editing
- ii. Holländer, H.M.: Project conceptualization, criticized methodology, supervision, review and editing, funding acquisition
- iii. Woodbury, A.D.: Criticized methodology, supervision, reviewing and editing

2. Chapter 4: Moore, K.R., Holländer, H.M., Basri, M., Roemer, M., 2019.

Published: Application of geochemical and groundwater data to predict sinkhole formation in a gypsum formation in Manitoba, Canada. *Environmental Earth Sciences*, 78(6): 193.
DOI:10.1007/s12665-019-8188-1

- i. Moore, K.R.: Project conceptualization, methodology development, data acquisition, field data collection, and modeling simulations, original draft, and editing
- ii. Holländer, H.M.: Project conceptualization, criticized methodology, supervision, reviewing and editing
- iii. Basri, M.: Project conceptualization, criticized methodology development, supervision, reviewing and editing
- iv. Roemer, M.: Project conceptualization, data acquisition, review, and editing

3. Chapter 5: Moore, K.R., Holländer, H.M., 2019

Under review with *Geothermal Energy*.

- i. Moore, K.R.: Project conceptualization, methodology development, data acquisition, modeling simulations, original draft, and editing
- ii. Holländer, H.M.: Project conceptualization, criticized methodology, supervision, review and editing, funding acquisition

4. Chapter 6: Moore, K.R., Holländer, H.M., 2019

Under review with *Applied Energy*

- i. Moore, K.R.: Project conceptualization, methodology development, data acquisition, modeling simulations, original draft, and editing
- ii. Holländer, H.M.: Project conceptualization, criticized methodology, supervision, review and editing, funding acquisition

Table of Contents

1. Introduction and Motivation	13
1.1. Background	13
1.2. Scope of work.....	16
1.3. Objectives.....	18
1.4. Manuscript-style thesis.....	20
2. Literature review.....	21
2.1. Geothermal	21
2.1.1. Williston Basin.....	21
2.1.2. Flow	26
2.1.3. Heat	27
2.1.4. Hydrogeochemistry	30
2.2. Modeling	33
2.2.1. Validation.....	34
2.2.2. Calibration.....	35
2.2.3. Parameters	36
2.3. Summary	41
2.4. Chapter 1 & 2 References	42
3. Manuscript 1: An experimental and numerical study for evaporite mineral dissolution and density-driven flow in porous media	47
3.1. Abstract	48
3.2. Introduction	49
3.3. Physical and numerical methods	51
3.3.1. Model concept and design	51
3.3.2. Experimental method	53
3.3.3. Hydrodynamic dispersion	57
3.3.4. Numerical methods	59
3.4. Results	63
3.4.1. PEMD physical model flow and dispersion results	63
3.4.2. PEMD physical model salt concentration results	64
3.4.3. Numerical simulation results	69
3.4.3.1. Uncalibrated model results	69
3.4.3.2. Uncalibrated gradients	73
3.4.3.3. FD flow patterns	75
3.4.3.4. Calibrated results and sensitivities.....	76
3.5. Discussion	78
3.5.1. Limitations.....	80
3.5.2. Comparison with numerical HYDROCOIN1:5	81

3.6.	Conclusions	82
3.7.	Acknowledgments, Samples, and Data	83
3.8.	References	84
4.	Manuscript 2: Application of geochemical and groundwater data to predict sinkhole formation in a gypsum formation in Manitoba, Canada	87
4.1.	Abstract	88
4.2.	Introduction	89
4.3.	Methods	92
4.3.1.	Study Area	92
4.3.2.	Regional geology, hydrology, and hydrogeology	94
4.3.3.	Tracer test.....	96
4.3.4.	Modeling approach	97
4.3.5.	Regional flow investigation	99
4.3.6.	Dissolution model	102
4.4.	Results	105
4.4.1.	Tracer test results	105
4.4.2.	Regional flow investigation	105
4.4.3.	Dissolution model	108
4.5.	Discussion	111
4.6.	Conclusions	114
4.7.	Acknowledgments	116
4.8.	References	116
5.	Manuscript 3: Evaluation of NaCl and MgCl ₂ heat exchange fluids in a deep binary geothermal system in a sedimentary halite formation	119
5.1.	Abstract	120
5.2.	Introduction	121
5.3.	Materials and methods	123
5.3.1.	Reservoir and thermal fluids	124
5.3.2.	Model conceptualization	125
5.3.3.	Temperature and pressure evaluations	126
5.4.	Numerical approach	127
5.4.1.	1-D model	127
5.4.2.	3-D model design	128
5.4.3.	Mathematical representation	131
5.5.	Results	134
5.5.1.	1-D chemical simulations	134
5.5.2.	3-D reservoir simulations	139
5.5.3.	Sensitivities	142

5.6.	Discussion	144
5.6.1.	Chemical processes within the flow system	144
5.6.2.	Implications of a modified heat exchange fluid.....	148
5.6.3.	Limitations and future work.....	148
5.7.	Conclusions	150
5.8.	Acknowledgements	151
5.9.	References	151
6.	Manuscript 4: Improving economic feasibility of low-temperature geothermal energy in the Williston Basin.....	156
6.1.	Abstract	157
6.2.	Introduction	158
6.3.	Methods.....	162
6.3.1.	Interpretation of geology and hydrogeology.....	162
6.3.2.	The conceptual model	169
6.3.3.	Numerical simulator.....	170
6.3.4.	Initial and boundary conditions	172
6.3.5.	Production calculations	178
6.3.6.	Model validation and calibration	179
6.4.	Results	179
6.4.1.	Well conversion economic impacts	179
6.4.2.	Flow	181
6.4.3.	Temperature	182
6.4.4.	Geochemistry	185
6.5.	Discussion	191
6.5.1.	Oil and gas well conversion and reservoir suitability	191
6.5.2.	High thermal conductivity dolomite and halite formations	193
6.5.3.	Scale and minerals	194
6.5.5.	Feasibility.....	197
6.6.	Conclusions	197
6.7.	Acknowledgments	199
6.8.	References	199
7.	Conclusions	206
8.	Outlook	211
8.1.	References	213

List of Tables

Table 2-1. Prairie Evaporite composition.	26
Table 2-2. Outline of parameters examined by the laboratory and field studies, as well as those required in the geothermal study.....	36
Table 3-1. Comparison of model settings for HYDROCOIN1:5 and PEMD.	52
Table 3-2. Physical and calculated properties of the porous media and flow for the physical models.	63
Table 3-3. Maximum concentrations during the initial time period, the largest peak, and the steady-state maximum observed for each replicate at each gradient.	66
Table 3-4. RMSE values from comparisons of observed and modeled time series data for two 5% replicates of the PEMD experiment and 2 model settings.	73
Table 4-1. Model parameters for the Regional Flow Model and the Dissolution Model.	102
Table 4-2. Initial water compositions for the Dissolution Model.	104
Table 5-1. Composition of Prairie Evaporite minerals from a salt solution mine (Christie, 2015).	124
Table 5-2. Initial compositions of the heat exchange fluids. SI indicates saturation index, where 0 indicates saturated, value >0 indicate supersaturation, and values <0 indicate undersaturation. ‘Yes’ and ‘no’ indicate whether trace ions were included in the initial heat exchange fluid composition.....	128
Table 5-3. Values used for fracture densities from 1×10^{-3} to 10 m^{-1} and fracture apertures 1×10^{-4} to $5 \times 10^{-3} \text{ m}$ used to assess model sensitivity.	131
Table 5-4. NaCl-brine heat exchange fluid composition and mineral saturation indices (SI) during heating and cooling processes as determined using PHREEQC and the PHREEQC2 database. Bold numbers indicate saturation or supersaturation.	136
Table 5-5. MgCl_2 -brine heat exchange fluid composition and mineral saturation indices (SI) during heating and cooling processes as determined using PHREEQC and the Pitzer (1973) database. Bold numbers indicate saturation or supersaturation.	137
Table 5-6. NaCl+ MgCl_2 -brine heat exchange fluid composition and mineral saturation indices (SI) during heating and cooling processes as determined using PHREEQC and the Pitzer (1973) database. Bold numbers indicate saturation or supersaturation.	138
Table 5-7. Concentration of Na^+ , Cl^- and Mg^{2+} in each heat exchange fluid with pressure changes from 0.1 to 202 MPa, simulated using the Pitzer (1973) database.	139
Table 6-1. Average thickness and depth for formations within the Williston Basin located between 49.0 to 49.2°N and -103.3 to -102.9°W (Anna, 2013; Sproule, 1964; TGI Williston Basin Working Group, 2008a; TGI Williston Basin Working Group, 2008b).....	163
Table 6-2. Formation properties and brine composition in the Williston Basin (Blondes et al., 2017; Christie, 2015). Data are taken from observations between 48.4 to 49.8°N and -102.0 to -104.5°W where available.	168
Table 6-3. Numerical model parameters for a doublet, horizontal geothermal well system in the Williston Basin.....	174
Table 6-4. The composition of injected heat exchange fluid in a geothermal doublet in the Williston Basin.....	178

Table 6-5. Temperature distribution at the top of each formation unit, based on a constant temperature of 125°C and 114°C at the top Red River formation.	183
Table 6-6. Power production sensitivity, temperatures at the top of the Prairie Evaporite with varying heat flow parameters.	183
Table 6-7. Power production, pumping power, and net production for various inlet and outlet temperature and flow rates in a geothermal doublet in the Williston Basin.	185
Table 6-8. Saturation indices (SI) for minerals expected to precipitate at the top and bottom of the production well in a geothermal doublet in the Williston Basin, with the production well in the Dawson Bay formation.	190

List of Figures

Figure 2-1. Outline of the extent of the Williston Basin.....	22
Figure 2-2. Generalized Paleozoic stratigraphy in the Williston Basin based on Nicolas and Barchyn (2008).	25
Figure 3-1. Physical model design for the 2-D experimental aquifer. Black dots indicate solute sampling locations. The height of the outflow was reduced to the appropriate gradients.....	56
Figure 3-2. A comparison of one replicate of observed salt concentration for each the 2%, 5%, and 10% gradients in the experimental aquifer overlying the salt core at approximately 0.14 days. The isolines are interpolated from resistance observations located at the '+' marks. Concentrations are relative to saturated NaCl brine at 22°C.	67
Figure 3-3. A comparison of the two replicates of the physical model at the 5% gradient in the experimental aquifer overlying the salt core. The isolines are interpolated from resistance observations located at the '+' marks. Concentrations are relative to saturated NaCl brine at 20°C.	68
Figure 3-4. Comparison of observed and calculated hydraulic head values for the 5% gradient replicate 1 for both observed hydraulic head and observed equivalent freshwater hydraulic head, shown with a 1:1 trend line.	70
Figure 3-5. Comparison of modeled isolines at 0.001 M M^{-1} and 0.01 M M^{-1} with flow pattern observed using Rhodamine-WT dye in 5% Replicate 2. a) Model 1, uncalibrated, measured conditions; b) Model 2, calibrated to 5% Replicate 2.....	71
Figure 3-6. Comparisons of experimentally observed concentration with time for the two 5% gradient replicates and 4 models, representing uncalibrated, calibrated conditions and variations in transverse dispersivity.....	72
Figure 3-7. Comparison of uncalibrated 2, 5, and 10% steady-state concentrations. Contour lines indicate concentration relative to saturation.	75
Figure 3-8. Uncalibrated results for a 5% gradient at 0.25 days produced using an FD model. Contour lines indicate concentration relative to saturation.....	76
Figure 3-9. The sensitivity of the steep concentration gradient at $x = 0.61 \text{ m}$ between $y = 0.00$ and 0.02 m	78
Figure 4-1. Study area for a) the Regional Model and b) the Dissolution Model.	94
Figure 4-2. Stratigraphy of wells located in the Regional Flow Investigation study area based on data from Hydata (2018), wells are sorted from north to south throughout the study area.	96
Figure 4-3. Monitoring well data showing long term patterns, wells located 50 km west of the study area near McCreary, Manitoba, Canada (Hydata, 2018).....	101
Figure 4-4. Groundwater equipotential map in m asl across the watershed, data is from sand and gravel and limestone aquifers observed between 1996 and 2017. Wells are labeled with the year they were drilled.	107
Figure 4-5. Regional Flow Model hydraulic head values for the watershed surrounding the quarry, values range from 270 in the west to 239 in the east, along Lake Manitoba.	108
Figure 4-6. Hydraulic head equipotential lines representative of a) high flow and b) low flow periods, as defined in the model. The dashed black lines depict the location of the roads.	110

Figure 4-7. Gypsum dissolution after a) 365 days and b) 3650 days as indicated by aqueous calcium concentration. The relationship between hydraulic conductivity and concentration was calculated using $n = 5$ in equation 4-5. The dashed black lines depict the location of the roads.	110
Figure 4-8. Gypsum dissolution after a) 1825 days (4 years), and b) after 3650 days (10 years) as indicated by aqueous calcium concentration. The hydraulic gradient was removed after 1825 days, reducing flow to a minimal value, simulating remedial measures. The dashed black lines depict the location of the roads. The relationship between hydraulic conductivity and concentration was calculated using $n = 5$.	114
Figure 5-1. Conceptual model with injection well, halite reservoir, production well, and surface conditions. Shown are the temperature conditions and flow rates.	126
Figure 5-2. Dissolved Cl^- ions for halite and bischofite solutions in freshwater with changes in temperature and pressure from the Pitzer (1973) database from Moore and Holländer (2017).	127
Figure 5-3. 3-D model domain and boundaries for a binary geothermal doublet.	129
Figure 5-4. A cross-section at the wells of a) hydraulic head and b) temperature in a geothermal doublet system with a pumping rate of $3000 \text{ m}^3 \text{ d}^{-1}$ in the cross-section after 10950 days (30 years). The fracture density is 1 m^{-1} and fracture aperture is 0.3 mm.	140
Figure 5-5. Geothermal doublet aqueous ion concentration after 365 days for a NaCl brine heat exchange fluid, saturated at 10°C (a), and an MgCl_2 brine heat exchange fluid, saturated at 10°C (b) injected into a halite formation at 70°C .	141
Figure 5-6. Comparison of Cl^- , Mg^{2+} , and Na^+ concentration at the production well over 730 days (2 years) in a geothermal doublet system initially saturated with NaCl, injected with (a) NaCl-brine and (b) MgCl_2 -brine heat exchange fluids.	141
Figure 5-7. Comparison of sensitivity to fracture frequency (N) and aperture (B) for a) observed temperature at the production well and b) Mg^{2+} at the production well in a geothermal doublet system.	143
Figure 5-8. Comparison of sensitivity to anisotropy for a) observed temperature at the production well and b) Mg^{2+} at the production well in a geothermal doublet system.	144
Figure 6-1. A geothermal-doublet energy production system with horizontal injection and production wells connected by 40 fractures in the Williston Basin.	170
Figure 6-2. Temperature and ion distributions for a geothermal system in the Williston Basin. Centre and front refer to locations within the formation, with the first ‘centre’ indicating placement between the wells, the second ‘centre’ located in the fractures, and ‘front’ in line with the wells.	188
Figure 6-3. Temperature distribution within the formation following 30 years of simulation.	189
Figure 6-4. Piper plot of the composition of fluids in the Williston Basin within the targeted formations in the Mississippian and Devonian periods.	189
Figure 6-5. Distribution of chlorides along a horizontal slice of the Dawson Bay formation at - 2510 m in a geothermal doublet.	190
Figure 6-6. Comparison of Cl^- concentration observed at the bottom of the production well when a brine versus freshwater was injected into the system, and for transient density and viscosity.	191

Nomenclature

α_i – activity of species i (mol kg⁻¹)
 a_L – longitudinal dispersivity (m)
 a_T – transverse dispersivity (m)
 b – fracture aperture (m)
 c – specific heat capacity (J kg⁻¹ K⁻¹)
 c_m – specific heat capacity of solid matrix (J kg⁻¹ K⁻¹)
 C – concentration (kg m⁻³)
 C_i – concentration of species i (kg m⁻³)
 C_0 – reference concentration (kg m⁻³)
 C_S – saturated concentration (kg m⁻³)
 d – thickness of overlying rock (m)
 d_i – fracture diameter (m)
 \mathbf{D} – coefficient of hydrodynamic dispersion (m² s⁻¹)
 D_L – coefficient of hydrodynamic dispersion in the longitudinal direction (m² s⁻¹)
 D_d – effective molecular diffusion (m² s⁻¹)
 D_d^* – diffusion coefficient of NaCl in water at 25°C (m² s⁻¹)
 \mathbf{D}_m – mechanical dispersion tensor (m² s⁻²)
 \vec{e} – gravitational unit vector (-)
 E – equilibrium constant (-)
 f_u – viscosity relation function (-)
 g – acceleration of gravity (m s⁻²)
 h – fluid hydraulic head (m)
 h_0 – equivalent freshwater hydraulic head (m)
 h_s – saltwater hydraulic head (m)
 He – overall source/sink of internal energy (kg m⁻¹ s⁻³)
 k – permeability (m²)
 k_r – relative permeability (-)
 k_f – fracture permeability (m²)
 K – hydraulic conductivity (m s⁻¹)
 K_d – hydraulic conductivity of the matrix surrounding the conduit (m d⁻¹)
 K_f – hydraulic conductivity of the fracture (m s⁻¹)
 K_{fr} – equivalent fracture hydraulic conductivity for porous media (m s⁻¹)
 K_m – hydraulic conductivity of the matrix (m s⁻¹)
 L – length (m)
 m_i – molality of species i (mol kg⁻¹)
 \dot{m} – mass flow rate at the outlet (kg s⁻¹),
 n – shaping factor (-)
 n_i – number of moles in solution (mol)
 N – fracture density (m⁻¹)
 p – fluid pressure (Pa)
 p_p – pumping power for a geothermal well (W)
 P – pressure (Pa)
 Pe – Peclet number (-)
 \vec{q} – Darcy flux (m s⁻¹)
 Q – flow sources and sinks (s⁻¹)
 Q_{EOB} – correction source/sink flow of flow for the extended Oberbeck-Boussinesq approximation (s⁻¹)
 Q_w – discharge (m³ s⁻¹)

\dot{Q} – regional heat flow (W m^{-2})
 R – retardation (-)
 Re – Reynolds number (-)
 S – size of fracture (m)
 S_0 – specific storage (m^{-1})
 S_c – advection/dispersion sources and sinks ($\text{kg m}^{-3} \text{s}^{-1}$)
 S_Q – volumetric flow rate per unit volume representing sources and sinks (s^{-1})
 t – time (s)
 T – temperature at depth (K)
 T_0 – reference or surface temperature (K)
 U – dimensionless time (-)
 \vec{v} – fluid velocity (m s^{-1})
 v_x – fluid velocity in the x direction (m s^{-1})
 v_L – fluid velocity in the longitudinal direction (m s^{-1})
 W_{aq} – mass of the solvent in water in an aqueous solution (kg)
 \dot{W} – maximum potential power output of a geothermal well (kW)
 x – x-direction (m)
 y – y-direction (m)
 z – elevation head (m)

Greek

β - dimensionless constant relating density and concentration (kg m^{-3})
 B – thermal expansivity of fluid ($^{\circ}\text{C}^{-1}$)
 γ_i – activity coefficient of species i (-)
 ε – porosity (-)
 ε_{fr} – equivalent fracture porosity for a porous medium (-)
 θ – relative liquid phase saturation ($\text{m}^3 \text{m}^{-3}$)
 λ – heat (thermal) conductivity ($\text{W m}^{-1} \text{K}^{-1}$)
 Λ – thermal hydrodynamic tensor ($\text{kg m s}^{-3} \text{K}^{-1}$)
 μ – fluid dynamic viscosity ($\text{kg m}^{-1} \text{s}^{-1}$)
 ρ – fluid density (kg m^{-3})
 ρ_0 – mass density of the reference water (kg m^{-3})
 ρ_s – mass density of the saltwater (kg m^{-3})
 ρ_m – mass density of the solid matrix (kg m^{-3})
 ω – coefficient related to tortuosity (-)
 χ – buoyancy coefficient (-)
 Γ – second-order thermal expansivity of fluid and ($^{\circ}\text{C}^{-2}$)
 κ – fluid compressibility (MPa^{-1})
 Ω – pump efficiency in a geothermal system (-)
 η_{prod} and η_{inj} – enthalpy of fluid at each the production and injection wells (kJ kg^{-1})
 φ_1 and φ_0 – specific entropy of fluid at the production and injection wells ($\text{kJ kg}^{-1} ^{\circ}\text{C}^{-1}$)

1. Introduction and Motivation

1.1. Background

Worldwide, fossil fuels contribute 65% of electricity production, while renewable sources count for 6.8% (The World Bank, 2017). Fossil fuels are generally associated with high carbon emissions. Under high carbon emissions, Prairie Climate Centre (2018) predicts about 14 additional days of 30°C+ temperatures in the Canadian Prairies by 2050, more than double the current amount. This will have many environmental and socio-economic impacts, including increased electricity demand. Canada has committed to the reduction of carbon emissions, and there is a push towards the development of low carbon emission, renewable energy in Canada and worldwide (Government of Canada, 2019).

Deep geothermal systems, used to produce electricity, are the future of low-carbon-emission energy. Geothermal systems have the potential to supply baseload power in Canada (Grasby et al., 2012). Geothermal does not rely on weather patterns, such as wind, sunlight, and rainfall, and therefore, has an advantage over solar, wind, and hydroelectricity. Climate change has caused alteration in patterns of wind, water, and cloud cover, making them less predictable.

Geothermal energy depends on heat extracted from the subsurface. The heat can be used for direct heating or electricity production. Deep systems (>200 m) are generally required for electricity production. These systems commonly consist of a production well and one or more injection wells, which reinject cooler water after heat extraction. High-enthalpy, high-temperature resources (>200°C) are used in dry and flash-steam power plants to drive turbines. While low-enthalpy, low-temperature (<150°C) resources are used in binary cycle power plants, which circulate a secondary fluid with a low boiling point. Low to medium temperature (<200°C)

resources are the most abundant worldwide, and require further research to improve the economic outlook and technical issues.

Economic and technological barriers currently exist which hinder deep, low-temperature geothermal systems. In sedimentary basins, temperatures adequate for binary geothermal systems often occur at depths greater than 2 km. Drilling accounts for over half of the cost of investment and increases exponentially with depth (Grasby et al., 2012; Serdjuk et al., 2013). Estimates of drilling costs in geothermal systems range from 2.5 to 50 million U.S. Dollars (Clauser and Ewert, 2018). Reducing the cost of drilling wells, and risk in investment would serve to advance the industry.

The most common technical issues in geothermal are related to fluid chemistry, including scaling, which can result in well-clogging, and corrosion (Gunnlaugsson et al., 2014). Gosnold et al. (2015) cited slow payoffs of initial investment costs, doubt of system profitability, and marginal profits of small geothermal systems as the reasons why oil and gas companies are not interested in investing in the technology. Additional reservoir data, including chemical characterization and methods for reduced drilling costs, could improve the profitability of geothermal systems.

Feasibility of geothermal development and depth to adequate temperature is often based on oil and gas data and regional heat flow, however, this is problematic due to the potential for thermal anomalies and poor quality of data, e.g., Firoozy and Holländer (2016); Grasby et al. (2012); Petersen and Lerche (1995); Wolff-Boenisch and Evans (2013). The cost of drilling, and therefore, initial investment, could be reduced by identifying and investigating site-specific thermal anomalies. In low-enthalpy basins, where conduction is the main process for heat flow, formations with high thermal conductivity can result in warm thermal anomalies.

In low-temperature sedimentary geothermal reservoirs, high thermal conductivity is observed in carbonate and evaporite formations, specifically, dolomite and halite (Daniilidis and Herber, 2017; Grasby et al., 2012). The average thermal conductivity of rocks in sedimentary basins is approximately $2.3 \text{ W m}^{-1} \text{ K}^{-1}$, whereas halite ranges from 5.4 to $5.9 \text{ W m}^{-1} \text{ K}^{-1}$ and dolomite 3.1 to $5.0 \text{ W m}^{-1} \text{ K}^{-1}$ (Grasby et al., 2012). As a result of the high thermal conductivity, heat is conducted towards the top of the formation, which increases the available temperature compared to other rocks at a similar depth. E.g., Daniilidis and Herber (2017) modeled temperature anomalies up to 25°C at the top of a salt formation. Considering geothermal gradients in sedimentary basins generally range from $25 - 40^{\circ}\text{C km}^{-1}$, this can reduce drilling depths by 25 to 50% (Grasby et al., 2012). Thus, targeting these formations could serve to reduce the cost of well-drilling in low-temperature settings, drastically reducing the initial investment costs of geothermal. Therefore, there is a need to study the heat flow associated with the novel idea of targeting halite and dolomite formations and optimizing their use.

When targeting highly soluble formations such as dolomite and halite, saturated formation waters are expected (Hanor, 1994). Therefore, conditions exist which can result in well-clogging. Well-clogging occurs when (super)saturated fluids in the production piping begin to precipitate minerals. Precipitation occurs due to temperature, pressure, and chemical changes. Changes in temperature and pressure occur as the formation waters are pumped from depth to surface, chemical changes can occur due to precipitation, creating feedback or changes in pH. Well clogging issues are currently generally managed after construction, e.g., Alt-Epping et al. (2013); Wanner et al. (2014). However, considering these factors as part of project planning can drive decision making regarding resource development and mitigation of well clogging, including the novel concept of engineered geothermal fluids, such as the introduction of MgCl_2 -brine heat

exchange fluids formed from highly soluble minerals, e.g., Moore and Holländer (2017). The interaction between the evaporite minerals and brines are an important factor in the success of geothermal development and provide an understanding of the potential for well clogging and corrosion in the system. Therefore, there is a need to study the geochemistry of the heat exchange fluid and formation when targeting evaporite and carbonate minerals with high thermal conductivity to understand potential technical issues and solutions.

In addition to the novel considerations of heat flow and geochemistry when targeting halite and dolomite, standard geothermal considerations in these formations are required. Adequate permeability must exist for production. In an evaporite formation dominated by halite, this would require hydraulic fracturing. Flow rates must be high enough for economic production rates. Adequate temperatures must exist at depth for binary geothermal production. Evaluations of the time it takes for the injected thermal plume to reach the production well are required to understand well longevity. Sedimentary basins are also commonly associated with oil and gas reservoirs, which results in available permeability, temperature, and geochemistry data. However, data from the oil and gas industry are notoriously error-ridden, with issues such as contamination from drilling fluids, inaccurate temperature readings, and missing data (Manz, 2011b; Wolff-Boenisch and Evans, 2013; Woroniuk et al., 2018). Caution must be used when evaluating geothermal systems using oil and gas data. Therefore, studies are required to characterize the full geothermal system associated with development in high thermal conductivity rocks and to characterize uncertainty.

1.2. Scope of work

Limited data are available on combined production, heat flow, and geochemistry in halite and dolomite formations in low-enthalpy geothermal settings. Daniilidis and Herber (2017)

investigated heat flow in a thick halite formation and found a significant thermal anomaly. Firoozy and Holländer (2016) characterized heat flow in the Manitoban portion of the Williston Basin, which contains, among others, halite and dolomite formations. Geothermal geochemistry is commonly investigated as a reaction to well-clogging issues. Alt-Epping et al. (2013) observed exsolution and carbonate precipitation in a geothermal production well. Wolff-Boenisch and Evans (2013) used oil and gas data to characterize the potential for scaling in wells in a hot sedimentary basin. Halite precipitation has been observed in several investigations, but none involved specifically targeting a halite formation, e.g., Borgia et al. (2012); Hesshaus et al. (2013). A targeted study coupling adequate production conditions, heat flow, and geochemistry in halite and dolomite formations is lacking and would serve to identify not only the potential for adequate temperatures but also potential risks for the development.

The research explored the potential for developing a geothermal system in the Williston Basin, Saskatchewan, Canada near high thermal conductivity halite, and dolomite minerals, including flow, heat transport, and geochemistry. Numerical coupled Thermo-Hydro-Chemical (THC) modeling, which takes into account physical and chemical-based flow, heat, and multicomponent reactive transport, was used to simulate the geothermal system. The model was used to characterize flow conditions including flow rates, well pressures, matrix, fracture permeability, density-driven convection, transient fluid properties and potential requirements for fracturing. Heat flow characterization involved vertical heat flow, the thermal conductivity of the individual formations, the movement of the plume of injected fluid at the production well, injection temperatures and varying fluid properties. The geochemistry was characterized for the formation and produced fluids, including hydrodynamic diffusion and geochemical reactions, and the

consideration of methods that would reduce precipitation, including an engineered heat exchange fluid.

Modeling of high-density, reactive transport systems, with transient fluid properties, complex mineral dissolution, and high ionic strengths is numerically challenging and requires model validation. Model validation generally involves testing model performance using test-cases or benchmarks. Problematic was the absence of a physically and chemically validated benchmark, which involved the interaction of a soluble evaporite or carbonate mineral such as halite at high ionic strength, the overlying aquifer, and density-driven flow. Field experiments documenting 2-D or 3-D high ionic strength carbonate and evaporite dissolution are also rare. Hamann et al. (2015) modeled precipitation that occurs during the formation of playas, and suggested a multicomponent reactive approach for this type of system. By understanding and measuring physical and chemical (laboratory and natural) systems, the understanding of modeling carbonate and evaporite geochemical reactions and fluid properties was improved. This knowledge can be transferred to deep geothermal reservoirs, where data are limited. Therefore, field, laboratory, and numerical studies were conducted on evaporite mineral formations to improve the understanding of the physical and chemical properties of water-rock interactions and modeling capabilities.

1.3. Objectives

The overall objective of this work was to evaluate the feasibility and potential benefits of a deep, low-temperature geothermal system targeting thermal anomalies caused by high thermal conductivity minerals such as halite and dolomite. The characterization of the geothermal system was completed using coupled thermal, hydraulic, and chemical (THC) numerical modeling.

To achieve the overall objective, four sub-objectives were used. First, to validate numerical methods used to calculate dissolution, flow, and transport of soluble mineral formations. This was completed in Chapters 3 and 4, where high ionic strength mineral – fluid subsurface interaction, was explored using physical and chemical laboratory, field, and numerical methods. These models also served to improve the modeler’s process understanding which can be as efficient as obtaining additional data (Holländer et al., 2009).

The second sub-objective was to assess the composition of heat exchange fluids produced when targeting halite formations using local geochemical data. This is completed in Chapter 5. This investigation both characterized potential precipitation of minerals in the system and explored the inhibition of scale formation by considering a designed heat exchange fluid composition.

The third sub-objective was to assess thermal anomalies in the Williston Basin associated with Halite and Dolomite formations and finally, the fourth sub-objective was to characterize a geothermal system in the Williston Basin, including flow, heat, and geochemistry. These two steps are completed in Chapter 6. This research details the thermal, physical, and chemical-based modeling, describing flow, temperature, and chemistry of a geothermal system overlying a salt formation. The geothermal potential was investigated using a case study in the Williston Basin in Saskatchewan, Canada, which has thick halite and dolomite formations from the Devonian period. The feasibility of the system was evaluated for adequate temperature for a binary system, flow for a 5 MW system.

The long-term vision is to contribute to the development of deep geothermal energy production in sedimentary basins worldwide by characterizing the benefits and risks of geothermal systems targeting thermal anomalies associated with high thermal conductivity. By choosing a case study in the Williston Basin, Canada, contributions were made toward the potential

development of geothermal power plants in Canada. Potential resources and assets that can improve the economics of geothermal development were also explored. The hydrogeochemical data enable geothermal developers to make informed decisions based on the geochemical characterization, to construct plants capable of handling the specific salinity parameters, preventing equipment corrosion, and mitigating geothermal well-clogging. Mineral-fluid geochemical modeling can also be used on developed wells to identify methods to understand mineral scaling and corrosion (Alt-Epping et al., 2013).

1.4. Manuscript-style thesis

This is a manuscript-type thesis consisting of 8 chapters. Chapter 1 provides an introduction to the research and objectives for targeting saline formations for geothermal development and testing numerical methods. Chapter 2 consists of a literature review of current geothermal knowledge in the Williston Basin, and saline systems and numerical modeling of fluid-mineral interactions. Chapters 3, 4, 5, and 6 are research manuscripts, along with a contextual preface. The first manuscript is the development of a benchmark box-problem where the dissolution of halite was measured in a benchtop aquifer and then numerically modeled (Chapter 3). The second manuscript is a numerical model outlining the use of reactive transport models to investigate the development of sinkholes in a gypsum formation, and comparison to site observations (Chapter 4). The third paper is the application of the data from the previous studies to an enhanced geothermal system geochemical model in the Canadian Prairies (Chapter 5). The fourth paper is a feasibility study investigating the targeting of halite and dolomite formations in the Williston Basin, Saskatchewan, Canada (Chapter 6). Finally, Chapter 7 offers overall conclusions and Chapter 8 provides recommendations based on this research.

2. Literature review

This literature review consists of two sections. Section 2.1 details the characterization of geothermal development targeting saline formation in the Williston Basin. Section 2.2 outlines the numerical approach to representing geothermal systems targeting soluble minerals and the methods used to validate these models. In the development of the methods used in this thesis, the Williston Basin was investigated to determine if it was an appropriate target for characterizing heat flow in high thermal conductivity formations for geothermal power production. Next, regions with adequate heat, high thermal conductivity, and flow were identified. Then potential issues with fluid geochemistry were identified by comparison to other geothermal scenarios. Finally, shortcomings and gaps in existing numerical methods were identified in the characterization of fluid-mineral interactions in the subsurface. Thus, the research topics and projects were selected to contribute to the scientific literature.

2.1. Geothermal

2.1.1. Williston Basin

The Williston Basin is an epicratonic Phanerozoic sedimentary basin, which extends into Manitoba, Saskatchewan, Alberta, North Dakota, South Dakota, and Montana (Figure 2-1). The Williston Basin is located within the larger Western Canada Sedimentary Basin (WCSB). The Williston Basin thermal reservoir was identified by Grasby et al. (2012) as having the potential to contribute to the baseload power supply in Canada. The U.S.A. portion of the Williston Basin was identified as having 28×10^{18} kJ of thermal energy in place, the greatest of any basins in America (Porro et al., 2012). The geothermal potential of Devonian carbonate rocks in the Alberta Basin was estimated to have the potential to produce up to 74 MW of electricity (Walsh, 2013). This

power could be produced by developing geothermal power plants in deep geothermal reservoirs (>200 m).



Figure 2-1. Outline of the extent of the Williston Basin.

The Williston Basin has been a previous target of geothermal development. In 1977, the University of Regina drilled a set of injection and production wells for heating, targeting the Winnipeg and Deadwood formations (Jessop and Vigrass, 1989). The wells produced high saline (110,000 ppm) water and achieved temperatures up to 74°C at 2088 m (Hutchence et al., 1986). The Winnipeg and Deadwood formations were initially targeted by the ongoing DEEP Earth Energy Production Corp. project. This project has drilled a test well to a depth of 3530 m into the Precambrian bedrock, with a bottom hole temperature of 125°C (Deep Corp., 2019a).

The most substantial barrier to further geothermal development in the Williston Basin is economics. Gosnold et al. (2015) indicated that investment has been limited due to high investment costs with slow payoffs, doubts that profit will be made, and marginal payoffs from small systems.

Clauser and Ewert (2018) indicated that deep geothermal requires proof of technology to drive further development in the industry. These current limitations to development have motivated this research on the potential for targeting saline formation with high thermal conductivity.

The DEEP Earth Energy Production Corp. project is estimated to cost \$51.3 million, with \$26.5 million in funding provided by the Government of Canada (Deep Corp., 2019b). Drilling costs, estimated at >50% of project costs, can be restrictive (Serdjuk et al., 2013). According to Majorowicz and Grasby (2010), in 2010 dollars, the cost to drill a doublet well would be:

$$Cost = 2 \cdot (3.23 * e^{0.000236 \cdot d}) \quad 2-1$$

where cost is in 10^6 dollars, d is the thickness of the overlying rock in m, and e is the mathematical operator. Based on Equation 2-1, a 5000 m well will cost approximately twice that of a 2000 m well. One advantage of development in the Williston Basin is the high number of oil and gas wells which can provide a vast amount of temperature and geological data. This greatly reduces the cost of the exploration phase, despite the uncertainty related to the quality of the data. In addition, the potential may exist to re-enter oil and gas wells.

A formation that contains higher temperatures at shallower depths would result in decreased drilling, and therefore capital costs. The high thermal conductivities of halite and dolomite result in the conduction of heat towards the top of the formation. Petersen and Lerche (1995) identified increased areas of heat at the top of salt formations, and lower heat below, compared to surrounding rock, due to the high thermal conductivity of salt. Daniilidis and Herber (2017) found at 25°C temperature increase resulting from a salt dome.

2.1.1.1. Stratigraphy

This study focuses on the portion of the Williston Basin located in Canada. The Williston Basin contains salt deposits in the Silurian, Devonian, Mississippian, Permian and Mesozoic periods. The Devonian period (419 to 358 million years ago) of the Paleozoic era (542 to 251 million years ago) were dominated by deposits of dolostone, limestone, shale, and evaporites (Figure 2-2). Within this period, a thick salt formation called the Prairie Evaporite was deposited in the Elk Point Basin (Bezys and McCabe 1996). Halite is the dominant mineral in the Prairie Evaporite Formation, deposited by the evaporation of fluids containing sodium chloride.

The Prairie Evaporite contains thick halite deposits with small amounts of potash and anhydrite, calcium chloride, and magnesium chloride (Earl and Nahm, 1981; Neuner and Fawcett, 2015). Across the Williston Basin, the thickness ranges from 0 to 300 m, and the depth of overburden ranges from 200 m to 2700 m (Grobe, 2000). In Saskatchewan, the Prairie Evaporite depth ranges from 1600 to 2700 m and the thickness from 0 to 220 m (Hamid et al., 2005). The Prairie Evaporite in Manitoba reaches a maximum thickness of 150 m, and depths of 760 to 1300 m near the Saskatchewan border in southwestern Manitoba (Davies et al., 1962; Lefond, 1969; TGI Williston Basin Working Group, 2008a; TGI Williston Basin Working Group, 2008b). The variable thickness of the salt deposits is influenced by not only topography during deposition, but by the influence of local dissolution by groundwater (Burke, 2001).

System	Group	Formation	Hydrocarbon
Mississippian	Madison	Charles	yes
		Mission Canyon	yes
		Souris Valley	
Devonian	Three Forks	Bakken	yes
		Big Valley	
	Saskatchewan	Torquay	yes
		Birdbear	yes
		Duperow	yes
	Manitoba	Souris River	

	Elk Point Basin	Dawson Bay	yes
		Prairie	
		Winnipegosis	
		Ashern	
Silurian		Interlake	yes
Ordovician		Stonewall	
	Bighorn	Stoney Mountain	yes
		Red River	yes
	Winnipeg	Winnipeg	yes
Cambrian		Deadwood	yes

Figure 2-2. Generalized Paleozoic stratigraphy in the Williston Basin based on Nicolas and Barchyn (2008).

During the formation of the Elk Point Basin, seas are believed to have entered and receded into the Williston Basin many times. Trapped seawater evaporated and deposited salts in layers based on the solubility of individual salts. The following sequence of deposition should be expected: limestone (CaCO_3), dolomite ($\text{CaMg}(\text{CO}_3)_2$), anhydrite (CaSO_4), halite (NaCl), sylvite (KCl), carnallite ($\text{KMgCl}_3 \cdot 6\text{H}_2\text{O}$) and bischofite ($\text{MgCl}_2 \cdot 6\text{H}_2\text{O}$) (Faure 1998). Sequencing of halite, anhydrite, and various potash salts is less than ideal due to seasonal layering (Wardlaw and Schwerdtner 1966), salinity fluctuations (Bannatyne 1983), and dissolution and re-mineralization (Holter 1969).

Formation fluids in the Williston Basin become saturated brines at 2500 – 2700 m, with a concentration of 200,000 mg L^{-1} chloride, 30,000 mg L^{-1} calcium, and 7,500 mg L^{-1} magnesium (Earl and Nahm, 1981). Based on freshwater injected into an evaporite formation, Hesshaus et al. (2013) measured a brine oversaturated with halite, barium, strontium, sulphates, with trace lead and iron oxides. Mineral composition of the Prairie Evaporite in southwest Manitoba was provided by Christie (2015) for an ERCO Worldwide salt solution mine (Table 2-1). The depth of the Prairie Evaporite in this region is approximately 1100 m (TGI Williston Basin Working Group, 2008a).

Table 2-1. Prairie Evaporite composition.

Compound or element	Concentration (mg L ⁻¹)
Na ⁺	126000
K ⁺	452
Ca ²⁺	677
Mg ²⁺	7.9
Fe ²⁺	0.1
SO ₄ ⁻	2300
Cl ⁻	223000
F ⁻	0.15
NO ₃ ⁻	9.38

2.1.2. Flow

Flow in geothermal systems is primarily controlled by permeability and pressure gradients. Natural advective flow in the Williston Basin is generally negligible (Ferguson, 2014). The pressure gradients in geothermal production are created by well pumping. Increasing pumping rates improves heat extraction and therefore power production, however, reduces the outlet temperature, and therefore the longevity of the well (Hofmann et al., 2014; Plummer et al., 2016; Xia et al., 2017). High flow rates can result in thermal short-circuiting (Jain et al., 2015). The distance between wells is an important factor in the lifetime of the well (Ferguson and Grasby, 2014). Several authors have concluded that optimal flow rates are project-specific e.g. Agemar et al. (2014). Additionally, the well diameter, number of wells, spacing of well, selection of horizontal or vertical wells, use of hydraulic fracturing, and number of perforations can be manipulated to enhance production e.g. Xia et al. (2017).

The Williston Basin was identified as having moderate porosity and permeability with an average porosity of 7.3 to 15.0% and permeability of 0.1 to 30.0 mD in the Lodgepole, Interlake, and Red River formations (Anderson, 2013). The values were considered lower than the acceptable minimum permeability of 50 – 100 mD for non-enhanced geothermal systems. However, the Devonian carbonate rocks in the Alberta Basin were found to have remarkable permeability, with a flow of $1800 \text{ m}^3 \text{ d}^{-1}$ (Walsh, 2013). Woroniuk et al. (2018) found little influence of Prairie Evaporite dissolution on the permeability of surrounding formations. Halite, on the other hand, has very poor permeability and would require fracturing

Reservoirs without adequate permeability can be hydraulically fractured, creating enhanced or engineered geothermal systems (EGS). Hydraulic fracturing is used to increase the permeability to increase flow rates in low permeability formation (Myers 2012). Hydraulic fracturing is the process of injecting high-pressure fluids into a formation to create, expand, and connect openings and deposit a propping agent, such as sand or beads to maintain the fracture width. Hydraulic fracturing can decrease the drop in pressure around the wellbore. The process can also be somewhat unpredictable, as natural fractures can be expanded and connected (Bennett, Calvez, et al. 2005). Many EGS projects are conducted in granite rock, including Cooper Basin, Australia; Soultz, France; Fenton Hill, United States; Hijiori, Japan; Ogachi, Japan; Desert Peak, United States; Rosemanowes, United Kingdom; Basel, Switzerland; and, Le Mayet, France; EGS projects in sedimentary basins include Groß Schönebeck, Germany (McClure and Horne 2014).

2.1.3. Heat

Geothermal systems for power production are generally either high ($>150^\circ\text{C}$) or medium ($80^\circ\text{C} - 150^\circ\text{C}$) temperature (Grasby et al., 2012). High-temperature systems produce steam, which directly drives turbines. Within the Williston Basin, medium temperatures are expected. At

these temperatures, geothermal fluid is not hot enough to drive turbines directly. Binary system technology uses a closed-loop heat exchanger to heat a working fluid, which flashes to steam (DiPippo, 2004). This technology has been used to produce electricity at temperatures as low as 80°C. Lower temperature geothermal fluids (< 80°C) can be used for direct heating.

Despite the limited development of geothermal power plants in the Williston Basin, numerous studies have provided valuable data to advance the field. Thermal gradients in the Williston Basin are estimated to range from 25-40°C km⁻¹ (Grasby et al., 2012). Additional data focusing on the geothermal gradient are also available from Ferguson and Grasby (2014) and Majorowicz and Grasby (2010). Heat transport was modeled and calibrated to oil and gas bottom hole temperature data by Firoozy and Holländer (2016); within the Manitoban portion of the basin, temperatures of 60°C were found at 2 km depth. A drilled well in southern Saskatchewan encountered a temperature of 125°C at 3530 m (Deep Corp., 2019a). Manz (2011a) estimated temperatures in North Dakota of 134°C at 2.35 km using 130 data points and the equation developed by Gosnold et al. (2015):

$$T = T_0 + \sum_{i=1}^N d \frac{\dot{Q}}{\lambda} \quad 2-2$$

where T_0 is the surface temperature (°C), d is the thickness of the overlying rock layer (m), \dot{Q} is regional heat flow (W m⁻²), and λ is the thermal conductivity of the overlying rock layers (W m⁻¹ K⁻¹). Thus, the thermal gradient is dependent on lithology. Heat transfer is a function of porosity, thermal conductivity, thermal diffusivity, specific heat capacity, and specific heat storage. Heat is transferred through advection, convection, and radiation. The primary natural driver of heat in deep, low to medium temperature formations targeted for geothermal use is conduction.

The thermal conductivity of a formation is the ability of that formation to conduct heat. Thermal conductivity is an important component in determining the thermal gradient. Rocks with high thermal conductivity have low resistance to heat flow and less temperature loss. As a result, heat moves through high thermal conductivity formations, and when low thermal conductivity formations are encountered the heat is held at the interface e.g., Daniilidis and Herber (2017) and Petersen and Lerche (1995). This study aims to characterize naturally occurring thermal anomalies resulting from high thermal conductivity formations.

Halite and dolomite have high thermal conductivity and therefore can have higher temperatures compared to other minerals at similar depths. Grasby et al. (2012) provided estimates of thermal conductivity for rock types in the Williston Basin, while Firoozy (2016) calculated in-site values based on temperature and pressure. Instead of focusing on the average geothermal gradient, the approach is taken to ascertain a range of measured data points at depth below the salt to apply as a boundary condition, and then use thermal conductivity data to calculate available heat within and above the salt formation. Heat flow is dependent on mineral thickness and depth, so site selection is an important consideration in thermal characterization.

A limited number of geothermal studies have focused on targeting salt formations for their high heat conductivity. The consideration of targeting the Prairie Evaporite is currently occurring at the University of Manitoba. Firoozy (2016) and Firoozy and Holländer (2016) studied heat flow to the Prairie Evaporite in the Manitoban portion of the Williston Basin and calculated 47°C at 1500 m. A site in Saskatchewan, at a Prairie Evaporite depth of 3 km, was calculated at 110°C. Devonian carbonate rocks in the Alberta Basin were found to have remarkable permeability and temperatures exceeding 110°C, with the Clarke Lake field estimated to have the potential to

produce up to 74 MW of electricity (Walsh, 2013). Therefore, adequate temperatures are expected to occur in the Saskatchewan portion of the basin.

Based on the Williston Basin stratigraphy, the formation most likely to benefit from the high heat conductivity of the Prairie Evaporite is the overlying Dawson Bay formation. The Dawson Bay Formation is 32 to 75 m thick., and comprised of limestone, shale, and dolomite (Bannatyne, 1983). The dolomite in this formation has high heat conductivity so that a geothermal well placed at the top of the formation should benefit from the heat conductivity of the Prairie Evaporite as well as that of the Dawson Bay formation. On the contrary, the Winnipegosis formation may experience cooler temperatures as a result of the high thermal conductivity of the Prairie Evaporite formation (Petersen and Lerche, 1995).

2.1.4. Hydrogeochemistry

An important geothermal consideration with utmost importance when targeting halite formations is the study of hydrogeochemistry. Geochemical characterization involves the study of the chemical composition of materials in the subsurface and the reactions they undergo. In geothermal systems, studying these features involves characterizing the primary composition of the reservoir rock as well as the secondary precipitates, scales, and secondary minerals that form as a result of geothermal operations. Hydrochemistry is the characterization of fluids, which can be highly saline and have unique properties. These properties are sensitive to temperature and pressure. Understanding hydrogeochemistry is important for the operation of geothermal power plants. As fluids cool in geothermal systems, minerals can precipitate leading to clogging of heat exchangers, injection wells, pipes, and the reservoir. Corrosion results from highly reducing conditions. As a result, the majority of technical issues in geothermal operation are related to chemistry (Gunnlaugsson et al., 2014). This includes corrosion, changes in permeability, scaling,

and clogging. Remedial actions can be taken to reduce clogging, for example, gypsum clogging is reduced by the addition of sodium phosphonate, which binds with calcium. Moore and Holländer (2017) considered MgCl_2 as a heat exchange fluid in highly saline systems that targeted thick halite formations for their high heat conductivity.

Calibration is difficult in feasibility studies, where construction has yet to occur. Therefore, the input of quality data is of paramount importance to the accurate representation of geothermal systems. Within the Williston Basin, hydrogeochemical data were taken from oil and gas databases, such as the USGS National Produced Waters Geochemical Database (Blondes et al., 2017), which contains geochemical, pressure and depth data from oil and gas wells. However, it is noted that oil and gas data are notoriously problematic (Wolff-Boenisch and Evans, 2013). Data on the composition of the Prairie Evaporite were available from a salt solution mine (Christie, 2015). Detailed isopach and structural data are available from the TGI Williston Basin Working Group (2008a).

Geothermal geochemistry has been investigated in several studies of geothermal wells, however, it was generally identified as an important factor after issues develop. No studies were identified which attempted to predict geothermal fluid composition prior to developing a specific formation, or region as part of a feasibility study. Clark et al. (2010) found that geothermal fluids tend to range from a pH of 5 to 10, 80% of samples had a TDS less than $5,000 \text{ mg L}^{-1}$, with 10% greater than $200,000 \text{ mg L}^{-1}$; the dissolved solids in geothermal fluids are dominated by sodium chloride.

Hydrogeochemical modeling has successfully been applied to predict and understand geothermal systems. The most common minerals of concern in geothermal systems were calcite and barite. Alt-Epping et al. (2013) modeled hydrogeochemical conditions, including carbonate

mineral precipitation, in a geothermal well in carbonate rock at Bad Blamu, Austria; the data were calibrated to pressure, temperature and fluid composition field data, to understand drivers of precipitation, exsolution, pH changes, and inhibitor use. Bächler (2003) and Bächler and Kohl (2005) found that for the Soultz-sous-Forêts, where calcite, dolomite, dissolved quartz, and pyrite precipitated, the Pitzer approach for the calculation of activity coefficients was suitable, due to the high salinity of fluids and implemented new kinetic laws for calcite, dolomite, quartz, and pyrite. Wanner et al. (2017) were able to successfully predict calcite scaling resulting from exsolution observed in a geothermal power plant in southern Germany using a reactive transport model. Bozau et al. (2015) modeled equilibrium reactions in the North German Basin dominated by Na^+ and Cl^- up to 400 g L^{-1} between formation fluid and well casing materials, scales were dominated by barite; they recommended more experimental work to test modeling. When seawater was injected into a sandstone reservoir, Barite, CaSO_4 , and dolomite were found to precipitate (Fu et al., 2012). In a high-temperature system, dominated by NaCl had scale dominated by galena and aragonite or calcite (PbS and CaCO_3) (Demir et al., 2014). Yanagisawa (2015) found calcium carbonate to be a major mineral of concern in hot spring binary systems.

Halite was notably missing as a mineral of concern in most geothermal systems. Halite was of concern in a system where CO_2 was used as a heat exchange fluid (Borgia et al., 2012) and in a deep geothermal well that was shut down for six months (Hesshaus et al., 2013). Hesshaus et al. (2013) suggested injecting freshwater along with produced water to remove salt from the vicinity of the fracture and decrease the saturation of the injected water. This is feasible in systems that contain local salt deposits, however, would not work in a halite formation.

Due to their high solubility, brines in evaporite formations generally reflect formations composition. Bassett and Bentley (1982) found that brines reflected reactivity with the host rock

and salinity was derived from evaporites; calculated equilibrium concentrations showed a good correlation with observed brines. Fu et al. (2012) found that equilibrium modeling produced a reasonable match between modeled and measured chemical composition of produced water within the residence time at reservoir conditions. Neuner and Fawcett (2015) modeled equilibrium reactive transport in the Prairie Evaporite in the Alberta Basin and found connections between hydrochemistry and dissolution at long time scales. Wolff-Boenisch and Evans (2013) used chemical analysis from petroleum wells, combined with an equilibrium treatment with chalcedony to reconstruct in-site concentrations.

2.2. Modeling

Geothermal problems are influenced by 3 main components (1) the flow through the system, (2) changes in mineral composition resulting from dissolution, precipitation, solute transport, and chemical reactions, and (3) heat transport (Grasby et al., 2012). The development of numerical models to evaluate the potential flow, well configuration, heat transport, and geochemical composition can be used to better understand potential power production in the Williston Basin. The research outlined in this thesis involves complex THC modeling of geothermal systems.

Numerical modeling can be used to understand, analyze and manipulate scenarios regarding geothermal power production including mass transport, heat transport, density-driven flow, thermal material properties, and fracture flow e.g. Alt-Epping et al. (2013), Bozau et al. (2015), Wanner et al. (2014), and Xia et al. (2017). Geochemical software such as PHREEQC (Parkhurst and Appelo, 2013) can be used to calculate saturation indices at different temperatures and predict the likelihood of precipitates based on individual speciation e.g. Alt-Epping et al.

(2013). This data can then be used to drive decision making regarding the development and operation of geothermal power plants.

The lack of calibration data and examples of systems with mineral-rock interaction is problematic. In this case, model performance through code validation is of paramount importance in ensuring accurate results. Therefore, in addition to the geothermal modeling, numerical codes were tested and validated for two additional problems, a physically-based benchmark exploring the mineral-water interaction and resulting density-driven flow and a near-surface field study of mineral-water interaction exploring sinkhole development.

2.2.1. Validation

Code validation is the process of ensuring that numerical calculations are giving correct numerical results e.g. Diersch (2014). Geothermal numerical models can be validated by using site-specific calibration data e.g. Alt-Epping et al. (2013), Bächler and Kohl (2005), and Bozau et al. (2015). However, studies such as this, which focus on the feasibility and potential for the development of geothermal systems, are theoretical and do not have available field data.

Benchmark problems are commonly used to validate codes, improving confidence in results. When analytical results for benchmarks are available for comparison, code validation is a simple process e.g. Henry (1964). However, for complex density-driven flow problems, analytical solutions do not exist. However, codes can be validated using comparable benchmarks with similar physics, where analytical or calibration data are available e.g. Konz (2010), Schincariol and Schwartz (1990), Simmons et al. (1999), Stoeckl et al. (2016) and Elder (1967). The benchmark most commonly associated with evaporite dissolution is NEA and OECD (1988) however, this problem has not been physically validated (Konikow et al., 1997). A physical-based benchmark

problem for salt flow in aquatic-solid systems/environments, which includes measured salt distribution due to salt dissolution, and includes kinetics of the dissolution process itself is required. Therefore, idealized, physical-based lab measurements were completed as part of this research for the verification of numerical models during fluid-mineral interactions and resulting density-driven flow.

2.2.2. Calibration

Model calibration is the process of adjusting the input parameters and boundary conditions to obtain a close fit to observed data. Calibration can be trial and error, using both hard hydrogeological principles and intuition, or mathematical optimization techniques. To calibrate a model, equations can be examined to understand the influence of individual parameters on the outcome. However, when considering systems with no available measurements, such as the proposed geothermal project, there is no way to determine closeness of fit. However, the relationship between parameters and outcomes can be investigated.

Mineral-fluid interactions in geothermal have been calibrated in limited scenarios involving inhibitors and scaling e.g. Alt-Epping et al. (2013), Bächler and Kohl (2005), Wanner et al. (2017). This geothermal scenario requires an understanding of calibration of reactive transport scenarios during precipitation and dissolution of the formation itself. Examples that are not physically validated include Hamann et al. (2015) and Neuner and Fawcett (2015). To further understand these scenarios, a field study was conducted where data were collected and used to calibrate a flow model used to predict mineral-rock interaction during the formation of a sinkhole.

2.2.3. Parameters

The research outlined in this thesis involves complex THC modeling of high ionic strength geothermal and other mineral-fluid interaction systems. Naturally occurring high ionic strength solutions (>1 M) have complex density, viscosity, and ionic interaction, complicated by interaction with geological media (Zhang et al., 2005). Numerical modeling of these scenarios is difficult because codes are generally developed for dilute aqueous solutions (Oldenburg and Pruess, 1995). High ionic strengths may cause the breakdown of models; e.g. the Debye-Hückle expressions require an ionic strength term to deal with concentrations greater than seawater (Parkhurst and Appelo, 2013). The Pitzer (1973) database can be used to study high ionic activity. To test the ability of numerical codes to handle complex, high ionic strength mineral dissolution and transport, field and laboratory studies that make use of the same parameters as geothermal problems were studied (Table 2-2).

Table 2-2. Outline of parameters examined by the laboratory and field studies, as well as those required in the geothermal study.

Minerals	PEMD study	Gypsum Dissolution	Geothermal Studies
Permeability	x	x	x
Pressure gradients	x	x	x
Porosity	x	x	x
Dispersion	x	x	x
Diffusion	x	x	x
Boundary conditions	x	x	x
Reactive Transport		x	x
Solute transport	x	x	x
Density-driven flow	x		x
Thermal conductivity			x
Viscosity	x	x	x

2.2.3.1. Flow

Flow is primarily defined in numerical models through hydraulic gradients and flow rate boundaries as well as permeability. Other factors resulting from heat and chemical transport can

result in density-driven flow patterns, which are discussed below. Assuming a nondeforming formation, with variable density Darcy-type, and saturated flow, mass conservation of fluid in a saturated porous medium is given by Diersch (2014):

$$S_0 \frac{\partial h_0}{\partial t} + \nabla \cdot \vec{q} = Q + Q_{EOB} \quad 2-3$$

where S_0 is specific storage due to fluid and medium compressibility (m^{-1}), h_0 is the equivalent freshwater hydraulic head (m), t is time (s), Q is flow sources and sinks (s^{-1}) and Q_{EOB} is a sink/source correction for the Oberbeck-Boussinesq approximation. The Darcy flux \vec{q} ($m s^{-1}$) is given as:

$$\vec{q} = -\mathbf{K} f_u \cdot (\nabla h_0 + \chi \vec{e}) \quad 2-4$$

where \mathbf{K} is hydraulic conductivity ($m s^{-1}$), f_u is a viscosity relation function (-), χ is the buoyancy coefficient (-), and \vec{e} is the gravitational unit vector (-). However, the use of permeability k (m^2) to define the fluid flow in deep geothermal systems is more appropriate than hydraulic conductivity, because hydraulic conductivity \mathbf{K} ($m s^{-1}$) is dependent on fluid properties:

$$\mathbf{K} = k \left(\frac{\rho g}{\mu} \right) \quad 2-5$$

where ρ is fluid density ($kg m^{-3}$), g is the acceleration of gravity ($m s^{-2}$), and μ is fluid dynamic viscosity ($kg m^{-1} s^{-1}$). For density-driven flow, fluid hydraulic head h (m) is related to the actual density of the fluid, ρ ($kg m^{-3}$). Freshwater hydraulic head, h_0 (m) is defined as:

$$h_0 = \frac{P}{\rho_0 g} + z \quad 2-6$$

where P is pressure ($kg m^{-1} s^{-2}$), g is the gravitational acceleration ($m s^{-2}$), ρ_0 is freshwater density and z is elevation head (m). Thus, at two points with equal pressure and elevation, but differing

fluid density, the hydraulic head will differ. Dissolving minerals result in increased fluid density. Flow calculations are made using the equivalent freshwater head. The equivalent freshwater hydraulic head can be calculated as:

$$h_0 = (1 + \chi)h_s - \chi z \quad 2-7$$

where h_s is the saltwater hydraulic head (m) and z is the elevation head (m).

The buoyancy coefficient (χ) (-) describes the ratio between maximum and minimum density and is defined as:

$$\chi = \frac{\rho_s - \rho_0}{\rho_0} \quad 2-8$$

where ρ_s (kg m^{-3}) is the saltwater density and ρ_0 (kg m^{-3}) is the freshwater density. For this work, a value of 0.2 was applied.

2.2.3.2. Solute Transport

In deep geothermal systems targeting halite formations, geochemical reactions and reactive transport, including mineral dissolution and precipitation, will play an important role in the development of hydrochemistry of the working fluid. Transport of these solutes will result in density-driven flow. Flow and spread of minerals within the fluid will depend on porosity, dispersion, and diffusion.

PHREEQC (Parkhurst and Appelo, 2013) can be used to calculate saturation indices, aqueous species distribution, density, and specific conductance. PHREEQC completes 7 types of speciation, batch reaction, and transport calculation: (1) initial solution or speciation calculations, (2) initial exchange calculations, (3) initial surface calculations, (4) initial gas-phase calculations, (5) batch-reaction calculations, (6) advective-transport calculations, and (7) advective-dispersive

transport calculations. These calculations are done by solving a series of algebraic equations. Functions, primarily derived from mole balance equations for each element, exchange site, or mass action are solved simultaneously to determine equilibrium.

Dissolved species (i) are characterized by activity, α_i (mol kg⁻¹), activity coefficient e.g. [Na⁺] γ (-), molality m_i (mol kg⁻¹), number of moles in solution n_i (mol), and the mass of the solvent in water in an aqueous solution W_{aq} (kg). One master species per element, e.g. Na⁺ for sodium or element valance state is defined along with the hydrogen ion activity, electron activity, and water activity.

$$\alpha_i = \gamma_i m_i \quad 2-9$$

$$n_i = m_i W_{aq} \quad 2-10$$

Equilibrium among aqueous species requires that all mass-action equations for aqueous species are satisfied, for example for Na⁺ + Cl⁻ = NaCl

$$E = \frac{[Na^+][Cl^-]}{[NaCl]} \quad 2-11$$

where E is the equilibrium constant. PHREEQC calculates the activity of ions and ion concentration. The Debye-Hückle theory defines the relationship between ion activity and ion strength. Solubility is a function of pressure, temperature, and the ionic strength of the solution.

Reaction modules take component concentrations from each model cell, run geochemical reactions using the capabilities of PHREEQC, and return updated component concentrations to the cells (Parkhurst and Wissmeier, 2015). In the split-operator technique, simultaneous and dependent solute transport and geochemical reactions are decoupled into independent, sequential

calculation steps. The split operator technique is applied in piChem using a non-iterative sequential approach (SNIA) with user-defined time steps. The ion species composition is reconstructed from the transported element assembly and charge balance before it is speciated with the solid and gas phases. The numerical error introduced by the split operator technique can be reduced by containing time steps.

Within piCHEM, aqueous flow is expressed as the transport of individual components (Wissmeier and Barry, 2008; Wissmeier et al., 2009). The advection-diffusion/dispersion equation is used for multi-component transport (Bear, 1972):

$$\frac{\partial \theta C_i}{\partial t} = -\nabla \cdot (\vec{q} C_i) + \nabla \cdot (\theta \mathbf{D} \nabla C_i) + S_c \quad 2-12$$

where θ is the relative liquid phase saturation ($\text{m}^3 \text{m}^{-3}$), C_i is the concentration of solution species i (kg m^{-3}), \vec{q} is the Darcy flux (m s^{-1}), \mathbf{D} is the coefficient of hydrodynamic dispersion including both mechanical dispersion and diffusion ($\text{m}^2 \text{s}^{-1}$) and S_c is sources and sinks ($\text{kg m}^{-3} \text{s}^{-1}$). The liquid phase is composed of solution species:

$$\theta = \frac{\sum_i n_i m_i}{\rho} \quad 2-13$$

where n_i (mol m^3) are the moles of solution species i in a control volume with a molar weight of m_i (kg mol^{-1}) and ρ is fluid density (kg m^{-3}). Phase mass balance based on all solution species in the liquid phase:

$$\frac{\partial \rho \theta}{\partial t} = -\nabla \cdot \rho \theta \vec{v} \quad 2-14$$

where \vec{v} is the fluid velocity (m s^{-1}).

2.2.3.3. Heat Transport

Heat transport is an important component in deep geothermal power production. Geothermal systems require adequate heat at the production well to produce electricity. Heat at depth can be calculated by considering known temperature values, regional heat flow, or individual formation thermal conductivity. The injection temperature is an important factor in determining the longevity of the system. Temperature influences mineral solubility, which impacts hydrogeochemistry, and fluid viscosity which influences flow patterns.

The convective form of heat transport for a variable-density, Darcy-type flow conduction and advection can be defined as (Diersch, 2014):

$$(\varepsilon\rho c + (1 - \varepsilon)\rho_m c_m) \frac{\partial T}{\partial t} + \rho c \vec{q} \cdot \nabla T - \nabla \cdot (\mathbf{A} \cdot \nabla T) = H_e - \rho c (T - T_0) Q \quad 2-15$$

where ε is porosity (-), ρ is the mass density of the fluid (kg m^{-3}), c is specific heat capacity ($\text{m}^2 \text{s}^{-2} \text{K}^{-1}$), ρ_s is the mass density of the solid (kg m^{-3}), c_s is the specific heat capacity of solid ($\text{m}^2 \text{s}^{-2} \text{K}^{-1}$), T is the temperature (K), T_0 is the reference temperature (K), t is time (s), \vec{q} is the Darcy flux (m s^{-1}), \mathbf{A} is the hydrodynamic thermodispersion tensor ($\text{kg m s}^{-3} \text{K}^{-1}$) and Q is a sink/source term (s^{-1}).

2.3. Summary

High thermal conductivity halite and dolomite formations with the potential to produce warm thermal anomalies are considered as geothermal reservoirs for power production in the Williston Basin. This improves economic feasibility of geothermal systems by reducing drilling costs. Halite and dolomite are highly reactive, so hydrogeochemistry is a key component in this study. Complex THC numerical modeling is used to assess the feasibility of the geothermal system. Since this is a feasibility study, field data for calibration and validation are limited.

Therefore, numerical models are validated for performance in fluid-mineral scenarios that can be physically validated.

2.4. Chapter 1 & 2 References

- Agemar, T., Weber, J., Schulz, R., 2014. Deep Geothermal Energy Production in Germany. *Energies*, 7(7): 4397-4416.
- Alt-Epping, P., Waber, H.N., Diamond, L.W., Eichinger, L., 2013. Reactive transport modeling of the geothermal system at Bad Blumau, Austria: Implications of the combined extraction of heat and CO₂. *Geothermics*, 45: 18-30. DOI:10.1016/j.geothermics.2012.08.002
- Anderson, T.C., 2013. Geothermal Potential of Deep Sedimentary Basins in the United States. Unconventional Resources Technology Conference (URTEC).
- Bächler, D., 2003. Coupled thermal-hydraulic-chemical modelling at the Soultz-sous-Forêts HDR reservoir (France), Swiss Federal Institute of Technology Zurich, Zurich, Switzerland, 151 pp.
- Bächler, D., Kohl, T., 2005. Coupled thermal–hydraulic–chemical modelling of enhanced geothermal systems. *Geophysical Journal International*, 161(2): 533-548. DOI:10.1111/j.1365-246X.2005.02497.x
- Bannatyne, B., 1983. Devonian potash deposits in Manitoba. 0317-0926, Manitoba Department of Energy and Mines, Winnipeg, Manitoba.
- Bassett, R.L., Bentley, M.E., 1982. Geochemistry and hydrodynamics of deep formation brines in the Palo Duro and Dalhart basins, Texas, U.S.A. *J Hydrol*, 59(3–4): 331-372. DOI: 10.1016/0022-1694(82)90095-6
- Bear, J., 1972. Dynamics of fluids in porous media. American Elsevier Publishing Company, Inc.
- Blondes, M.S. et al., 2017. U.S. Geological Survey National Produced Waters Geochemical Database v2.4. In: Survey, U.S.G. (Ed.).
- Borgia, A., Pruess, K., Kneafsey, T.J., Oldenburg, C.M., Pan, L., 2012. Numerical simulation of salt precipitation in the fractures of a CO₂-enhanced geothermal system. *Geothermics*, 44: 13-22. DOI:10.1016/j.geothermics.2012.06.002
- Bozau, E., Häußler, S., van Berk, W., 2015. Hydrogeochemical modelling of corrosion effects and barite scaling in deep geothermal wells of the North German Basin using PHREEQC and PHAST. *Geothermics*, 53: 540-547. DOI: 10.1016/j.geothermics.2014.10.002
- Burke, R., 2001. Some aspects of salt dissolution in the Williston Basin of North Dakota. In: Survey, N.D.G. (Ed.), NDGS Newsletter, pp. 1-5.
- Christie, J., 2015. Prairie Evaporite Composition. In: Moore, K. (Ed.). ERCO Worldwide, Toronto, Ontario.
- Clark, C., Harto, C., Sullivan, J., Wang, M., 2010. Water use in the development and operation of geothermal power plants, Argonne National Laboratory (ANL).
- Clauser, C., Ewert, M., 2018. The renewables cost challenge: Levelized cost of geothermal electric energy compared to other sources of primary energy – Review and case study. *Renewable and Sustainable Energy Reviews*, 82: 3683-3693. DOI: 10.1016/j.rser.2017.10.095

- Daniilidis, A., Herber, R., 2017. Salt intrusions providing a new geothermal exploration target for higher energy recovery at shallower depths. *Energy*, 118: 658-670. DOI:10.1016/j.energy.2016.10.094
- Davies, J.F., Bannatyne, B.B., Barry, G.S., McCabe, H.R., 1962. *Geology and Mineral Resources of Manitoba*, Winnipeg, Manitoba.
- Deep Corp., 2019a. DEEP successfully completes first geothermal test well. In: Production, D.E.E. (Ed.), *Our latest news*. Deep Corp., Saskatoon, Canada.
- Deep Corp., 2019b. Prime Minister announces support for Canada's first geothermal power facility. In: Production, D.E.E. (Ed.), *Our latest news*. Deep Corp., Saskatoon, Canada.
- Demir, M.M., Baba, A., Atila, V., İnanlı, M., 2014. Types of the scaling in hyper saline geothermal system in northwest Turkey. *Geothermics*, 50(0): 1-9. DOI: 10.1016/j.geothermics.2013.08.003
- Diersch, H., 2002. *FEFLOW-White papers vol. I*. WASY Ltd., Berlin.
- Diersch, H., 2014. *FEFLOW Finite Element Modeling of Flow, Mass and Heat Transport in Porous and Fractured Media*. Springer, New York.
- DiPippo, R., 2004. Second Law assessment of binary plants generating power from low-temperature geothermal fluids. *Geothermics*, 33(5): 565-586. DOI: 10.1016/j.geothermics.2003.10.003
- Earl, S.L., Nahm, J.J., 1981. Use Of Chemical Salt Precipitation Inhibitors To Maintain Supersaturated Salt Muds For Drilling Salt Formations. Society of Petroleum Engineers. DOI:10.2118/10097-MS
- Elder, J.W., 1967. Transient convection in a porous medium. *J Fluid Mech*, 27(03): 609-623. DOI:10.1017/S0022112067000576
- Ferguson, G., 2014. Deep Injection of Waste Water in the Western Canada Sedimentary Basin. *Groundwater*: n/a-n/a. DOI:10.1111/gwat.12198
- Ferguson, G., Grasby, S., 2014. The geothermal potential of the basal clastics of Saskatchewan, Canada. *Hydrogeol J*, 22(1): 143-150. DOI:10.1007/s10040-013-1061-5
- Firoozy, N., 2016. *Assessment of Geothermal Application for Electricity Production from the Prairie Evaporite Formation of Williston Basin in South-West Manitoba*, University of Manitoba, Winnipeg, Manitoba, 165 pp.
- Firoozy, N., Holländer, H.M., 2016. Numerically derived temperature data set of Manitoba's subsurface formations GEOVancouver. *Proceedings of the 69th CGS Conference*, Vancouver, Canada.
- Fu, Y., van Berk, W., Schulz, H.-M., 2012. Hydrogeochemical modelling of fluid-rock interactions triggered by seawater injection into oil reservoirs: Case study Miller field (UK North Sea). *Appl Geochem*, 27(6): 1266-1277. DOI: 10.1016/j.apgeochem.2012.03.002
- Gosnold, W., Crowell, A., Nordeng, S., Mann, M., 2015. Co-Produced and Low-Temperature Geothermal Resources in the Williston Basin. *GRC Transactions*, 39: 653-660.
- Government of Canada, 2019. *Canada's Action on Climate Change*. In: Government of Canada (Ed.), *Weather, climate and hazards*. Government of Canada, Ottawa, Canada.
- Grasby, S.E. et al., 2012. *Geothermal Energy Resource Potential of Canada*, Geological Survey of Canada. DOI:10.4095/291488
- Grobe, M., 2000. *Distribution and thickness of salt within the Devonian Elk Point Group*, Western Canada Sedimentary Basin, Alberta Energy and Utilities Board, Edmonton, Alberta.

- Gunnlaugsson, E., Ármannsson, H., Þórhallsson, S., Steingrímsson, B., 2014. Problems in geothermal operation-scaling and corrosion. In: Program, U.N.U.-G.T., LaGeo (Eds.), Short Course VI on Utilization of Low- and Medium-Enthalpy Geothermal Resources and Financial Aspects of Utilization, Santa Tecla, El Salvador.
- Hamann, E., Post, V., Kohfahl, C., Prommer, H., Simmons, C.T., 2015. Numerical investigation of coupled density-driven flow and hydrogeochemical processes below playas. *Water Resources Research*, 51(11): 9338-9352. DOI:10.1002/2015WR017833
- Hamid, H., Morozov, I.B., Kreis, L.K., 2005. Seismic Delineation of the Prairie Evaporite Dissolution Edge in South-central Saskatchewan. In: Survey, S.G. (Ed.), Summary of Investigations 2005. Saskatchewan Geological Survey, Saskatoon, pp. 11.
- Hanor, J.S., 1994. Origin of saline fluids in sedimentary basins. *Geological Society, London, Special Publications*, 78(1): 151-174. DOI:10.1144/gsl.sp.1994.078.01.13
- Henry, H.R., 1964. Effects of dispersion on salt encroachment in coastal aquifers, sea water in coastal aquifers. *US Geological Survey Water Supply Paper*, 1613-C: 70-84.
- Hesshaus, A., Houben, G., Kringel, R., 2013. Halite clogging in a deep geothermal well – Geochemical and isotopic characterisation of salt origin. *Physics and Chemistry of the Earth, Parts A/B/C*, 64(0): 127-139. DOI:10.1016/j.pce.2013.06.002
- Hofmann, H. et al., 2014. Potential for enhanced geothermal systems in Alberta, Canada. *Energy*, 69: 578-591. DOI:10.1016/j.energy.2014.03.053
- Holländer, H.M. et al., 2009. Comparative predictions of discharge from an artificial catchment (Chicken Creek) using sparse data. *Hydrol. Earth Syst. Sci.*, 13(11): 2069-2094. DOI:10.5194/hess-13-2069-2009
- Hutchence, K., Weston, J.H., Law, A.G., Vigrass, L.W., Jones, F.W., 1986. Modeling of a Liquid Phase Geothermal Doublet System at Regina, Saskatchewan, Canada. *Water Resources Research*, 22(10): 1469-1479. DOI:10.1029/WR022i010p01469
- Jain, C., Vogt, C., Clauser, C., 2015. Maximum Potential for Geothermal Power in Germany Based on Engineered Geothermal Systems. *Geothermal Energy*, 3(15): 1-20. DOI:10.1186/s40517-015-0033-5
- Jessop, A.M., Vigrass, L.W., 1989. Geothermal measurements in a deep well at Regina, Saskatchewan. *J Volcanol Geoth Res*, 37(2): 151-166. DOI: 10.1016/0377-0273(89)90067-X
- Konikow, L., Sanford, W., Campbell, P., 1997. Constant-concentration boundary condition: Lessons from the HYDROCOIN variable-density groundwater benchmark problem. *Water Resources Research*, 33(10): 2253-2261.
- Konz, M., 2010. 2D benchmark experiments and simulations of density coupled flow problems, Universität Basel, Basel.
- Lefond, S.J., 1969. Handbook of world salt resources. Springer Science & Business Media, New York.
- Majorowicz, J., Grasby, S.E., 2010. Heat flow, depth–temperature variations and stored thermal energy for enhanced geothermal systems in Canada. *Journal of Geophysics and Engineering*, 7(3): 232.
- Manz, L.A., 2011a. Deep Geothermal Resources: Estimated Temperatures on Top of the Duperow Formation Kenmare 100K Sheet, North Dakota. In: Murphy, E.C., Helms, L.D. (Eds.), North Dakota Geothermal Maps. North Dakota Geological Survey, Bismark, ND.

- Manz, L.A., 2011b. Deep Geothermal Resources: Estimated Temperatures on Top of the Red River Formation Kenmare 100K Sheet, North Dakota. In: Murphy, E.C., Helms, L.D. (Eds.), North Dakota Geothermal Maps. North Dakota Geological Survey, Bismark, ND.
- Moore, K.R., Holländer, H.M., 2017. Geochemical Modelling of the Dissolution of Salt Minerals and Application to Geothermal Energy, GeoOttawa 2017. Canadian Geotechnical Society, Ottawa, Canada.
- Moore, K.R., Holländer, H.M., Basri, M., Roemer, M., 2019. Application of geochemical and groundwater data to predict sinkhole formation in a gypsum formation in Manitoba, Canada. *Environmental Earth Sciences*, 78(6): 193. DOI:10.1007/s12665-019-8188-1
- NEA, OECD, 1988. International Hydrocoin project: Groundwater hydrology modelling strategies for performance assessment of nuclear waste disposal. Level 1: Code verification, Nuclear Energy Agency (NEA), Organisation for Economic Co-operation and Development (OECD), Paris.
- Neuner, M., Fawcett, S., 2015. Reactive Transport Model of the Carbonate-Evaporite Elk Point Group Underlying the Athabasca Oil Sands, 10th Annual International Conference on Acid Rock Drainage & IMWA Annual Conference, Santiago, Chile.
- Nicolas, M.P.B., Barchyn, D., 2008. Williston Basin Project (Targeted Geoscience Initiative II): Summary report of Paleozoic stratigraphy, mapping and hydrocarbon assessment, southwestern Manitoba. In: Survey, M.G. (Ed.). Geoscientific Paper. Government of Manitoba, Winnipeg.
- Oldenburg, C.M., Pruess, K., 1995. Dispersive Transport Dynamics in a Strongly Coupled Groundwater-Brine Flow System. *Water Resources Research*, 31(2): 289-302. DOI:10.1029/94WR02272
- Parkhurst, D.L., Appelo, C., 2013. Description of input and examples for PHREEQC version 3-- A computer program for speciation, batch-reaction, one-dimensional transport, and inverse geochemical calculations. In: Survey, U.S.G. (Ed.), U.S. Geological Survey Techniques and Methods Section A, Groundwater Book 6, Modeling Techniques, Denver, Colorado, pp. 497.
- Parkhurst, D.L., Wissmeier, L., 2015. PhreeqcRM: A reaction module for transport simulators based on the geochemical model PHREEQC. *Advances in Water Resources*, 83: 176-189. DOI:10.1016/j.advwatres.2015.06.001
- Petersen, K., Lerche, I., 1995. Quantification of thermal anomalies in sediments around salt structures. *Geothermics*, 24(2): 253-268. DOI:10.1016/0375-6505(94)00051-D
- Pitzer, K.S., 1973. Thermodynamics of electrolytes. I. Theoretical basis and general equations. *The Journal of Physical Chemistry*, 77(2): 268-277. DOI:10.1021/j100621a026
- Plummer, M.A. et al., 2016. Primary Constraints on the Design of an Enhanced Geothermal System Reservoir, 50th U.S. Rock Mechanics/Geomechanics Symposium. American Rock Mechanics Association, Houston, Texas, pp. 12.
- Porro, C., Esposito, A., Augustine, C., Roberts, B., 2012. An estimate of the geothermal energy resource in the major sedimentary basins in the United States. *Geothermal Resources Council Transactions*, 36: 1359-1369.
- Prairie Climate Centre, 2018. Historical and Projected Values High Carbon 2021 - 2050, High Carbon 2021 - 2050. Prairie Climate Centre, Winnipeg, Canada.
- Schincariol, R.A., Schwartz, F.W., 1990. An experimental investigation of variable density flow and mixing in homogeneous and heterogeneous media. *Water Resources Research*, 26(10): 2317-2329. DOI:10.1029/WR026i010p02317

- Serdjuk, M., Dumas, P., Angelino, L., Tryggvadottir, L., 2013. Geothermal Investment Guide.
- Simmons, C.T., Narayan, K.A., Wooding, R.A., 1999. On a test case for density-dependent groundwater flow and solute transport models: The Salt Lake Problem. *Water Resources Research*, 35(12): 3607-3620. DOI:10.1029/1999wr900254
- Stoeckl, L., Walther, M., Graf, T., 2016. A new numerical benchmark of a freshwater lens. *Water Resources Research*, 52(4): 2474-2489. DOI:10.1002/2015WR017989
- TGI Williston Basin Working Group, 2008a. Devonian Prairie Evaporite: isopach. In: Manitoba Science, T., Energy and Mines, Survey, M.G. (Eds.), *Stratigraphic Map SM2008-DPE-I*.
- TGI Williston Basin Working Group, 2008b. Devonian Prairie Evaporite: structure contour. In: Manitoba Science, T., Energy and Mines, Manitoba Geological Services Branch (Eds.), *Stratigraphic Map SM2008-DPE-S*.
- The World Bank, 2017. World Development Indicators: Electricity production, sources, and access, World Development Indicators. The World Bank.
- Walsh, W., 2013. Geothermal resource assessment of the Clarke Lake Gas Field, Fort Nelson, British Columbia. *Bulletin of Canadian petroleum geology*, 61(3): 241-251.
- Wanner, C., Eichinger, F., Jahrfeld, T., Diamond, L.W., 2017. Unraveling the Formation of Large Amounts of Calcite Scaling in Geothermal Wells in the Bavarian Molasse Basin: A Reactive Transport Modeling Approach. *Procedia Earth and Planetary Science*, 17: 344-347. DOI: 10.1016/j.proeps.2016.12.087
- Wanner, C. et al., 2014. Reactive transport modeling of the Dixie Valley geothermal area: Insights on flow and geothermometry. *Geothermics*, 51: 130-141. DOI:10.1016/j.geothermics.2013.12.003
- Wissmeier, L., Barry, D.A., 2008. Reactive transport in unsaturated Soil: Comprehensive modelling of the dynamic spatial and temporal mass balance of water and chemical components. *Advances in Water Resources*, 31(5): 858-875. DOI:10.1016/j.advwatres.2008.02.003
- Wissmeier, L., Brovelli, A., Robinson, C., Stagnitti, F., Barry, D.A., 2009. Pollutant Fate and Transport in the Subsurface. In: Hanrahan, G. (Ed.), *Complex Environmental Systems*. ILM Publications, Thousand Oaks, USA, pp. 99-143.
- Wolff-Boenisch, D., Evans, K., 2013. Geochemical modelling of petroleum well data from the Perth Basin. Implications for potential scaling during low enthalpy geothermal exploration from a hot sedimentary aquifer. *Appl Geochem*, 37(Supplement C): 12-28. DOI:10.1016/j.apgeochem.2013.07.004
- Woroniuk, B., Tipton, K., Grasby, S.E., McIntosh, J.C., Ferguson, G., 2018. Salt dissolution and permeability in the Western Canada Sedimentary Basin. *Hydrogeol J*: 1-10. DOI:10.1007/s10040-018-1871-6
- Xia, Y., Plummer, M., Mattson, E., Podgorney, R., Ghassemi, A., 2017. Design, modeling, and evaluation of a doublet heat extraction model in enhanced geothermal systems. *Renewable Energy*, 105: 232-247. DOI: 10.1016/j.renene.2016.12.064
- Yanagisawa, N., 2015. Case study of calcium carbonate scale at EGS and hot spring binary system, *Proceedings World Geothermal Congress*, Melbourne, Australia.
- Zhang, G., Zheng, Z., Wan, J., 2005. Modeling reactive geochemical transport of concentrated aqueous solutions. *Water Resources Research*, 41(2). DOI:10.1029/2004wr003097

3. Manuscript 1: An experimental and numerical study for evaporite mineral dissolution and density-driven flow in porous media

The value and reliability of a subsurface numerical model are only as good as the quality of input data and the suitability of the numerical code used to calculate the flow and transport. Numerical codes must be tested to ensure they have adequate performance under required scenarios. For THC modeling in geothermal systems, mineral-fluid interactions and resulting density-driven flow are a key component of numerical code requirements. Physical measurements of mineral-fluid interactions under controlled conditions are not available in the literature. Therefore, this paper presents a study of the dissolution of a halite mineral in freshwater and the resulting flow patterns.

This manuscript contributed to the first sub-objective, to validate numerical methods used to calculate dissolution, flow, and transport of soluble mineral formations. This validation was required to build confidence in the ability of the numerical code to accurately represent interactions between the geothermal heat exchange fluid and the *in situ* formation. The calibration process and characterization of the sensitivity of solute transport to fields, parameters, and model choice served to provide insight into the major controls in the dissolution and solute transport process. This project also contributed significantly to the development of the modeler's process understanding.

An experimental and numerical study for evaporite mineral dissolution and density-driven flow in porous media

K. R. Moore, H. M. Holländer, and A.D. Woodbury

3.1. Abstract

Subsurface mineral dissolution problems exhibit complex behaviors, which are difficult to model and validate numerically. Controlled, physically-validated experimental problems can be used to better understand mineral dissolution and subsequent numerical representation. The objective of this work was to collect the first controlled, physical measurements in a porous aquifer overlying an evaporite mineral, and to create a numerical model of the system. The problem studied was modified from the classic HYDROCOIN Level 1 Case 5 problem. Three flow gradients in a porous aquifer were investigated in duplicate in a 2-D box-problem. The duplicate measurements had unexpectedly high variability, shown by numerical modeling to be a result of initial conditions, variable flux representing dissolution, sharp gradients, and potential changes in dispersivity. The physical measurements of parameters and fields were important for calibration success. The numerical models were capable of simulating flow patterns, observed concentrations, and peaks resulting from observed initial conditions. The numerical models were a key tool in understanding factors influencing the flow and spread of salt within the system. The models were limited by the ability to detail physical observations, difficult in both the laboratory and for potential field applications. Reproducing unstable dissolution effects was difficult, even under controlled conditions, and field-scale models would benefit from a strong uncertainty analysis and accurate measurements of flow and transport parameters. The results also provided insight in the HYDROCOIN Level 1 Case 5 numerical simulations, with flow appearing to be swept-forward; however, observed concentrations were lower than commonly modeled.

3.2. Introduction

Mineral dissolution is an important consideration in groundwater management scenarios that involve salt mining, nuclear waste storage, karstification, land subsidence, oil and gas, and geothermal projects; e.g. NEA and OECD (1988), Acero et al. (2015), Zidane et al. (2014), Hesshaus et al. (2013) and Krupp (2005). Representations of these systems are difficult to create due to a combination of complex flow patterns and the lack of measured geochemical data available for study. For example, groundwater flow near evaporite mineral formations where high density contrasts occur is generally characterized by erratic convective flow patterns and instability development or ‘fingering,’ e.g., Elder (1967), Voss and Souza (1987) and Schincariol et al. (1994). Analytic-mathematical solutions to these problems are limited in scope, and realistic solutions are best represented with numerical models. However, numerical codes must be validated to ensure they are capable of adequately capturing complex density-driven flow and dissolution.

Observations and carefully controlled experiments can greatly increase the strength of non-linear, density-dependent flow benchmarks by providing actual measurements of solute concentrations, thus enabling calibration and validation. Two main methods used to create benchmarks are (1) model inter-comparison and (2) physical measurements from experiments or case studies. Model inter-comparison benchmarks are based on results from several simulators and potentially some field data, e.g., NEA and OECD (1988) and Voss and Souza (1987). Physical measurements involve collecting data in a controlled laboratory setting and then calibrating a numerical model to match the data e.g. Konz (2010), Schincariol and Schwartz (1990), Stoeckl et al. (2016), Wooding et al. (1997a), Wooding et al. (1997b), Simmons et al. (1999) and Elder (1967).

Validation datasets for the dissolution of salt minerals are limited, however, one example is HYDROCOIN Level 1 Case 5: Salt Water Distribution in a Saturated Porous Medium (NEA and OECD 1988), hereafter referred to as HYDROCOIN1:5. This benchmark is a simplification of the Gorleben salt dome in Germany and deals with the salt concentration in an aquifer overlying a salt dome. However, it is a model inter-comparison and is not physically-validated. This lack of physical-validation has led to a substantial debate over ‘correct’ results. Younes et al. (1999), Diersch (2014) and Herbert et al. (1988) modeled the HYDROCOIN1:5 problem and observed recirculation patterns, which occurs when diffusion is relatively high, and brine spreads laterally across the lower part of the system (Oldenburg and Pruess 1995). However, NEA and OECD (1988), Konikow et al. (1997) and Oldenburg and Pruess (1995) observed “swept-forward flow”, which occurs when diffusion is small, and brine spreads in the same general direction of regional flow. Although Konikow et al. (1997) indicated variations in results are a result of boundary conditions at the salt dome, Younes et al. (1999) observed recirculation under multiple boundary conditions and indicated swept-forward or recirculation flow pattern may depend on the selection of finite element (FE) or finite difference (FD) methods. Konikow et al. (1997) stated that although the numerical solutions for HYDROCOIN1:5 are considered benchmarks and model consistency can be compared, physically-based observations are required to determine if the models are accurate and precise. Clearly, without a physical solution, the results cannot be fully understood.

As mentioned, controlled, physically-based datasets are valuable for the validation of groundwater solute transport numerical codes. However, none of the controlled, physically-based datasets reviewed involved the dissolution of the mineral itself. Therefore, studies have assumed the adequate performance of numerical models in high-density, mineral dissolution problems, while in fact, there are no known accounts of controlled, physically-based experiments for these

scenarios. Therefore, the objective of this work is to collect controlled, physical measurements, and create a simplified representative numerical model in a scenario where density-driven flow results from mineral dissolution.

In this study, physical measurements of salt dissolution and solute were collected in a porous experimental aquifer overlying a dissolving salt mineral under controlled, experimental conditions. These are the first known flow and transport measurements in an experimental aquifer resulting from mineral dissolution in a controlled setting. Considered in this problem are the dissolution of the mineral, mineral flux rate, aqueous phase solute, and transient-density-driven flow. Numerical modeling is used to examine parameter and boundary conditions settings that can best represent the observed results. The flow and solute transport reported in this physical evaporite mineral dissolution (PEMD) study explores the relationship between dissolution, density-driven solute transport, and hydrodynamic dispersion. The physical measurements will also provide insight into HYDROCOIN1:5 physical results.

3.3. Physical and numerical methods

3.3.1. Model concept and design

For this physical and numerical study, a 2-D flow tank filled with porous material was modified from the classic HYDROCOIN1:5 problem (NEA and OECD 1988). The HYDROCOIN1:5 setup is a 900 m wide by 300 m high cross-section with a salt dome along the centre third of the bottom (Table 1). Freshwater is introduced and removed via a sloping head boundary along the top, and all other boundaries are no flow. The salt is represented as an aqueous brine. The model is idealized as, 2-D, and all material and properties are considered homogeneous, and isotropic (NEA and OECD 1988).

For this PEMD study, the physical experimental setup was a much smaller system based on HYDROCOIN1:5 (Table 1). This study changed the sloping head boundary applied in HYDROCOIN1:5 to constant head boundaries in the upper right and upper left corners of the aquifer for increased control in the physical measurements. Based on numerical results, a constant head boundary will increase the vertical movement of the salt isolines. This PEMD study had higher hydraulic conductivity and porosity than HYDROCOIN1:5. Salt was introduced using a block of salt mineral. Finally, HYDROCOIN1:5 applied a freshwater head gradient of approximately 1.1%, while in this investigation, three head gradients were used, 2%, 5%, and 10%.

Table 3-1. Comparison of model settings for HYDROCOIN1:5 and PEMD.

Feature	Symbol	Units	HYDROCOIN1:5 (NEA and OECD, 1988)	PEMD Study
Sloping pressure boundary	-	%	1.1	2, 5, 10
Sides and bottom boundary	-	-	No flow	No flow
Porosity	ε	-	0.2	0.3 ^a
Saturated sand hydraulic conductivity	K	m s ⁻¹	9.679x10 ⁻⁶	2.3x10 ^{-3a}
Salt hydraulic conductivity	-	m s ⁻¹	9.679x10 ⁻⁹	1x10 ^{-15b}
Clay hydraulic conductivity	-	m s ⁻¹	n/a	1x10 ^{-9c}
Longitudinal dispersivity	α_L	m	20	0.0025 ^a
Transverse dispersivity	α_T	m	2	0.00025 ^d
Salt molecular diffusion coefficient in water	D_d	m ² s ⁻¹	0	1.0x10 ^{-9d}
Inflow concentration	C_0	M M ⁻¹	0	0
Inflow fluid density	ρ_0	kg m ⁻³	1000	1000
Concentration flux	-	g s ⁻¹	n/a	Measured ^a
Concentration	C_s	M M ⁻¹	0.78	1
Maximum saturated fluid density	ρ_s	kg m ⁻³	1200	1202 ^e
Mineral density	-	kg m ⁻³	n/a	2200 ^f
Length	x	m	900	0.9
Width	y	m	300	0.3
Depth	-	m	1	0.12
Width of salt dome	-	m	300	0.3
Temperature	-	°C	n/a	22

^a measured; ^b Beauheim and Roberts (2002); ^c Fetter (2001); ^d Pickens and Grisak (1981); ^e - (O'Neil, 2013); ^f Hamid et al. (2005)

3.3.2. Experimental method

To investigate mineral dissolution and solute transport through a porous media, a series of physical measurements were made in a benchtop aquifer. Duplicate experiments were conducted at 2%, 5%, and 10% head gradients. The basic design of the physical experiments was a 0.3 m x 0.9 m x 0.12 m plexiglass tank filled with sand, with an inflow in the upper left, outflow in the upper right and a 0.3 m salt core along the centre of the bottom (Figure 3-1, Table 3-1). The size of the experimental aquifer allowed for the development of a stable flow field. The flow was created using a peristaltic pump (Masterflex L/S 07522-20), with an overflow to maintain the constant head boundary. Due to the large water demand for each experimental run, tap water was used. Concentrations are reported in M M^{-1} relative to saturation of 6.14 M so that 0.01 M M^{-1} represents a concentration relative to saturation equivalent to 0.0641 M. The electrical conductivity of the tap water remained below $1.6 \times 10^{-4} \text{ M M}^{-1}$. The water temperature was maintained at $22^\circ\text{C} \pm 2^\circ\text{C}$. The porous medium was *Unimin 0.65 filter Sil* silica sand, sieved between 841 and 1700 μm ; the average particle size was $1.3 \pm 0.2 \text{ mm}$. The sand was added while damp and packed every 4 cm to create homogeneous (and isotropic) packing, and eliminate air pockets. The hydraulic conductivity of the sand, measured using a falling head test with 3 measurements at 5 head differences ranging from 0.032 to 0.27 m, was $2.3 \times 10^{-3} \pm 2.9 \times 10^{-4} \text{ m s}^{-1}$ (ASTM International, 2000). The porosity of the sand was calculated as the fraction of the void volume over the total volume, based on mass measurements and a sand specific gravity of 2.65 g cm^{-3} .

The salt dome was simulated using salt cores composed primarily of halite from the Prairie Evaporite Formation in the Williston Basin near Rocanville, Saskatchewan, Canada. Cores were selected to represent the mineral density and composition at depth in a salt formation. The halite

cores were cut and arranged so that there was a 0.30 m by 0.12 m flat surface. A mass balance was used to determine the average dissolution rate of the cores. Inductively coupled plasma (ICP) analysis at the Manitoba Chemical Analysis Laboratory indicated that the salt cores contained a ratio of sodium, calcium, strontium (100 Na: 2.3 Ca: 0.018 Sr), and trace amounts of magnesium, lead, tellurium, thorium, beryllium, and potassium. The analysis was done using a Varian plasma ICP-OES, model 725-ES, with a Varian 323 autosampler. Clay was packed around the cores to restrict water contact with the salt cores to the top. The diffusion of salt into the clay was assumed to be negligible during the experiment, due to the low hydraulic conductivity of the clay. The initial condition in HYDROCOIN Level 1 Case 5, where freshwater overlies a salt dome is an idealized condition that can be simulated numerically but not physically. Mineral dissolution appears to have occurred immediately after water contacted the salt mineral, prior to the establishment of the flow field.

Measurements began once the tank was full and flow was developed and continued until steady-state appeared to be achieved. The hydraulic head was observed at the inflow and outflow as well as at 36 locations, at y-locations of 0.03, 0.08, 0.16, and 0.24 m between x-locations of 0.08 and 0.81 m. Hydraulic head measurements in regions with detectable salt concentrations at the time of observation were converted to equivalent freshwater heads using the relationships described below (see 2.3.1 Density definitions). Measurement error was estimated at 0.005 m for these readings.

Salt concentrations were measured at 16 discrete points every 15 seconds using electrical resistance measurements and manually using 5 extracted samples. Extracted samples were taken to calibrate and verify resistance readings. The locations of the points were selected to capture the region immediately above and within the solute plume (Table 3-1). Resistance measurements were

spaced at a minimum distance of 0.05 m to reduce interference, e.g Hassanizadeh and Leijnse (1995). Resistance measurements were collected using a Datascan 7321 measurement system with copper terminals spaced at 0.01 m. A 0.75 mA energization source was applied. Resistance readings were calibrated using extracted samples, thus included the formation factor. Resistivity measurements measure the environment around electrodes and thus represent an integral value, so that exact measurement volume is unknown, e.g. Konz (2010). Photometric dye methods were not used due to the inability to consistently dye the halite core. However, rhodamine WT was used to characterize flow patterns.

Samples were extracted from the same location as the discrete measurements 5 times during the experimental run. Extraction samples were taken in 8 mL volumes using a syringe. The extracted samples were calibrated using standards created from the salt cores, as well as a pure NaCl solution. For all calculations, it was assumed that all present ions were Na^+ and Cl^- . Quality assurance and quality control were carefully maintained; field blanks, sampling duplicates, laboratory duplicates, and calibration standards were used. Laboratory duplicate errors were 2.4%, 3.0% and 2.7%. Sampling duplicate errors for the 2%, 5% and 10% gradients were 15.0%, 15.0% and 5.0%. This translates to $5.2 \times 10^{-4} \text{ M M}^{-1}$ precision. Sampling duplicate error may have been high due to the disturbance in flow patterns and concentration caused by the initial sample collection.

A power curve best represented the relationship between the in-situ resistance and extracted fluid equivalent NaCl concentration. The correlation coefficient of the calibration r^2 was in the range of 0.60 – 0.99 for high concentration ($5.5 \times 10^{-4} \text{ M M}^{-1}$ above background) and 0 to 0.60 for freshwater concentration values. The poor r^2 values for the low concentrations were due to the very small change in observed resistance. The average percent standard error in EC

measurements between the resistance and extracted samples for the 2%, 5%, and 10% gradients were 14.7%, 7.8%, and 8.7%. These errors may result from a difference in precise sampling location, volume sampled, or disturbance from the drawn sample. The high end of the error, 14.7%, relates to a $6.0 \times 10^{-4} \text{ M M}^{-1}$ sensitivity or smallest detectable change. Based on the sampling error and measurement error, the minimum detectable change in concentration was conservatively estimated to be 0.001 M M^{-1} .

The discrete concentration measurements were used to create isohalines for average steady-state observations for each the 2%, 5%, and 10% gradients. The isohalines were used to extrapolate between points using triangulation with linear interpolation. Values were recorded after approximately 0.14 days. Data were gridded from $x = 0.25$ to 0.9 m and $y = 0$ to 0.2 m . The gridded data were used to create an interpretation of the laboratory data. However, the physical-based numerical modeling, validated with point data, is required to provide an interpretation of the flow and transport results.

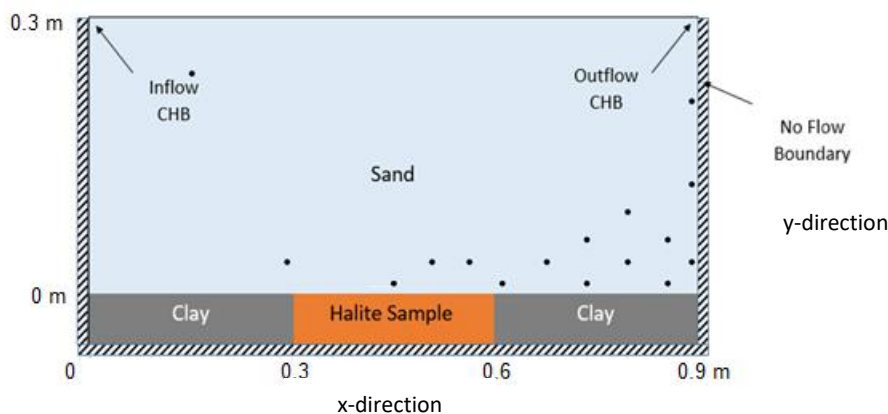


Figure 3-1. Physical model design for the 2-D experimental aquifer. Black dots indicate solute sampling locations. The height of the outflow was reduced to the appropriate gradients.

3.3.3. Hydrodynamic dispersion

The spread of solute occurs as a result of mechanical dispersion and molecular diffusion, which cannot be separated in flowing groundwater. The coefficient of hydrodynamic dispersion in the longitudinal direction, D_L ($\text{m}^2 \text{s}^{-1}$), is the combined effect of mechanical dispersion, D_m and diffusion D_d .

$$D_L = D_m + D_d \quad 3-1$$

Dispersion of dissolved sodium chloride was measured in a column using the methods described in Pickens and Grisak (1981):

$$D_L = \left(\frac{v_x L}{8} \right) (J_{0.84} - J_{0.16})^2 \quad 3-2$$

where a_L is the longitudinal dispersivity (m), v_x is average linear groundwater velocity in the x-direction (m s^{-1}), L is the length of the column (m) and:

$$J_{0.84} = \frac{U-1}{U^{1/2}} \text{ when } \frac{C}{C_0} \text{ is } 0.84 \quad 3-3$$

$$J_{0.16} = \frac{U-1}{U^{1/2}} \text{ when } \frac{C}{C_0} \text{ is } 0.16$$

where U represents dimensionless time:

$$U = \frac{v_x t}{L} \quad 3-4$$

Longitudinal dispersivity can then be calculated as:

$$a_L = \frac{D_L - D_d}{v_x} \quad 3-5$$

where D_d is the effective molecular diffusion coefficient estimated as:

$$D_d = \omega D_d^* \quad 3-6$$

where ω is a coefficient related to tortuosity and is estimated to be 0.6 to 0.7 for unconsolidated granular material (Perkins and Johnston, 1963). D_d^* is the diffusion coefficient of NaCl in water at 25°C, and ranges from $1.612 \times 10^{-9} \text{ m}^2 \text{ s}^{-1}$ at 0 mol L^{-1} to a low of $1.474 \times 10^{-9} \text{ m}^2 \text{ s}^{-1}$ at 0.5 mol L^{-1} to $1.584 \times 10^{-9} \text{ m}^2 \text{ s}^{-1}$ at 4 mol L^{-1} (Stokes, 1950). An average value of $1.5 \text{ m}^2 \text{ s}^{-1}$ was taken and therefore, a value of $1.0 \times 10^{-9} \text{ m}^2 \text{ s}^{-1}$ was used for D^* . The sensitivity to diffusion was low. Variation of diffusion values in the range of $1.12 \times 10^{-9} \text{ m}^2 \text{ s}^{-1}$ to $0.88 \times 10^{-9} \text{ m}^2 \text{ s}^{-1}$, minimum and maximum values based on estimated tortuosity and diffusion of NaCl, resulted in an average of 0.26% difference between concentration values, with a maximum difference of 1.3%

The ratio of transverse to longitudinal dispersivity was estimated using dye. The ratio was measured for 6 timesteps in the 5% gradients and found to be 0.11 ± 0.05 . This is comparable to the common estimate of 0.10, and within suggested values from Fetter (1999) of 0.05 to 0.16 and Pickens and Grisak (1981) of 0.003 to 0.33, both at the field scale. Transverse dispersivity was therefore initially estimated as:

$$a_T = a_L * 0.1 \quad 3-7$$

Longitudinal dispersivity was also estimated empirically for flow lengths of $\leq 100 \text{ m}$ based on laboratory and field data (Neuman, 1990):

$$a_L = 0.0169(L)^{1.53} \quad 3-8$$

The Peclet number is a dimensionless number that indicates the relationship between advective transport and hydrodynamic dispersivity:

$$Pe = \frac{L \cdot v}{D_L} \quad 3-9$$

where Pe is the Peclet number (-), L is the typical length of the transport phenomena (m), v is the effective flow velocity (m s^{-1}) and D_L is the longitudinal hydrodynamic dispersion coefficient ($\text{m}^2 \text{s}^{-1}$). When $Pe < 10$ diffusion makes a significant contribution to hydrodynamic dispersion (Olsson and Grathwohl, 2007).

3.3.4. Numerical methods

The numerical model was a 2-D idealized concept of the physical benchtop aquifer. The benchtop aquifer was designed to have boundaries that easily translated to numerical models. The flow was assumed to occur through only the porous media and the clay packing was not considered in the numerical model. Mineral dissolution was represented with a flux boundary, which was initially assumed to be constant throughout the experiment. Field potentials and parameters were measured wherever possible, including hydraulic head, solute concentration, hydraulic conductivity, porosity, longitudinal dispersivity, and average mineral flux (Table 1, Table 2). Based on the Peclet number, diffusion was determined to be negligible compared to dispersion. To calibrate the numerical model to concentration results, transverse dispersivity, initial concentration, and flux were adjusted. The initial and inflow temperatures were set at 22°C.

The primary concern for this simulation was a code capable of simulating density-driven flow. Individual mineral reactions were not considered because, in high-density contrast problems, density effects dominate over individual reactive transport (Post and Prommer 2007). The finite

element (FE) code, FEFLOW (Diersch 2014) was selected to complete the numerical investigation. The problem included transport of mass of a single species. Transient, saturated flow, was described using the equation of continuity with a Darcy flux law. Multiple iterative equation solvers were used; a preconditioned conjugate-gradient (PCG) solver was used for flow and BICGSTABP-type solver for transport. The model was a 2-D vertical projection. Quadrilateral mode transport-mapping was used to create the grid; as this grid type increased numerical stability. The model grid size was reduced until the grid Peclet number was below 2, based on the length of each element. Values in the model ranged from 0.31 to 1.78. Cell lengths in the model were 0.0032 m above $y = 0.075$ and 0.0016 m below. The time-step length was reduced until the Courant Number was below 1, which is beneficial for the result accuracy and numerical stability of transport calculations. The initial time was set at 1×10^{-7} d, with a maximum time step of 1×10^{-3} d. However, time step length was reduced where numerical oscillation or model instability was detected.

To compare finite element and finite difference (FD) results, SEAWAT (Guo and Langevin 2002) was used with a conjugate gradient solver (PCG2). The initial time step was 0.001 d and the maximum time step was 0.03 d, with a total of 25 time-steps. The cells were 0.0025 by 0.0025 m. The salt dome was simulated using a constant concentration boundary in the FD model.

3.3.4.1. Density definitions

In density-driven problems, at two points with equal pressure and elevation, but different fluid density, the hydraulic head will differ. Both FEFLOW and SEAWAT use equivalent freshwater head to calculate Darcy flow. Saltwater fluid hydraulic head h_s (m) is related to the density of the water, ρ_s (kg m^{-3}):

$$h_s = \frac{P}{\rho_s g} + z \quad 3-10$$

where P is pressure ($\text{kg m}^{-1} \text{s}^{-2}$), g is the gravitational acceleration (m s^{-2}), and z is elevation head (m).

The mass conservation equation of a saturated fluid is given as:

$$S_0 \frac{\partial h_0}{\partial t} + \nabla \cdot \vec{q} = Q \quad 3-11$$

where S_0 is specific storage (m^{-1}), and Q is sinks and sources (s^{-1}). Saturated Darcy flux \vec{q} (m s^{-1}) in FEFLOW is defined as:

$$\vec{q} = -\mathbf{K} \cdot (\nabla h_0 + \chi \vec{e}) \quad 3-12$$

where \mathbf{K} (m s^{-1}) is the hydraulic conductivity tensor (note: in this study \mathbf{K} is treated as homogeneous and isotropic), h_0 (m) is the equivalent freshwater hydraulic head, \vec{e} is the gravitational unit vector (1). The density ratio (χ) (-) in FEFLOW describes the ratio between maximum and minimum density and is defined as:

$$\chi = \frac{\rho_s - \rho_0}{\rho_0} \quad 3-13$$

where ρ_s (kg m^{-3}) is the saltwater density and ρ_0 (kg m^{-3}) is the freshwater density. For this work, a value of 0.2 was applied. The equivalent freshwater hydraulic head can be calculated as:

$$h_0 = (1 + \chi)h_s - \chi z \quad 3-14$$

FEFLOW uses freshwater and saturated concentrations as references for density calculations.

Using SEAWAT, a similar set of equations are used. Conservation of mass is defined as:

$$-\nabla \cdot (\rho \vec{q}) + \rho S_Q = \frac{\partial(\rho \varepsilon)}{\partial t} \quad 3-15$$

where \vec{q} is the Darcy flux (m s^{-1}), ρ is the density of water of sources and sinks (kg m^{-3}), S_Q is the volumetric flow rate per unit volume representing sources and sinks (s^{-1}), and ε is porosity.

The relationship between fluid density and solute concentration is commonly described using a linear equation, developed as an empirical equation by Baxter and Wallace (1916),

$$\rho_s = \rho_0 + \beta \cdot C \quad 3-16$$

where ρ_s (kg m^{-3}) is the fluid density, ρ_0 (kg m^{-3}) is the freshwater density, β is a dimensionless constant relating density and concentration and C (kg m^{-3}) is the observed concentration. For concentrations ranging from 0 to that of seawater, a value of 0.7143 is commonly used for β .

However, β (-) can be calculated,

$$\beta = \frac{\rho_s - \rho_0}{C_s - C_0} \quad 3-17$$

where ρ_s (kg m^{-3}) is the saltwater density, C_s (kg m^{-3}) is the saltwater concentration, and C_0 (kg m^{-3}) is the freshwater concentration. Conversions between freshwater h_0 (m) and saltwater h (m) hydraulic heads are defined as:

$$h_0 = \frac{\rho_s}{\rho_0} h_s - \frac{\rho_s - \rho_0}{\rho_0} \cdot z \quad 3-18$$

Mass flux in the x-direction is calculate using Darcy's law for a fluid of variable density

$$q_x = \frac{k}{\mu} \cdot \frac{\partial P}{\partial x} \quad 3-19$$

where q_x Darcy flux in the x-direction, μ is dynamic viscosity (Pa-s), and k is intrinsic permeability (m^2). Similar equations are used in the y and z directions, see Guo and Langevin (2002).

3.4. Results

3.4.1. PEMD physical model flow and dispersion results

Flow in the PEMD benchtop aquifer was maintained at a constant rate, and gradients were calculated from the saltwater head at the inflow and outflow for each replicate (Table 3-2). The use of saltwater head resulted in a maximum error of 0.0045 m, based on a maximum density of 1014 kg m^{-3} . Flow patterns, observed using Rhodamine WT, appeared to be smooth, swept-forward flow which traveled down from the inflow, across the salt dome and up to the inflow e.g. Figure 3-2. Swept-forward flow was supported by concentration observations at upstream locations (0.50, 0.03 m) and (0.29, 0.03 m) which were 2 to 56 times lower than downstream concentrations. Whereas, recirculation patterns would result in increased upstream concentration. No short-circuiting of flow or preferred pathways were observed, with the exception of potential boundary influence from (0.9, 0 m) to (0.9, 0.30 m) along the outflow, where no concentration was observed at (0.89, 0.17 m).

Table 3-2. Physical and calculated properties of the porous media and flow for the physical models.

Parameter	Symbol	Unit	Value
Observed gradients for each replicate	2%		0.028 ¹
			0.019 ²
	5%	$\Delta y/\Delta x$ -	0.050 ¹
			0.047 ²
	10%		0.083 ¹
			0.088 ²

Mineral dissolution	2%			576 ²
	5%			705 ¹
			g d ⁻¹	489 ²
	10%			878 ²
Longitudinal velocity (method 1) $v_L = K/n_e * \Delta h/\Delta l$	2%			1.5x10 ⁻⁴
	5%	v_L	m s ⁻¹	3.8x10 ⁻⁴
	10%			7.67x10 ⁻⁴
Longitudinal dispersivity ^a		a_L	m	0.0025
Longitudinal dispersivity ^b		a_L	m	0.0026
Average tracer velocity (method 2) measured	2%			3.4x10 ⁻⁵
	5%	v_L	m s ⁻¹	5.4x10 ⁻⁴
	10%			6.7x10 ⁻⁴
Peclet Number	2%			396
	5%	Pe	-	400
	10%			400

¹ and ² indicate model replicates; ^a: Equation 3-5; ^b: Equation 3-8

3.4.2. PEMD physical model salt concentration results

The benchtop aquifer physical measurements examined solute concentrations observed in the aquifer overlying a salt mineral. Both methods of calculating dispersion produced similar results (Table 3-2). The Peclet number indicated that diffusion was negligible for all tests. A positive correlation existed between the head gradient and mass of dissolved salt introduced into the aquifer with 2% at 576 g d⁻¹, 5% at 705 g d⁻¹, and 10% at 878 g d⁻¹. This indicated that the dissolution of salt was transport or diffusion-limited. However, the mass of dissolved salt fluctuated between replicates. Duplicate data were only available for the 5% gradients which were 705 and 489 g d⁻¹. This indicated that flux likely varied during the experiment. The dissolution of the salt resulted in a change in volume of 7.2x10⁻⁵, 9.6x10⁻⁵, and 1.1x10⁻⁴ m³ for the 2, 5, and 10% gradients respectively. This is a height of 0.0020, 0.0026, and 0.0031 m over the 0.12 m by 0.30 m salt cores.

The interpolated isohalines provide a potential interpretation of the physical results (Figure 3-2, Figure 3-3). The experimental replicates exhibited variability; however, they exhibited similar overall flow and transport patterns. As flow began, peaks in concentration were observed

downstream from the salt block, indicating a surge of salt concentration through the system Table 3-3). Following the peaks was a decrease in concentration to a relatively steady value after 30 – 150 minutes. Fluctuating concentration patterns were observed approximately every 50 minutes in the 5% gradients. The possibility that these patterns were related to withdrawal sampling was considered. However, sampling did not coincide with the circular concentration pattern.

Time to steady-state was negatively correlated with the gradient; the 2% gradient experiment took the longest time to reach steady-state. In the corner below the outflow (0.85, 0.01 m), a continuous increase in concentration was observed in some experiments, resulting in the highest steady-state concentration, while in other experiments the highest steady-state concentration was observed at the downstream end of the salt block (0.61, 0.01 m) (Table 3-3). No relationship was observed between maximum concentration and gradient.

Consistent initial conditions were difficult to achieve, with increased concentrations observed at the beginning of the test while filling the tank, immediately after water contacted the salt mineral. Duplicates at the various gradients indicated that the steady-state conditions were sensitive to initial concentration distribution (Figure 3-3). This is in contrast to groundwater flow-only models, which given different initial conditions under the same boundary conditions, will reach the same steady-state conditions (Reilly and Harbaugh, 2004). The differences in observed concentration isolines for the two 5% gradient duplicates at the beginning of the test and after steady-state, were compared. Replicate 1 had a lower initial concentration above and upstream of the salt block, whereas Replicate 2 had a high concentration above and upstream of the salt block. The resulting steady-state concentration isolines showed similarities, with increased concentrations near the edge of the salt block at (0, 0.6 m) and under the outlet at (0, 0.9 m).

However, Replicate 2 had increased concentration overlying the upstream side of the salt core at 0.3 m not observed in Replicate 1.

Table 3-3. Maximum concentrations during the initial time period, the largest peak, and the steady-state maximum observed for each replicate at each gradient.

Timing		Rep.	Concentration M M ⁻¹	Location
Maximum initial	2%	1	0.034	(0.85, 0.01 m)
		2	0.021	(0.29, 0.01 m).
	5%	1	0.054	(0.29, 0.03 m).
		2	0.021	(0.29, 0.03 m).
	10%	1	0.036	(0.29, 0.01 m)
		2	0.023	(0.89, 0.03 m)
Peak	2%	1	no peak	-
		2	0.067	(0.73, 0.01 m)
	5%	1	0.037	(0.61, 0.01 m)
		2	0.081	(0.61, 0.01 m)
	10%	1	0.065	(0.45, 0.01 m)
		2	0.037	(0.89, 0.10 m)
Steady-state maximum	2%	1	0.083	(0.85, 0.01 m)
		2	0.015	(0.61, 0.01 m)
	5%	1	0.039	(0.61, 0.01 m)
		2	0.070	(0.85, 0.01 m)
	10%	1	0.072	(0.85, 0.01 m)
		2	0.026	(0.85, 0.01 m)

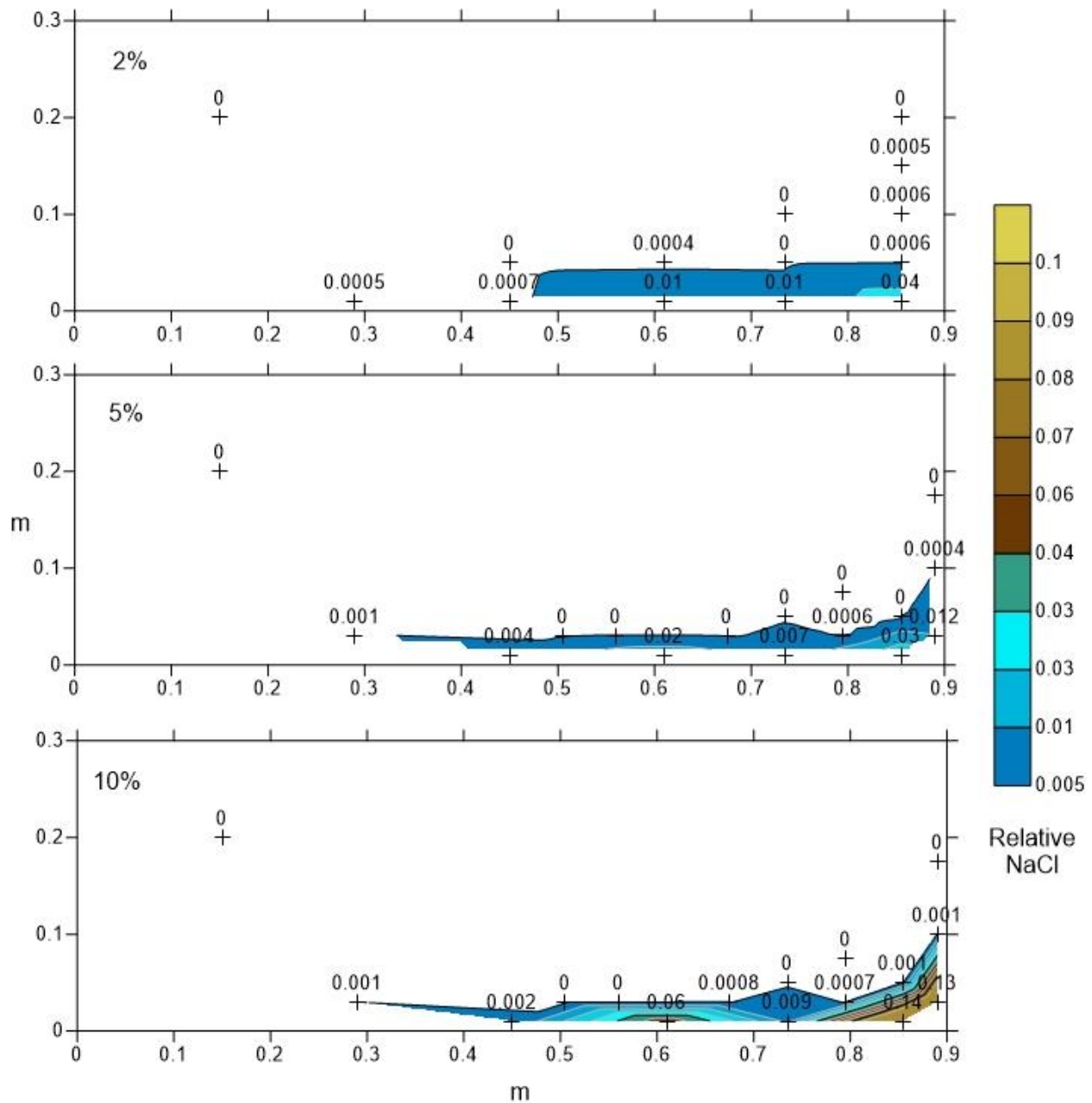


Figure 3-2. A comparison of one replicate of observed salt concentration for each the 2%, 5%, and 10% gradients in the experimental aquifer overlying the salt core at approximately 0.14 days. The isolines are interpolated from resistance observations located at the '+' marks. Concentrations are relative to saturated NaCl brine at 22°C.

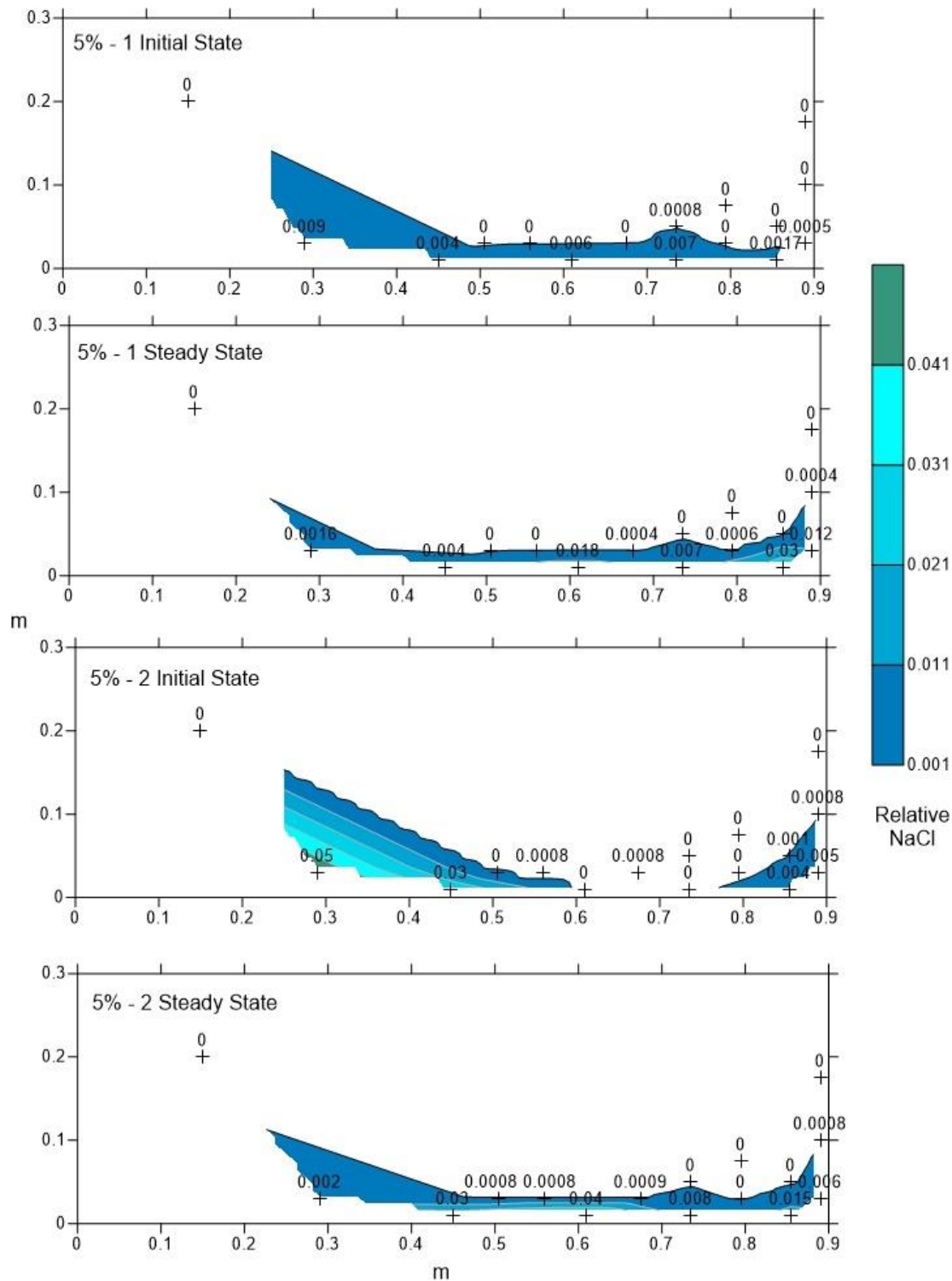


Figure 3-3. A comparison of the two replicates of the physical model at the 5% gradient in the experimental aquifer overlying the salt core. The isolines are interpolated from resistance observations located at the '+' marks. Concentrations are relative to saturated NaCl brine at 20°C.

3.4.3. Numerical simulation results

The observed phenomena in the physical benchtop aquifer experiments were investigated using numerical modeling. Due to the high variation between experimental replicates, the approach to the numerical modeling was first, to create a model that represented the physical observations under uncalibrated conditions. Following that, one of the 5% gradient replicates were examined to understand influences on match to laboratory results by examining values found to have the greatest effect on flow, including initial conditions, flux, density, and transverse dispersivity. These comparisons between the benchtop aquifer experimental results and numerical models focused on the 5% gradient.

3.4.3.1. Uncalibrated model results

Modeled parameters were measured for K , n , D_L , D_T , average mineral flux, and fields for equivalent freshwater hydraulic head and concentration. For the uncalibrated model, the initial concentration throughout the numerical model and at the salt dome was set at that of tap water. Model 1 represented the uncalibrated results and used measured flux of $1500 \text{ g m}^{-2} \text{ s}^{-1}$ and transverse dispersivity of 0.00025 m based on laboratory measurements. The numerical models were sensitive to grid size and time step length, with too large of grid or time step resulting in numerical oscillation that resembled convective flow patterns. The grid size was primarily sensitive to the longitudinal dispersivity values, with decreasing values requiring decreasing grid size.

A comparison of the observed and calculated head values at 0.075 days showed good correlation, 0.892 and 0.895, for observed heads and equivalent freshwater head (Figure 3-4). The

largest error was observed at well closest to the inflow, 0.0089 m at (0.08, 0.03 m), and the outflow, 0.0033 m at (0.822, 0.24 m) where a high gradient is expected. For the saltwater head calculation, observation wells in the benchtop aquifer observed to contain saltwater were converted to equivalent freshwater head. The nearest concentration observation point was used to calculate the equivalent freshwater head using a linear relationship between density and concentration, equation 18. The largest correction freshwater and saltwater heads was 0.002 m.

The uncalibrated model concentration isohalines exhibited swept-forward flow, similar to the experimental results. Concentration magnitudes were similar to observed values (Figure 3-5). However, calibration to data points was poor in some locations. For example, concentrations were overestimated near the outflow and initial peaks in concentration were not captured (Figure 3-6).

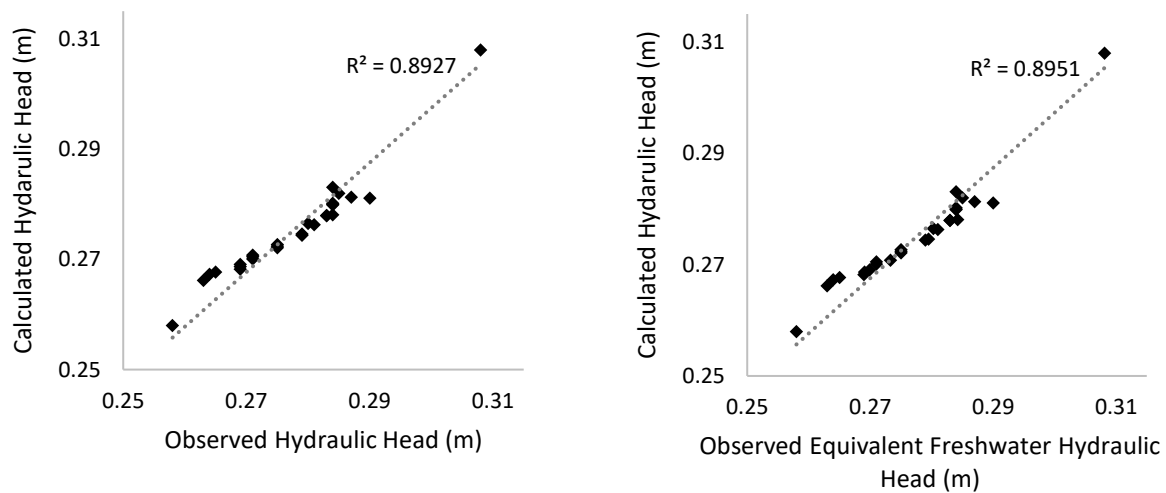


Figure 3-4. Comparison of observed and calculated hydraulic head values for the 5% gradient replicate 1 for both observed hydraulic head and observed equivalent freshwater hydraulic head, shown with a 1:1 trend line.

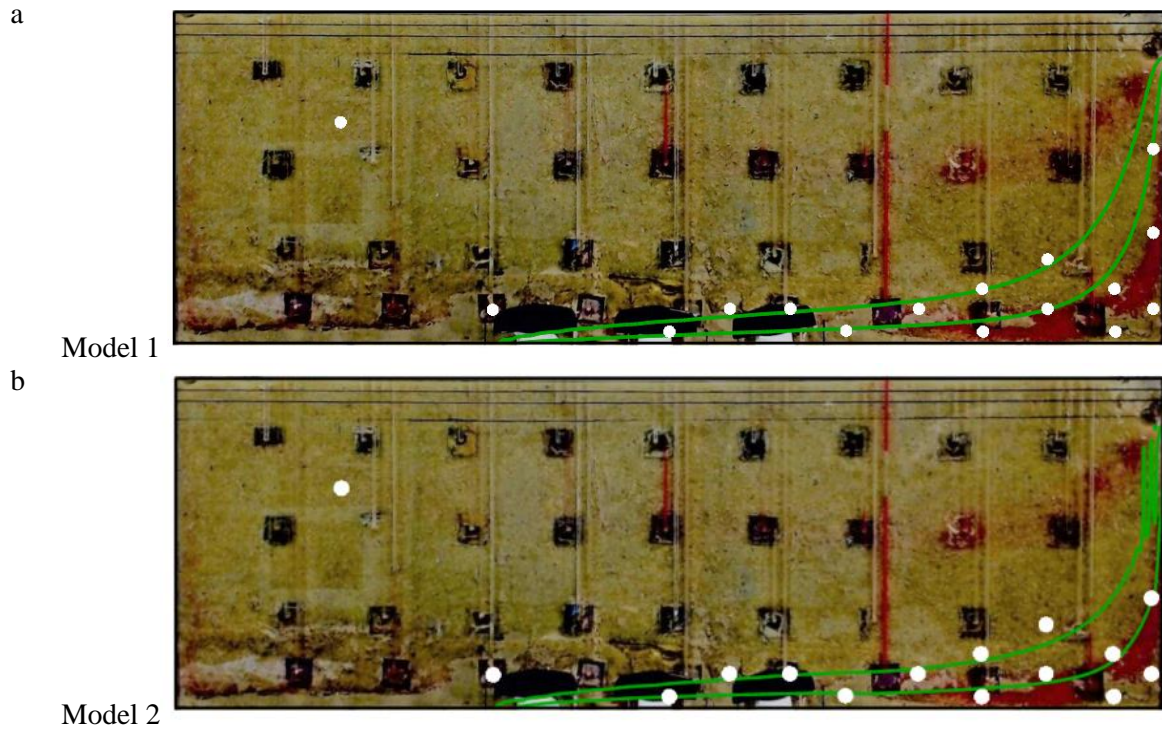


Figure 3-5. Comparison of modeled isolines at 0.001 M M^{-1} and 0.01 M M^{-1} with flow pattern observed using Rhodamine-WT dye in 5% Replicate 2. a) Model 1, uncalibrated, measured conditions; b) Model 2, calibrated to 5% Replicate 2.

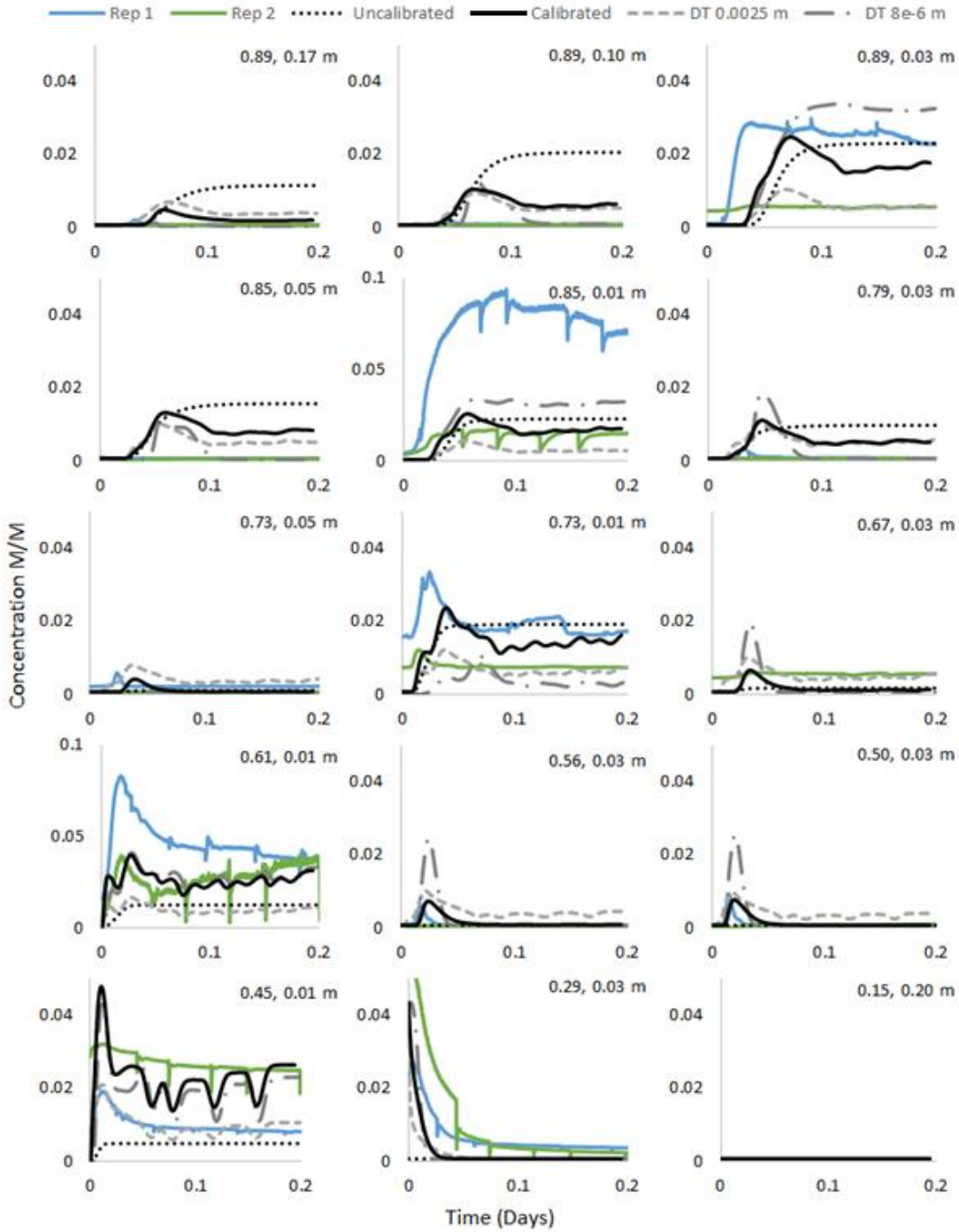


Figure 3-6. Comparisons of experimentally observed concentration with time for the two 5% gradient replicates and 4 models, representing uncalibrated, calibrated conditions and variations in transverse dispersivity.

3.4.3.2. Uncalibrated gradients

Comparisons were made between the 2%, 5% and 10% gradients under uncalibrated conditions (Figure 3-7). Similar to the laboratory observations, the lower the gradient, the longer it took the system to reach steady-state. In the experimental results, measured flux increased with increasing gradient, for 2, 5, and 10% respectively, these values were input into the numerical model (Table 3-2). Maximum values observed in the numerical model were 0.20, 0.067, and 0.039 $M M^{-1}$ for the 2%, 5%, and 10% gradients, respectively, thus exhibiting a pattern of decreasing maximum concentration with increasing gradient, in contrast to the experimental results where no pattern was observed. In the numerical model for all gradients, the maximum concentration was generally observed at (0.60, 0 m), this is similar to the experimental results where the highest concentration in the laboratory measurements was located at (0.61, 0.01 m) or (0.85, 0.01 m) (Table 3-3).

Table 3-4. RMSE values from comparisons of observed and modeled time series data for two 5% replicates of the PEMD experiment and 2 model settings.

			Rep 1 and 2	Model 1	Model 2
Longitudinal Dispersivity			m	-	2.5×10^{-3}
Transverse Dispersivity			m	-	2.5×10^{-4}
Flux			$g m^{-2} d^{-1}$	-	-1500
Initial Conditions			$M M^{-1}$	-	7.0×10^{-4}
Location					
Vertical at outflow	(0.89, 0.17 m)	Rep 2	2.70×10^{-4}	8.31×10^{-3}	1.73×10^{-3}
	(0.89, 0.10 m)	Rep 2	2.23×10^{-4}	1.54×10^{-2}	5.73×10^{-3}
	(0.89, 0.03 m)	Rep 2	1.92×10^{-2}	1.38×10^{-2}	1.14×10^{-2}
	(0.85, 0.05 m)	Rep 2	2.05×10^{-4}	1.25×10^{-2}	7.60×10^{-3}
D o w	(0.85, 0.01 m)	Rep 2	6.13×10^{-2}	8.09×10^{-3}	5.27×10^{-3}

Upstream and
Above Salt

(0.79, 0.03 m)	Rep 2	5.82×10^{-4}	7.88×10^{-3}	5.33×10^{-3}
(0.73, 0.05 m)	Rep 2	1.68×10^{-3}	2.72×10^{-4}	9.74×10^{-4}
(0.73, 0.01 m)	Rep 2	1.21×10^{-2}	1.09×10^{-2}	7.88×10^{-3}
(0.67, 0.03 m)	Rep 2	-	3.87×10^{-3}	3.97×10^{-3}
(0.61, 0.01 m)	Rep 2	2.34×10^{-2}	1.67×10^{-2}	7.07×10^{-3}
(0.56, 0.03 m)	Rep 2	9.93×10^{-4}	5.87×10^{-5}	1.66×10^{-3}
(0.50, 0.03 m)	Rep 2	1.45×10^{-3}	2.46×10^{-4}	1.90×10^{-3}
(0.45, 0.01 m)	Rep 2	1.70×10^{-2}	2.23×10^{-2}	7.60×10^{-3}
(0.29, 0.03 m)	Rep 2	8.31×10^{-3}	1.58×10^{-2}	1.24×10^{-2}
Average RMSE ($M\ M^{-1}$)	Rep 2	1.13×10^{-2}	9.72×10^{-3}	5.75×10^{-3}

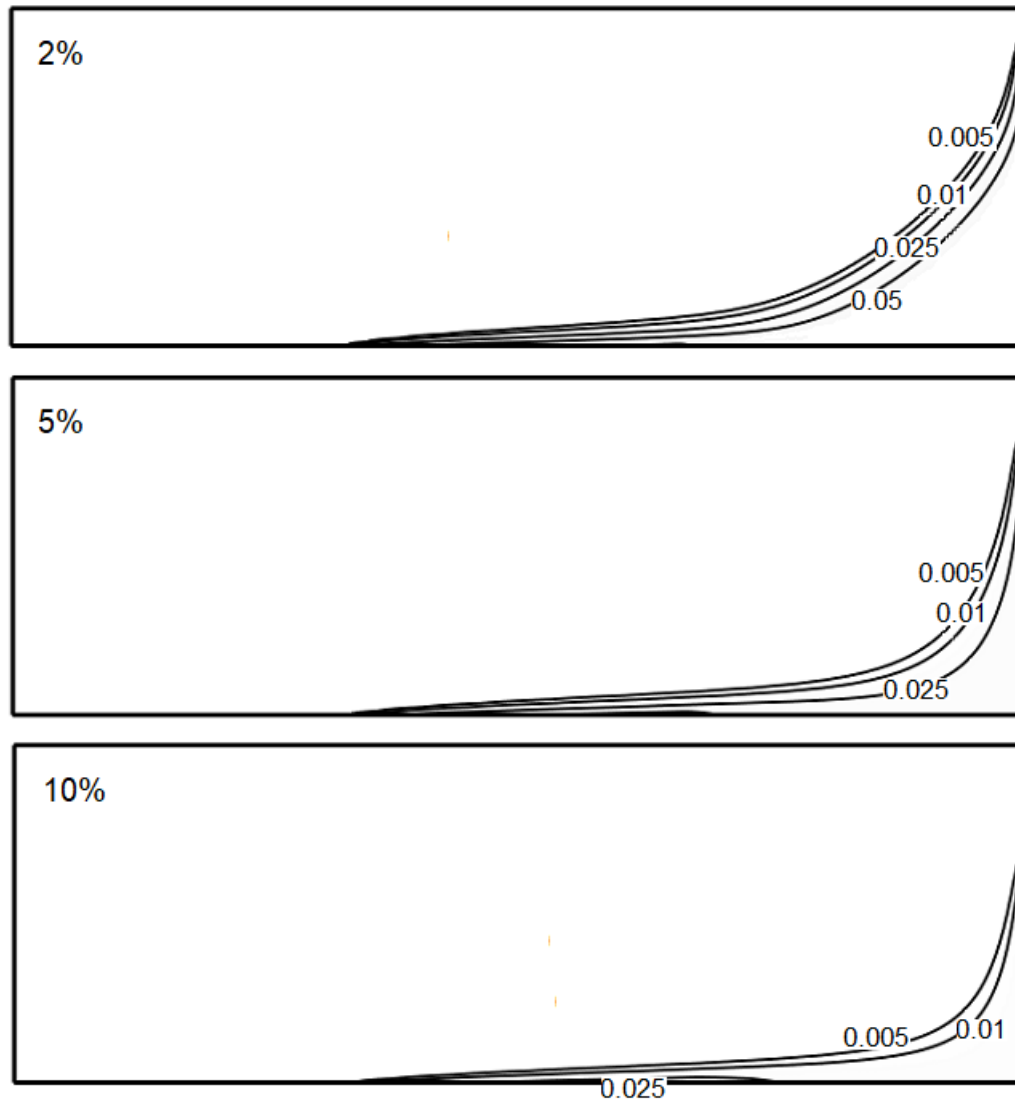


Figure 3-7. Comparison of uncalibrated 2, 5, and 10% steady-state concentrations. Contour lines indicate concentration relative to saturation.

3.4.3.3. FD flow patterns

Previous studies e.g., Younes et al. (1999) have suggested that swept-forward versus recirculation patterns may be related to model selection, so the uncalibrated conditions were simulated in an FD model. The FD model resulted in a similar swept-forward flow to the FE model (Figure 3-8). The FD code produced stable results with a similar grid spacing. However, the model was more stable with larger time steps using the FD code.

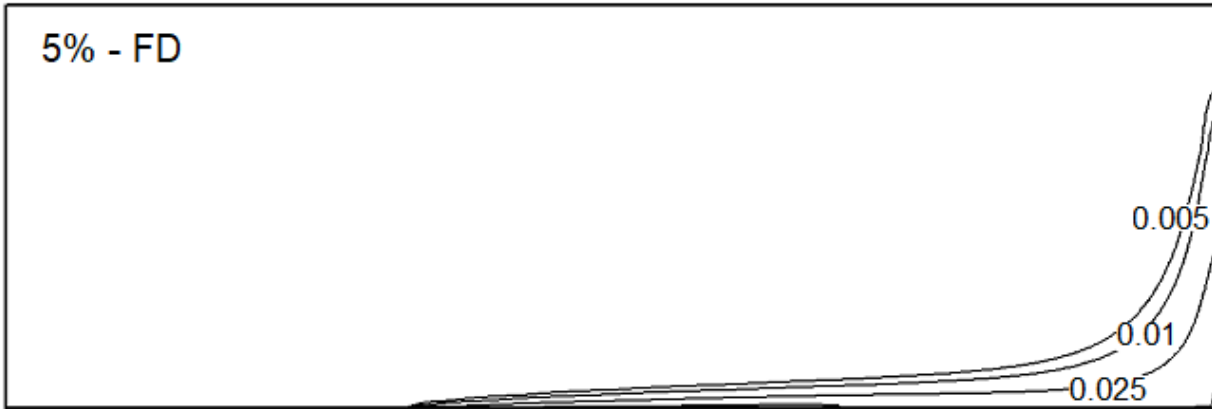


Figure 3-8. Uncalibrated results for a 5% gradient at 0.25 days produced using an FD model. Contour lines indicate concentration relative to saturation.

3.4.3.4. Calibrated results and sensitivities

Calibration to physical results was primarily dependent on flux values, hydrodynamic dispersivity, and initial concentration. Model 2 represents calibration to 5% Replicate 2 (Figure 3-5).

A modulation function was applied to simulate changing flux, with flux over the salt block divided into three equal sections with $2000 \text{ g m}^{-2} \text{ s}^{-1}$, $500 \text{ g m}^{-2} \text{ s}^{-1}$, and $1000 \text{ g m}^{-2} \text{ s}^{-1}$ from downstream to upstream. Calibration was based on the reduction of RMSE and comparison to observed data. The calibration of flux was an important component in the model calibration. Variable flux worked to explain peaks in concentration.

The peaks in concentration were closely related to the initial concentrations throughout the aquifer. The initial concentration at (0.29, 0.03 m) was assumed to create the concentration observed at that point. The timing of the physically-observed peaks was dependent on the initial location and magnitude of the increased concentration in the aquifer. However, similar peaks could be created using different patterns of initial concentration. The influence of initial conditions resulted in changes in location and magnitude of isolines, which may explain the high variability

observed between replicates. This explains why the maximum concentration was located at (0.85, 0.01 m) in some observations. In the numerical models, the unstable initial conditions increased the time to steady-state; however, similar isohalines to the uncalibrated scenario were achieved at steady-state. This is in contrast to the experimental results, where steady-state isohalines appeared to be sensitive to initial conditions. However, due to the slow shifting of concentrations, continued physical measurements may have reflected more similar results between replicates. A continuous simulation was limited by the dissolving salt mineral.

A transverse dispersivity value of 2.5×10^{-4} m was used from $x = 0$ to 0.8, and a reduced value of 5×10^{-5} m from 0.8 to 0.9 m in an attempt to reflect the overestimation of concentration observed at (0.89, 0.03 m) however, the improvement was marginal. The sensitivity of the model results to transverse dispersivity shows that high and low values improve results at different points in the model (Figure 3-6). A low estimate of 8.61×10^{-6} m, indicating a ratio longitudinal to transverse dispersivity of 305 and a high estimate of 0.0025 m, indicating a ratio of 1 were evaluated. The values immediately surrounding the salt block were better matched by low values, while downstream observation points were split between those best represented by each the high or low values. The low values resulted in larger peaks that were not observed in the model. However, while transverse dispersivity was reduced to match concentration observations in the section of vertical flow near the outflow, increased transverse dispersivity best matched the salt concentrations near the salt mineral and in the nearby downstream (Table 4). This indicates that different dispersivities may have been occurring throughout the experiment.

The sensitivity of the gradient was evaluated by comparing concentration measurements over a 2 cm vertical distance in the model. The resulting difference was approximately 0.32 M M^{-1} concentration, or 11 g L^{-1} of salt (Figure 3-9). This large gradient is important considering

measurement errors and heterogeneity in the physical model, as well as the unknown measurement volume. Due to the unknown measurement volume and measurement errors, observation points were adjusted by up to 1 cm to improve calibration.

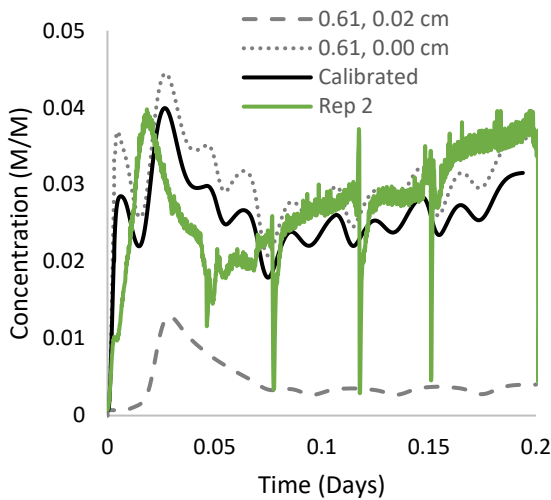


Figure 3-9. The sensitivity of the steep concentration gradient at $x = 0.61$ m between $y = 0.00$ and 0.02 m.

3.5. Discussion

Capturing data from an experiment in a benchtop aquifer resulted in a better understanding of flow and transport resulting from mineral dissolution. Variability between experiments was observed, highlighting the variable nature of this phenomenon. Data collection was difficult due to (1) sharp gradients, (2) potentially fluctuating mineral dissolution, and (3) initial concentrations in the overlying aquifer.

The numerical models were capable of generally producing flow and concentration contours at locations and magnitudes observed in the benchtop aquifer, and offered insight into the variation observed in the benchtop aquifer. Variable initial conditions were shown to be an important factor in simulating peaks observed in the physical results. Erratic flow patterns observed in the physical measurements were confirmed to be a result of variable initial conditions

and variable flux in the numerical model. Note Schincariol and Schwartz (1990) found that in variable-density groundwater flow models, different patterns developed based on the brine concentration. In these experiments, both the physical measurements and the FE and FD numerical model, flow stabilized to a swept-forward pattern. In the numerical models the steady-state isohalines were the same regardless of initial conditions on an extended time scale, while in the physical simulation, steady-state appeared to be dependent on initial conditions. This may have been a result of the physical measurements ending prior to reaching a true steady-state or varying flux rates. Variations in the steady-state distribution of concentration isohalines, based on changes in initial conditions have previously been observed in non-linear flow experiments (Schincariol and Schwartz, 1990). The time to reach a steady-state was dependent on the hydraulic gradient. Increased concentrations in the overlying aquifer increased the time it took for the numerical simulations to reach a steady-state.

The numerical models assumed that the system could be represented by one transverse and one longitudinal dispersivity value and that they were a physical property, not chemically controlled. However, in 1-D experiments, Hassanizadeh and Leijnse (1995) indicated that dispersivity was not only a property of the porous medium, but also dependent on the concentration gradient, and values had to be changed from case to case to get sufficient fits. In the case of this PEMD problem, different calibration points fit better with high or low transverse dispersivity. Further study is warranted in understanding dispersivity and concentration in this context.

The PEMD measurements collected one average mineral flux value for each physical model. However, spatially and temporally variable flux rates were used in the calibration to provide a better fit to the data. Heterogeneities in dissolution have previously been identified in the literature. Stiller et al. (2007) showed that the initial salinity and overlying salinity in solutions

was correlated to the dissolution rate. Weisbrod et al. (2012) found that dissolution patterns, either channel or frontal, in halite cores were controlled by flow rate. Alkattan et al. (1997a) and Alkattan et al. (1997b) found that under varying temperatures, halite saturation, flow velocity, and trace metal concentration, dissolution of halite ranged from about 1×10^{-1} and 9×10^{-3} mol m⁻² s⁻¹. The largest changes in flux are, therefore, expected prior to the experiment reaching steady-state. Dissolution rates appear to be transport or diffusion-limited, as solute overlying the salt block was not saturated. Future mineral dissolution studies would benefit from continuous flux measurements.

3.5.1. Limitations

The interpretation of the physical model results was limited by the inability to detail the concentration distribution within the tank. The interpretations of the point observations (Figures 2 & 3) were limited by measurement density. However, a closer spacing of the resistance measurements may have resulted in interference. Withdrawal samples influenced flow patterns by removal of fluid, and some ports were subject to leaks. Therefore, replicates were completed to improve confidence in the results. Resistance measurement error ranged from 7.8 to 14%; however, provided good temporal data. Withdrawal samples had errors of 2.4 to 3.0% for laboratory duplicates and up to 15% for sampling duplicates; however, they provided poor temporal data. Photometric methods could not be used, due to the difficulty dyeing a salt mineral and electrical magnetic scans with adequate resolution could not penetrate the Plexiglas.

Hydraulic heterogeneities in the benchtop aquifer, from the shape of the particles, packing of the sand, or dissolution of the salt mineral, have been shown to play an important role in the plume movement (Prasad and Simmons, 2003; Schincariol and Schwartz, 1990). Slight fluctuations observed in the physical model were assumed to be a result of physical

heterogeneities, such as particle packing and shape and slight head fluctuations. Dissolution of the salt mineral may have resulted in increased hydraulic conductivity in the overlying sand as dissolution resulted in a reduction in mineral height from 0.0020 to 0.0031 m, approximately twice the particle size of the porous media. The diffusion of the salt into the clay pack around the mineral and clay into the physical tank was assumed to be negligible. However, any release of clay ions into the aquifer may have resulted in an overestimation of salt entering the aquifer. The lack of detection of any concentration at (0.89, 0.10 m) in some replicates is assumed to be a result of preferential flow along the physical model boundary.

The modeling was limited by the ability of the numerical code to iteratively calculate flux as a function of concentration overlying the salt block. Mineral flux can be calculated as a function of concentration e.g. (Alkattan et al., 1997a). The assumption of constant flux would have the most impact at the beginning of the experiment, as that is when the largest changes in concentration occurred, and after that period, there is a general steady-state concentration.

3.5.2. Comparison with numerical HYDROCOIN1:5

The observed concentrations in the physical experiments and numerical models had steep concentration gradients and swept-forward flow. The field data associated with the HYDROCOIN1:5 problem supported the theory of a steep gradient (NEA and OECD, 1988). Results such as Diersch and Kolditz (1998), which support recirculation in the bottom portion of the aquifer indicate increased concentrations at points upstream of the salt block, similar to downstream. The measured results indicate no or low salt concentrations at steady-state at points above or upstream of the salt block. However, the concentrations are lower, and head gradients are higher in this PEMD study than HYDROCOIN1:5. HYDROCOIN1:5 applied concentration or flux boundaries much higher than found in these PEMD simulations. As a result, the

HYDROCOIN1:5 solute concentration results from NEA and OECD (1988) were approximately 10 times higher than the PEMD physical model observations. Kinetically controlled solute transport between the solid and aqueous phase can be limited by surface reactions, diffusion, or transport.

3.6. Conclusions

Flow and concentration data were collected in a porous benchtop aquifer overlying a dissolving salt mineral to provide physical evaporite mineral dissolution (PEMD) data. Duplicate measurements were made for 2%, 5%, and 10% flow gradients. Measured values for dispersion, hydraulic conductivity, porosity, and flux were input into a numerical model. Flow and concentration observations were input into an FE code (FEFLOW) and FD code (SEAWAT).

These benchtop aquifer measurements and computer models started as a relatively simple exercise in code verification to support model results from mineral-water interaction and resulting density-driven flow. However, considerable data were collected to support a better understanding of mineral dissolution, and numerical representation. Both FE and FD numerical codes were capable of simulating the general flow patterns, concentration magnitudes, locations of increased concentrations, and peaks resulting from initial conditions. The numerical models provided a reliable method of interpretation of flow patterns and causal relationships, indicating initial conditions, mineral flux, and dispersivity played major roles in salt distribution.

The measurements of physical parameters such as hydraulic head, permeability, porosity, hydrodynamic dispersivity, and flux were of paramount importance in model calibration. Variations between laboratory duplicates provided insight into the importance of initial conditions. Concentration measurement accuracy was vulnerable to high concentration gradients, small

measurement targets, and unknown measurement volumes. Numerical calibration to flux and transverse dispersivity resulted in improvement in some areas and deterioration in others. Improved calibration would require characterization of variability related to mineral dissolution including time-series flux and spatial variations in dispersivity.

The results suggest that high variability in concentration is intrinsic to salt dissolution problems and factors influencing dissolution should be characterized in a sensitivity analysis to indicate the potential range in concentrations. Groundwater solute data can be used to calibrate models, however, steep gradients can lead to widely varying concentrations in a small area. Numerical models are capable of predicting general concentrations and flow patterns, however, the numerical modeling in this study was limited by the ability to iteratively calculate flux as a function of changing conditions. Numerical models require input data related to dissolution including varying flux rates, hydrodynamic dispersion, and even suspended particles resulting from mineral dissolution that occurs even under controlled conditions. Similar issues are expected at the field scale.

Further work to calibrate the produced data and numerical model representations of flux boundaries are suggested to further improve the understanding of mineral dissolution in groundwater systems.

3.7. Acknowledgments, Samples, and Data

The authors would like to acknowledge Dr. Georg Houben, German Federal Institute for Geosciences and Natural Resources (BGR) for his valuable contributions to this research. Lab work was supported by Kerry Lynch and students Katie Sheir and Lu Wu. Support is acknowledged from Potash Corp for the salt cores, Canada Vanier Graduate Scholarships, and

University of Manitoba University Research Grant Program for funding and CMC Microsystems for products that facilitated this research. Experimental data are stored in the University of Manitoba's MSpace repository <https://mspace.lib.umanitoba.ca/handle/1993/33199>.

3.8. References

- Acero, P. et al., 2015. Evaluation of geochemical and hydrogeological processes by geochemical modeling in an area affected by evaporite karstification. *J Hydrol*, 529: 1874-1889. DOI: 10.1016/j.jhydrol.2015.07.028
- Alkattan, M., Oelkers, E.H., Dandurand, J.-L., Schott, J., 1997a. Experimental studies of halite dissolution kinetics, 1 The effect of saturation state and the presence of trace metals. *Chem Geol*, 137(3-4): 201-219. DOI: 10.1016/S0009-2541(96)00164-7
- Alkattan, M., Oelkers, E.H., Dandurand, J.-L., Schott, J., 1997b. Experimental studies of halite dissolution kinetics: II. The effect of the presence of aqueous trace anions and $K_3Fe(CN)_6$. *Chem Geol*, 143(1-2): 17-26. DOI: 10.1016/S0009-2541(97)00097-1
- ASTM International, 2000. ASTM D 2434-68 Standard Test Method for Permeability of Granular Soils. ASTM International, Conshohocken, PA.
- Baxter, G.P., Wallace, C.C., 1916. Changes in volume upon solution in water of the halogen salts of the alkali metals. II *Journal of the American Chemical Society*, 38(1): 70-105. DOI:10.1021/ja02258a010
- Beauheim, R.L., Roberts, R.M., 2002. Hydrology and hydraulic properties of a bedded evaporite formation. *J Hydrol*, 259(1-4): 66-88. DOI: 10.1016/S0022-1694(01)00586-8
- Carlson, R., Foley, T., 1991. Radial basis interpolation methods on track data.
- Diersch, H., 2014. FEFLOW Finite Element Modeling of Flow, Mass and Heat Transport in Porous and Fractured Media. Springer, New York.
- Diersch, H.J.G., Kolditz, O., 1998. Coupled groundwater flow and transport: 2. Thermohaline and 3D convection systems. *Advances in Water Resources*, 21(5): 401-425. DOI:10.1016/S0309-1708(97)00003-1
- Elder, J.W., 1967. Transient convection in a porous medium. *J Fluid Mech*, 27(03): 609-623. DOI:10.1017/S0022112067000576
- Fetter, C.W., 1999. Contaminant hydrogeology, 500. Prentice hall Upper Saddle River, NJ.
- Fetter, C.W., 2001. Applied Hydrogeology Prentice Hall, Toronto, Canada.
- Guo, W., Langevin, C.D., 2002. User's Guide to SEAWAT: A Computer Program for Simulation of Three-Dimensional Variable-Density Ground-Water Flow: Techniques of Water Resources Investigations. U.S. Geological Survey Techniques of Water-Resources Investigations, 77. U.S. Geological Survey.
- Hamid, H., Morozov, I.B., Kreis, L.K., 2005. Seismic Delineation of the Prairie Evaporite Dissolution Edge in South-central Saskatchewan. In: Survey, S.G. (Ed.), Summary of Investigations 2005. Saskatchewan Geological Survey, Saskatoon, pp. 11.
- Hassanizadeh, M.S., Leijnse, A., 1995. A non-linear theory of high-concentration-gradient dispersion in porous media. *Advances in Water Resources*, 18(4): 203-215. DOI: 10.1016/0309-1708(95)00012-8

- Herbert, A.W., Jackson, C.P., Lever, D.A., 1988. Coupled groundwater flow and solute transport with fluid density strongly dependent upon concentration. *Water Resources Research*, 24(10): 1781-1795. DOI:10.1029/WR024i010p01781
- Hesshaus, A., Houben, G., Kringel, R., 2013. Halite clogging in a deep geothermal well – Geochemical and isotopic characterisation of salt origin. *Physics and Chemistry of the Earth, Parts A/B/C*, 64(0): 127-139. DOI:10.1016/j.pce.2013.06.002
- Konikow, L., Sanford, W., Campbell, P., 1997. Constant-concentration boundary condition: Lessons from the HYDROCOIN variable-density groundwater benchmark problem. *Water Resources Research*, 33(10): 2253-2261.
- Konz, M., 2010. 2D benchmark experiments and simulations of density coupled flow problems, Universität Basel, Basel.
- Krupp, R.E., 2005. Formation and chemical evolution of magnesium chloride brines by evaporite dissolution processes--Implications for evaporite geochemistry. *Geochim Cosmochim Ac*, 69(17): 4283-4299. DOI:10.1016/j.gca.2004.11.018
- Moore, K.R., Holländer, H.M., 2018. Data for: An experimental and numerical study for salt dissolution and density-driven flow in porous media, MSpace. University of Manitoba, Winnipeg, MB.
- NEA, OECD, 1988. International Hydrocoin project: Groundwater hydrology modelling strategies for performance assessment of nuclear waste disposal. Level 1: Code verification, Nuclear Energy Agency (NEA), Organisation for Economic Co-operation and Development (OECD), Paris.
- Neuman, S.P., 1990. Universal scaling of hydraulic conductivities and dispersivities in geologic media. *Water Resources Research*, 26(8): 1749-1758. DOI:10.1029/WR026i008p01749
- O'Neil, M.J., 2013. The Merck index: an encyclopedia of chemicals, drugs, and biologicals. Sodium Chloride. Royal Society of Chemistry, Whitehouse Station, NJ.
- Oldenburg, C.M., Pruess, K., 1995. Dispersive Transport Dynamics in a Strongly Coupled Groundwater-Brine Flow System. *Water Resources Research*, 31(2): 289-302. DOI:10.1029/94WR02272
- Olsson, Å., Grathwohl, P., 2007. Transverse dispersion of non-reactive tracers in porous media: A new nonlinear relationship to predict dispersion coefficients. *J Contam Hydrol*, 92(3–4): 149-161. DOI:10.1016/j.jconhyd.2006.09.008
- Perkins, T.K., Johnston, O.C., 1963. A review of diffusion and dispersion in porous media. *Society of Petroleum Engineers Journal*, 3(01): 70-84.
- Pickens, J.F., Grisak, G.E., 1981. Scale-dependent dispersion in a stratified granular aquifer. *Water Resources Research*, 17(4): 1191-1211. DOI:10.1029/WR017i004p01191
- Post, V.E.A., Prommer, H., 2007. Multicomponent reactive transport simulation of the Elder problem: Effects of chemical reactions on salt plume development. *Water Resources Research*, 43(10): W10404. DOI:10.1029/2006wr005630
- Prasad, A., Simmons, C.T., 2003. Unstable density-driven flow in heterogeneous porous media: A stochastic study of the Elder [1967b] “short heater” problem. *Water Resources Research*, 39(1): SBH 4-1-SBH 4-21. DOI:10.1029/2002WR001290
- Reilly, T.E., Harbaugh, A.W., 2004. Guidelines for evaluating ground-water flow models. US Department of the Interior, US Geological Survey.
- Schincariol, R.A., Schwartz, F.W., 1990. An experimental investigation of variable density flow and mixing in homogeneous and heterogeneous media. *Water Resources Research*, 26(10): 2317-2329. DOI:10.1029/WR026i010p02317

- Schincariol, R.A., Schwartz, F.W., Mendoza, C.A., 1994. On the generation of instabilities in variable density flow. *Water Resources Research*, 30(4): 913-927.
DOI:10.1029/93WR02951
- Simmons, C.T., Narayan, K.A., Wooding, R.A., 1999. On a test case for density-dependent groundwater flow and solute transport models: The Salt Lake Problem. *Water Resources Research*, 35(12): 3607-3620. DOI:10.1029/1999wr900254
- Stiller, M., Yechieli, Y., Gavrieli, I., 2007. The rate of dissolution of halite in diluted Dead Sea brines, Ministry of National Infrastructure. Geological Survey of Israel, Jerusalem.
- Stoeckl, L., Walther, M., Graf, T., 2016. A new numerical benchmark of a freshwater lens. *Water Resources Research*, 52(4): 2474-2489. DOI:10.1002/2015WR017989
- Stokes, R.H., 1950. The diffusion coefficients of eight uni-univalent electrolytes in aqueous solution at 25. *Journal of the American Chemical Society*, 72(5): 2243-2247.
- Voss, C.I., Souza, W.R., 1987. Variable density flow and solute transport simulation of regional aquifers containing a narrow freshwater-saltwater transition zone. *Water Resources Research*, 23(10): 1851-1866. DOI:10.1029/WR023i010p01851
- Weisbrod, N., Alon-Mordish, C., Konen, E., Yechieli, Y., 2012. Dynamic dissolution of halite rock during flow of diluted saline solutions. *Geophysical Research Letters*, 39(9).
DOI:10.1029/2012GL051306
- Wooding, R.A., Tyler, S.W., White, I., 1997a. Convection in groundwater below an evaporating Salt Lake: 1. Onset of instability. *Water Resources Research*, 33(6): 1199-1217.
DOI:10.1029/96wr03533
- Wooding, R.A., Tyler, S.W., White, I., Anderson, P.A., 1997b. Convection in groundwater below an evaporating Salt Lake: 2. Evolution of fingers or plumes. *Water Resources Research*, 33(6): 1219-1228. DOI:10.1029/96wr03534
- Younes, A., Ackerer, P., Mose, R., 1999. Modeling Variable Density Flow and Solute Transport in Porous Medium: 2. Re-Evaluation of the Salt Dome Flow Problem. *Transport Porous Med*, 35(3): 375-394. DOI:10.1023/a:1006504326005
- Zidane, A., Zechner, E., Huggenberger, P., Younes, A., 2014. Simulation of rock salt dissolution and its impact on land subsidence. *Hydrol. Earth Syst. Sci.*, 18(6): 2177-2189.
DOI:10.5194/hess-18-2177-2014

4. Manuscript 2: Application of geochemical and groundwater data to predict sinkhole formation in a gypsum formation in Manitoba, Canada

The problem above presented the collection and modeling of mineral-fluid interaction under controlled laboratory conditions. This problem explores field-scale mineral-fluid interactions at high ionic strength, as well as the resulting solute transport as gypsum dissolves in freshwater. The problem began with the collection of flow data and development of a flow model, similar to the first stages of the geothermal THC model, and then adds solute transport data to validate the model. Solute-transport is the main process resulting in technical issues in geothermal systems, including the deposition of mineral scale in wellbores.

This manuscript contributed to the first sub-objective, to validate numerical methods used to calculate dissolution, flow, and transport of soluble mineral formations. A field-scale validation was necessary to build confidence in the ability of the numerical code to accurately represent the interactions between the geothermal heat exchange fluid and the in situ formation on a large scale. This study provided a bridge between the controlled laboratory conditions, where flow and geochemical measurements allowed for concise calibration, and the geothermal feasibility study, where flow rates were estimated, and geochemical observations were based on limited observation and rock type. This study used field measurements of flow, general formation composition, and field observations to characterize the formation of a sinkhole, thus validating the ability of reactive transport flow and geochemical model to calculate field scale mineral-rock interactions. This project also contributed significantly to the development of the modeler's process understanding.

Application of geochemical and groundwater data to predict sinkhole formation in a gypsum formation in Manitoba, Canada

Moore, K.R.¹, Holländer, H.M.¹, Basri, M.², Roemer, M.³

¹ *Department of Civil Engineering – University of Manitoba, Winnipeg, Manitoba, Canada*

² *Stantec Consulting Ltd., Winnipeg, Manitoba, Canada*

³ *TREK Geotechnical Inc., Winnipeg, Manitoba, Canada*

4.1. Abstract

Numerical modeling approaches were used to investigate coupled groundwater flow and reactive transport processes in gypsum karst sub-terrain. A regional equipotential map and steady-state flow model were created using scarce data to gain insights into flow patterns and to identify potential areas at risk for cavity and sinkhole development in a shallow gypsum formation. Coupled flow and reactive transport modeling was used to simulate the dissolution of gypsum between a sinkhole in a man-made drainage ditch and a quarry. Freshwater enters the drainage ditch and flows toward the quarry. Field data from a tracer test were used to calibrate flow within the model. The resulting regional equipotential map was valuable in identifying potential areas of sinkhole development; sinkholes occurred in areas underlain by thick gypsum formations with steep flow gradients and radial flow. The reactive transport model was valuable in identifying the growth of the cavity and the timeline for the potential risk to road infrastructure. The reactive transport model indicated that cavity growth could be slowed by removing the inflow of freshwater into the drainage ditch. Groundwater equipotential maps, flow models, and reactive transport models are valuable tools for the investigation of sub-terrain karst development including cavity development and sinkhole formation in evaporite minerals.

4.2. Introduction

The formation of karst, such as sinkholes, caves, and conduits in evaporite formations is a natural process, especially under rising and falling water tables, which commonly occur seasonally. Anthropogenic activities can cause or accelerate the development of karst through changes in groundwater flow patterns and disturbances to geology e.g. Benson and Kaufmann (2001), Fidelibus et al. (2011), Guerrero et al. (2008); Vigna et al. (2010). According to Fidelibus et al. (2011), the development of karst can result from fluctuations in the water table, changes to the groundwater flow direction, increases in water input, continuous renewal of undersaturated water in contact with gypsum, and freezing and thawing. Gypsum formations are especially susceptible to anthropogenic activities due to the mineral's high solubility compared to other common karst-prone minerals, such as limestone. In highly soluble evaporite formations, large conduits form and flow similar to pipe flow can occur. Sinkhole formation in gypsum due to anthropogenic activities has occurred worldwide, including Canada (Martinez and Boehner, 1997), USA (Benson and Kaufmann, 2001), Italy (Fidelibus et al., 2011) and Spain (Guerrero et al., 2008).

Sinkholes and other karst features are traditionally investigated using geological and geophysical investigations e.g. Carbonel et al. (2015) and Youssef et al. (2016). Geological investigations are important for understanding if the area is conducive to karst generation. Borehole drilling can provide valuable information but may exacerbate karst dissolution by introducing fractures or fluids, and blind drilling is unlikely to result in the encounter of cavities (Dobecki and Upchurch, 2006). Geophysical surveys can be used to predict where sinkholes and cavities are likely to occur, determine the underlying cause of subsidence or depressions, and evaluate the success or failure of stabilization techniques (Dobecki and Upchurch, 2006). Geophysical surveys include Ground-Penetrating-Radar (GPR), electrical resistivity tomography

(ERT) seismic methods, and microgravity surveying are used to investigate sinkholes, generally by locating and measuring cavities that have already formed (Carbonel et al., 2015; Dobecki and Upchurch, 2006).

Lapenskie and Bamburak (2015) discussed the importance of groundwater in gypsum dissolution; however, they were unable to predict the dissolution area or influence of the groundwater flow system. Groundwater flow modeling, along with basic field data can be used to characterize local flow and potential for dissolution. Dissolution, a multi-scale process that results in karst development, is a mass transfer limited process, therefore higher flow rates cause more dissolution, and local hydraulic gradients are an important factor (Guo et al., 2016; Kuechler et al., 2004). At the laboratory scale, Singurindy and Berkowitz (2003) observed the formation of highly conductive wormholes at high flow rates, but no wormholes at slow rates. The characterization of local flow properties can be used to predict the growth and risk of cavity development. Local data are important, as karst systems are highly heterogeneous and site-specific, and can be dominated by conduit or matrix flow and saturated or unsaturated conditions. Tracer tests have been identified as an important tool in the characterization of karst aquifers where the flow can be highly variable (Field, 1999).

Reactive transport modeling is used to simulate groundwater flow and chemical reactions, such as dissolution, the process that results in cavity and sinkhole formation. In addition to advection-driven transport, the influence of dissolution and density-driven convection can be simulated. Gypsum solubility is a function of minerals in solution and using reactive transport modeling, mineral specific activities and concentrations are used to calculate reactions. As such, the accurate representations of dissolution and therefore, cavity growth and size can be predicted. Important factors in dissolution, such as the volume of groundwater that moves through the system,

and the mineral composition and degree of saturation of the water, along with fractures or conduits and flow paths, can be simulated using reactive transport modeling (Palmer and Cherry, 1984). Solution pathways tend to form in the recharge area and move to the discharge area. As mineral dissolution occurs and conduits form, hydraulic conductivity generally increases, up to streamflow values. Shuster and White (1971) observed two types of groundwater in a carbonate karst system, small openings with low flow velocities tend to hold saturated water, while large conduits with high flow velocities tend to have undersaturated water. Reactive transport modeling has been used to study carbonate karst development in undisturbed catchments using a 1-D transport equation e.g. Bauer et al. (2002), Clemens et al. (1996). Numerical modeling has been shown to be a useful tool in simulating contaminant transportation through anisotropic and heterogeneous karst systems (Ghasemizadeh et al., 2012). Analytical modeling has been used to successfully simulate transport-controlled and reaction-controlled gypsum dissolution in columns under laboratory conditions (Li and Einstein, 2017).

Although sinkholes can be identified and characterized using current geophysical methods and geological features e.g. Carbonel et al. (2015), the prediction of the location and growth of karst features remains a challenge. Groundwater flow data, along with local groundwater and geology data provide a method for predicting areas prone to cavity growth and potential sinkhole development. Reactive transport modeling could be used as a tool to predict the development and growth of karst features such as cavities and potential for sinkhole development and to test and understand potential practical remediation strategies. Tools for understanding karst development are especially important in gypsum formations, which have a high dissolution rate, are commonly impacted by anthropogenic activities, and can quickly develop into hazards. The objectives of this study were to: (1) predict the locations of potential sinkhole development in a regional area

overlying a gypsum formation susceptible to sinkhole formation using available field data; (2) predict the gypsum dissolution and cavity formation with space and time using a coupled flow and reactive transport model calibrated with field data; and, (3) apply the coupled flow and reactive transport model to propose and investigate mitigation measures to inhibit sinkhole formation. A case study in the Rural Municipality (RM) of Alonsa, Manitoba, Canada is used to illustrate the potential for groundwater flow and reactive transport modeling for predicting sub-terrain karst development.

4.3. Methods

4.3.1. Study Area

The conceptual model for this project was based on a region of the RM of Alonsa, Manitoba, Canada (Figure 4-1 a). The region is experiencing damage to, and closure of roads, damage to electricity transmission poles and other infrastructure, as well as the loss of farming equipment due to sinkhole development. The sinkholes and cavities are forming in gypsum ($\text{CaSO}_4 \cdot 2\text{H}_2\text{O}$) in the shallow Upper Amaranth formation (Lapenskie and Bamburak, 2015). The study site is characterized by a till layer overlying a gypsum layer, both of which have been heavily disturbed in the construction of roads, drainage ditches, and quarries. In 2014, sinkholes up to 1.5 m in diameter were observed along the south side of South Leifur Road (117 N) near the intersection with road 56 W (Gurke, 2015). This intersection is located approximately 100 m south of a quarry (Figure 4-1 b). This drainage ditch, called the Marcus Drain, is part of a system of interconnected drains that services 45 km², with three outlets to Lake Manitoba, managed by the Alonsa Conservation District. Water is meant to continue past the local study area to Lake Manitoba but has been draining into the sinkhole. An attempt was made to divert the water around the ditch, however, sinkholes developed in the diversion (Bamburak, 2015). Sloping, slumping,

disturbed vegetation, and small openings were visible at the surface. In an attempt to stabilize the site in 2015, 30 m³ of bentonite were pumped into the sinkhole, a clay cap was added and the ditch was contoured (Gurke, 2015). However, in 2017 slumping and disturbed vegetation were visible.

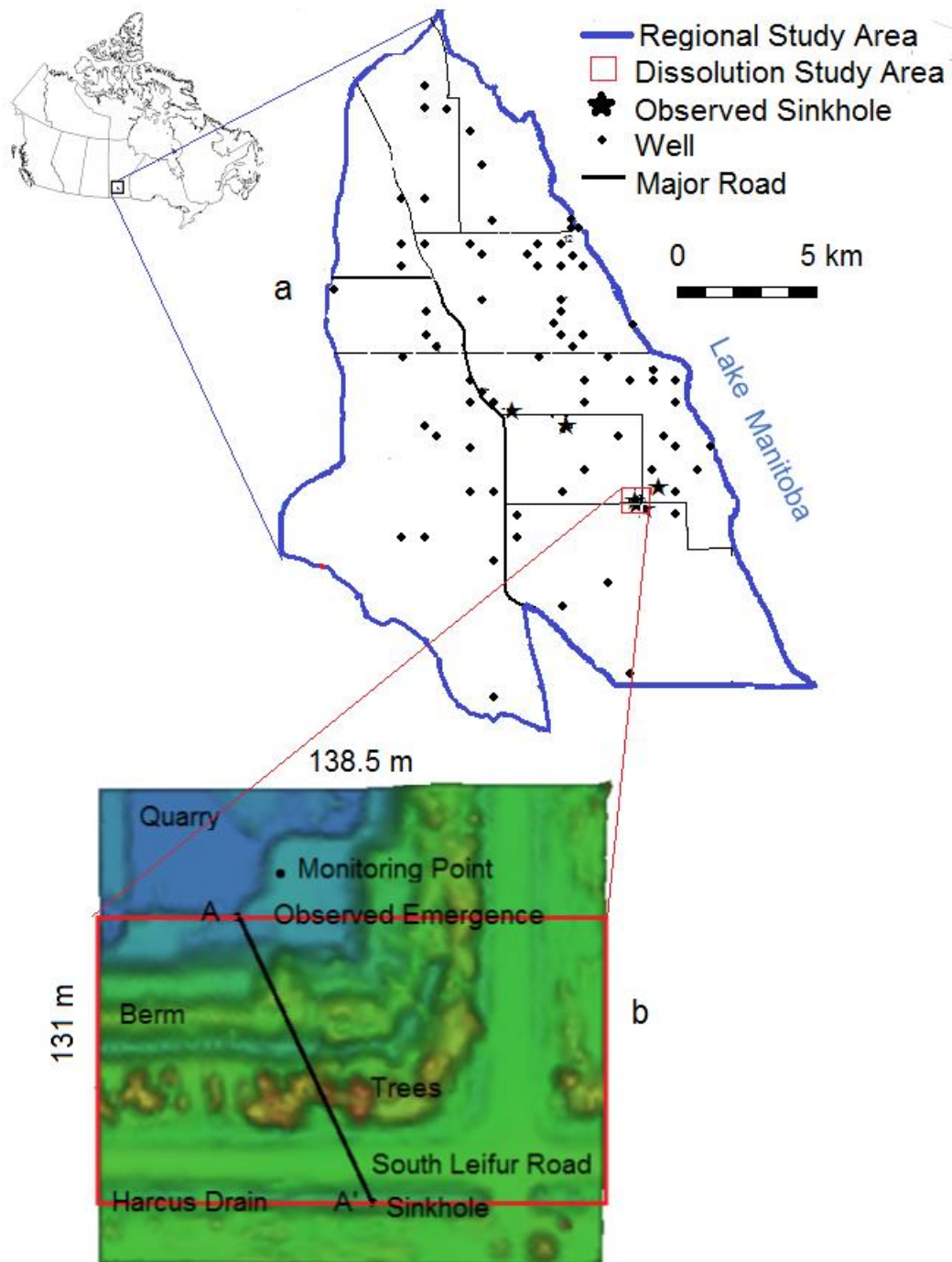


Figure 4-1. Study area for a) the Regional Model and b) the Dissolution Model.

4.3.2. Regional geology, hydrology, and hydrogeology

The gypsum, and associated karsting, observed in the RM of Alonsa is located in the Upper Amaranth formation from the Jurassic period, which outcrops near the study site (Poulton et al., 1994). The Upper Amaranth formation consists of an evaporite member with white anhydrite (CaSO_4) and gypsum with dolomite and shales, underlain by a red beds member with dolomitic red shale and siltstone (Bezys and McCabe, 1996). The stratigraphy of the regional area is characterized by a gypsum formation up to 10 m thick in the southern part of the region, with no gypsum present in the northern part (Figure 4-2) (Lapenskie and Bamburak, 2016). Till overlay increases from south to north, with the shallowest overlay over the region containing the quarries (Figure 4-2). The stratigraphy of the local study area, directly around the sinkhole and quarry (Figure 4-1 b), is characterized by approximately 6 m of glacial till overlying 7 m of gypsum (Lapenskie and Bamburak, 2016).

Sinkholes were observed in the Marcus area as early as 1965 (Bamburak, 2015). Gypsum has been mined at approximately 100,000 tonnes annually since 1978 (Bamburak, 2015). When production began, the quarry walls were observed to contain till-filled sinkholes. When anhydrite becomes hydrated there is a 30-60% increase in volume, the formation loosens, and the permeability increases; this change from anhydrite to gypsum may have initially slowed the formation of the cavities (Bannatyne 1959). Cores taken at the site by Manitoba Mineral Resources show signs of fracturing, weathering, and discontinuity, which indicate a larger number of fractures or conduits may be present and dissolution is occurring at depth. Although some fractures appear to have occurred during sampling, other fractures have noticeable weathering including rounded edges and changes in mineral structure, indicating dissolution.

The surface water catchment in the study area is part of the Alonsa district, a lowland along the western shore of Lake Manitoba in the centre of the Westlake Watershed (Manitoba Water Stewardship, 2010). Surface drainage is imperfect with many shallow lakes, marshes, and swamps (Rutulis, 1980). The area is drained by well-defined natural and man-made channels maintained by the Alonsa Conservation District, such as the Harcus Drain. The near-surface water flows from the Rocky Mountain highland, situated west of the site, to Lake Manitoba, which forms the eastern boundary. The area experiences both drought and flood conditions depending on major continental weather. Drains in the area have an intermittent flow, with a majority of the flow occurring between May and November. Following high water levels from June to November 2014, the Harcus drain (Figure 4-1 b) held 0.75 to 1.0 m of water.

The study area is located outside of major aquifer boundaries, north of the sand and gravel Assiniboine Delta Aquifer, east of the Odanah carbonate rock aquifer and south of the saline portion of the Carbonate rock Aquifer (Betcher, 1997). Within the study area, several freshwater wells have been completed in the sand and gravel and limestone aquifers (Hydata, 2018). The hydraulic conductivity in the till can be very low where it is dominated by clay. Shale and gypsum beds are used for withdrawal only where there is no sand and gravel, or poor quality in the limestone and dolostone aquifer (Rutulis, 1980). In the region underlain by shallow gypsum beds, groundwater is generally saturated in Ca and SO₄. Very little exploration has been conducted on the Amaranth Formation as a potential aquifer as the water is generally brackish to saline and not desirable as drinking water (Betcher et al., 1995). Thus limited groundwater data are available.

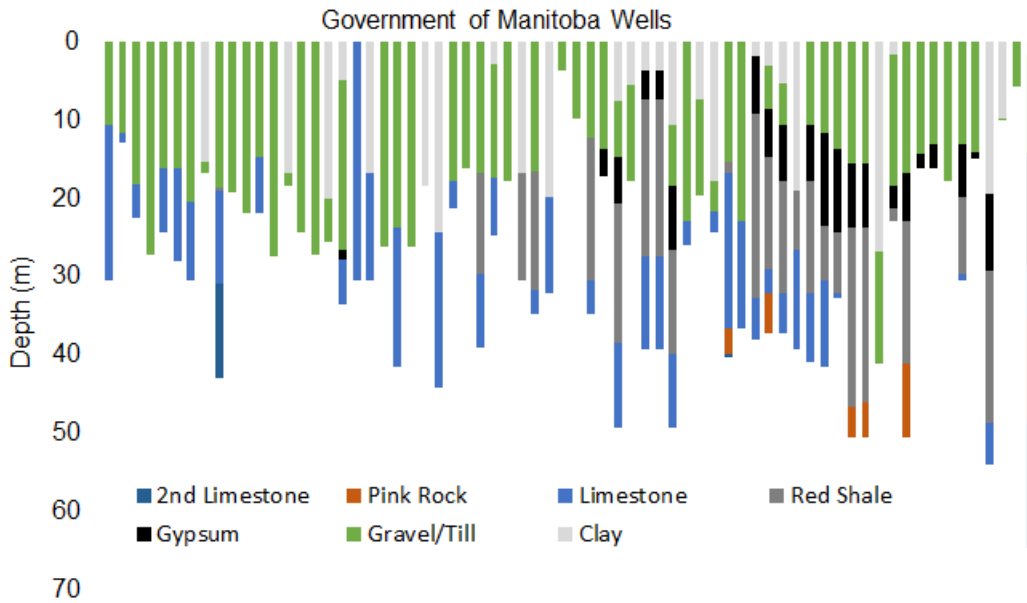


Figure 4-2. Stratigraphy of wells located in the Regional Flow Investigation study area based on data from Hydata (2018), wells are sorted from north to south throughout the study area.

4.3.3. Tracer test

Methods from Field (1999) and Carleton et al. (1999) were used to conduct a quantitative tracer test between the Harcus Drain and the quarry, with permission from the Government of Manitoba. A slug of 535 g of rhodamine-WT along with 3750 L of potable water for a concentration of 141 mg L^{-1} of rhodamine-WT was introduced into the sinkhole. Infiltration was 126 L min^{-1} . A Turner 10AU-005-CE fluorometer was used to monitor the emergence of Rhodamine-WT in the quarry. A second slug of 5678 L of potable water with no rhodamine-WT was introduced 21 hours after the beginning of the test, infiltration was 189 L min^{-1} . The travel distance between the inflow and the observation point was approximately 95.5 m. Monitoring continued in the quarry for approximately 48 hours. Tracer test results were published in Moore et al. (2018).

4.3.4. Modeling approach

Simulations were completed in two stages, first, a regional flow investigation to characterize the regional flow in the watershed surrounding the gypsum formations (Figure 4-1 a), and second, a local dissolution model to simulate the gypsum dissolution occurring directly between the Marcus drain and the quarry (Figure 4-1 b). For the regional flow investigation, a grid-based mapping program, where irregularly spaced coordinate data are interpolated using kriging was used to create the equipotential map. The regional groundwater model was created using a code capable of simulating steady-state groundwater flow.

Important for the dissolution model was the flow of water into and through a conduit and porous media as well as the dissolution of gypsum into the groundwater and multicomponent reactions. Ideal is a model that simulates density-driven flow, mass transport, and multispecies reaction equilibrium, which enables further use and expansion of the model for solving additional problems. FEFLOW (Diersch, 2014) is a finite-element model that solves the governing flow, mass, and heat transport equations in porous and fractured media. FEFLOW can simulate porous as well as conduit flow, variable fluid density, variable saturation, and multispecies reaction kinetics. When coupled with the piChem Plug-in (Wissmeier, 2015), FEFLOW is capable of calculating advanced geochemical reactions together with aqueous phase flow, including precipitation and dissolution (Wissmeier, 2015).

Groundwater flow in the matrix, assumed to be saturated and variable density, is described as:

$$\vec{q} = -\mathbf{K}f_u \cdot \left(\nabla h_0 + \left(\frac{\rho_s - \rho_0}{\rho_0} \right) \vec{e} \right) \quad 4-1$$

where \vec{q} is the Darcy flux (m s^{-1}), \mathbf{K} is hydraulic conductivity for the saturated matrix (m s^{-1}), f_u is a viscosity relation function (-), h_0 is the equivalent freshwater hydraulic head (m), ρ_s is the fluid density kg m^{-3} , ρ_0 is the reference fluid density (kg m^{-3}) and \vec{e} is the gravitational unit vector (-).

Karst aquifers are characterized by a dual flow system consisting of the primary matrix, which has a lower hydraulic conductivity but can hold a large quantity of water and a secondary flow system consisting of conduits, through which water flows quickly. The exchange between the two systems is a result of hydraulic head differences. Cavity development is dependent on the fracture density and conductivity of fractures (Bauer et al., 2002). The Darcy equation was used to describe the discrete feature (Diersch, 2014):

$$\vec{q} = -\frac{k_r \mathbf{k}_f}{\mu} \cdot (\nabla p - \rho g) \quad 4-2$$

where \vec{q} is Darcy flux (m s^{-1}), k_r is relative permeability (-), \mathbf{k}_f is the intrinsic permeability of the fracture (m^2), μ is the fluid viscosity, p is the reference fluid pressure (kg m^{-2}), ρ is fluid density (kg m^{-3}), and g is the gravity (m s^{-2}).

The use of the Darcy equation is dependent on laminar flow. The suitability of the Darcy equation for the discrete feature was assessed using the dimensionless Reynolds number (Re).

$$Re = \frac{\rho q d_i}{\mu} \quad 4-3$$

where q is the maximum Darcy flux (m s^{-1}), d_i is the diameter of the fracture (m) and μ is viscosity (Pa-s). A fluid density of 999 kg m^{-3} , based on freshwater at 20°C , a viscosity of $1 \times 10^{-3} \text{ Pa-s}$, and a diameter of 0.11 m based on a conduit cross-sectional area of 0.01 m^2 . For the fracture, the discharge velocity, based on the high value from the tracer test was 0.002 m s^{-1} . This

results in an R-value of 263. In open-channels such as the fracture, transition from laminar to turbulent flow occurs when R exceeds 2000 (Hornberger et al., 1998). Flow through the matrix was assumed at $1.15\text{e-}6 \text{ m s}^{-1}$, for an R-value of 0.1. Values of less than 1 to 10 are considered laminar (Lindquist, 1933). Thus, the flow was assumed laminar in both the fracture and the matrix, and Darcy's law is valid.

The coupling of geochemistry and flow is based on the assumption that aqueous phase flow can be expressed as the transport of individual components that constitute the aqueous phase (Wissmeier, 2015). Multi-component transport is calculated using the classical advection-diffusion/dispersion equation:

$$\frac{\partial \theta C_i}{\partial t} = -\nabla \cdot (\vec{q} C_i) + \nabla \cdot (\theta \mathbf{D} \nabla C_i) + S_c \quad 4-4$$

where θ is the relative liquid phase saturation ($\text{m}^3 \text{ m}^{-3}$), C_i (kg m^{-3}) is the concentration of the solution species i, \mathbf{D} ($\text{m}^2 \text{ s}^{-1}$) is the hydrodynamic dispersion tensor and S_c ($\text{kg m}^3 \text{ s}^{-1}$) is a source-sink term (Wissmeier, 2015).

4.3.5. Regional flow investigation

The regional flow investigation was used to characterize the larger flow regime to provide insight into areas at risk for gypsum dissolution. The areas identified by Lapenskie and Bamburak (2016) as having thick underlying gypsum ($>1 \text{ m}$), and having high flow gradients identified in this study were considered at risk for sinkhole development. A regional groundwater equipotential map and regional groundwater flow model were created using available regional well hydraulic head data from 1996 to 2017. A surface watershed boundary approximately 25 m north-south by 16 m east-west was selected for the model boundary (Figure 4-1 a). Groundwater levels in the nearest provincial monitoring wells, the Historical Regional Well Data, located approximately 40

km due west of the local study region are generally cyclical (Hydata, 2018). Average yearly fluctuations in well WRB58044 were an average of 1.53 m between 1998 and 2016 (Hydata, 2018) (Figure 4-3). Less pronounced fluctuations were observed in well WRB41603.

First, a regional groundwater equipotential map was created using available well data from Hydata (2018). Wells constructed in the unconfined sand and gravel and limestone or dolostone aquifers drilled from 1996 to 2017 were considered for water levels. The eastern boundary of the model was Lake Manitoba, which was considered to have a value of 231.5 m asl based on wells adjacent to the lake (Hydata, 2018). Equipotential lines were calculated using ordinary kriging. Based on observations from the nearest monitoring wells located approximately 50 km west of the site, trends indicate that the average water level has only a small variation over the period that the samples were collected (Hydata, 2018) (Figure 4-3). Well 58044 has an average increase of 0.037 m per year over the period of data collection (1987 - 2017). Well 41603 has an average increase of 0.011 m per year from 1964 to 2017. Based on the data, seasonal fluctuations are likely to be more than 2 m. These increases observed in the historical regional well data do not account for some of the huge gradients observed in the Regional Flow Model.

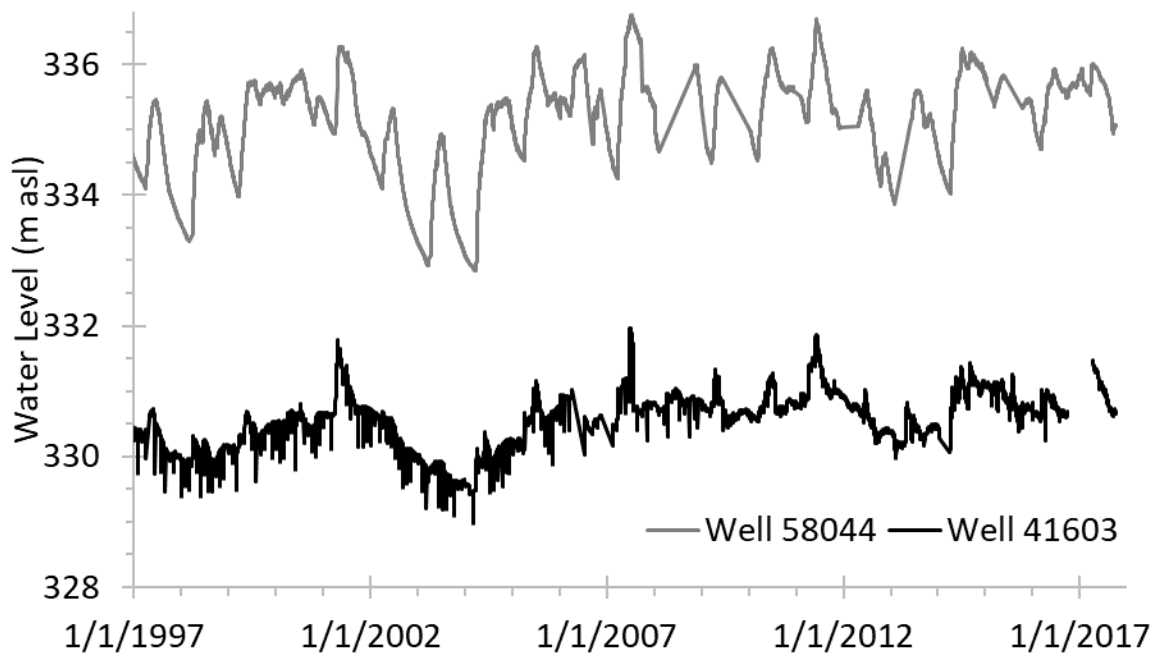


Figure 4-3. Monitoring well data showing long term patterns, wells located 50 km west of the study area near McCreary, Manitoba, Canada (Hydata, 2018).

Next, idealized, steady-state, 2-D horizontal flow in a continuous porous media of the same region was modeled, the regional groundwater flow model (Table 4-1). All wells drilled in the study area were considered for stratigraphy (Figure 4-2). Based on the stratigraphy, the aquifer was assumed to be unconfined from the surface to the bottom of the limestone or red shale. Although some layers contained significant amounts of clay at the top of the well, there was generally a small or no clay layer. Hydraulic conductivity was calibrated based on well observations. The eastern boundary of the model was Lake Manitoba, which was considered as a constant head boundary with a value of 231.5 m asl based on wells adjacent to the lake (Hydata, 2018). The western boundary was set as a constant head boundary of 270 m asl and calibrated for length and hydraulic head based on well observations. Recharge was not taken into account in this model. Using the available data, flow conditions were approximated, but a relatively high error

was expected due to the fluctuations that occur during wet and dry periods (Figure 4-3). The model was calibrated to reduce the root mean square error (RMSE).

Table 4-1. Model parameters for the Regional Flow Model and the Dissolution Model.

Parameter	Units	Regional	Dissolution
Domain length	m	27,000	134
Domain width	m	19,300	80
Elements	-	26,396	11974
Hydraulic anisotropy ratio	-	1	1
Effective porosity	-	0.3	0.3
Specific storage	m ⁻¹	1x10 ⁻⁴	1x10 ⁻⁴
Initial hydraulic conductivity matrix	m d ⁻¹	10	0.1
Discrete fracture law for conduit	-	-	Darcy
Initial hydraulic conductivity fracture	m d ⁻¹	-	100
Conduit cross sectional area	m ²	-	0.01
Longitudinal dispersivity	m	-	5
Horizontal dispersivity	m	-	0.5
Diffusion coefficient	m ² s ⁻¹	-	1x10 ⁻⁹
Ca initial solution	mol	-	1.418x10 ⁻²
SO ₄ initial solution	mol	-	1.418x10 ⁻²
pH initial solution	-	-	7
pE initial solution	-	-	5
Density	g cm ⁻³	-	1.002
Gypsum saturation index	-	-	0

4.3.6. Dissolution model

The dissolution flow model is a simulation of the geochemical reactions near the sinkhole and mine (Figure 4-1 b, Table 4-1). The purpose of the model was to simulate flow from the Harcus drainage ditch toward the quarry to improve the understanding of the flow of the water through gypsum, the dissolution effects on the cavity, the potential size and growth rate of the cavity and the potential risk to nearby infrastructure, such as the road. This model is a transient 2-D, horizontal model, containing the region between the sinkhole and the mine. The time-period for this model was 10 years. Only the gypsum formation was considered, and the thickness of the model was set at 1 m, as the effective thickness where the cavity has formed is unknown. Elevation data for the project came from The Advanced Spaceborne Thermal Emission and Reflection Radiometer

(ASTER) Global Digital Elevation Model, Hydata (2018), and the RM of Alonsa. Several different projections were used which may have caused some discrepancies in the data.

To create flow, a 5.46 m fluid-flux boundary was centered on the sinkholes to simulate water flowing in from the Marcus drain. The fluid-flux inflow boundary fluctuated every 182.5 days between 246 m and 244.1 m to simulate the wet and dry periods that occur in the intermittent drain. The 1.9 m fluctuation was based on the nearest Historical Regional Well Data (Hydata, 2018), the elevation of the ditch, and the elevation of water in the quarry (Figure 4-3). The outflow boundary, located along the northwest corner of the model simulating the quarry was a constant head boundary set at 244 m. The initial estimate for the hydraulic conductivity of the gypsum formation was between 0.1 m d^{-1} and 200 m d^{-1} , based on values for carbonate and sandstone aquifers in Manitoba (Betcher et al., 1995) and the results from the tracer test. In addition to the matrix, a conduit with a hydraulic conductivity of 100 m d^{-1} and a cross-sectional area of 0.01 m^2 connected the sinkhole to the quarry. Recharge from rainfall was not considered since the fluctuation in water level was a rough estimate, based on maximum flow rates.

The geochemistry of the model was simplified to include only fluids in equilibrium with gypsum and freshwater. Since the inflowing water was assumed to be primarily from precipitation, freshwater was assumed. The initial composition of the fluid in contact with the gypsum formation was assumed to be in equilibrium with gypsum, which was supported by field measurements (Tracer Test Results). Constant concentration boundaries were set along the east and west model boundaries in equilibrium with gypsum. A freshwater boundary was set at the inflow to simulate infiltrating water from the drainage ditch. Equilibrium reactions were used to simulate the interaction between the gypsum matrix and the freshwater. The timescale for the chemical step, where concentrations reach equilibrium is much shorter than the transport step or dissolution

timescale, meaning the dissolution of gypsum is transport controlled and, an equilibrium approach is appropriate (Li and Einstein, 2017). A thermodynamic equilibrium approach was within a 4% difference in mass flux compared to a two-reaction rate calculation in a gypsum formation (Guo et al., 2016). However, the use of an equilibrium boundary may result in concentrating the dissolution near the inflow.

Table 4-2. Initial water compositions for the Dissolution Model.

Parameter	Units	Inflowing	Formation
Ca	mol L ⁻¹	0	1.354 x 10 ⁻²
SO ₄ as S(6)	mol L ⁻¹	0	1.354 x 10 ⁻²
Gypsum	SI	-	0
Anhydrite	SI	-	-0.60
Temp	°C	6	6

The model was considered as a dual-porosity media, with the majority of the formation considered as porous media, and one large conduit. Ideally, the hydraulic conductivity would vary with gypsum concentration, as the gypsum concentration decreases, hydraulic conductivity should increase. Hydraulic conductivity values were expected to be highly variable in the study area due to the karst conditions. A time-dependent hydraulic conductivity was used to relate hydraulic conductivity to calcium concentration. To simulate the increasing size of the conduit, and considering numerical restriction, the hydraulic conductivity of the matrix surrounding the conduit K_d (m d⁻¹) was increased as per equation 4-5 in yearly time step.

$$K_d = K_m + K_f \left(\frac{(C_{Ca,Max} - C_{Ca})}{C_{Ca,Max}} \right)^n \quad 4-5$$

where K_m , the hydraulic conductivity of the matrix was assumed to be 0.01 m d⁻¹, K_f the hydraulic conductivity of the conduit was assumed to be 100 m d⁻¹ based on the tracer test, $C_{Ca,Max}$ is the saturated calcium concentration (mg L⁻¹), C_{Ca} is the observed calcium concentration (mg L⁻¹) and

n is an exponent, used to control the shape of the curve. A value of $n = 5$ in equation 4-5 was used for the simulations, with the calculation of the K_d value made annually.

4.4. Results

4.4.1. Tracer test results

The tracer test was used to measure potential hydraulic conductivity and fracture or conduit characteristics at the site (Moore et al., 2018). The data were used for calibration of the coupled flow and reactive transport model. The distance between the injection and monitoring sites was approximately 95 m. Rhodamine-WT was visible in the quarry 19 hours after injection and detected by the fluorometer between 20 hours and 39 hours. Two peaks occurred, likely associated with the two additions of water. The Rhodamine-WT concentration peaked at 23.4 hours at 50 ppb and 39 hours at 84 ppb. Dilution was assumed to have occurred when the tracer emerged into the quarry, which contained open water. Travel time was determined between 4.3 to 8.4 m hr⁻¹, mean residence time was 11.4 - 31.7 hours, and flow system volume was 129 - 228 m³ (Online Resource 1). Water samples from the quarry were compared to pure gypsum standards. Water within the quarry was found to contain 2.70 ± 0.02 g L⁻¹ of gypsum, based on 6 samples. In contrast, the injected water contained 0.78 ± 0.05 g L⁻¹.

4.4.2. Regional flow investigation

The Regional Groundwater Equipotential Map (Figure 4-4) was created using data collected during well construction in the sand and limestone aquifers over 20 years from 1998-2017. The purpose of this model was to identify areas with an increased likelihood of karst formation, where increased groundwater flow occurs near thick gypsum formations. The equipotential lines indicate that flow is from west to east, which is in agreement with Manitoba Water Stewardship (2010). Concentrated groundwater flow is observed near the quarry site, likely

associated with excavation, and in the northeast, near Lake Manitoba. A majority of the thick gypsum layer is located in the southern portion of the watershed. Sinkhole formation was primarily observed where gypsum was > 1 m in thickness and near increased hydraulic gradients, which occurred near the quarries. Increased flow gradients also occur in the northern part of the watershed, however, gypsum formations were < 1 m or of unknown thickness. Susceptibility to sinkhole formation requires both a high flow gradient and a thick gypsum formation and can be identified using equipotential maps.

A steady-state Regional Groundwater Flow Model (Figure 4-5) was created using data collected during well construction in the sand and limestone aquifers over 20 years from 1998-2017. The purpose of this model was to identify areas with an increased likelihood of karst formation, where increased groundwater flow occurs near thick gypsum formations. The equipotential lines indicate that flow is from west to east, which is in agreement with the equipotential map and Manitoba Water Stewardship (2010). This model does not indicate any areas of concentrated groundwater flow, aside from the quarry site. Thus, using this method, no areas susceptible to dissolution were identified beyond the quarry.

4.4.2.1. Regional Flow Model sensitivity analysis

During the development of the Regional Groundwater Equipotential Map and Regional Flow Model, the selection of representative wells were considered for the year they were drilled, and the formation into which they were drilled. Including additional older wells in the equipotential map resulted in a similar west to east flow pattern, however more areas of concentrated flow in the northern (no gypsum) part of the study area. The consideration of the lake level caused the flow to stabilize near the lake in a west-east pattern (Figure 4-4). These considerations had no major effect

on the results of this study. The Regional Flow Model was sensitive to the location of the constant head boundaries, and not sensitive to hydraulic conductivity ranging from 1 m d^{-1} to 1000 m d^{-1} .

4.4.2.2. Regional Flow Model calibration

Calibration results indicate a relatively high discrepancy between observations and model results, the mean difference was 3.9 m, root mean square error (RMSE) was 5.1 m, and the standard deviation was 5.3 m. This model was useful in estimating the approximate change in the hydraulic gradient for the tracer test and the dissolution model. These large errors may have been a result of the long time over which data were collected, measurement errors, and time of year measurements were taken.

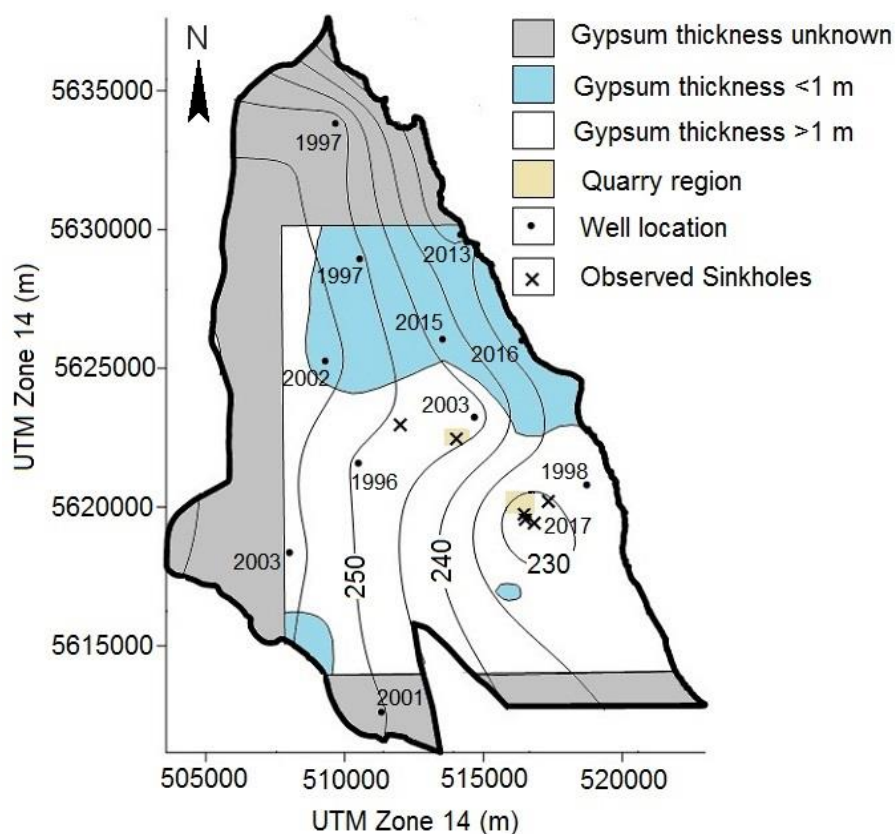


Figure 4-4. Groundwater equipotential map in m asl across the watershed, data is from sand and gravel and limestone aquifers observed between 1996 and 2017. Wells are labeled with the year they were drilled.

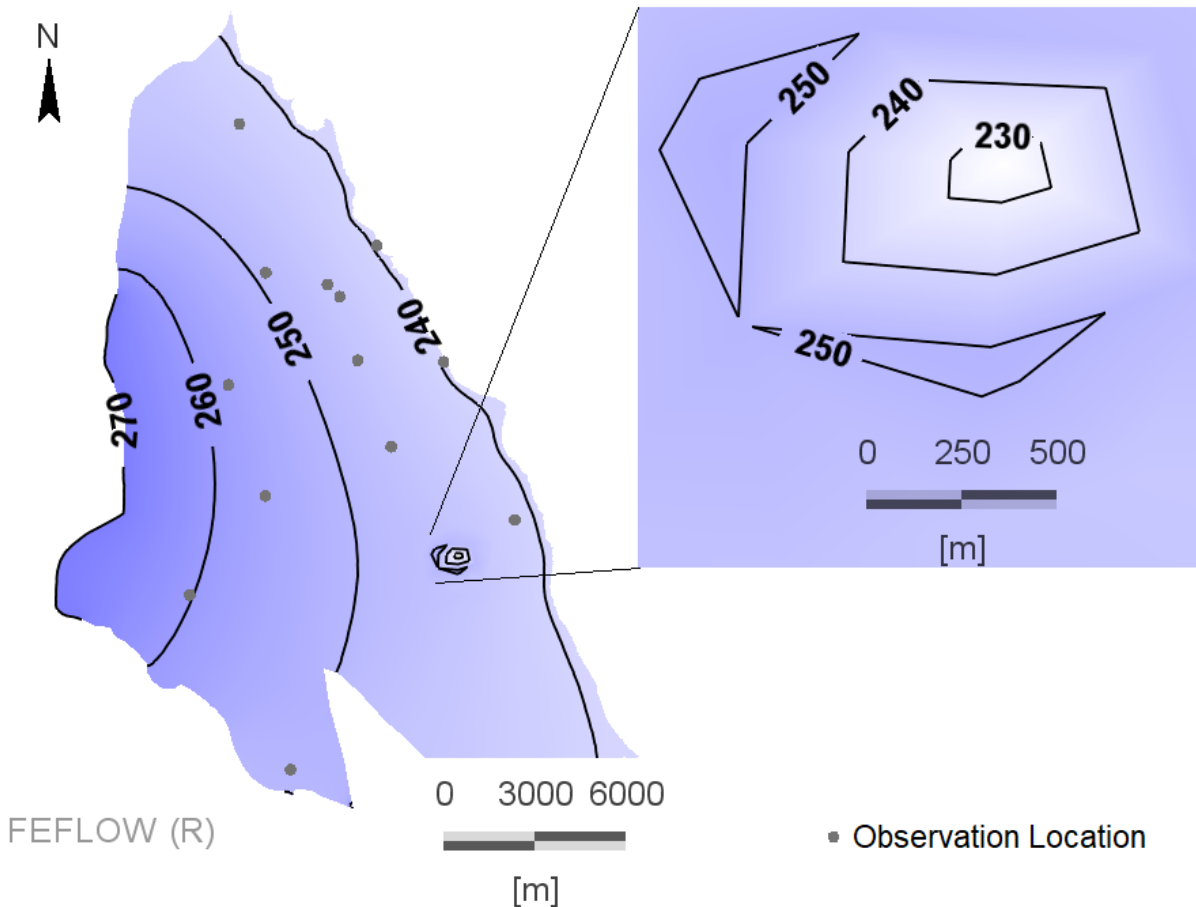


Figure 4-5. Regional Flow Model hydraulic head values for the watershed surrounding the quarry, values range from 270 in the west to 239 in the east, along Lake Manitoba.

4.4.3. Dissolution model

The Dissolution Flow Model is a coupled flow and reactive transport model used to simulate groundwater flow and geochemical reactions in the immediate vicinity of the sinkhole, including the prediction of karst cavity growth. Hydraulic head values were cyclical, semi-annually with a 1.9 m fluctuation between high flow and low flow periods (Figure 4-6). During high flow periods, there is a clear flow from the ditch towards the quarry, southeast to northwest. During low flow periods, flow continues from southeast to northwest, but with less concentration around the drain.

Dissolution occurred immediately as freshwater entered the system, identified by decreasing Ca^+ concentrations; at the end of the first year, decreased aqueous Ca^+ levels of 500 mg L^{-1} or less were observed in an area 10 m north-south and 20 m east-west (Figure 4-7 a). The dissolution progressed to 30 m north-south and 60 m east-west after 10 years (Figure 4-7 b). This indicates transport of gypsum from the formation and thus a large cavity.

4.4.3.1. Dissolution model sensitivity analysis

The cavity growth was sensitive to the hydraulic conductivity of the matrix; increasing the matrix hydraulic conductivity from 0.001 to 0.1 m d^{-1} increased the extent of the dissolution at 3650 days by approximately 50 m. Setting the matrix hydraulic conductivity equal to that observed in the tracer test (99 m d^{-1}) caused the entire site to experience total dissolution. The model was not sensitive to the hydraulic conductivity or cross-sectional area of the conduit.

The cavity growth was sensitive to the relationship between Ca^+ concentration and hydraulic conductivity. The power relationship where $n = 5$ assumed that major dissolution occurs when aqueous calcium concentrations reached approximately 300 mg L^{-1} . Dissolution was greatly increased assuming a linear relationship, $n = 1$.

The growth of the cavity was sensitive to the annual water flow. Decreased flow through the drainage ditch, and therefore the fracture, decreases dissolution and therefore, cavity growth. This is further discussed below as a remediation method.

4.4.3.2. Dissolution Model validation and calibration

The gypsum geochemical reactions were validated by evaluating the performance of PHREEQC (Parkhurst and Appelo, 2013) using results from column experiments studying the dissolution of gypsum from the site. PHREEQC performed well in simulating the dissolution and resulting concentration of dissolved gypsum in the effluent. Additionally, the growth of the karst

cavity has been validated by qualitative observations at the study site. Slumping within the Marcus Drain and across South Leifur Road has occurred, with the crown of the road slumping 0.26 m in 12 months from 2017 to 2018.

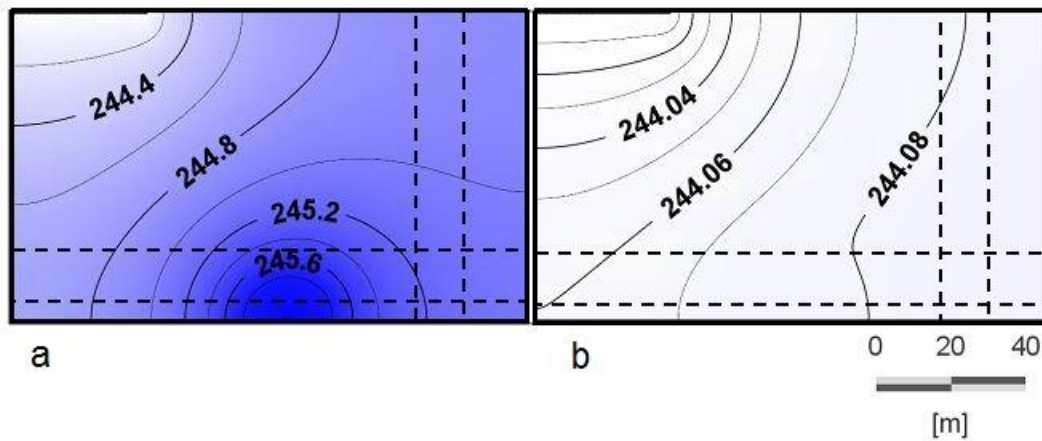


Figure 4-6. Hydraulic head equipotential lines representative of a) high flow and b) low flow periods, as defined in the model. The dashed black lines depict the location of the roads.

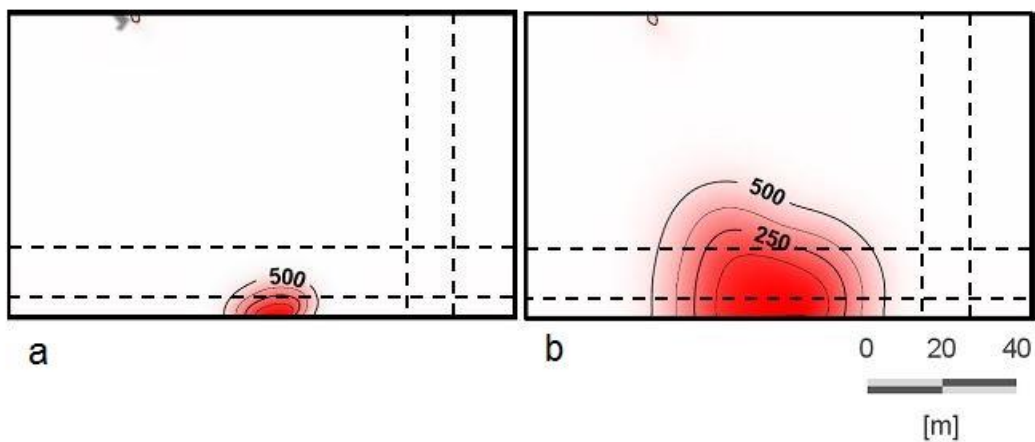


Figure 4-7. Gypsum dissolution after a) 365 days and b) 3650 days as indicated by aqueous calcium concentration. The relationship between hydraulic conductivity and concentration was calculated using $n = 5$ in equation 4-5. The dashed black lines depict the location of the roads.

4.5. Discussion

The Regional Groundwater Equipotential Map was a beneficial tool in identifying areas of sinkhole development, which were qualitatively correlated with thick gypsum (>1 m), high flow gradients, and changes in the flow direction (Figure 4-4). The majority of the sinkholes occurred near the quarries, where the landscape has been excavated. Groundwater was intersected during the construction of the quarries, which may have affected groundwater flow patterns. Groundwater flow was generally west to east in the study area, however, it was radial around the quarry. Using data from well construction in the watershed, high flow areas and thick gypsum formations were found to correlate with sinkhole development. Despite being collected outside of the study area, Historical Regional Well Data (Figure 4-3) were important in understanding long term trends, and their potential effects on the well data, since the Regional Equipotential Map was created using data observed over 20 years.

The steady-state Regional Groundwater Flow Model was not as beneficial as the Regional Equipotential Map in predicting areas of increased dissolution, as no regions with high flow gradients were observed. However, the poor calibration values for some of the wells may indicate that areas of increased flow do exist. The trends observed in the Historical Regional Well Data do not account for some of the huge gradients observed in the Regional Flow Model. Additional well monitoring data and hydraulic conductivity data could be used to create a transient flow model, which may be more beneficial for predicting dissolution. Both the Regional Groundwater Equipotential Map and the Regional Flow Model indicate that regional flow is generally west to east and that the radial flow observed at the quarry site is likely a result of the excavation activities.

The tracer test was an important component for providing calibration data for the Dissolution Flow Model. The Dissolution Flow Model was an important tool in identifying the

potential spread of the cavity, at-risk areas for sinkhole development, and potential growth factors. The results indicate that karstification in the gypsum is dependent on the hydraulic conductivity of the matrix and conduit, and the relationship between the hydraulic conductivity and the concentration of aqueous calcium. The maximum hydraulic conductivity used in the model, 100 m d^{-1} , could potentially be lower than actual values. The assumption that water flow in the Marcus Drain infiltrated at a head difference of 2 m for 6 months is high, so that dissolution may be overestimated.

It is difficult to assess the time that the hydraulic connection occurred between the drainage ditch and the quarry and to characterize past conditions. In 2014, the sinkholes first became visible at the surface, however, a significant amount of dissolution had to occur before that time. Based on the assumed initial conditions, the model indicated a 10 m by 20 m region of dissolution in the first year. Assuming the formation of the cavity started around 2014 when water levels were high, a cavity is expected underneath South Leifur Road by 2024 (Figure 4-7 b). At the current time, the cavity is likely beginning to move underneath South Leifur Road (Figure 4-8 a). Based on the tracer test results, predicting a flow system volume up to 228 m^3 , and a dissolved area approximately 18 x 45 m with a concentration $<450 \text{ mg L}^{-1}$, expected is a 0.3 m opening in the vertical direction. Assuming a dissolved area 11 m by 20 m based on a concentration $<250 \text{ mg L}^{-1}$, expected is a 1 m opening in the vertical direction. Guerrero et al. (2008) rated sinkholes as highly susceptible where karstic depressions or collapse structures were visible near the surface and intermediate susceptible where there was less than 10 m of alluvium, irregular rockhead, cavities, and sagging structures. Based on this description the road is high-risk for the spread of sinkholes, as there is a sinkhole and collapsing visible near the surface.

The mining and drainage activities in the Harcus region likely resulted in the hydraulic connectivity that causes the water to flow southeast to northwest in the from the ditch to the quarry. General water flow in the region is west to east. Changes in water level in the mine excavation and drainage ditch can increase and decrease the hydraulic gradient. As the hydraulic gradient and therefore, flow increases, the gypsum dissolution will also increase (Kuechler et al., 2004). Draining the quarry is not recommended, as this will result in an increased hydraulic gradient, and surrounding groundwater will likely drain towards the site, increasing dissolution. Previous remedial measures at the site involved grouting and clay capping. Since the gypsum is a continuous formation, grouting will fill sinkholes that have already formed but will do nothing to prevent the formation of new cavities, which are likely to occur under the same flow conditions. Cooper and Saunders (2002) indicated that methods such as grouting in gypsum are not useful when there is still high water flow. The reduction of water flow through the gypsum is the best way to reduce dissolution. At the Harcus Drain site, by reducing flow, or water level in the ditch, the spread of the cavity can be reduced e.g. Figure 4-8 b, after 10 years compared to Figure 4-7 b. Attempts to install a liner in the Harcus drain were unsuccessful, due to shifting soils, which likely caused a tear in the liner. An effective remediation plan may involve re-routing the water that currently travels down the Harcus Drain to an area with no underlying gypsum. This will reduce the hydraulic gradient between the ditch and the quarry. Based on the map in Lapenski (2016), at this site, the drainage would need to be redirected by less than 10 km.

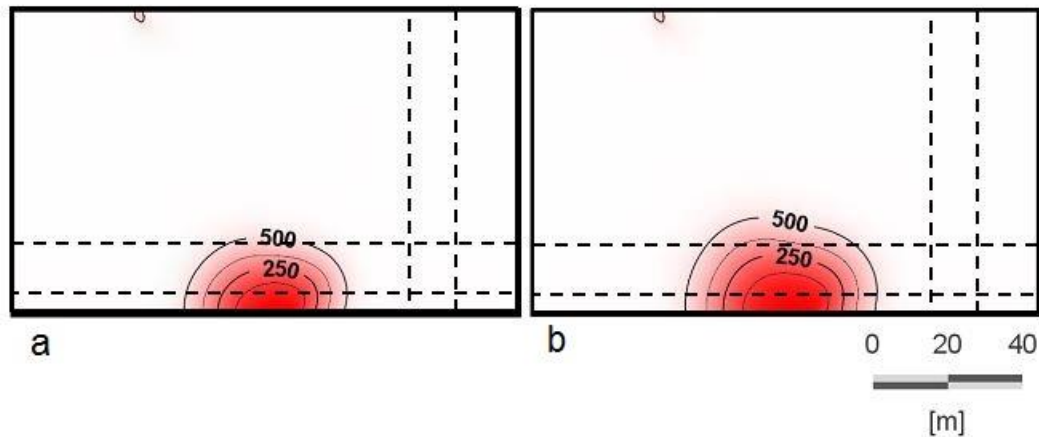


Figure 4-8. Gypsum dissolution after a) 1825 days (4 years), and b) after 3650 days (10 years) as indicated by aqueous calcium concentration. The hydraulic gradient was removed after 1825 days, reducing flow to a minimal value, simulating remedial measures. The dashed black lines depict the location of the roads. The relationship between hydraulic conductivity and concentration was calculated using $n = 5$.

Additional data that would be valuable for the reactive transport model are the chemical composition of the inflowing water, the chemical composition of the water in the quarry, and the volume of water in the quarry. Additional monitoring well data would be valuable in understanding the hydraulic gradient at the site. Temporal recharge data or stream inflow volumes could be used to increase the model accuracy. Further information on the vertical spread of the cavity, which may provide further information on sinkhole susceptibility, could be done using a 3-D modeling approach.

4.6. Conclusions

The karst formations in the RM of Alonsa are the result of fresh groundwater interacting with thick gypsum formations. Geophysical methods can be used to identify and characterize karst sub-terrain, however, the formation and at-risk areas for sinkholes can be best identified by simulating the groundwater flow processes that dissolve the formation.

A groundwater equipotential map developed using historical well construction data was valuable in the identification of high flow regions. Important in this evaluation was the map of sub-terrain gypsum thickness. The equipotential map was an excellent tool in predicting sinkhole formation, which was noted in areas with high flow gradients and radial flow where thick gypsum (>1 m) was present. A steady-state regional flow model constructed using the same data was less beneficial in identifying areas at risk to sinkhole development. However, radial groundwater flow in the vicinity of the quarry, where thick gypsum was present was identified as a high-risk area. The steady-state regional flow model was beneficial in the prediction of hydraulic gradients for the localized coupled flow and reactive transport model.

The coupled flow and reactive transport model was valuable in the prediction of the growth rate and direction of the karst cavity adjacent to the sinkhole. Using basic field data, such as a tracer test and geological maps, the flow and reactive transport model was calibrated and used to predict gypsum dissolution. The results indicate that karstification in the gypsum occurs fastest at the inflow and is highly dependent on the hydraulic conductivity of the matrix and conduit, and the relationship between the hydraulic conductivity and the concentration of aqueous calcium. Using the model, the growth of the cavity was calculated to identify the timeline for the risk to the road infrastructure. Surface slumping observed at the site validates the results of the model, however additional measurements of the cavity would also prove valuable for model validation. Finally, mitigation measures were considered using the coupled flow and reactive transport model. Draining the quarry would exacerbate the growth of the cavity by increasing the hydraulic gradient. Increased hydraulic gradients will result in increased dissolution and faster cavity formation. The reduction of water flow through the gypsum is the best way to reduce dissolution.

4.7. Acknowledgments

The authors would like to acknowledge the Vanier Canada Graduate Scholarship and Natural Sciences and Engineering Research Council of Canada Engage for funding, Shawn Gurke and the Alonsa Conservation District, along with the RM of Alonsa for their assistance with the project, and Gebeyehu Ayele and Kerry Lynch for their contribution to the fieldwork.

4.8. References

- Bamburak, J., 2015. Marcus sinkholes in the Amaranth Area (NTS Area: 62J10NW, 15 SW), Alonsa Conservation District, Winnipeg, MB.
- Bauer, S., Liedl, R., Sauter, M., 2002. Modelling of karst genesis at the catchment scale – influence of spatially variable hydraulic conductivity. *ACTA GEOLOGICA POLONICA*, 52(1).
- Benson, R.C., Kaufmann, R.D., 2001. Characterization of a highway sinkhole within the gypsum karst of Michigan. In: Beck, B.F., herring, J.G. (Eds.), *Geotechnical and Environmental Applications of Karst Geology and Hydrology*. Balkema Publishers, Miami, FL.
- Betcher, R.N., 1997. Rural Groundwater Quality Surveys: Southern and Central Manitoba, Rural Water Quality Symposium., Winnipeg, pp. 19-38.
- Betcher, R.N., Pupp, C., Grove, G., 1995. Groundwater in Manitoba: hydrogeology, quality concerns, management. Environment Canada, National Hydrology Research Institute.
- Bezys, R.K., McCabe, H.R., 1996. Lower to middle Paleozoic stratigraphy of southwestern Manitoba, Geological Association of Canada, Winnipeg, Manitoba.
- Carbonel, D. et al., 2015. Investigating a damaging buried sinkhole cluster in an urban area (Zaragoza city, NE Spain) integrating multiple techniques: Geomorphological surveys, DInSAR, DEMs, GPR, ERT, and trenching. *Geomorphology*, 229: 3-16. DOI: 10.1016/j.geomorph.2014.02.007
- Carleton, G.B., Welty, C., Buston, H.T., 1999. Design and Analysis of Tracer Tests to Determine Effective Porosity and Dispersivity in Fractured Sedimentary Rocks, Newark Basin, New Jersey, U.S. Department of the Interior, U.S. Geological Survey, West Trenton, New Jersey.
- Clemens, T., Huckinghaus, D., Sauter, M., Liedl, R., Teutsch, G., 1996. A combined continuum and discrete network reactive transport model for simulation of karst development, Calibration and Reliability in Groundwater Modelling, ModelCARE 96. IAHS Golden, Colorado.
- Cooper, A.H., Saunders, J.M., 2002. Road and bridge construction across gypsum karst in England. *Eng Geol*, 65(2): 217-223. DOI: 10.1016/S0013-7952(01)00131-4
- Diersch, H., 2014. FEFLOW Finite Element Modeling of Flow, Mass and Heat Transport in Porous and Fractured Media. Springer, New York.
- Dobecki, T.L., Upchurch, S.B., 2006. Geophysical applications to detect sinkholes and ground subsidence. *The Leading Edge*, 25(3): 336-341. DOI:10.1190/1.2184102
- Fidelibus, M.D., Gutiérrez, F., Spilotro, G., 2011. Human-induced hydrogeological changes and sinkholes in the coastal gypsum karst of Lesina Marina area (Foggia Province, Italy). *Eng Geol*, 118(1): 1-19. DOI: 10.1016/j.enggeo.2010.12.003

- Field, M.S., 1999. The QTRACER program for tracer-breakthrough curve analysis for karst and fractured-rock aquifers, 98. National Center for Environmental Assessment--Washington Office, Office of Research and Development, US Environmental Protection Agency.
- Ghasemizadeh, R. et al., 2012. Review: Groundwater flow and transport modeling of karst aquifers, with particular reference to the North Coast Limestone aquifer system of Puerto Rico. *Hydrogeol J*, 20(8): 1441-1461. DOI:10.1007/s10040-012-0897-4
- Guerrero, J., Gutiérrez, F., Bonachea, J., Lucha, P., 2008. A sinkhole susceptibility zonation based on paleokarst analysis along a stretch of the Madrid–Barcelona high-speed railway built over gypsum- and salt-bearing evaporites (NE Spain). *Eng Geol*, 102(1): 62-73. DOI:10.1016/j.enggeo.2008.07.010
- Guo, J., Laouafa, F., Quintard, M., 2016. A theoretical and numerical framework for modeling gypsum cavity dissolution. *International Journal for Numerical and Analytical Methods in Geomechanics*, 40(12): 1662-1689. DOI:10.1002/nag.2504
- Gurke, S., 2015. Harcus Drain Sinkhole Report, Alonsa, Manitoba.
- Hornberger, G.M., Wiberg, P.L., Raffensperger, J.P., D'Odorico, P., 1998. *Elements of physical hydrology*. JHU Press, Baltimore, 302 pp.
- Hydata, 2018. Water Level Data. In: Province of Manitoba, G.M. (Ed.).
- Kuechler, R., Noack, K., Zorn, T., 2004. Investigation of gypsum dissolution under saturated and unsaturated water conditions. *Ecological Modelling*, 176(1): 1-14. DOI: 10.1016/j.ecolmodel.2003.10.025
- Lapenskie, K., Bamburak, J., 2015. Preliminary results from geological investigations into gypsum, Harcus area, southwestern Manitoba (NTS 62J10), Manitoba Mineral Resources, Manitoba Geological Survey, Winnipeg, Manitoba.
- Lapenskie, K., Bamburak, J., 2016. Gypsum investigations in the Harcus area, southwestern Manitoba (NTS 62J10): 2016 update, Manitoba Growth, Enterprise and Trade, Manitoba Geological Survey.
- Li, W., Einstein, H.H., 2017. Theoretical and Numerical Investigation of the Cavity Evolution in Gypsum Rock. *Water Resources Research*, 53(11): 9988-10001. DOI:10.1002/2017WR021776
- Lindquist, E., 1933. On the flow of water through porous soil, *Premier Congres des grands barrages* (Stockholm), pp. 81-101.
- Manitoba Water Stewardship, 2010. Groundwater Resources of the Westlake Integrated Conservation District, Manitoba Water Stewardship Groundwater Management Section.
- Martinez, J.D., Boehner, R., 1997. Sinkholes in glacial drift underlain by gypsum in Nova Scotia, Canada. *Carbonates and Evaporites*, 12(1): 84. DOI:10.1007/bf03175806
- Moore, K.R. et al., 2018. A field and numerical study of a tracer test in a gypsum formation beneath a road, GeoEdmonton 2018. Canadian Geotechnical Society, Edmonton, Canada.
- Palmer, C.D., Cherry, J.A., 1984. Geochemical reactions associated with low-temperature thermal energy storage in aquifers. *Canadian Geotechnical Journal*, 21(3): 475-488. DOI:10.1139/t84-051
- Parkhurst, D.L., Appelo, C., 2013. Description of input and examples for PHREEQC version 3-- A computer program for speciation, batch-reaction, one-dimensional transport, and inverse geochemical calculations. In: Survey, U.S.G. (Ed.), *U.S. Geological Survey Techniques and Methods Section A, Groundwater Book 6, Modeling Techniques*, Denver, Colorado, pp. 497.

- Poulton, T. et al., 1994. Jurassic and lowermost Cretaceous strata of the Western Canada sedimentary basin. In: Mossop, G., Shetsen, I. (Eds.), Geological Atlas of the Western Canada Sedimentary Basin. Canadian Society of Petroleum Geologists and Alberta Research Council, Calgary, Alberta, pp. 297-316.
- Rutulis, M., 1980. Groundwater Resources in the Alonsa Conservation District, Manitoba Department of Natural Resources Water Resources Branch, Winnipeg, Manitoba.
- Shuster, E.T., White, W.B., 1971. Seasonal fluctuations in the chemistry of limestone springs: A possible means for characterizing carbonate aquifers. *J Hydrol*, 14(2): 93-128. DOI: 10.1016/0022-1694(71)90001-1
- Singurindy, O., Berkowitz, B., 2003. Evolution of hydraulic conductivity by precipitation and dissolution in carbonate rock. *Water Resources Research*, 39(1): 8-1 - 8-14. DOI:10.1029/2001WR001055
- Vigna, B., Fiorucci, A., Banzato, C., Forti, P., De Waele, J., 2010. Hypogene gypsum karst and sinkhole formation at Moncalvo (Asti, Italy). *Zeitschrift für Geomorphologie, Supplementary Issues*, 54(2): 285-306. DOI:10.1127/0372-8854/2010/0054S2-0015
- Wissmeier, L., 2015. piChem - A FEFLOW Plugin for Advanced Geochemical Reactions. In: Institute, D.H. (Ed.), MIKE powered by DHI, Hørsholm, Denmark, pp. 28.
- Youssef, A.M. et al., 2016. Natural and human-induced sinkhole hazards in Saudi Arabia: distribution, investigation, causes and impacts. *Hydrogeol J*, 24(3): 625-644. DOI:10.1007/s10040-015-1336-0

5. Manuscript 3: Evaluation of NaCl and MgCl₂ heat exchange fluids in a deep binary geothermal system in a sedimentary halite formation

The validation of numerical codes using laboratory and field models provides confidence in the ability to predict the subsurface reactions occurring between halite minerals and injected heat exchange fluids. While it is assumed that geothermal fluids in contact with halite minerals will generally be saturated with halite at site-specific temperature and pressure, reactive transport modeling can be used to understand the fluctuations in saturation that occur as geothermal fluids move through the geothermal system. The potential for mitigation of dissolution and precipitation using chemical inhibitors such as MgCl₂ is explored.

This manuscript contributed to the second sub-objective, to assess the composition of heat exchange fluids produced when targeting halite formations using local geochemical data. This was achieved by characterizing the geochemistry of heat exchange fluids targeting the Prairie Evaporite in the Williston Basin. This study explores the potential composition of produced fluids, and introduces the concept of engineering heat exchange fluids to inhibit precipitation and dissolution within the geothermal system. Each stage of movement and temperature change through a geothermal system, along with potential precipitates are explored. This study identifies potential risks of scaling and clogging associated with the geochemistry of the formation and geothermal fluid. This presents a novel, proactive approach to investigating geothermal hydrogeochemistry, as opposed to the reactive approach to investigate after problems occur.

Evaluation of NaCl and MgCl₂ heat exchange fluids in a deep binary geothermal system in a sedimentary halite formation

Kayla R. Moore and Hartmut M. Holländer

5.1. Abstract

Deep geothermal systems in sedimentary basins involve complex chemical reactions between heat exchange fluids and evaporate reservoir formations. Precipitation and dissolution can affect the long-term viability of deep geothermal systems. An understanding of the geochemical reactions at depth between heat exchange fluids and formations can be used to inform decision making regarding well construction, prevention of well clogging, formation dissolution, and thermal short-circuiting. Halite formations, which occur in sedimentary basins, have the geothermal advantage of high heat conductivity, resulting in higher temperatures than other formations at similar depths. However, halite formations are highly reactive with undersaturated water. Numerical 1-D and 3-D flow and equilibrium reactive transport modeling was used to simulate the interaction between a halite reservoir and saturated NaCl, MgCl₂, and NaCl+MgCl₂-brines in a geothermal doublet system. The MgCl₂-brine resulted in a decreased potential for dissolution as the heat exchange fluid entered the formation and within the formation itself, as well as decreased precipitation within the production well, compared to the NaCl-brine. Considering a NaCl+MgCl₂-brine, which was similar to the MgCl₂-brine, the desired reduction in precipitation and dissolution were improved. The NaCl-brine solubility was altered by changes in pressure up to 0.18 mol L⁻¹. This indicates that designing and monitoring the composition of heat exchange fluids in highly saline environments is an important component in geothermal project design.

5.2. Introduction

Deep geothermal systems can be used to produce electricity and have the potential to become a renewable baseload power source (Jain et al., 2015). Geothermal systems require adequate temperature, natural or engineered permeability, and a heat exchange fluid. Enhanced geothermal systems (EGS) are geothermal systems where hot rock is available, but the permeability or fluid saturation are created. Investigations into EGS for electricity production are underway in Canada and abroad, e.g. (Ferguson and Grasby, 2014; Grasby et al., 2012; Hadgu et al., 2016; Ledéseret and Hébert, 2012; Limberger et al., 2018; Majorowicz and Moore, 2014). The Western Canadian Sedimentary Basin and Williston Basin in the Canadian Prairies have the potential for sedimentary geothermal energy production (Jacek and Stephen, 2010; Majorowicz and Moore, 2014; Manz, 2011; Walsh, 2013). However, due to the high cost of drilling, development has been limited.

One method for reducing drilling depth, and therefore cost, is to target thermal anomalies. In low-temperature formations ($<200^{\circ}\text{C}$), conduction is the main process of heat transport (Scheck-Wenderoth et al., 2014). Due to high thermal conductivity, the tops of salt formations are associated with warm thermal anomalies, with higher temperatures than other rocks at similar depths (Petersen and Lerche, 1995). Daniilidis and Herber (2017) modeled a 40% increase in energy extraction and 25°C temperature increase associated with a salt formation. Therefore, halite formations may be desirable as a geothermal target. However, saturated brine in the formation creates a challenge for geothermal operation (Moore and Holländer, 2017).

The heat and flow requirements for deep geothermal systems have been extensively studied, e.g. Bujakowski et al. (2015), Plummer et al. (2016), and Xia et al. (2017). However, the geochemistry and geochemical reactions of heat exchange fluids, which can contain high mineral

concentrations, remains a challenge (Frick et al., 2011; Gunnlaugsson et al., 2014). Formation waters are often the heat exchange fluid of choice in deep geothermal systems (Gunnlaugsson et al., 2014). However, halite holds little water and forms saturated saline brines in contact with freshwater. Therefore, clogging due to mineral precipitation would be a major issue (Gunnlaugsson et al., 2014). Hesshaus et al. (2013) observed clogging due to precipitation of salt minerals between 655 and 1350 m in a 4000 m geothermal well in a sandstone formation. Borgia et al. (2012) simulated a CO₂ heat exchange fluid and found halite precipitation within the granite formation, which reduced permeability. At Bad Blumau, Austria, mineral scaling, corrosion, and chemical reactions between injection water and formation could result in carbonate clogging within 5 days (Alt-Epping et al., 2013). When targeting a halite formation, complex precipitation and dissolution are expected.

Saturation, dissolution, and precipitation of minerals within geothermal systems may be controlled by the choice of heat exchange fluid. Salts from the evaporating sea, or evaporates, under ideal conditions deposit in layers based on their solubility (Appelo and Postma, 2005). The following sequence of deposition should be expected: limestone (CaCO₃), dolomite (CaCO₃ • MgCO₃), anhydrite (CaSO₄), halite (NaCl), sylvite (KCl), carnallite (KCl • MgCl₂ • 6H₂O) and bischofite (MgCl₂ • 6H₂O). Therefore, an MgCl₂ brine is most likely to stay in solution. When two brines share a common ion, they do not both dissolve into the same solution, and a saturated brine comprised of a highly soluble mineral will not dissolve mineral formations with lower solubility. Therefore, an MgCl₂ brine should not dissolve a halite formation. To reduce the precipitation and dissolution in a halite reservoir, a designed heat exchange fluid is proposed as a chemical inhibitor.

The changes in solubility that occur in geothermal systems, as heat exchange fluids experience changes in temperature and pressure, drive the precipitation and dissolution that occur

at depth and in the wells. Uncertainty in sedimentary enhanced geothermal systems targeting halite formations motivates research to understand the potential well clogging issues. The purpose of this research is to characterize and compare three heat exchange fluids, a saturated NaCl-brine, saturated MgCl₂-brine, and saturated NaCl+MgCl₂-brine in a binary geothermal system targeting a sedimentary halite formation. The objective is to evaluate the value in designing heat exchange fluids and recommend the composition of an engineered heat exchange fluid in a halite formation.

5.3. Materials and methods

The suitability of saturated NaCl and MgCl₂-brine heat exchange fluids in a deep geothermal halite formation were investigated using reactive transport modeling. The conceptual model was based on a 5 MW geothermal doublet in the Prairie Evaporite, a halite formation of Devonian age in the Williston Basin. Saturated NaCl and MgCl₂-brines and an MgCl₂-brine in equilibrium with the formation composition (NaCl+MgCl₂-brine) were evaluated as heat exchange fluids.

Similar methods employing reactive transport modeling have been applied in geothermal problems such as saline fluids in a granite system (Bächler and Kohl, 2005), precipitation in CO₂ heat exchange fluid systems (Alt-Epping et al., 2013; Borgia et al., 2012), precipitation at an acid-neutral fluid interface (Todaka et al., 2004) and to assess fluid pathways and geochemical reactions (Wanner et al., 2014). In this study, the suitability of heat exchange fluid compositions in highly saline environments were investigated using PHREEQC Version 3 (Parkhurst and Appelo, 2013) a computer program designed to calculate a wide variety of aqueous geochemical calculations, including saturation-index calculations, as well as FEFLOW (Diersch, 2014) and piCHEM (Wissmeier, 2015) a finite element method (FEM) for calculating flow and transport in porous and fractured media.

5.3.1. Reservoir and thermal fluids

The concepts for temperature, pressure, and geochemistry were based on the Prairie Evaporite. This formation is located within the Williston Basin, part of the larger Western Canadian Sedimentary Basin (WCSB). The formation is dominantly halite with anhydrite and potash inclusions. The formation is of Devonian age (Bezys and McCabe, 1996). The thickness of the Prairie Evaporite ranges from 25 to 300 m (Grobe, 2000). Across western Canada, the depth of overburden ranges from 200 m in northeastern Alberta, to 2300 m in central Alberta, 700 m in central Saskatchewan to 2700 m in southern Saskatchewan (Grobe, 2000), and approximately 1100 m at the Manitoba Saskatchewan border (TGI Williston Basin Working Group, 2008). High heat flow, up to 70 to 90 mW m⁻² is expected in this region, resulting in temperatures of 80 to 130°C at a depth of 3.5 km (Majorowicz and Grasby, 2010). The estimated average porosity of the WCSB is 11.8% (Grasby et al., 2012); however, the porosity of halite is much lower, approximately 2% (Winkler, 2011). The permeability of halite is very low; estimates range from 1x10⁻¹³ to 1x10⁻²⁰ m² (Beauheim et al., 1999).

Earl and Nahm (1981) assessed salt concentrations in the Williston Basin. They found that the solutions were saturated with NaCl, but often contain large amounts of CaCl and MgCl₂. At 2500 – 2700 m chloride levels of 200,000 mg L⁻¹ would ensure supersaturation at the bottom hole temperature (Earl and Nahm, 1981). The density of halite is 2323 g L⁻¹, and a saturated brine is expected to have a density of 1200 kg m⁻³ at atmospheric conditions. A measured composition of the Prairie Evaporite was provided by a salt solution mine located at Hargrave, Manitoba (Table 5-1).

Table 5-1. Composition of Prairie Evaporite minerals from a salt solution mine (Christie, 2015).

	Unit	Prairie Evaporite
Temperature	°C	30

Na ⁺	mol L ⁻¹	5.48
Cl ⁻	mol L ⁻¹	6.29
Mg ²⁺	mol L ⁻¹	3.25 x10 ⁻⁴
K ⁺	mol L ⁻¹	1.15 x10 ⁻²
Ca ²⁺	mol L ⁻¹	1.68 x10 ⁻²
Fe ³⁺	mol L ⁻¹	1.76 x10 ⁻⁶
SO ₄ ²⁻	mol L ⁻¹	2.39 x10 ⁻²
F ⁻	mol L ⁻¹	7.89 x10 ⁻⁶
NO ₃ ⁻	mol L ⁻¹	1.51 x10 ⁻⁴

5.3.2. Model conceptualization

The concept for the geothermal setup is a 5 MW binary doublet system, with one production well and one injection well (Figure 5-1). The permeability in the area surrounding the wells was assumed to be stimulated using hydraulic fracturing. Hydraulic fracturing is effective in sedimentary geothermal reservoirs and is commonly used in oil and gas in the WCSB (Legarth et al., 2005). A flow rate of 6000 m³ d⁻¹ was used, based on literature values for hydraulic head and temperature values (Firoozy, 2016; Jain et al., 2015; Luo et al., 2014; Xia et al., 2017). The geothermal system is a low temperature (<150°C), low enthalpy (<800 kJ kg⁻¹), liquid dominated system (Axelsson and Gunnlaugsson, 2000). The operational time for the well is 30 years.

Three heat exchange fluid compositions were evaluated for the geothermal system. First, a NaCl-brine saturated at 10°C, based on the composition of the Prairie Evaporite, second a pure MgCl₂-brine saturated at 10°C, and third, a NaCl+MgCl₂-brine based on the composition of the formation in equilibrium with minerals found in the Prairie Evaporite (Table 5-1). Initial fluid saturations were considered at 10°C, based on average ambient temperatures for storage. The injection temperature was 40°C. After traveling down the injection well, and upon entering the formation the temperature was 60°C. Temperature is initially a homogeneous 120°C throughout the halite formation. Within the production well the temperature is expected to cool to 100°C (Alt-

Epping et al., 2013). At the ground surface, a minimum temperature of 10°C is considered. Solubility was calculated and compared at these temperatures.

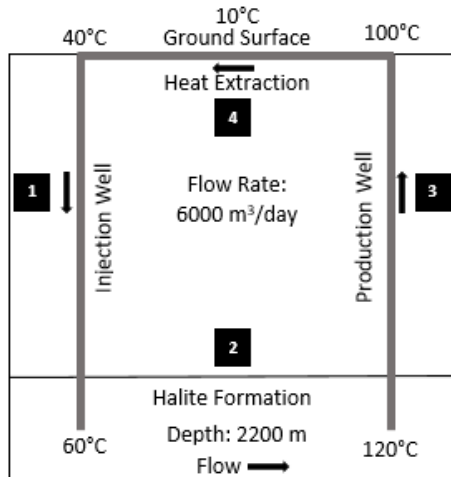


Figure 5-1. Conceptual model with injection well, halite reservoir, production well, and surface conditions. Shown are the temperature conditions and flow rates.

5.3.3. Temperature and pressure evaluations

The solubility of salts is dependent on pressure and temperature. The solubility of saturated halite and bischofite solutions were considered at the range of values expected in geothermal wells, 0.1 to 60 MPa and 5 to 130°C (Figure 5-2). For both minerals, the solubility is more sensitive to changes in temperature than pressure. Therefore, the temperature was considered the main driver in solubility changes for the simulations. Dissolved bischofite reaches a maximum solubility as $\text{H}_2\text{O}_{\text{gas}}$ becomes supersaturated.

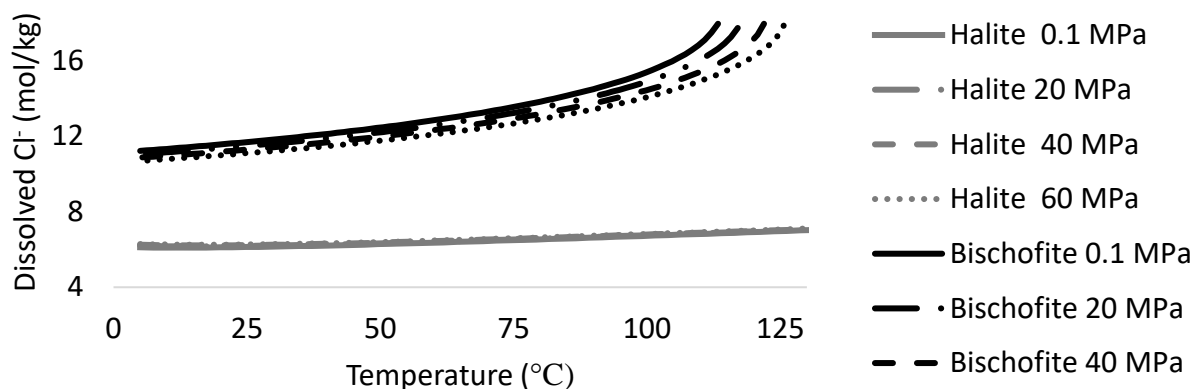


Figure 5-2. Dissolved Cl^- ions for halite and bischofite solutions in freshwater with changes in temperature and pressure from the Pitzer (1973) database from Moore and Holländer (2017).

5.4. Numerical approach

5.4.1. 1-D model

The geothermal system geometry was simplified to a 1-D flow path, similar to the approach adopted by Alt-Epping et al. (2013) (Figure 5-1). The 1-D reactive transport simulations were conducted using PHREEQC 3 (Parkhurst and Appelo, 2013). The geothermal geometry is strongly simplified; however, geochemical data were examined. The flow of the fluid is discussed in 4 intervals: (1) the reactions as the heat exchange fluid descends and temperature and pressure increase; (2) the reactions between the heat exchange fluid and formation; (3) the reactions within the heat exchange fluid as it ascends and temperature and pressure decrease; (4) the reactions that occur as a result of the extraction of heat at the surface.

The compositions of heat exchange fluids in contact with the Prairie Evaporite were evaluated for potential mineral precipitates. Saturated NaCl , MgCl_2 , and $\text{NaCl}+\text{MgCl}_2$ -brines were evaluated as heat exchange fluids (Table 5-2). The heat exchange fluids are initially saturated at 10°C , reflecting average surface temperatures. First, the saturation of key minerals was considered

as fluid warmed from 10°C to 60°C from the surface to the bottom of the injection well (interval 1); then 60°C to 120°C within the reservoir (interval 2). Next, the cooling phases were considered: first 120°C to 100°C within the extraction well (interval 3); then 100°C to 60°C and 10°C at the surface (interval 4). The concentrations of individual ions were calculated based on equilibrium with the saturated minerals. The fluid is assumed to be in equilibrium with halite (SI = 0.0) throughout the process. The precipitation and dissolution of halite were estimated based on the concentration of sodium in the fluid. The effect of changes in pressure as the fluid moves up the production well was further explored, with pressures from 0.1 to 303 MPa evaluated for each heat exchange fluid composition, and temperatures of 100 and 120°C considered.

Table 5-2. Initial compositions of the heat exchange fluids. SI indicates saturation index, where 0 indicates saturated, value >0 indicate supersaturation, and values <0 indicate undersaturation. ‘Yes’ and ‘no’ indicate whether trace ions were included in the initial heat exchange fluid composition.

Fluid	Na ⁺	Cl ⁻	Mg ²⁺	Trace Ions	pH	Temp	Halite	Bischofite
	mol L ⁻¹	mol L ⁻¹	mol L ⁻¹			°C	SI	SI
NaCl-brine	6.026	6.026	0	Yes	7.0	10	0	-
MgCl ₂ -brine	0	11.35	5.694	No	6.7	10	0	0
NaCl+MgCl ₂ -brine	7.53 x10 ⁻²	11.45	5.614	Yes	6.7	10	0	0

5.4.2. 3-D model design

The model design consists of a binary geothermal reservoir, with a 300 m thick simulation domain (z-direction). A region 1200 m (x-direction) by 1000 m (y-direction) by 300 m (z-direction) was considered, with a cross-section occurring at the wellbore (Figure 5-3). Considering the top of the formation at (0, 0, 0) m, the injection well was located at (300, 0, 75) m and production well was located at (900, 0, 225) m. The distance between the wells was 618 m. The

model domain was divided into 195,520 elements in 28 layers, with increased discretization near the injection well. The pressure was hydrodynamic, assuming a depth of 3000 m.

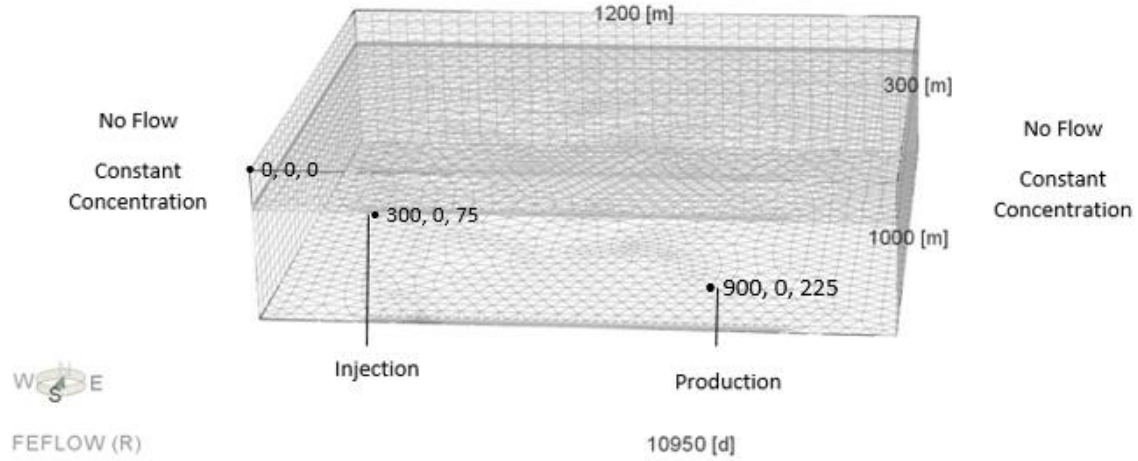


Figure 5-3. 3-D model domain and boundaries for a binary geothermal doublet.

The simulation domain was considered in a low permeability halite, enhanced by hydraulic fracturing. The model region was assumed to have been fractured, except for the outer 25 m of the model, which was assumed to be intact halite. Fractures were simulated as an equivalent porous matrix, which has been shown to be acceptable for geothermal simulations at the reservoir scale (Jarrahi et al., 2019). The equivalent hydraulic conductivity (K_{fr}) and porosity (ε_{fr}) were estimated from (Snow, 1968):

$$K_{fr} = \frac{\rho g N b^3}{6\mu} \quad 5-1$$

$$\varepsilon_{fr} = 3Nbg \quad 5-2$$

where ρ (kg m^{-3}) is the fluid density, g (m s^{-2}) is the acceleration due to gravity, and μ (kg m s^{-1}) is viscosity. A fracture density, N of 1 m^{-1} was assumed, with a range examined from 0.001 to 10 m^{-1} (Kalinina et al., 2014). The fracture aperture, b is assumed to be “partly open” with a value of 0.3 mm, examined at a range of 0.1 mm to 5 mm (Dehkordi et al., 2014). Assuming water density of 1200 kg m^{-3} , viscosity of $2 \times 10^{-4} \text{ kg m s}^{-1}$, and acceleration of gravity of 9.81 m s^{-2} , the density of 1 m^{-1} and aperture of 0.3 mm results in a K_{fr} of $2.65 \times 10^{-4} \text{ m s}^{-1}$ and ε_{fr} of 9×10^{-4} . The model was assumed to be anisotropic with hydraulic conductivity in the horizontal direction 10 times flow in the vertical direction.

The injection and production wells were simulated as Neumann condition well boundary types with a flow rate of $3000 \text{ m}^3 \text{ day}^{-1}$, which is half of the targeted flow rate, appropriate for a cross-section. A constant head boundary of 0 m was assigned to the top of the model, and the initial head was set at 0 m. Two heat exchange fluids were evaluated, NaCl and MgCl_2 -brines saturated at 10°C and 0.1 MPa. For geochemical boundaries, no flow boundaries are assumed to exist at the top, bottom, and sides of the model. The initial geochemical composition of the formation fluid was assumed to be in equilibrium with the known composition of the Prairie Evaporite, saturated at formation pressure and temperature (Table 5-1). Constant concentration boundaries, saturated with formation fluid were assigned along the left and right model boundaries. Heat exchange fluids were assumed to be saturated with NaCl at 10°C and MgCl_2 at 10°C respectively and were simulated as constant concentrations at the injection well (Table 5-2). An initial temperature of 120°C was used in the formation. The fluid was injected at 70°C . Mass transport parameters were set at: porosity 0.3, diffusion to $1 \times 10^{-9} \text{ m}^2 \text{ s}^{-1}$, longitudinal dispersivity 12 m, and transverse dispersivity 1.2 m. For heat transport, the volumetric heat capacity of fluid was $4.2 \text{ MJ m}^{-3} \text{ K}^{-1}$,

the volumetric heat capacity of solid was $2.52 \text{ MJ m}^{-3} \text{ K}^{-1}$, the thermal conductivity of fluid $0.65 \text{ J m}^{-1} \text{ s}^{-1} \text{ K}^{-1}$ and the thermal conductivity of soil $5 \text{ J m}^{-1} \text{ s}^{-1} \text{ K}^{-1}$ (Firoozy, 2016).

5.4.2.1. 3-D Model Sensitivity Analysis

An equivalent porous media approach was used to represent fractures within the 3-D model. This has been shown to work effectively; however, it is sensitive to the calibration of porosity and permeability (Jarrahi et al., 2019). Therefore, the sensitivity of the 3-D model to fracture aperture and density was analyzed.

Fractures in deep geothermal systems develop perpendicular to the least stress (Fisher and Warpinski, 2012). This creates anisotropy. Flow in the horizontal direction is initially assumed to be 10 times flow in the vertical direction. Sensitivity is investigated for flow in the vertical direction 10 times hydraulic conductivity in the horizontal direction.

Table 5-3. Values used for fracture densities from 1×10^{-3} to 10 m^{-1} and fracture apertures 1×10^{-4} to $5 \times 10^{-3} \text{ m}$ used to assess model sensitivity.

Simulation	N	b	ϵ_{fr}	K_{fr}
	m^{-1}	m	-	m s^{-1}
1	1	3×10^{-4}	9×10^{-4}	2.65×10^{-4}
2	10	5×10^{-3}	0.15	12.2
3	10	1×10^{-4}	3.0×10^{-3}	9.81×10^{-5}
4	1×10^{-3}	5×10^{-3}	1.5×10^{-6}	1.23×10^{-4}
5	1×10^{-3}	1×10^{-4}	3×10^{-7}	9.81×10^{-9}

5.4.3. Mathematical representation

PHREEQC Version 3 (Parkhurst and Appelo, 2013) calculations were made using the Pitzer (1973) database, which is designed for use with high ionic strengths and high temperatures (Plummer et al., 1988). Where minerals were unavailable in the Pitzer (1973) database, the PHEEQC 2 database was used. PHREEQC reads a database file of thermodynamic data, which

was used to calculate solubility and thermodynamic stability. Equilibrium values were used for the simulations, which have been observed at the reservoir scale (Fu et al., 2012).

FEFLOW (Diersch, 2014) uses a multidimensional FEM to solve the governing flow, mass and heat transport equations in porous and fractured media. The plug-in piCHEM (Wissmeier, 2015) which couples PHREEQC (Parkhurst and Appelo, 2013) with FEFLOW is used to solve reactive transport. Reactive transport reactions were calculated at equilibrium.

The flow of groundwater was calculated assuming a non-deforming media following (Garven, 1995) and limited deformation calculated by Jarrahi et al. (2019). The mass conservation equation of a saturated fluid is given as:

$$S_0 \frac{\partial h_0}{\partial t} + \nabla \cdot \vec{q} = Q \quad 5-3$$

where S_0 is specific storage (m^{-1}), h_0 (m) is the equivalent freshwater hydraulic head, and Q is sinks and sources (s^{-1}). Saturated Darcy flux \vec{q} ($m s^{-1}$) in FEFLOW is defined as:

$$\vec{q} = -\mathbf{K} \cdot (\nabla h_0 + \chi \vec{e}) \quad 5-4$$

where \mathbf{K} ($m s^{-1}$) is the hydraulic conductivity, and \vec{e} is the gravitational unit vector (1). The density ratio (χ) (-) in FEFLOW describes the ratio between maximum and minimum density and is defined as:

$$\chi = \frac{\rho_s - \rho_0}{\rho_0} \quad 5-5$$

where ρ_s ($kg m^{-3}$) is the saltwater density and ρ_0 ($kg m^{-3}$) is the freshwater density. For this work, a value of 0.2 was applied. The equivalent freshwater hydraulic head can be calculated as:

Heat transfer at equilibrium between the solid and fluid phase can be described as:

$$(\varepsilon\rho c + (1 - \varepsilon)\rho_m c_m) \frac{\partial T}{\partial t} + \rho c \vec{q} \cdot \nabla T - \nabla \cdot (\mathbf{A} \cdot \nabla T) = H_e - \rho c (T - T_0) Q \quad 5-6$$

where ε is porosity (-), ρ is the mass density of the fluid (kg m^{-3}), c is specific heat capacity ($\text{m}^2 \text{s}^{-2} \text{K}^{-1}$), ρ_s is the mass density of the solid (kg m^{-3}), c_s is the specific heat capacity of solid ($\text{m}^2 \text{s}^{-2} \text{K}^{-1}$), T is temperature (K), T_0 is reference temperature (K), t is time (s), \vec{q} is the Darcy flux (m s^{-1}), \mathbf{A} is the tensor of hydrodynamic thermodispersion ($\text{kg m s}^{-3} \text{K}^{-1}$) and Q is a sink/source term (s^{-1}).

Solute transport involves the complex, nonlinear interactions of ions, as well as the changes in density. The presence of undersaturated fluid within a matrix can cause dissolution, while supersaturated fluids result in precipitation. The coupling of geochemistry and flow using piCHEM assumes that aqueous phase flow can be represented by the transport of individual dissolved components. The governing equation used for solute transport is classic advection-diffusion/dispersion equation (Wissmeier, 2015):

$$\frac{\partial C_i}{\partial t} = -\nabla \cdot (\vec{q} C_i) + \nabla \cdot (\theta \mathbf{D} \nabla C_i) + S_C \quad 5-7$$

where C_i (kg m^{-3}) is the concentration of solution species i , t is time (s), θ ($\text{m}^3 \text{m}^{-3}$) is the relative liquid phase saturation, \mathbf{D} ($\text{m}^2 \text{s}^{-1}$) is the hydrodynamic dispersion tensor and S_C ($\text{kg m}^{-3} \text{s}^{-1}$) is a source-sink term. The liquid phase is composed of solution species according to (Wissmeier, 2015):

$$\theta = \frac{\sum_i n_i m_i}{\rho} \quad 5-8$$

where n_i (mol m³) is the volume of species i in a control volume with molar weight m_i (kg mol⁻¹).

The phase mass balance is then (Wissmeier, 2015):

$$\frac{\partial \rho \theta}{\partial t} = -\nabla \cdot \rho \theta \vec{v} \quad 5-9$$

where \vec{v} (m s⁻¹) is the fluid velocity.

5.5. Results

Reactive transport modeling was used to evaluate the interaction between a halite formation, and three heat exchange fluids in a deep geothermal system. Potential mineral precipitates were evaluated for a saturated NaCl-brine, MgCl₂-brine, and NaCl+MgCl₂-brine over temperature changes expected in the reservoir using the 1-D model (Table 5-4, Table 5-5, Table 5-6).

Next, a 3-D reactive transport model was used for reservoir simulations to investigate the suitability of these fluids as heat exchange fluids in geothermal systems over a 30 year period. The formation was assumed to be saturated with halite and contained other trace minerals. Heat exchange fluids were assumed to be saturated with NaCl at 10°C and MgCl₂ at 10°C respectively.

5.5.1. 1-D chemical simulations

5.5.1.1. Potential Precipitation

Within the injection well, the NaCl-brine becomes undersaturated with respect to halite due to an increase in temperature (Table 5-4). When reaching the halite formation, dissolution of 0.57 mol L⁻¹ occurs to bring the solution to saturation. The fluid then travels up the production well cooling from 120 to 100°C. This cooling results in precipitation of 0.20 mol L⁻¹ halite as well as anhydrite, brucite, carnallite, goergeyite, gypsum, halite, kieserite, and polyhalite.

Within the injection well, the MgCl_2 -brine becomes undersaturated with respect to halite (Table 5-5). After reaching the halite formation, dissolution of 0.23 mol L^{-1} occurs to bring the solution to saturation. The fluid then travels up the production well cooling from 120 to 100°C . This cooling results in precipitation of 0.091 mol L^{-1} halite as well as unmeasured amounts of anhydrite, brucite, carnallite, goergeyite, gypsum, halite, kieserite, and polyhalite.

Within the injection well, the $\text{NaCl}+\text{MgCl}_2$ -brine becomes undersaturated with respect to halite (Table 5-6). After reaching the halite formation, dissolution of 0.22 mol L^{-1} occurs to bring the solution to saturation. The fluid then travels up the production well cooling from 120 to 100°C . This cooling results in precipitation of 0.088 mol L^{-1} halite as well as unmeasured amounts of anhydrite and bischofite.

Pressure changes were evaluated for the changes in pressure at 100 and 120°C , simulating the production well (Table 5-7). As pressure increases, the solubility of NaCl generally increases. For the NaCl -brine, pressure change from 0.1 to 202 MPa increased the solubility of the solution by 0.18 mol L^{-1} . The MgCl_2 and $\text{NaCl}+\text{MgCl}_2$ -brines were less susceptible to pressure changes with a 0.011 mol L^{-1} change for a pressure change from 0.1 to 202 MPa (Table 5-7). PHREEQC does not evaluate negative pressure values.

Table 5-4. NaCl-brine heat exchange fluid composition and mineral saturation indices (SI) during heating and cooling processes as determined using PHREEQC and the PHREEQC2 database. Bold numbers indicate saturation or supersaturation.

Mineral	Formula	Unit	Heating (Injection)			Max 120°C	Cooling (Extraction)		
			10°C	40°C	60°C		100°C	60°C	10°C
Anhydrite	CaSO ₄	SI	-0.46	-0.14	0.03	0.33	0.26	0.02	-0.46
Bischofite	MgCl ₂ * 6H ₂ O	SI	-6.58	-6.38	-6.26	-6.00	-6.07	-6.26	-6.58
Brucite	Mg(OH) ₂	SI	-6.51	-6.48	-6.29	-5.84	-5.94	-6.29	-6.50
Carnallite	KMgCl ₃ :6H ₂ O	SI	-7.41	-7.63	-7.71	-7.80	-7.79	-7.71	-7.41
Glauberite	Na ₂ Ca(SO ₄) ₂	SI	-1.02	-0.71	-0.55	-0.27	-0.32	-0.55	-1.03
Goergeyite	K ₂ Ca ₅ (SO ₄) ₆ H ₂ O	SI	0.32	-1.54	-2.30	-3.47	-3.21	-2.31	0.32
Gypsum	CaSO ₄ :2H ₂ O	SI	-0.16	-0.22	-0.27	-0.51	-0.41	-0.27	-0.16
Halite	NaCl	SI	0.00	0.00	0.00	0.00	0.00	0.00	0.00
Kieserite	MgSO ₄ :H ₂ O	SI	-5.99	-5.64	-5.35	-4.42	-4.72	-5.35	-5.99
Polyhalite	K ₂ MgCa ₂ (SO ₄) ₄ * 2H ₂ O	SI	-8.82	-9.01	-9.43	-11.85	-10.88	-9.44	-8.82
Sylvite	KCl	SI	-1.98	-2.24	-2.37	-2.63	-2.56	-2.37	-1.98
pH			7.00	6.31	6.06	5.683	5.771	6.06	7.00
Ca	Ca ²⁺	mol L ⁻¹	2.59e-2	2.59e-2	2.59e-2	2.59e-2	2.59e-2	2.59e-2	2.59e-2
Cl	Cl ⁻	mol L ⁻¹	6.737	6.848	7.00	7.566	7.37	7.00	6.74
Fe	Fe ³⁺	mol L ⁻¹	2.76e-6	2.76e-6	2.76e-6	2.76e-6	2.76e-6	2.76e-6	2.76e-6
K	K ⁺	mol L ⁻¹	1.78e-2	1.78e-2	1.78e-2	1.78e-2	1.78e-2	1.78e-2	1.78e-2
Mg	Mg ²⁺	mol L ⁻¹	5.02e-4	5.02e-4	5.02e-4	5.02e-4	5.02e-4	5.02e-4	5.02e-4
Na	Na ⁺	mol L ⁻¹	5.467	5.578	5.731	6.296	6.10	5.73	5.47
S	SO ₄ ²⁻	mol L ⁻¹	3.69e-2	3.69e-2	3.69e-2	3.69e-2	2.856e-2	3.69e-2	3.69e-2
ΔHalite	Incremental	mol L ⁻¹	0	-0.11	-0.15	-0.57	0.20	0.37	0.26
ΔHalite	Total	mol L ⁻¹	0	-0.11	-0.26	-0.83	-0.63	-0.26	-0.0030

Table 5-5. MgCl₂–brine heat exchange fluid composition and mineral saturation indices (SI) during heating and cooling processes as determined using PHREEQC and the Pitzer (1973) database. Bold numbers indicate saturation or supersaturation.

Mineral	Formula	Unit	Heating (Injection)			Max 120°C	Cooling (Extraction)		
			10°C	40°C	60°C		100°C	60°C	10°C
Anhydrite	CaSO ₄	SI	-	0.88	0.55	-0.59	-0.19	0.55	1.31
Bischofite	MgCl ₂ * 6H ₂ O	SI	0.00	-0.25	-0.38	-0.79	-0.65	-0.38	-0.04
Brucite	Mg(OH) ₂	SI	0.00	-0.23	-0.50	-1.47	-1.13	-0.50	0.12
Carnallite	KMgCl ₃ :6H ₂ O	SI	-	-0.53	-0.95	-1.93	-1.64	-0.95	0.23
Glauberite	Na ₂ Ca(SO ₄) ₂	SI	-	-2.03	-2.46	-3.99	-3.44	-2.46	-1.44
Goergeyite	K ₂ Ca ₅ (SO ₄) ₆ H ₂ O	SI	-	2.85	-0.64	-9.78	-6.88	-0.64	8.80
Gypsum	CaSO ₄ :2H ₂ O	SI	-	0.17	-0.31	-1.86	-1.33	-0.31	0.89
Halite	NaCl	SI	-	0.00	0.00	0.00	0.00	0.00	0.00
Kieserite	MgSO ₄ :H ₂ O	SI	-	-0.28	-0.49	-0.94	-0.80	-0.49	0.17
Polyhalite	K ₂ MgCa ₂ (SO ₄) ₄ * 2H ₂ O	SI	-	-2.33	-4.49	-11.90	-9.29	-4.49	0.51
Sylvite	KCl	SI	-	-1.27	-1.48	-1.97	-1.82	-1.48	-0.89
pH			6.73	6.09	5.72	4.972	5.176	5.72	6.82
Ca	Ca ²⁺	mol L ⁻¹	0	2.59e-2	2.59e-2	2.59e-2	2.59e-2	2.59e-2	2.59e-2
Cl	Cl ⁻	mol L ⁻¹	11.3	11.3	11.3	11.6	11.5	11.3	11.3
Fe	Fe ³⁺	mol L ⁻¹	0	2.76e-6	2.76e-6	2.76e-6	2.76e-6	2.76e-6	2.76e-6
K	K ⁺	mol L ⁻¹	0	1.78e-2	1.78e-2	1.78e-2	1.78e-2	1.78e-2	1.78e-2
Mg	Mg ²⁺	mol L ⁻¹	5.68	5.59	5.69	5.59	5.59	5.59	5.59
Na	Na ⁺	mol L ⁻¹	0	0.126	0.173	0.399	0.309	0.173	7.91e-2
S	SO ₄ ²⁻	mol L ⁻¹	0	3.69e-2	3.69e-2	3.69e-2	3.69e-2	3.69e-2	3.69e-2
ΔHalite	Incremental	mol L ⁻¹	0	-0.13	-0.047	-0.23	0.091	0.14	0.094
ΔHalite	Total	mol L ⁻¹	0	-0.13	-0.17	-0.40	-0.31	-0.17	-0.080

Table 5-6. NaCl+MgCl₂-brine heat exchange fluid composition and mineral saturation indices (SI) during heating and cooling processes as determined using PHREEQC and the Pitzer (1973) database. Bold numbers indicate saturation or supersaturation.

Mineral	Formula	Unit	Heating (Injection)			Max 120°C	Cooling (Extraction)		
			10°C	40°C	60°C		100°C	60°C	10°C
Anhydrite	CaSO ₄	SI	0.00	-0.43	-0.77	-1.91	-1.50	-0.76	0.01
Bischofite	MgCl ₂ * 6H ₂ O	SI	0.00	-0.21	-0.35	-0.76	-0.62	-0.34	0.01
Brucite	Mg(OH) ₂	SI	-0.07	-0.41	-0.68	-1.64	-1.30	-0.69	-0.08
Carnallite	KMgCl ₃ :6H ₂ O	SI	-0.69	-1.44	-1.86	-2.85	-2.56	-1.86	-0.68
Glauberite	Na ₂ Ca(SO ₄) ₂	SI	-3.49	-4.09	-4.53	-6.06	-5.51	-4.52	-3.49
Goergeyite	K ₂ Ca ₅ (SO ₄) ₆ H ₂ O	SI	-0.41	-6.38	-9.88	-19.03	-16.13	-9.86	-0.37
Gypsum	CaSO ₄ :2H ₂ O	SI	-0.44	-1.16	-1.65	-3.20	-2.66	-1.64	-0.43
Halite	NaCl	SI	0.00	0.00	0.00	0.00	0.00	0.00	0.00
Kieserite	MgSO ₄ :H ₂ O	SI	-0.49	-0.94	-1.16	-1.62	-1.48	-1.15	-0.48
Polyhalite	K ₂ MgCa ₂ (SO ₄) ₄ * 2H ₂ O	SI	-5.42	-8.28	-10.45	-17.88	-15.26	-10.43	-3.53
Sylvite	KCl	SI	-1.84	-2.23	-2.43	-2.92	-2.77	-2.43	-1.43
pH			6.7	5.98	5.61	4.86	5.06	5.60	6.69
Ca	Ca ²⁺	mol L ⁻¹	5.76e-3	5.76e-3	5.76e-3	5.76e-3	5.76e-3	5.76e-3	5.76e-3
Cl	Cl ⁻	mol L ⁻¹	11.5	11.5	11.5	11.8	11.7	11.6	11.5
Fe	Fe ³⁺	mol L ⁻¹	3.00e-7	3.00e-7	3.00e-7	3.00e-7	3.00e-7	3.00e-7	3.00e-7
K	K ⁺	mol L ⁻¹	1.93e-3	1.93e-3	1.93e-3	1.93e-3	1.93e-3	1.93e-3	1.93e-3
Mg	Mg ²⁺	mol L ⁻¹	5.61	5.61	5.61	5.61	5.61	5.61	5.61
Na	Na ⁺	mol L ⁻¹	7.53e-2	1.20e-1	1.65e-1	3.82e-1	2.94e-1	1.64e-1	7.48e-2
S	SO ₄ ²⁻	mol L ⁻¹	6.95e-3	6.95e-3	6.95e-3	6.95e-3	6.95e-3	6.95e-3	6.95e-3
ΔHalite	Incremental	mol L ⁻¹	0	-0.045	-0.045	-0.22	0.088	0.13	0.089
ΔHalite	Total	mol L ⁻¹	0	-0.045	-0.090	-0.31	-0.21	-0.089	0.00045

Table 5-7. Concentration of Na⁺, Cl⁻ and Mg²⁺ in each heat exchange fluid with pressure changes from 0.1 to 202 MPa, simulated using the Pitzer (1973) database.

		Temp °C	0.1 MPa	20 MPa	40 MPa	60 MPa	101 MPa	202 MPa
NaCl-brine	Cl ⁻	100	7.38	7.40	7.43	7.46	7.51	7.55
	Na ⁺	100	6.10	6.13	6.16	6.19	6.24	6.28
	Cl ⁻	120	7.57	7.60	7.63	7.65	7.71	7.71
	Na ⁺	120	6.30	6.33	6.36	6.38	6.44	6.44
MgCl ₂ -brine	Na ⁺	100	0.294	0.294	0.294	0.294	0.294	0.294
	Cl ⁻	100	11.7	11.7	11.7	11.7	11.7	11.7
	Mg ²⁺	100	5.61	5.61	5.61	5.61	5.61	5.61
	Na ⁺	120	0.399	0.397	0.397	0.3981	0.404	0.402
	Cl ⁻	120	11.6	11.6	11.6	11.6	11.6	11.6
	Mg ²⁺	120	5.59	5.59	5.59	5.59	5.59	5.59
NaCl+MgCl ₂ -brine	Na ⁺	100	0.307	0.307	0.308	0.310	0.314	0.319
	Cl ⁻	100	11.5	11.5	11.5	11.5	11.5	11.5
	Mg ²⁺	100	5.59	5.59	5.59	5.59	5.59	5.59
	Na ⁺	120	0.380	0.379	0.378	0.380	0.385	0.384
	Cl ⁻	120	11.8	11.8	11.8	11.8	11.8	11.8
	Mg ²⁺	120	5.61	5.61	5.61	5.61	5.61	5.61

5.5.2. 3-D reservoir simulations

A 3-D reactive transport model was used to simulate heat transfer and mass transport in a geothermal doublet system over 30 years. The 3-D reservoir simulation focuses on chemical processes and temperature change within the reservoir (interval 2). A reservoir temperature of 120°C and a reinjection temperature of 70°C were used (Alt-Epping et al., 2013). Hydraulic head at the production well increases to 34 m head, while head at the production well drops to -16 m, relative to the surface (Figure 5-4). The pressure at the injection well was 27551 kPa and at the production well 28524 kPa. The temperature at the production well is constant at 120°C until it begins to decrease at 7300 days with a decrease by 10950 days of 2.5°C to 117.5°C.

Two heat exchange fluids were evaluated, NaCl and MgCl₂-brines saturated at 10°C. For both heat exchange fluid compositions, the following stages occurred: initially, the formation was saturated with halite at 120°C and relative pressure of 0 kPa; next, as pumping began, pressure increased near the production well, the temperature decreased and changes in geochemical composition began; finally, the cool thermal plume and region of geochemical change continued to grow and move toward the production well (Figure 5-5). The simulations for both the NaCl-brine and MgCl₂-brine heat exchange fluids indicate the rapid movement of fluid through the formation.

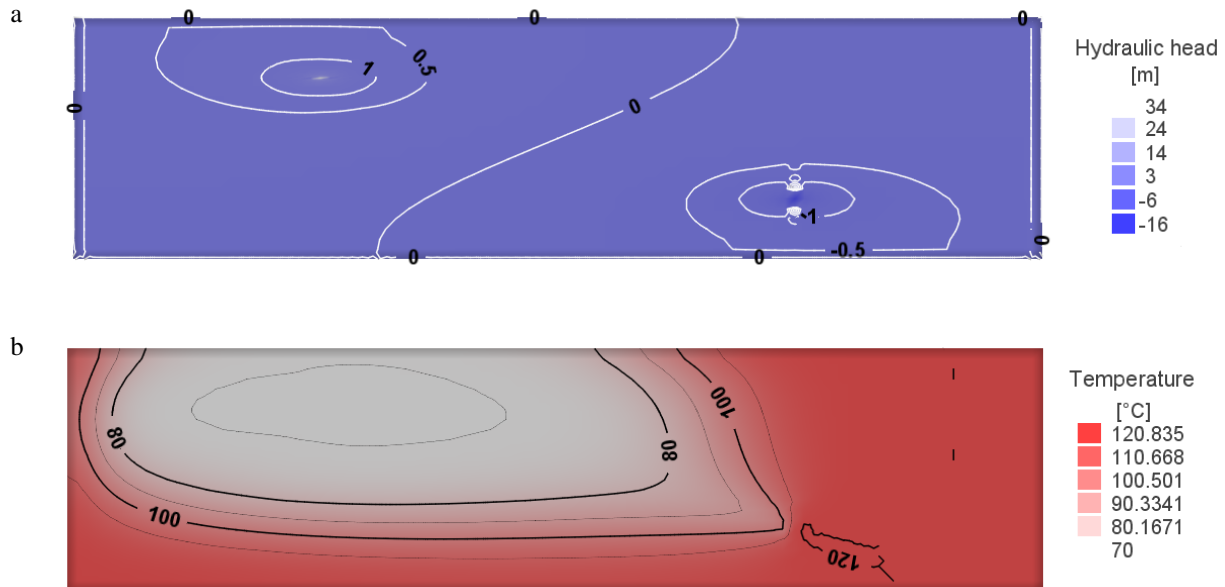


Figure 5-4. A cross-section at the wells of a) hydraulic head and b) temperature in a geothermal doublet system with a pumping rate of 3000 m³ d⁻¹ in the cross-section after 10950 days (30 years). The fracture density is 1 m⁻¹ and fracture aperture is 0.3 mm.

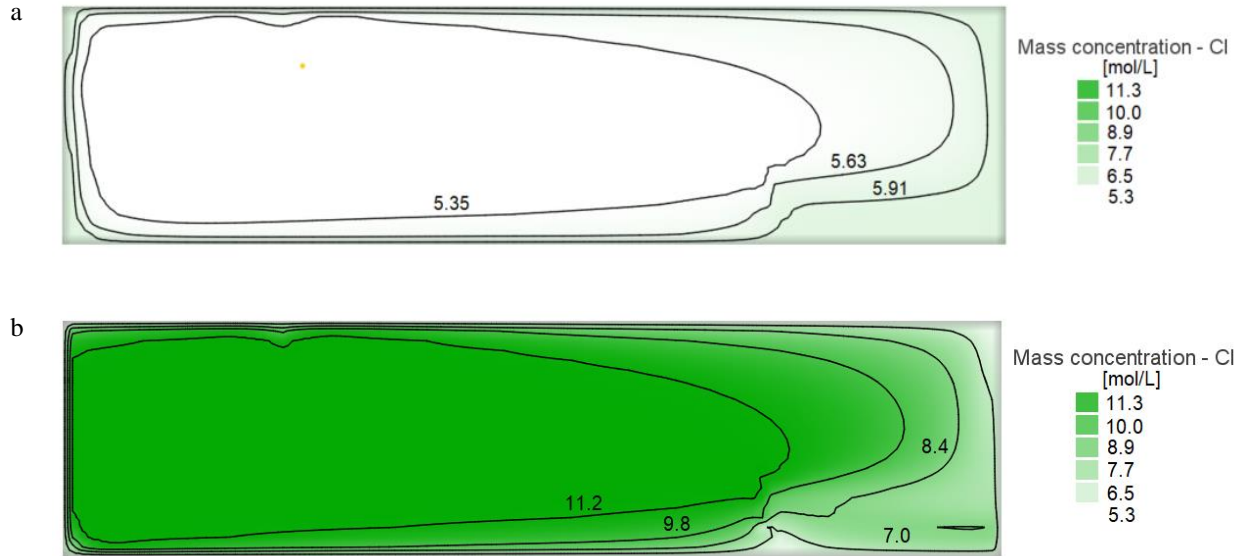


Figure 5-5. Geothermal doublet aqueous ion concentration after 365 days for a NaCl brine heat exchange fluid, saturated at 10°C (a), and an MgCl_2 brine heat exchange fluid, saturated at 10°C (b) injected into a halite formation at 70°C.

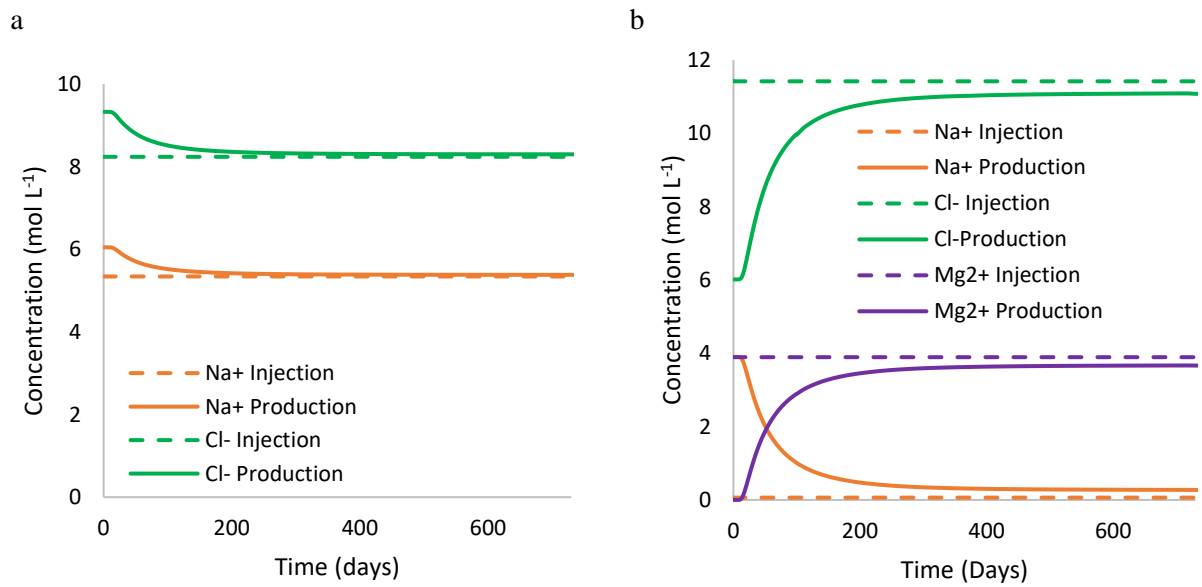


Figure 5-6. Comparison of Cl^- , Mg^{2+} , and Na^+ concentration at the production well over 730 days (2 years) in a geothermal doublet system initially saturated with NaCl, injected with (a) NaCl-brine and (b) MgCl_2 -brine heat exchange fluids.

The concentrations of Cl^- , Na^+ , and Mg^{2+} at the injection and production wells were evaluated (Figure 5-6). The concentration of Cl^- at the production well begins to decrease, reaching equilibrium at approximately half a year for the NaCl-brine model. This indicates the displacement of the formation water with the injected brine in the flow path. For the MgCl_2 -brine, Mg^{2+} emerges at the production well, replacing Na^+ and reaching equilibrium after approximately 1 year.

5.5.3. Sensitivities

Sensitivities were examined to understand the impact of uncertainties at depth. The pressure, temperature, and geochemical breakthrough indicated sensitivities to fracture aperture and frequency. The difference in head between the injection well and production well was greatest for scenario 5 (Table 5-3) with tight fractures and infrequent spacing, with a value of 1.35×10^7 kPa. The lowest pressure occurred in scenario 3 with small apertures and frequent spacing, at 115 kPa. The temperature at the production well began to decrease around 20 years for all simulations except simulation 5, with small, infrequent fractures (Figure 5-7). The Character IDs 1, 3, and 4 resulted in similar curves, with an approximate decrease in temperature after 30 years of 2.3°C . Simulation 2 resulted in similar curves with a temperature decrease after 30 years of 1.2°C . Simulation 5 resulted in very little decrease in produced temperature, 0.1°C after 30 years. The breakthrough of Mg^{2+} at the production well was similar for simulations 1, 3, and 4. Breakthroughs for simulations 2 and 5, with high fracture aperture and frequent spacing and lower fracture aperture and infrequent spacing resulting in produced fluids at the production well that were not saturated with Mg^{2+} .

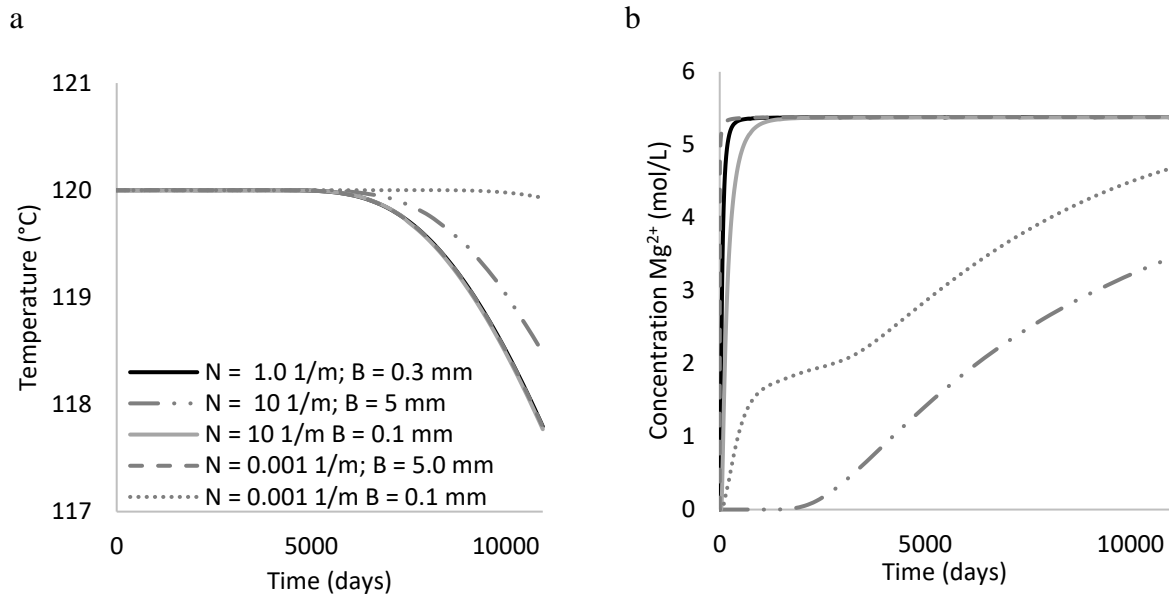


Figure 5-7. Comparison of sensitivity to fracture frequency (N) and aperture (B) for a) observed temperature at the production well and b) Mg^{2+} at the production well in a geothermal doublet system.

Sensitivity to the direction of anisotropy indicated that breakthrough time for temperature decrease is similar for both horizontal flow equal to 10 times vertical flow and the inverse (Figure 5-8). However, when the flow is increased in the vertical direction ($K_z = K_y = 0.1 K_x$) temperature at the production well decreases by an additional 3.5°C at 30 years. For the breakthrough of mass, the timing was similar for both directions of anisotropy. However, for Mg^{2+} , the concentration of produced magnesium was reduced by 0.3 mol/L when the flow is increased in the vertical direction.

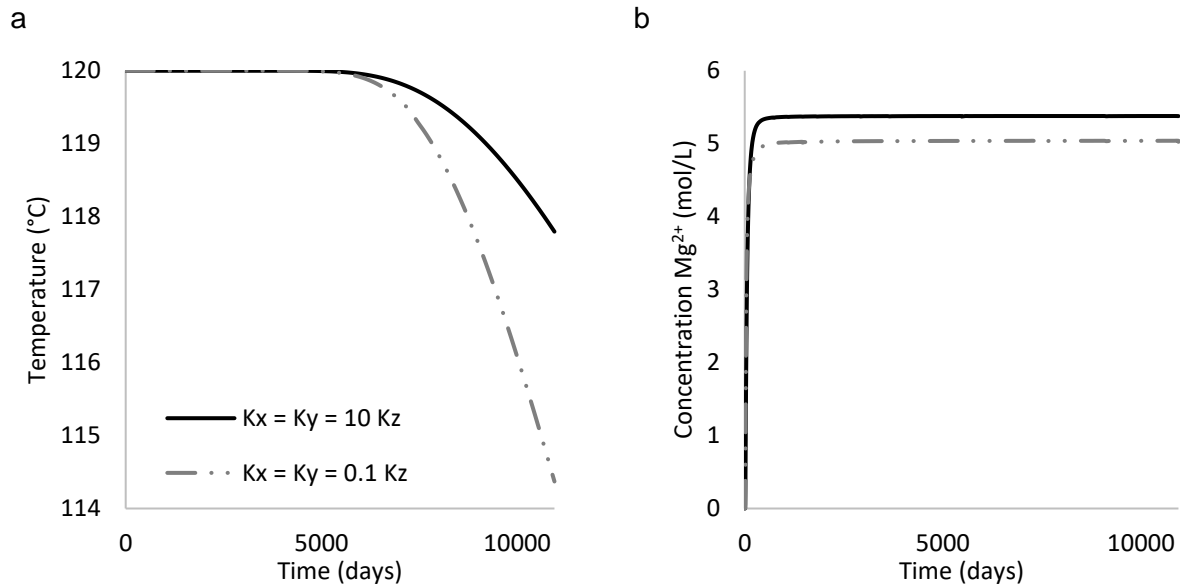


Figure 5-8. Comparison of sensitivity to anisotropy for a) observed temperature at the production well and b) Mg^{2+} at the production well in a geothermal doublet system.

5.6. Discussion

5.6.1. Chemical processes within the flow system

5.6.1.1. Chemical processes within the injection well (interval 1)

Within the injection well, the temperature change from 40°C to 60°C increased the solubility of halite, creating the potential for dissolution at the formation. The results indicate that this change in temperature from 40 to 60°C results in potential halite dissolution of 0.15 mol L⁻¹ for the NaCl-brine, 0.047 mol L⁻¹ for the MgCl₂-brine and 0.045 for the NaCl+MgCl₂-brine. The initial saturated composition of the heat exchange fluids was at 10°C. A change in temperature from 10 to 60°C results in potential halite dissolution of 0.26 mol L⁻¹ for the NaCl-brine, 0.17 mol L⁻¹ for the MgCl₂-brine, and 0.090 for the NaCl+MgCl₂-brine. This indicates that the smallest halite dissolution potential is created when using the NaCl+MgCl₂-brine.

The high ionic composition and changes in temperature also create the potential for additional mineral precipitation. Minimal precipitation is expected within the injection well, as temperature and pressure are increasing, which both generally increase the solubility of halite. The MgCl_2 -brine results indicate the potential for brucite and anhydrite mineral precipitation within the injection well. The brucite precipitation can generally be controlled by adjusting the pH.

5.6.1.2. Chemical processes within the reservoir (interval 2)

The processes within the reservoir were simulated in both the 1-D model as well as the 3-D model. Within the reservoir, the greatest amount of fluid heating occurred, as temperature increased from 60°C to 120°C. The pressure within the reservoir was highest at the injection well and lowest at the production well. Temperature is the primary driver of the fluid solubility, with the fluid entering the formation undersaturated for all brine compositions. High pressure increases halite solubility, and low pressure decreases halite solubility, especially for the NaCl-brine therefore, the temperature change is slightly buffered by the pressure change.

Considering temperature in the 1-D simulation, the estimated halite dissolution is greatest using the NaCl-brine, 0.83 mol L⁻¹, then MgCl_2 -brine, 0.40 mol L⁻¹ with the smallest dissolution coming from the NaCl+ MgCl_2 -brine, 0.31 mol L⁻¹. During the simulation of the saturated MgCl_2 -brine in the halite formation, the region near the injection well was saturated with Cl^- and Mg^{2+} , while Na^+ decreased to accommodate the Mg^{2+} (Figure 5-6). The MgCl_2 and NaCl+ MgCl_2 -brines resulted in increased preservation of the halite formation.

In the 3-D, 30-year simulation, the concentration and temperature gradients for the inflowing temperature and heat exchange fluid were generally sharp (Figure 5-4, Figure 5-5). The 3-D model indicates that the injected fluid moved quickly through the formation, with the produced

fluid constant after approximately 365 days. However, depending on the permeability and porosity of the formation, and the fracture or matrix properties, this may occur earlier (Figure 5-7).

At the injection well, the increased pressure will result in increased solubility for the 70°C solution. At the production well, the decreased pressure will result in decreased NaCl solubility for the 120°C solution. As a result, the solution may enter the production well with lower concentrations than predicted in the chemical analysis.

Dissolution is most likely to occur at the front of the temperature plume, and progress over time with the front. The progression of fluid through halite as a front versus channelized flow depends on the flow rate (Weisbrod et al., 2012). In this model, we expect a channelized flow. However, Borgia et al. (2012) observed an advancing front of NaCl that moved from the injection well to the production well similar to what we expect based on the temperature profile. Weisbrod et al. (2012) found that flow rates control whether brines move as a propagating front or through channels, and at low flow rates, salt precipitation resulting in clogging was more likely to occur. Dissolution is expected to occur at the temperature front, whereas precipitation is expected to occur near the production well and when the fluid begins to cool, as it moves up through the geothermal well (Bächler and Kohl, 2005; Borgia et al., 2012). Woroniuk et al. (2018) found in formations overlying the Prairie Evaporite, the presence of salts did not significantly affect permeability. Important in future considerations of heat exchange fluids in highly saline environments will be the change in porosity and permeability.

5.6.1.3. Chemical processes within the production well (interval 3)

As the fluid moves up the production well, it begins at maximum temperature, 120°C, and cools to an estimated 100°C. This cooling process results in precipitation of halite. The results indicate that this change in temperature results in a 0.20 mol L⁻¹ for the NaCl-brine, 0.091 mol L⁻¹

¹ for the MgCl_2 -brine, and 0.088 mol L^{-1} for the $\text{NaCl}+\text{MgCl}_2$ -brine. This indicates that the $\text{NaCl}+\text{MgCl}_2$ -brine will result in the least amount of precipitation in the production well. Pressure changes from 0.1 to 202 MPa can be used to increase or decrease the solubility of halite and NaCl solutions by 0.18 mol L^{-1} , however smaller changes in solubility are observed in the MgCl_2 and $\text{NaCl}+\text{MgCl}_2$ -brines 0.008 mol L^{-1} (Table 5-7).

Decreasing pressure near the production well in the reservoir results in decreased solubility for high-temperature solutions. Increasing pressure in the production well at the surface results in increased solubility when temperatures are cooling. The NaCl -brine precipitation was easier to control with pressure.

5.6.1.4. Chemical processes within the surface production (interval 4)

At the surface, a change in temperature from 100°C to 60°C is expected. The results indicate that this change in temperature results in a 0.37 mol L^{-1} for the NaCl -brine, 0.14 mol L^{-1} for the MgCl_2 -brine, and 0.013 for the $\text{NaCl}+\text{MgCl}_2$ -brine. This indicates that the $\text{NaCl}+\text{MgCl}_2$ -brine will result in the least amount of precipitation at the surface. Halite precipitation at the surface could be collected as a mining process; however additional study is required to determine the effect this would have on the permeability and flow within the formation.

The consideration of the brine cooling to 10°C was also evaluated. The change from 120°C to 10°C results in a 0.83 mol L^{-1} for the NaCl -brine, 0.33 mol L^{-1} for the MgCl_2 -brine, and 0.31 for the $\text{NaCl}+\text{MgCl}_2$ -brine. The MgCl_2 -brine precipitates anhydrite, brucite, carnallite, goergeyite, gypsum, kieserite, and polyhalite. The $\text{NaCl}+\text{MgCl}_2$ -brine is saturated with anhydrite and bischofite, however, the SI is low (0.01).

5.6.2. Implications of a modified heat exchange fluid

Chemical inhibitors are used to reduce scaling in geothermal and oil and gas wells, e.g. Alt-Epping et al. (2013). The concept of designing a heat exchange fluid is similar to the use of inhibitors. Trace metals and aqueous trace ions, I^- , Br^- and Fe^- are considered to inhibit halite dissolution (Alkattan et al., 1997a; Alkattan et al., 1997b). In oil and gas, halite is considered difficult to control and is treated with freshwater flushes (Chen et al., 2009). Wellbore cleanout and mechanical tools have also been used in halite clogged wells; however, the effects were short-lived (Soomro et al., 2015). However, controlling optimum pressure at depth for the given fluid chemistry was found to decrease salt precipitation in the well (Soomro et al., 2015). A combination of a designed heat exchange fluid with pressure control may be an effective method for reducing precipitation or controlling the composition of precipitates.

At a rate of $8000 \text{ m}^3 \text{ d}^{-1}$, and a concentration of $5.61 \text{ mol L}^{-1} \text{ Mg}$, the process would require 4280 t d^{-1} of MgCl_2 . Much of this could be recycled after the first year. The NaCl -brine results in 93 t d^{-1} NaCl produced, the MgCl_2 -brine 42 t d^{-1} NaCl and the $\text{NaCl}+\text{MgCl}_2$ -brine 41 t d^{-1} NaCl . In comparison, American Rock Salt Co., which operates the largest salt mine in the United States produces approximately 9000 to 16000 t d^{-1} (American Rock Salt, 2019). Continuous mining of the formation would result in a large cavity, producing the potential for increased flow through the formation or collapse and potential sinkhole formation, e.g. Johnson (1989).

5.6.3. Limitations and future work

This model works under the assumption that the porosity and permeability will remain relatively consistent with time. The matrix was assumed to be nondeforming with constant porosity and permeability throughout the simulations. However, within the Williston Basin Devonian salts, brittle behaviour and plastic salt creep have been observed (Scott Duncan and Lajtai, 1993).

Deformation can therefore result in both the closing and opening of fractures simultaneously. Open and closing of fractures is also controlled by dissolution and precipitation (Blaisonneau et al., 2016). Creep in a geothermal system, unlike creep in an open cavity, can be prevented by maintaining fluid pressure to balance stresses and strains (Warren, 2006). However, this may be difficult during shut down in production. The physical opening and closing of porosity and permeability due to deformation, salt creep, and dissolution and precipitation warrants further study.

The 1-D analysis was limited by the simplified geometry. However, it provides excellent insight into the complex chemical reactions that occur as the heat exchange fluid changes temperature. A constant temperature distribution is assumed throughout the system. The location of the temperature changes within the reservoir is further investigated in the 3-D analysis. The results would benefit from calibration field data; however, such data do not exist.

The 3-D simulations were limited by the assumption that the fractures expected in the system can be simulated using a matrix. A matrix has been shown to accurately simulate a fractured reservoir when calibrated (Blessent et al., 2014; Jarrahi et al., 2019). However, without calibration data, the simulation is more uncertain. Some numerical instability was observed in the simulations. Negative concentration values occur in finite elements solutions near sharp concentration fronts due to oscillatory behavior (Wissmeier, 2015). Negative concentrations are set to zero during reaction calculations, then added to the output concentrations from the reaction step (Wissmeier, 2015). In this way, mass balance errors are remedied.

5.7. Conclusions

Halite has a high heat flow and create thermal anomalies. However, systems targeting these formations will have complex geochemical systems. Therefore, numerical simulations were used to compare heat exchange fluids in a highly saline binary geothermal system. The numerical simulations were beneficial in understanding the complex precipitation and dissolution that occur within geothermal systems and changes to pressure and temperature. Heat exchange fluid compositions were designed as a chemical inhibitor for halite dissolution. A NaCl-brine, MgCl₂-brine, and NaCl+MgCl₂-brine, each saturated at 10°C, were evaluated in the Prairie Evaporite, a formation dominated by halite. The 3-D simulation used a 618 m well spacing, 6000 m³ d⁻¹ flow rate, and an equivalent porous media to represent the fractured area. Temperatures ranged from 10 to 120°C.

The 1-D simulations indicated the MgCl₂-brine heat exchange fluid reduced dissolution within the halite formation compared to the NaCl-brine. The NaCl+MgCl₂-brine resulted in the smallest amount of dissolution in the formation and precipitation in the production well, with 0.52 mol L⁻¹ less dissolution in the formation and 0.11 mol L⁻¹ less precipitation in the production well compared to the NaCl-brine. This indicates that MgCl₂ can be used as an inhibitor to precipitation and dissolution in a halite reservoir. When comparing solubility under pressure, the NaCl-brine was susceptible to changes in pressure, with up to a 0.22 mol L⁻¹ change in solubility at one temperature. The MgCl₂ and NaCl+MgCl₂-brines produced a 0.011 mol L⁻¹ change in solubility.

Based on 3-D simulations, the emergence of the MgCl₂-brine at the production well increased to steady-state by 365 days. The MgCl₂-brine works to reduce precipitation within the formation, while the precipitation of halite within the production well can be reduced with pressure controls. Mg²⁺ could potentially be recycled throughout the lifetime of the well.

Further study into wells in halite systems would benefit from field observations to provide calibration data for model data. Geochemical modeling is an important tool in the development of geothermal systems, providing an understanding of the processes that result in well clogging and potential inhibitors.

5.8. Acknowledgements

This work was supported by the Natural Sciences and Engineering Research Council of Canada Vanier Canada Graduate Scholarship program and the Manitoba Graduate Scholarship Program.

5.9. References

- Alkattan, M., Oelkers, E.H., Dandurand, J.-L., Schott, J., 1997a. Experimental studies of halite dissolution kinetics, 1 The effect of saturation state and the presence of trace metals. *Chem Geol*, 137(3–4): 201-219. DOI: 10.1016/S0009-2541(96)00164-7
- Alkattan, M., Oelkers, E.H., Dandurand, J.-L., Schott, J., 1997b. Experimental studies of halite dissolution kinetics: II. The effect of the presence of aqueous trace anions and $K_3Fe(CN)_6$. *Chem Geol*, 143(1–2): 17-26. DOI: 10.1016/S0009-2541(97)00097-1
- Alt-Epping, P., Waber, H.N., Diamond, L.W., Eichinger, L., 2013. Reactive transport modeling of the geothermal system at Bad Blumau, Austria: Implications of the combined extraction of heat and CO₂. *Geothermics*, 45: 18-30. DOI:10.1016/j.geothermics.2012.08.002
- American Rock Salt, 2019. American Rock Salt: About Us.
- Appelo, C.A.J., Postma, D., 2005. *Geochemistry, groundwater and pollution*. A.A. Balkema Publishers, Amsterdam, 649 pp.
- Axelsson, G., Gunnlaugsson, E., 2000. Long-term monitoring of high- and low-enthalpy fields under exploitation., *World Geothermal Congress 2000 Short Course*. International Geothermal Association, Kokonoe, Japan, pp. 226.
- Bächler, D., Kohl, T., 2005. Coupled thermal–hydraulic–chemical modelling of enhanced geothermal systems. *Geophysical Journal International*, 161(2): 533-548. DOI:10.1111/j.1365-246X.2005.02497.x
- Beauheim, R.L., Domski, P.S., Roberts, R.M., 1999. *Hydraulic Testing of Salado Formation Evaporites at the Waste Isolation Pilot Plant Site: Final Report*, Sandia National Labs., Albuquerque, NM (US); Sandia National Labs., Livermore, CA (US).
- Bezys, R.K., McCabe, H.R., 1996. *Lower to middle Paleozoic stratigraphy of southwestern Manitoba*, Geological Association of Canada, Winnipeg, Manitoba.

- Blaisonneau, A., Peter-Borie, M., Gentier, S., 2016. Evolution of fracture permeability with respect to fluid/rock interactions under thermohydromechanical conditions: development of experimental reactive percolation tests. *Geothermal Energy*, 4(1): 3. DOI:10.1186/s40517-016-0045-9
- Blessent, D., Jørgensen, P.R., Therrien, R., 2014. Comparing Discrete Fracture and Continuum Models to Predict Contaminant Transport in Fractured Porous Media. *Groundwater*, 52(1): 84-95. DOI:10.1111/gwat.12032
- Borgia, A., Pruess, K., Kneafsey, T.J., Oldenburg, C.M., Pan, L., 2012. Numerical simulation of salt precipitation in the fractures of a CO₂-enhanced geothermal system. *Geothermics*, 44: 13-22. DOI:10.1016/j.geothermics.2012.06.002
- Bujakowski, W. et al., 2015. Modelling geothermal and operating parameters of EGS installations in the lower triassic sedimentary formations of the central Poland area. *Renewable Energy*, 80(0): 441-453. DOI: 10.1016/j.renene.2015.02.018
- Chen, T., Clauser, C., Marquart, G., 2017. Efficiency and accuracy of equivalent fracture models for predicting fractured geothermal reservoirs: the influence of fracture network patterns. *Energy Procedia*, 125: 318-326. DOI:10.1016/j.egypro.2017.08.206
- Chen, T., Montgomerie, H., Chen, P., Vikane, O., Jackson, T., 2009. Understanding the Mechanisms of Halite Inhibition and Evaluation of Halite Scale Inhibitor by Static and Dynamic Tests, SPE International Symposium on Oilfield Chemistry. Society of Petroleum Engineers, The Woodlands. Texas, pp. 8. DOI:10.2118/121458-MS
- Christie, J., 2015. Prairie Evaporite Composition. In: Moore, K. (Ed.). ERCO Worldwide, Toronto, Ontario.
- Daniilidis, A., Herber, R., 2017. Salt intrusions providing a new geothermal exploration target for higher energy recovery at shallower depths. *Energy*, 118: 658-670. DOI:10.1016/j.energy.2016.10.094
- Dehkordi, S.E., Olofsson, B., Schincariol, R.A., 2015. Effect of groundwater flow in vertical and horizontal fractures on borehole heat exchanger temperatures. *Bulletin of Engineering Geology and the Environment*, 74(2): 479-491. DOI:10.1007/s10064-014-0626-4
- Dehkordi, S.E., Schincariol, R.A., Olofsson, B., 2014. Impact of Groundwater Flow and Energy Load on Multiple Borehole Heat Exchangers. *Groundwater*. DOI:10.1111/gwat.12256
- Diersch, H., 2014. FEFLOW Finite Element Modeling of Flow, Mass and Heat Transport in Porous and Fractured Media. Springer, New York.
- Earl, S.L., Nahm, J.J., 1981. Use Of Chemical Salt Precipitation Inhibitors To Maintain Supersaturated Salt Muds For Drilling Salt Formations. Society of Petroleum Engineers. DOI:10.2118/10097-MS
- Ferguson, G., Grasby, S., 2014. The geothermal potential of the basal clastics of Saskatchewan, Canada. *Hydrogeol J*, 22(1): 143-150. DOI:10.1007/s10040-013-1061-5
- Firoozy, N., 2016. Assessment of Geothermal Application for Electricity Production from the Prairie Evaporite Formation of Williston Basin in South-West Manitoba, University of Manitoba, Winnipeg, Manitoba, 165 pp.
- Frick, S. et al., 2011. Geochemical and Process Engineering Challenges for Geothermal Power Generation. *Chemie Ingenieur Technik*, 83(12): 2093-2104. DOI:10.1002/cite.201100131

- Fu, Y., van Berk, W., Schulz, H.-M., 2012. Hydrogeochemical modelling of fluid–rock interactions triggered by seawater injection into oil reservoirs: Case study Miller field (UK North Sea). *Appl Geochem*, 27(6): 1266-1277. DOI: 10.1016/j.apgeochem.2012.03.002
- Garven, G., 1995. Continental-Scale Groundwater Flow and Geologic Processes. *Annual Review of Earth and Planetary Sciences*, 23(1): 89-117.
- Grasby, S.E. et al., 2012. Geothermal Energy Resource Potential of Canada, Geological Survey of Canada. DOI:10.4095/291488
- Grobe, M., 2000. Distribution and thickness of salt within the Devonian Elk Point Group, Western Canada Sedimentary Basin, Alberta Energy and Utilities Board, Edmonton, Alberta.
- Gunnlaugsson, E., Ármannsson, H., Thorhallsson, S., Steingrímsson, B., 2014. Problems in geothermal operation-scaling and corrosion. In: UNU_GTP, LaGeo (Eds.), *Short Course VI on Utilization of Low- and Medium-Enthalpy Geothermal Resources and Financial Aspects of Utilization*, Santa Tecla, El Salvador.
- Hadgu, T., Kalinina, E., Lowry, T.S., 2016. Modeling of heat extraction from variably fractured porous media in Enhanced Geothermal Systems. *Geothermics*, 61: 75-85. DOI: 10.1016/j.geothermics.2016.01.009
- Hesshaus, A., Houben, G., Kringel, R., 2013. Halite clogging in a deep geothermal well – Geochemical and isotopic characterisation of salt origin. *Physics and Chemistry of the Earth, Parts A/B/C*, 64(0): 127-139. DOI:10.1016/j.pce.2013.06.002
- Jacek, M., Stephen, E.G., 2010. Heat flow, depth–temperature variations and stored thermal energy for enhanced geothermal systems in Canada. *Journal of Geophysics and Engineering*, 7(3): 232.
- Jain, C., Vogt, C., Clauser, C., 2015. Maximum Potential for Geothermal Power in Germany Based on Engineered Geothermal Systems. *Geothermal Energy*, 3(15): 1-20. DOI:10.1186/s40517-015-0033-5
- Jarrahi, M., Moore, K.R., and Holländer, H.M. 2019. Comparison of solute/heat transport in fractured formations using discrete fracture and equivalent porous media modeling at the reservoir scale. *Physics and Chemistry of the Earth, Parts A/B/C*. DOI: 10.1016/j.pce.2019.08.001.
- Johnson, K.S., 1989. Development of the Wink Sink in west Texas, U.S.A., due to salt dissolution and collapse. *Environmental Geology and Water Sciences*, 14(2): 81-92. DOI:10.1007/bf01728499
- Kalinina, E.A., Klise, K.A., McKenna, S.A., Hadgu, T., Lowry, T.S., 2014. Applications of fractured continuum model to enhanced geothermal system heat extraction problems. *Springerplus*, 3: 110-110. DOI:10.1186/2193-1801-3-110
- Ledésert, B.A., Hébert, R.L., 2012. The Soultz-sous-Forêts' Enhanced Geothermal System: A Granitic Basement Used as a Heat Exchanger to Produce Electricity. In: Mitrovic, J. (Ed.), *Heat Exchangers - Basic Design Applications*. INTECH Open Access Publisher, pp. 477 - 504.

- Legarth, B., Huenges, E., Zimmermann, G., 2005. Hydraulic fracturing in a sedimentary geothermal reservoir: Results and implications. *Int J Rock Mech Min*, 42(7–8): 1028–1041. DOI: 10.1016/j.ijrmms.2005.05.014
- Limberger, J. et al., 2018. Geothermal energy in deep aquifers: A global assessment of the resource base for direct heat utilization. *Renewable and Sustainable Energy Reviews*, 82: 961–975. DOI: 10.1016/j.rser.2017.09.084
- Luo, F., Xu, R.-N., Jiang, P.-X., 2014. Numerical investigation of fluid flow and heat transfer in a doublet enhanced geothermal system with CO₂ as the working fluid (CO₂–EGS). *Energy*, 64: 307–322. DOI: 10.1016/j.energy.2013.10.048
- Majorowicz, J., Grasby, S.E., 2010. Heat flow, depth–temperature variations and stored thermal energy for enhanced geothermal systems in Canada. *Journal of Geophysics and Engineering*, 7(3): 232.
- Majorowicz, J., Moore, M., 2014. The feasibility and potential of geothermal heat in the deep Alberta foreland basin-Canada for CO₂ savings. *Renewable Energy*, 66(0): 541–549. DOI: 10.1016/j.renene.2013.12.044
- Manz, L.A., 2011. Deep Geothermal Resources: Estimated Temperatures on Top of the Duperow Formation Kenmare 100K Sheet, North Dakota. In: Murphy, E.C., Helms, L.D. (Eds.), *North Dakota Geothermal Maps*. North Dakota Geological Survey, Bismark, ND.
- Moore, K.R., Holländer, H.M., 2017. Geochemical Modelling of the Dissolution of Salt Minerals and Application to Geothermal Energy, GeoOttawa 2017. Canadian Geotechnical Society, Ottawa, Canada.
- Parkhurst, D.L., Appelo, C., 2013. Description of input and examples for PHREEQC version 3-- A computer program for speciation, batch-reaction, one-dimensional transport, and inverse geochemical calculations. In: Survey, U.S.G. (Ed.), *U.S. Geological Survey Techniques and Methods Section A, Groundwater Book 6, Modeling Techniques*, Denver, Colorado, pp. 497.
- Petersen, K., Lerche, I., 1995. Quantification of thermal anomalies in sediments around salt structures. *Geothermics*, 24(2): 253–268. DOI:10.1016/0375-6505(94)00051-D
- Pitzer, K.S., 1973. Thermodynamics of electrolytes. I. Theoretical basis and general equations. *The Journal of Physical Chemistry*, 77(2): 268–277. DOI:10.1021/j100621a026
- Pitzer, K.S. et al., 1985. Thermodynamics of aqueous magnesium and calcium bicarbonates and mixtures with chloride. *Journal of Chemical & Engineering Data*, 30(1): 14–17. DOI:10.1021/je00039a005
- Plummer, L.N., Parkhurst, D.L., Fleming, G.W., Dunkle, S.A., 1988. A computer program incorporating pitzer's equations for calculation of geochemical reactions in brines. In: Interior, U.S.D.o.t., Survey, U.S.G. (Eds.). *Water-Resources Investigation Report 88-4153*, Reston, Virginia, pp. 310.
- Plummer, M.A. et al., 2016. Primary Constraints on the Design of an Enhanced Geothermal System Reservoir, 50th U.S. Rock Mechanics/Geomechanics Symposium. American Rock Mechanics Association, Houston, Texas, pp. 12.
- Saeid, S., Al-Khoury, R., Barends, F., 2013. An efficient computational model for deep low-enthalpy geothermal systems. *Comput Geosci-Uk*, 51: 400–409. DOI: 10.1016/j.cageo.2012.08.019

- Scheck-Wenderoth, M. et al., 2014. Models of heat transport in the Central European Basin System: Effective mechanisms at different scales. *Mar Petrol Geol*, 55: 315-331. DOI: j.marpetgeo.2014.03.009
- Scott Duncan, E.J., Lajtai, E.Z., 1993. The creep of potash salt rocks from Saskatchewan. *Geotechnical & Geological Engineering*, 11(3): 159-184. DOI:10.1007/bf00531249
- Snow, D.T., 1968. Rock fracture spacings, openings, and porosities. *Proceedings of the American Society of Civil Engineers*, 94: 73-91.
- Soomro, A.A., Hadi, A., Awase, A., Koondhar, N.H., Ahmed, N., 2015. Method To Optimally Produce Wells Having Salt Precipitation Issues, SPE/PAPG Pakistan section Annual Technical Conference. Society of Petroleum Engineers, Islamabad, Pakistan, pp. 7. DOI:10.2118/181133-MS
- TGI Williston Basin Working Group, 2008. Devonian Prairie Evaporite: structure contour. In: Manitoba Science, T., Energy and Mines, Manitoba Geological Services Branch (Eds.), *Stratigraphic Map SM2008-DPE-S*.
- Todaka, N., Akasaka, C., Xu, T., Pruess, K., 2004. Reactive geothermal transport simulations to study the formation mechanism of an impermeable barrier between acidic and neutral fluid zones in the Onikobe Geothermal Field, Japan. *Journal of Geophysical Research: Solid Earth*, 109(B5). DOI:10.1029/2003JB002792
- Walsh, W., 2013. Geothermal resource assessment of the Clarke Lake Gas Field, Fort Nelson, British Columbia. *Bulletin of Canadian petroleum geology*, 61(3): 241-251.
- Wanner, C. et al., 2014. Reactive transport modeling of the Dixie Valley geothermal area: Insights on flow and geothermometry. *Geothermics*, 51: 130-141. DOI:10.1016/j.geothermics.2013.12.003
- Warren, J.K., 2006. *Evaporites: sediments, resources and hydrocarbons*. Springer Science & Business Media.
- Weisbrod, N., Alon-Mordish, C., Konen, E., Yechieli, Y., 2012. Dynamic dissolution of halite rock during flow of diluted saline solutions. *Geophysical Research Letters*, 39(9). DOI:10.1029/2012GL051306
- Winkler, M., 2011. *Generation-4 Integrated Reservoir Modeling Report*.
- Wissmeier, L., 2015. piChem - A FEFLOW Plugin for Advanced Geochemical Reactions. In: Institute, D.H. (Ed.), *MIKE powered by DHI*, Hørsholm, Denmark, pp. 28.
- Woroniuk, B., Tipton, K., Grasby, S.E., McIntosh, J.C., Ferguson, G., 2018. Salt dissolution and permeability in the Western Canada Sedimentary Basin. *Hydrogeol J*: 1-10. DOI:10.1007/s10040-018-1871-6
- Xia, Y., Plummer, M., Mattson, E., Podgorney, R., Ghassemi, A., 2017. Design, modeling, and evaluation of a doublet heat extraction model in enhanced geothermal systems. *Renewable Energy*, 105: 232-247. DOI: 10.1016/j.renene.2016.12.064

6. Manuscript 4: Improving economic feasibility of low-temperature geothermal energy in the Williston Basin

This paper presents THC models that simulate a site-specific deep geothermal system in the Williston Basin. The production well targets the Dawson Bay formation, which benefits from high thermal conductivity in the underlying Prairie Evaporite formation, dominated by halite, and Winnipegosis, Ashern, Interlake, Stonewall, and Stony Mountain formations, dominated by dolomite. The dolomite and halite are expected to create a warm thermal anomaly in the Dawson Bay formation. The selection of a specific site enabled the consideration of additional assets, including converting existing wells for injection and observed lithium concentrations.

This manuscript contributed to the third and fourth sub-objectives, to assess thermal anomalies in the Williston Basin associated with Halite and Dolomite formations and characterize a geothermal system in the Williston Basin, including flow, heat, and geochemistry. The feasibility of characterizing sedimentary geothermal systems targeting high thermal conductivity dolomite and halite is illustrated using data from the Williston Basin. This study serves as a feasibility study for the development of binary geothermal targeting the Devonian period, by providing simulations based on actual temperature, flow parameters, and geochemistry observed in the basin. The exploration of methods for improving the economic feasibility contributes to the development of deep geothermal power production in Canada's sedimentary basins. With this paper, the overall objective, to evaluate the feasibility and potential benefits of a deep, low-temperature geothermal system targeting thermal anomalies caused by high thermal conductivity minerals such as halite and dolomite is achieved.

Improving economic feasibility of low-temperature geothermal energy in the Williston Basin

Kayla R. Moore and Hartmut M. Holländer

6.1. Abstract

Geothermal power production feasibility studies should assess site-specific resources and assets to determine economic feasibility in low-temperature sedimentary basins. In the Williston Basin, assets include oil and gas wells, and local geochemical data, while resources include high thermal conductivity formations such as halite and dolomite and co-production of lithium. Coupled thermal, hydraulic, and (geo)chemical modeling was used to simulate a horizontal geothermal well system in the Williston Basin. Converting a horizontal, fractured oil and gas well in the Bakken formation for injection provided adequate flow for a 5 MW system and reduced the cost of constructing an injection well up to \$8 million. The Dawson Bay formation was selected for the production well because it was underlain by approximately 370 m of halite and dolomite, which have high thermal conductivities and therefore, increased heat flow. Targeting this formation produced a 6°C temperature anomaly, or 16°C km⁻¹ increase in thermal gradient. However, drilling a horizontal well was not likely to provide cost savings over a vertical well with a similar total length. Formation fluids were of sodium chloride water type for the targeted depths. Precipitation of aragonite, artinite, calcite, celestite, dolomite, halite, huntite, and magnesite were predicted within the production well, presenting a risk of scaling. Lithium in the formation fluids presented the potential for coupled geothermal production and mining, however, profitability is highly dependent on flow rate and local lithium concentration. Considering the available resources and assets provided unique data prior to the development of the geothermal system. Site-specific

resources warrant investigation at potential geothermal sites worldwide to inform the initial investment in the technology and risk of technical errors.

6.2. Introduction

The Williston Basin, a sedimentary sub-basin of the Western Canada Sedimentary Basin (WCSB) has been widely identified as a potential target for a geothermal power plant (Gosnold et al., 2015; Grasby et al., 2012; Manz, 2011b). The deepest parts of the basin, and most promising geothermal targets, are located in Saskatchewan, North Dakota, and Montana (Manz, 2011b). However, development has been slow as a result of high investment costs and uncertainty surrounding profitability (Clauser and Ewert, 2018; Jain et al., 2015).

Gosnold et al. (2015) indicated that geothermal development in the Williston Basin is hindered by the long period it takes for the investment to create revenue, doubts that revenue is possible, and marginal profits from small systems. In this study, site-specific geological and geochemical features are used to characterize a potential geothermal site and examine factors affecting geothermal power production and economic feasibility. Four factors for reducing financial investment and risk of technical issues considered here are (1) conversion of oil and gas wells, reducing or removing the cost of drilling, (2) targeting formations with positive thermal anomalies, (3) understanding site-specific risks of technical issues such as well clogging and well longevity using temperature and geochemical data, and, (4) co-production of minerals such as lithium.

Doublet geothermal systems, consisting of both injection and production wells, allow for the balance of pressure gradients, which are required to move fluid toward the production well (Ricard et al., 2015). Doublet systems have the advantage over single wells that pressure losses

are not affected by time, potentially extending the lifetime of the well (Ricard et al., 2015). In the absence of injection wells, there is also the problem of disposal of large amounts of produced fluids. Converting an oil and gas well reduces or removes the cost of drilling an injection well for geothermal systems (Walsh, 2013; Wang et al., 2016; Weydt et al., 2018). While some existing oil and gas wells may not have an adequate temperature for production, they may be suitable for injection. Additionally, through oil and gas observations, the risk of geothermal exploration is reduced, due to available temperature and geochemical data (Hu et al., 2017; Weydt et al., 2018; Wolff-Boenisch and Evans, 2013; Woroniuk et al., 2018).

Targeting of warm thermal anomalies can result in more economically viable systems, due to the reduced drilling depth to reach similar temperatures. In low-enthalpy sedimentary basins, such as the Williston Basin, the geothermal gradient is dominated by conduction (Scheck-Wenderoth et al., 2014). Within sedimentary basins, halite and dolomite formations have high thermal conductivity and are often associated with warm thermal anomalies e.g., Daniilidis and Herber (2017), Firoozy and Holländer (2016), Petersen and Lerche (1995). Positive temperature anomalies occur at the top of halite and dolomite formations, as heat is channeled through the high thermal conductivity formations. Daniilidis and Herber (2017) modeled temperature differences up to 25°C associated with salt formations at a depth between 1,600 and 2,000 m and thickness of up to 1500 m. Within the Williston Basin, the Devonian period has a number of halite and dolomite formations which may contain adequate temperatures for low-temperature geothermal production. This is the first study to characterize these temperature anomalies and assess their benefit to geothermal development.

Characterizing the geochemical composition of the fluid is important in the planning of construction, ensuring power plant materials are compatible, understanding the risks of clogging,

and potentially engineering heat exchange fluids to mitigate scale formation (Hesshaus et al., 2013). High concentrations of minerals and gases can result in corrosion and scaling, generally identified when problems arise (Alt-Epping et al., 2013; Borgia et al., 2012; Wanner et al., 2017; Wanner et al., 2014; Wolff-Boenisch and Evans, 2013). However, the consideration of geochemistry in the resource assessment stages was not present in the reviewed literature. Corrosion can generally be controlled through careful selection of material used to construct the well. Scaling can be controlled chemically and through well design, however uncontrolled, leads to well clogging. Geothermal scales often consist of carbonate minerals (calcite and aragonite), amorphous silicates, metal oxides, and sulphides (Gunnlaugsson et al., 2014). Coupled thermal, hydraulic, and (geo)chemical modeling (THC) modeling has been used to characterize geothermal systems and identify well-clogging issues, e.g. (Alt-Epping et al., 2013; Daniilidis and Herber, 2017; Firoozy and Holländer, 2016; Wolff-Boenisch and Evans, 2013). Within halite and dolomite formations, high solute concentrations are expected, which can create technical problems related to the chemistry of the geothermal fluids (Gunnlaugsson et al., 2014; Hesshaus et al., 2013). However, geothermal systems targeting evaporite and carbonate formations is a new concept, with limited heat and geochemical modeling examples, e.g. (Daniilidis and Herber, 2017; Firoozy and Holländer, 2016; Moore and Holländer, 2017). The potential for mineral precipitation in a highly saline system, characterized in this paper using 3-D geothermal modeling, has not previously been explored.

Geochemical data can also be used to evaluate the potential for the co-production of minerals such as lithium e.g. Controlled Thermal Resources (2019). The co-production of lithium with geothermal brines is economical in the western United States, in studies which include a pilot plant (Harrison, 2014; Neupane and Wendt, 2017; Ventura et al., 2016). Observed geothermal

brines ranged from 0.19 to 440 mg kg⁻¹ lithium at flow rates from 0.0099 to 3.159 m³ s⁻¹ (Neupane and Wendt, 2017). Neupane and Wendt (2017) evaluated lithium content in brines in the USGS open file database for geothermal brines, which did not include the Williston Basin. Lithium concentrations in the Williston Basin in southeastern Saskatchewan generally range from 36-63 mg L⁻¹, including samples from the Winnipegosis, Birdbear, Ratcliffe, Frobisher, and Duperow formations and 2.7 and 31.0 mg L⁻¹ in the Prairie Evaporite (Jensen, 2016; Rostron et al., 2002). The potential for the production of lithium from deep brines has been considered in Manitoba, but not in tandem with geothermal development (Nicolas, 2017). The economic threshold for a standalone lithium mine is about 100 mg L⁻¹ from a 1 km well depth (Munk et al., 2016). Lithium production in the Saskatchewan portion of the Williston basin produced by a geothermal system is considered here for the first time.

This work provides the first fully-coupled thermal, hydraulic, and (geo)chemical (THC) investigation into a geothermal system targeting high thermal conductivity halite and dolomite minerals. This is accomplished by creating the first site-specific characterization of a geothermal system in the Williston Basin in south-central Saskatchewan. Despite the validation of geochemical models in representing geochemical regimes of geothermal systems, no pre-production chemical analyses were available in the literature. This work examines the first coupling of factors that can improve economic feasibility in Saskatchewan including (1) the potential for adequate flow conditions when converting an oil and gas well into a geothermal production well; (2) characterization of temperature anomalies achieved by targeting dolomite and halite formations; (3) characterization of the produced fluid from dolomite formations overlying halite; and, (4) potential for co-producing lithium. These resources and assets are used to evaluate

the potential for power production and profit in a geothermal system in southeastern Saskatchewan.

6.3. Methods

A site in the Williston Basin in the province of Saskatchewan, Canada was selected as the study area because of the demand for clean energy in the province, along with the availability of temperature and geochemical data from oil and gas development. Saskatchewan has a high energy demand, 660 PJ for the 1.1 million residents in 2016 (National Energy Board, 2019). In 2017, the province of Saskatchewan produced 81% of its electricity using natural gas, coal, and coke, and CO₂ emissions have generally been rising (National Energy Board, 2019). The population is steadily increasing, with energy demand expected to follow. Currently, the Government of Canada Low Carbon Economy Fund invests in projects that generate clean growth and reduce greenhouse gas emissions (Government of Canada, 2019). One geothermal power plant is under development in the Williston Basin in Saskatchewan, targeting the bedrock, supported by government funding (Deep Corp., 2019). However, additional economic incentives are required to encourage mass development.

6.3.1. Interpretation of geology and hydrogeology

The study area was located in the Estevan region in Saskatchewan, Canada. Within the Williston Basin formations from the Mississippian and Devonian periods were considered. This area and these formations were targeted based on (1) general heat flow data, which indicate adequate temperatures are likely to exist in this area (2) the presence of a thick salt formation, likely to be associated with a thermal anomaly and (3) available oil and gas data. The Williston Basin has been extensively characterized during oil and gas development. However, this data must

be treated carefully as oil and gas data are notoriously error-ridden (Wolff-Boenisch and Evans, 2013).

A saline, primarily halite formation, the Prairie Evaporite from the Devonian period, is located at a depth of approximately 2520 m in the study area (Table 6-1). This formation is approximately 116 m thick. Halite has a high heat conductivity and is commonly associated with thermal anomalies (Petersen and Lerche, 1995). Above and below the salt formation in the Devonian and Silurian periods, are thick dolomite formations, including the Dawson Bay, Winnipegosis, Ashern, Interlake Group, Stonewall, and Stony Mountain. Dolomite also has high heat conductivity (Grasby et al., 2012). Formation presence and composition in the study area were estimated based on observed data (Bezys and McCabe, 1996; Smith et al., 2017; Williston Basin TGI, Unknown). Average formation thickness and average depth were calculated from wells located between 49.0 to 49.2 N and -103.3 to -102.9 W (Williston Basin TGI, Unknown). These formations were considered for the production well.

The Estevan area is an active oil and gas field. The Williston Basin has several oil and gas targets including the Bakken, Amsden, Madison, Duperow, Birdbear, Dawson Bay, Interlake, Stony Mountain, Red River, Winnipeg, and Deadwood formations. The Bakken unit of the Mississippian period is located at an average depth of 2095 m in the Estevan area, approximately 350 to 500 m above the Prairie Evaporite (TGI Williston Basin Working Group, 2008a) (Table 6-1). The Bakken formation has a low natural permeability, and hydraulic fracturing is commonly used to increase permeability (Hu et al., 2017). Wells drilled in the Bakken are generally horizontal (Kreis et al., 2006). This formation was considered for the injection well.

Table 6-1. Average thickness and depth for formations within the Williston Basin located between 49.0 to 49.2°N and -103.3 to -102.9°W (Anna, 2013; Sproule, 1964; TGI Williston Basin Working Group, 2008a; TGI Williston Basin Working Group, 2008b).

Period	Formation	Avg Thickness (m)	Standard Deviation (m)	Avg Depth (m below grade)	Composition
Mississippian	Lodgepole	131	22	1965	Calcite and dolomite
	Bakken	30	9	2095	Shale and siltstone
Devonian	Torquay	56	4	2124	Shale
	Birdbear	32	1	2179	Limestone, dolomite
	Duperow	152	12	2211	Limestone, dolomite, calcite
	Souris River	111	7	2361	Shale, limestone, dolomite
	Dawson Bay	48	5	2472	Limestone, dolomite, porosity salt-filled
	Prairie Evaporite	116	37	2520	Halite, potash, and anhydrite
	Winnipegosis	39	18	2636	Dolomite, porosity salt-filled
	Ashern	16	2	2683	Dolomite
Silurian	Interlake Group	135	8	2818	Dolomite
	Stonewall	20	1	2838	Dolomite
	Stony Mountain	45	5	2883	Dolomite, shale
	Red River	170	4	3053	Dolomite, limestone

Values from (Bezys and McCabe, 1996; Smith et al., 2017; Williston Basin TGI, Unknown)

6.3.1.1. Flow and Pressure characterization

The pressure at depth was estimated from Blondes et al. (2017) using all Williston Basin data. Pressure data were scarce within the database, and could not be limited to the immediate study area. The pressure gradient was estimated as:

$$P = \frac{(d - 0.1013)}{-77.4} \quad 6-1$$

where d is the depth below grade (m) and P the pressure in $\text{Pa} \times 10^6$ (MPa). At the depth of the Prairie Evaporite, -2520 m, a pressure of 36 MPa was calculated. This is close to the expected hydrostatic value.

Formation permeabilities vary widely within the Williston Basin (Table 6-2). Generally, the shale and halite formations would require hydraulic fracturing, while the dolomite formations have adequate permeability for geothermal systems (Ricard et al., 2015).

6.3.1.2. Temperature characterization

Temperatures of 101°C at the top of the Duperow formation at approximately -2378 m and 128°C at the top of the Red River formation at approximately -3323 m, in the region immediately south of the study area were calculated by Manz (2011b) and Manz (2011a). These estimates are higher than the oil and gas observed temperatures reported by Blondes et al. (2017), however, they are considered to be more accurate by the authors due to the larger error in measurement values from available oil and gas.

High thermal conductivity was identified within the Prairie Evaporite (halite) at $4.2 \text{ W m}^{-1} \text{ K}^{-1}$, as well as the Winnipegosis (dolomite) at $5.2 \text{ W m}^{-1} \text{ K}^{-1}$ and Ashern, Interlake, Stonewall, and Stony Mountain formations (limestone) at $4.4 \text{ W m}^{-1} \text{ K}^{-1}$ (Firoozy and Holländer, 2016). The

Dawson Bay (dolomite) formation overlying the Prairie Evaporite also had high heat conductivity, $3.6 \text{ W m}^{-1} \text{ K}^{-1}$. The Red River formation marks the first formation underlying the Prairie Evaporite where thermal conductivity was average, $2.8 \text{ W m}^{-1} \text{ K}^{-1}$ (Table 6-2). These are comparable with values from Grasby et al. (2012) with an average of $5.5 \text{ W m}^{-1} \text{ K}^{-1}$ for halite, $4.3 \text{ W m}^{-1} \text{ K}^{-1}$ for dolomite, and $2.8 \text{ W m}^{-1} \text{ K}^{-1}$ for limestone.

6.3.1.3. Geochemical characterization

Each formation has unique geochemical properties. The dissolved minerals may originate in meteoric or ancient oceanic water but are assumed to be the result of water-rock interaction. The minerals of concern for precipitation in the basin are primarily halite (NaCl), carbonate minerals including calcite (CaCO_3) and aragonite (CaCO_3), gypsum ($\text{CaSO}_4 \cdot 2\text{H}_2\text{O}$), anhydrite (CaSO_4) and dolomite ($\text{CaMg}(\text{CO}_3)_2$).

Geochemical data were retrieved from the USGS Produced Waters Database (Blondes et al., 2017). The study area had the highest level of total dissolved solids (TDS) in the Williston Basin, with values exceeding 300 g L^{-1} (Palombi, 2008). Therefore, the collection of data within the basin as close to the study area as possible was important. For the formations considered, a single well was selected to represent the formation, to maintain chemical balance. Geochemical observations were selected based on proximity to the study area, and comparable depths to those observed. Geochemical data values were rejected if they were not in the TDS range suggested by Palombi (2008). Values were limited to those observed in the study area, between -102.0 and -104.5°W longitude and 48.4 and 49.8°N latitude, where possible (Table 6-2). The depth of data collection is reported in Table 6-2. The average depth of the formation itself in the study area is reported in Table 6-1.

For the geochemical values above the Lodgepole, a well from the Kinderhook formation from the USGS database, Blondes et al. (2017) located between -102.0 and -104.4°W longitude and 48.4 and 49.8°N latitude was selected as representative. Flow in this portion of the formation was not expected to influence geochemical results at the production well. For the Bakken to Winnipegosis formations, individual wells were selected to represent each formation. The Winnipegosis formation composition was assumed to be representative of the underlying dolomite formations, which are not expected to influence geochemical results at the production well.

Table 6-2. Formation properties and brine composition in the Williston Basin (Blondes et al., 2017; Christie, 2015). Data are taken from observations between 48.4 to 49.8°N and -102.0 to -104.5°W where available.

		Kinderhook	Lodgepole	Bakken Lower Shale	Three Forks	Birdbear	Duperow	Souris River	Dawson Bay	Prairie Evaporite	Winnipeg is
References		(Blondes et al., 2017)	(Blondes et al., 2017; Smith et al., 2017)	(Blondes et al., 2017)	(Blondes et al., 2017)	(Blondes et al., 2017; Nwachukwu et al., 2018)	(Blondes et al., 2017; Yang, 2015)	(Woroniuk et al., 2018)	(Anna, 2013; Blondes et al., 2017; Woroniuk et al., 2018)	(Beauheim et al., 1999; Blondes et al., 2017; Jain et al., 2015)	(Blondes et al., 2017; Winkler, 2011)
IDUSGS		73560	72727	20503	73171	20512	20516	73580	20535	20539	20543
Depth of data collection	m	598	2310	1700	3185	2309	2615	1968	3217	1024	2251
Temp at depth	°C	32*	84*	71	110*	78	91	74*	109	45*	81
Pressure	MPa	28	30*	22*	41*	30*	34*	25*	42*	13*	29*
pH		6.6	5.4	6.41	6.70	6.31	5.66	5.0	5.99	-	6.69
TDS	g L ⁻¹	292	236	224	212	249	320	325	289	518	407
Br ⁻	mol L ⁻¹	-	-	2.49x10 ⁻³	-	5.78x10 ⁻³	7.78x10 ⁻³	-	1.14x10 ⁻²	6.87x10 ⁻²	5.27x10 ⁻³
HCO ₃ ⁻	mol L ⁻¹	3.61x10 ⁻³	7.75x10 ⁻³	5.15x10 ⁻³	5.92x10 ⁻³	2.87x10 ⁻³	1.77x10 ⁻³	9.20x10 ⁻³	-	9.83x10 ⁻⁴	4.08x10 ⁻³
Ca ²⁺	mol L ⁻¹	1.25 x10 ⁻¹	2.11x10 ⁻¹	5.36x10 ⁻²	6.37x10 ⁻²	1.56x10 ⁻¹	1.47x10 ⁻¹	8.48x10 ⁻¹	4.77x10 ⁻¹	2.59x10 ⁻²	1.83x10 ⁻¹
Cl ⁻	mol L ⁻¹	5.01	4.04	3.75	3.48	4.24	5.39	5.64	4.95	7.566	5.12
K ⁺	mol L ⁻¹	1.62x10 ⁻²	-	5.22x10 ⁻²	4.32x10 ⁻³	7.78x10 ⁻²	2.42x10 ⁻¹	1.99x10 ⁻¹	2.14x10 ⁻¹	1.78x10 ⁻²	1.37x10 ⁻¹
Li ⁺	mol L ⁻¹	4.97x10 ⁻²	-	2.32x10 ⁻³	-	6.84x10 ⁻³	1.93x10 ⁻³	1.58x10 ⁻³	1.16x10 ⁻²	2.00x10 ⁻³	6.67x10 ⁻³
Mg ²⁺	mol L ⁻¹	3.76x10 ⁻²	8.71x10 ⁻²	1.56x10 ⁻²	9.10x10 ⁻³	3.70x10 ⁻²	3.31x10 ⁻²	1.76x10 ⁻¹	7.20x10 ⁻²	5.02x10 ⁻⁴	8.72x10 ⁻²
Na ⁺	mol L ⁻¹	4.73	3.49	3.67	3.46	3.77	4.85	3.41	3.61	5.731	4.56
SO ₄ ⁻	mol L ⁻¹	5.68x10 ⁻³	2.04x10 ⁻²	2.21x10 ⁻²	6.55x10 ⁻²	6.39x10 ⁻³	5.27x10 ⁻³	3.7x10 ⁻³	2.61x10 ⁻³	3.69x10 ⁻²	5.08x10 ⁻³
Sr ²⁺	mol L ⁻¹	-	-	7.65x10 ⁻⁴	1.56x10 ⁻⁴	3.25x10 ⁻³	4.23x10 ⁻³	-	8.05x10 ⁻³	4.82x10 ⁻²	3.60x10 ⁻³
H ₂ S	mol L ⁻¹	-	-	0	-	0	0	-	-	-	0
Permeability	mD	15 [^]	15	2.24	52.5 [^]	52.5	93	80	202	1.00x10 ⁻⁵	10
Horizontal hydraulic conductivity	m s ⁻¹	2.91x10 ^{-7^}	2.91x10 ⁻⁷	4.34x10 ⁻⁸	4.34x10 ^{-8^}	1.02x10 ⁻⁶	1.80x10 ⁻⁶	1.55x10 ⁻⁶	3.91x10 ⁻⁶	1.94x10 ⁻¹³	1.94x10 ⁻⁷
Vertical : horizontal hydraulic conductivity	-	0.1*	0.1*	1	0.1*	0.1*	0.48	0.1*	0.1*	1	0.15
Porosity	%	11.8*	13.5	10.0	6.0	17.5	13	11.8*	11.8*	1	10
Thermal conductivity soil (Firoozy, 2016)	W m ⁻¹ K ⁻¹	2.74*	2.92	2.57	2.57	2.91	3.63	2.88	3.68	4.2	5.2
Thermal conductivity fluid	W m ⁻¹ K ⁻¹	0.609	0.609	0.609	0.609	0.609	0.609	0.609	0.609	0.609	0.609
Volumetric heat capacity solid (Firoozy, 2016)	MJ m ⁻³ K ⁻¹	2.00	1.75	1.353	1.32	1.181	1.17	1.184	2.70	2.70	2.50
Volumetric heat capacity fluid	MJ m ⁻³ K ⁻¹	4.18	4.18	4.18	4.18	4.18	4.18	4.18	4.18	4.18	4.18

*Estimated from entire basin values; ^Estimated from surrounding values and composition

6.3.2. The conceptual model

The conceptual model was a horizontal doublet (2 well) geothermal system with interconnecting fractures located in the Williston Basin (Figure 6-1). The system was assumed to use a binary cycle to produce electricity so that temperatures of 85 to 150°C are acceptable.

The well layout, adapted from Xia et al. (2017), consisted of two parallel horizontal wells, connected by 40 fractures (Figure 6-1). The injection well was located in the Bakken formation at -2110 m. The production well was located in the Dawson Bay formation at -2510 m. Interconnecting the two wells were 40 vertically extended fractures spaced at 30 m, plus a 75 m separation for a total horizontal well length of 1350 m. Fracture permeability was assumed to be created using hydraulic fracturing (Table 6-3). The fractures were initially assumed to be 750 m by 2 m (Xia et al., 2017). The fractures begin at the top of the Bakken formation and extend to the bottom of the Dawson Bay formation. Thus, fractures pass through the Torquay, Birdbear, Duperow, and Souris River formations (Table 6-1). Water circulation was created using an injection pump at the surface and submersible pump installed at the depth of the fluid. The model was a cross-section through the centre of the fractures, so the flow rate was reduced to half.

A horizontal well layout was selected based on existing oil and gas wells in the Bakken formation. A horizontal well concept was thoroughly characterized by Xia et al. (2017) and Plummer et al. (2016) to be capable of producing 5 MW with pumping power of less than 1 MW. Previous studies strengthen the results of this study, which along with thermal and hydro focuses on geochemistry, whereas Xia et al. (2017) and Plummer et al. (2016) characterized thermal, hydro, and mechanical properties.

The thickness and depth of the geological units were defined based on the Williston Basin Targeted Geoscience Initiative II geoscience database (Williston Basin TGI, Unknown) (Table

6-1). The model was divided into 10 formations. The first unit represented the Upper Williston Basin and was based on observations in the Kinderhook formation. The middle units were the Lodgepole, Bakken, Three Forks/Torquay, Birdbear, Duperow, Souris River, Dawson Bay, and Prairie Evaporite formations (Table 6-2). The lower unit represents the Winnipegosis formation to the Stony Mountain formation, and characteristics were based on the Winnipegosis formation. Each of the 10 geological units was assumed to be characterized by individual, representative geochemical, thermal, and flow properties (Table 6-2). The fluid injected into the system was assumed to have geochemical properties represented by the targeted production formation, the Dawson Bay formation, with injection temperatures based on field data from DiPippo (2004) (Table 6-4).

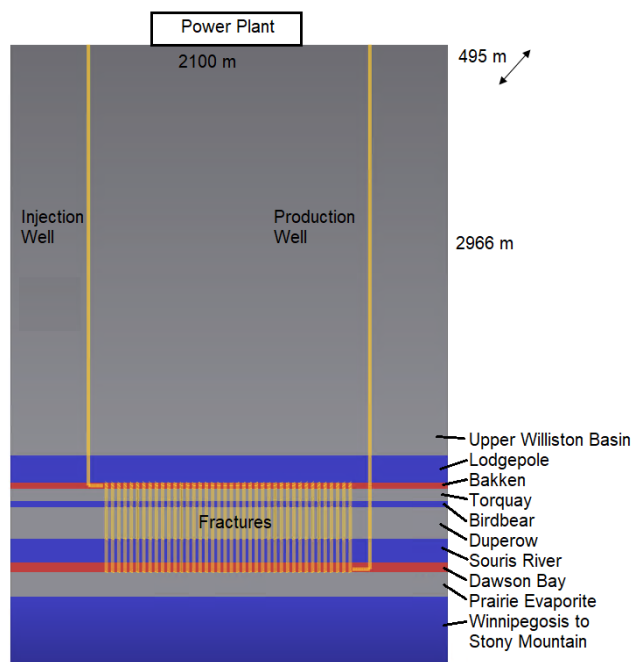


Figure 6-1. A geothermal-doublet energy production system with horizontal injection and production wells connected by 40 fractures in the Williston Basin.

6.3.3. Numerical simulator

The primary focus of this research was to determine the potential for the development of a geothermal system considering flow through a converted oil and gas well, temperature conduction

based on thermal conductivity, and high ionic strength produced geochemistry in the Williston Basin. Therefore, a model capable of coupled flow, temperature, and geochemical simulations was selected. FEFLOW (Diersch, 2014) with the geochemical plug-in piCHEM (Wissmeier, 2015) was selected to simulate fully coupled fluid flow, heat transport, and mineral reactive transport. FEFLOW uses a multi-dimensional finite element model to solve governing flow, mass and heat transport equations in both porous and fractured media. The piCHEM plug-in (Wissmeier, 2015) couples FEFLOW with PHREEQC (Parkhurst and Appelo, 2013). Within piCHEM, all transport species have the same transport properties (porosity, diffusion, dispersivity). The Pitzer (1973) database was used due to its capability of simulating high ionic strength scenarios.

FeFlow has been extensively validated for flow, variable density, and heat transport problems e.g. Diersch (2014). The use of piCHEM for reactive transport modeling has been validated using theoretical e.g. Wissmeier (2015) and physical examples e.g. Moore et al. (2019). The use of PHREEQC to predict the mineral composition in geothermal systems has been validated with physical data e.g. Tarcan et al. (2016) and Bozau et al. (2015).

The model was a 3-D domain that intersected a geothermal system in the Williston Basin (Table 6-3). Horizontally, 10 formations were represented using 12 layers, with additional layers located in each the Bakken and Dawson Bay formations at the horizontal wells. The geological formations were represented using two interconnected domains, porous flow in the unfractured rock matrix and the discrete features representing fractures and wells. The permeability, porosity, rock properties, and geochemistry were considered homogenous within each rock formation layer (Table 6-2). The top of the Williston Basin was set at 0 m and the bottom -2966 m. The model extended 2100 m by 500 m horizontally, with transport mapping quadrilateral elements 7.5 m by 7.5 m. The total number of nodes used in the model was 244,751.

The model was assumed to be fully saturated, non-isothermal, and single phase. Binary systems are generally considered to be water systems with no steam phase. Fluid density was linearly dependent on temperature, and density was considered using the Boussinesq approximation. The reservoir was considered as a slightly compressible, porous media. Water is a slightly compressible fluid; assuming a fluid bulk modulus based on water of 2200 MPa, and a maximum observed pressure of 30.3 MPa, the fractional volume of compression is 1.3%, which was considered here as negligible (Sorey, 1978). Assuming constant mechanical properties will result in conservative production estimates (Xia et al., 2017).

Geochemical reactions including precipitation and dissolution can create decreases and increases in permeability and porosity, which are not calculated using piCHEM. Woroniuk et al. (2018) evaluated permeability in the Dawson Bay and Souris River formations and found a weak relationship between NaCl inclusions and permeability and suggested that reactive transport models in formations near the Prairie Evaporite do not need to couple permeability with salt content. Equilibrium reactions are used, which are valid under low-flow scenarios in sedimentary basins (Palandri and Kharaka, 2004). Based on the relatively high residence time of the fluid within the formation, the estimate is assumed to be valid.

6.3.4. Initial and boundary conditions

6.3.4.1. Flow and pressure boundaries

Initial pressure was based on observed values (Equation 6-1). Surface conditions were 0.1013 MPa and 6°C. The initial hydraulic head was -10 m. A constant hydraulic head boundary of -10 m was set at $z = 0$ m, except at the top of the production and injection wells. No-flow conditions existed along the sides and bottom of the model (Table 6-3).

Assuming a nondeforming formation, with variable density Darcy-type, and saturated flow Mass conservation of fluid in a saturated porous medium is given by Diersch (2014):

$$S_0 \frac{\partial h_0}{\partial t} + \nabla \cdot (\mathbf{K} \cdot (\nabla h_0 + \chi \vec{e})) = Q \quad 6-2$$

where S_0 is specific storage (m^{-1}), h_0 is the equivalent freshwater hydraulic head (m), t is time (s), χ is the buoyancy coefficient (-), \vec{e} is the gravitational unit vector (-) and Q is sources and sinks (s^{-1}). \mathbf{K} refers to hydraulic conductivity (m s^{-1}). However, the use of permeability \mathbf{k} (m^2) to define fluid flow in deep geothermal systems is more appropriate, because hydraulic conductivity \mathbf{K} (m s^{-1}) is dependent on fluid properties:

$$\mathbf{K} = \mathbf{k} \left(\frac{\rho g}{\mu} \right) \quad 6-3$$

where ρ is fluid density (kg m^{-3}), g is the acceleration of gravity (m s^{-2}), and μ is fluid dynamic viscosity ($\text{kg m}^{-1} \text{s}^{-1}$).

Flow in the wells was represented using a Neumann well boundary condition at a (half) rate of $0.1 \text{ m}^3 \text{s}^{-1}$ at both the injection and production wells (Xia et al., 2017). The wells themselves were 2-D discrete features along an edge defined by Darcy flow. The permeability in the elements surrounding the wells was 0, indicating a solid pipe. Fractures extended from the Bakken formation to the Dawson Bay formation and were represented using 1-D discrete features on a join face defined by Darcy flow (Table 6-3). Hydraulic conductivities for the formations were calculated from permeability (Table 6-2), assuming constant fluid properties with a density of 1100 kg m^{-3} , gravity of 9.81 m s^{-2} , and viscosity of $5.494 \times 10^{-4} \text{ Pa-s}$.

The sensitivity of pressure was evaluated by varying the flow rate between 0.1 and 0.4 m³ s⁻¹ and varying fracture permeability between that of the Bakken formation and Dawson Bay formation.

Changes in temperature, pressure, and fluid composition will affect the density and viscosity of the fluid. Effect of temperature and pressure on fluid density were adapted from Sorey (1978) as:

$$\rho = \rho_0[1 - B(T - T_0) - \Gamma(T - T_0)^2 + \kappa(P - P_0)] \quad 6-4$$

where ρ is fluid density (kg m⁻³), ρ_0 is initial fluid density (kg m⁻³), T and T_0 are observed and initial temperature (°C), P and P_0 are observed and initial pressure (MPa), B is the thermal expansivity of fluid (°C⁻¹), Γ is the second-order thermal expansivity of fluid (°C⁻²) and κ is fluid compressibility (MPa⁻¹). The effect of transient fluid properties was examined in the sensitivity analysis.

Table 6-3. Numerical model parameters for a doublet, horizontal geothermal well system in the Williston Basin.

Parameter		Reservoir properties	Source
System type		Doublet	(Xia et al., 2017)
Operation time	years	30	(Xia et al., 2017)
X	m	2100	(Xia et al., 2017)
Y	m	500	(Xia et al., 2017)
Z	m	2966	(Xia et al., 2017)
XY elements	-	18,480	
Layers	-	12	
Total nodes	-	244,751	
Pressure gradient	kPa m ⁻¹	18	(Blondes et al., 2017)
Initial Pressure (Top)	kPa	100	(Blondes et al., 2017)
Initial Pressure (Bottom)	kPa	48,500	(Blondes et al., 2017)
Initial Temperature (Top)	°C	6	(Blondes et al., 2017)
Initial Temperature (Bottom)	°C	125	(Manz, 2011b)
WELLS			
Flow rate	m ³ s ⁻¹	0.2	(Xia et al., 2017)

Production well depth (Dawson Bay)	m	-2510	(TGI Williston Basin Working Group, 2008a)
Production well horizontal extent	m	1290	(Xia et al., 2017)
Injection well depth (mid-Bakken)	m	-2110	(TGI Williston Basin Working Group, 2008a)
Injection well horizontal extent	m	1290	(Xia et al., 2017)
Cross-sectional area	m ²	0.13	(Xia et al., 2017)
Conductivity	m s ⁻¹	1x10 ⁻⁶	(Xia et al., 2017)
Porosity	-	1	(Xia et al., 2017)
FRACTURES			
Number of fractures	-	40	(Xia et al., 2017)
Fracture spacing	m	30	(Xia et al., 2017)
Permeability	mD	245	(Xia et al., 2017)
Conductivity	m s ⁻¹	1 x10 ⁻⁶	(Xia et al., 2017)
Thickness	m	2	(Xia et al., 2017)
Porosity	-	0.2	(Xia et al., 2017)
MATRIX			
Diffusion coefficient	m s ⁻¹	10 x10 ⁻⁹	(Schelkes et al., 2001)
Longitudinal dispersivity	m	250	(Wissmeier, 2015)
Specific storage (Compressibility)	m ⁻¹	1x10 ⁻⁴	(Diersch, 2014)

6.3.4.2. Temperature boundaries

A steady-state model was used to determine initial heat distribution within the formation. Based on Manz (2011b), a constant temperature boundary of 125°C was set at the bottom of the model. A constant temperature boundary of 6°C was applied at the top of the model, with two exceptions. A constant temperature boundary of 70°C was applied at the injection well, and no boundary was set at the production well. An injection temperature of 70°C was chosen as a conservative estimate (DiPippo, 2004). The vertical sides have no heat flow boundaries. Thermal conditions were based on calibrated, effective thermal conductivity, and volumetric heat capacity value for the Williston Basin (Table 6-2) (Firoozy, 2016).

The sensitivity to temperature parameters was evaluated by varying the injection temperature between 60 and 80°C to evaluate the effect of cooler injection temperatures on the

lifetime of the well. As discussed above, the predictions of the temperature at the top of the Red River formation were highly variable, so the effect of a 125°C temperature and 114°C temperature were evaluated.

Heat transport was calculated using thermal conductivity values from both the fluid and rock phases and the volumetric heat capacity of the fluid and rock. The convective form of heat transport for a variable-density, Darcy-type flow conduction and advection can be defined as (Diersch, 2014):

$$(\varepsilon \rho c + (1 - \varepsilon) \rho_s c_s) \frac{\partial T}{\partial t} + \rho c \vec{q} \cdot \nabla T - \nabla \cdot (\mathbf{A} \cdot \nabla T) = H_e - \rho c (T - T_0) Q \quad 6-5$$

where ε is porosity (-), ρ mass density of the fluid (kg m^{-3}), c is specific heat capacity ($\text{m}^2 \text{s}^{-2} \text{K}^{-1}$), ρ_s is the mass density of the solid (kg m^{-3}), c_s is the specific heat capacity of solid ($\text{m}^2 \text{s}^{-2} \text{K}^{-1}$), T is temperature (K), T_0 is reference temperature (K), t is time (s), \vec{q} is the Darcy flux (m s^{-1}), \mathbf{A} is the tensor of hydrodynamic thermodispersion ($\text{kg m s}^{-3} \text{K}^{-1}$) and Q is a sink/source term (s^{-1}).

6.3.4.3. Geochemical boundaries

The basin was divided into 10 layers with unique geochemical properties (Table 6-2). The composition of the basin focused on Br^- , HCO_3^- , Ca^{2+} , Cl^- , K^+ , Li^+ , Mg^{2+} , Na^+ , SO_4^{2-} , and Sr^{2+} . The observed fluid composition from Table 6-2 was balanced and equilibrated to dominant minerals at the observed temperature, then adjusted to the modeled temperature based on SI using PHREEQC Version 3 (Parkhurst and Appelo, 2013) and the Pitzer (1973) database. It was assumed that the observed composition of the fluid within the reservoir was representative of the mineral composition of the formation. In the model simulation, the large number of minerals with targeted saturation indices (SI) created instabilities. Therefore, the mineral with the largest positive SI was chosen to represent each ion (e.g., gypsum vs. anhydrite).

For each layer, constant concentration boundaries were set on two horizontal edges for ions as well as minerals. The initial mineral composition was set for each layer as per the above description. The composition of the injected fluid was constant throughout the simulation and was applied using a constant head boundary at the top of the production well. The composition of the injected heat exchange fluid was based on the Dawson Bay fluid with the Li^+ removed (Table 6-4). All geochemical reactions were evaluated at equilibrium.

Within piCHEM, aqueous flow are expressed as the transport of individual components (Wissmeier and Barry, 2008; Wissmeier et al., 2009). The advection-diffusion/dispersion equation is used for multi-component transport (Bear, 1972):

$$\frac{\partial \theta C_i}{\partial t} = -\nabla \cdot (\vec{q} C_i) + \nabla \cdot (\theta \mathbf{D} \nabla C_i) + S_c \quad 6-6$$

where θ is the relative liquid phase saturation ($\text{m}^3 \text{m}^{-3}$), C_i is the concentration of solution species i (kg m^{-3}), \vec{q} is the Darcy flux (m s^{-1}), θ is the relative liquid phase saturation ($\text{m}^3 \text{m}^{-3}$), \mathbf{D} is hydrodynamic dispersion ($\text{m}^2 \text{s}^{-1}$) and S_c is sources and sinks ($\text{kg m}^{-3} \text{s}^{-1}$).

The geochemical analysis was primarily for the determination of potential precipitation within the production well. The piCHEM reactive transport module does not provide mineral outputs. Therefore, a 1-D analysis was used to evaluate the potential for mineral precipitation as the fluid moved from the bottom of the production well to the top of the production well at the appropriate temperature and pressures.

The geochemistry was based on the assumption that the formation water was representative of the formation composition. Samples collected from oil and gas well may be inaccurate due to the great depth they are working over and potential contamination from other formation or drilling

fluids (Manz, 2011b). The sensitivity of the model to the composition of the injected heat exchange fluid was evaluated using two heat exchange fluid compositions. First, a heat exchange fluid representative of the Dawson Bay composition and second a freshwater heat exchange fluid.

Table 6-4. The composition of injected heat exchange fluid in a geothermal doublet in the Williston Basin.

Ion	Concentration mol L ⁻¹
Br ⁻	1.14x10 ⁻²
HCO ₃ ⁻	0
Ca ²⁺	4.77x10 ⁻¹
Cl ⁻	4.95
K ⁺	2.14x10 ⁻¹
Li ⁺	0
Mg ²⁺	7.20x10 ⁻²
Na ⁺	3.61
SO ₄ ²⁻	2.61x10 ⁻³
Sr ²⁺	8.05x10 ⁻³

6.3.5. Production calculations

The pressure observed in the production well in the model can be used to calculate pumping power, p_p (W):

$$p_p = \frac{Q_w \Delta P}{\Omega} \quad 6-7$$

where Q_w is discharge (m³ s⁻¹), Ω is pump efficiency, and ΔP is total dynamic pressure change (Pa) calculated as the sum of hydrostatic pressure, the aquifer pressure drawdown, skin effect drawdown, friction losses, and injection overpressure (Ricard et al., 2015).

The maximum potential power output, \dot{W} (kW) was calculated using the methods described in DiPippo (2004) for binary geothermal systems:

$$\dot{W} = \dot{m} \left(\eta_{prod} - \eta_{inj} - T(\varphi_{prod} - \varphi_{inj}) \right) \quad 6-8$$

where \dot{m} is the mass flow rate at the outlet (kg s^{-1}), T is the dead state temperature ($^{\circ}\text{C}$), φ_{prod} and φ_{inj} are the specific entropy of fluid at the inlet and outlet ($\text{kJ kg}^{-1} ^{\circ}\text{C}^{-1}$) and η_{prod} and η_{inj} is the enthalpy of fluid at each inlet or outlet (kJ kg^{-1}), calculated as:

$$\eta = T * c_{fluid} \quad 6-9$$

where T is the fluid temperature ($^{\circ}\text{C}$) and c_{fluid} is the specific heat of the fluid ($\text{kJ kg}^{-1} ^{\circ}\text{C}^{-1}$), $4.2 \text{ kJ kg}^{-1} ^{\circ}\text{C}^{-1}$ was used for the calculations.

6.3.6. Model validation and calibration

Model validation and calibration were difficult in this scenario, where no actual data were available. The well layout has been thoroughly studied by Xia et al. (2017) and Plummer et al. (2016). PHREEQC has been successfully used to predict mineral dissolution and brine production in physical geothermal systems, e.g., Alt-Epping et al. (2013) and Wolff-Boenisch and Evans (2013). Therefore, piCHEM was expected to be a valid method for the prediction of the geothermal fluid composition. Mineral values from the formation and permeability were assumed to be correct as reported. Since calibration to field data was not possible, a thorough sensitivity analysis was conducted to examine the potential range of results.

6.4. Results

6.4.1. Well conversion economic impacts

The suitability of the existing Bakken well for conversion was evaluated for distance from the Dawson Bay formation, required permeability, and cost savings. The conceptual model from Xia et al. (2017), shown to produce a viable 5 MW geothermal power plant, recommended a vertical distance between wells of 500 m. The distance between the Bakken and Dawson Bay

formations at the study location was 377 m. The model simulations below explore power production using that distance.

Permeability thickness products consider the permeability of the formation, as well as the completed (perforated) portion of the well. If the well is completed across the entire reservoir thickness than the completion length and reservoir thickness are the same (Ricard et al., 2015). Horizontal wells have the advantage of being completed over the horizontal length of the well, in this model, 1350 m. In the scenario presented here, the 1350 m completion would require a permeability of 42 mD. Hydraulic fracturing would be required in the low permeability Bakken and Torquay/Three Forks formations, both estimated at 2.24 mD. However, this is often completed as part of the oil and gas production process. The intrinsic permeability in the Dawson Bay formation was 202 mD, Souris River was 80 mD, Duperow was 93 mD, and Birdbear was 52.5 mD, indicating adequate flow.

The cost to drill a well in Canada was estimated at Can\$500 m⁻¹, and completion costs were Can\$400 m⁻¹ (JWN, 2017; Rose & Associates, 2016). Based on depth in the Bakken of 2110 m and Dawson Bay 2510 m, plus 1350 m horizontal section for each well, the Bakken well would cost \$1.7 million to drill plus \$1.4 million in completion costs and the Dawson Bay well \$1.9 million, plus \$1.5 million in completion costs. This results in total drilling and completion costs of \$6.5 million. Alternative estimates for drilling and completion of a single oil and gas well in the Bakken formation are closer to \$8.0 million (Rose & Associates, 2016). By converting a well in the Bakken, there are cost savings of \$3.1 to \$8.0 million in drilling and completion costs, up to 40% of the drilling cost.

6.4.2. Flow

Flow, temperature, and geochemical model simulation results are presented in the next 3 sections. The simulation time for the geochemical model was 416 minutes. The computer had 48.0 GB of RAM with a 64-bit Operating System and AMD Opteron™ Processor 6176 2.30 GHz.

6.4.2.1. Fluid Properties

Constant density and viscosity were compared to non-linear density and temperature-dependent viscosity settings. Changes in density from 1000 kg m^{-3} to 1200 kg m^{-3} resulted in minimal changes in hydraulic conductivity. However, viscosity changes with temperatures from 6 to 125°C have the potential to alter the hydraulic conductivity by up to 1 magnitude. Considering Equation 6-4, with β of $5 \times 10^{-4} \text{ }^{\circ}\text{C}^{-1}$, γ of $2.56 \times 10^{-6} \text{ }^{\circ}\text{C}^{-1}$, and κ of $4.54 \times 10^{-4} \text{ MPa}^{-1}$, assuming a maximum temperature change of 119°C and a maximum pressure change of 31.7 MPa and initial fluid density of 1100 kg m^{-3} density changes of 14 kg m^{-3} and 44 kg m^{-3} . Fluid density resulting from a $54,000 \text{ mg L}^{-1}$ change in NaCl concentration results in a density change of 37 kg m^{-3} .

6.4.2.2. Pressure

The well configuration and assumed conditions resulted in adequate permeability and flow for a geothermal doublet. The pressure at the top of the injection well increased and then remained stable, at the top of the production well the pressure decreased and then remained stable. Flow rates were representative of half of the potential production. At a flow rate of $0.2 \text{ m}^3 \text{ s}^{-1}$, after stabilizing, the maximum pressure at the top of the injection well was 4345 kPa, and maximum pressure at the top of the production well was -3,776 kPa. The negative pressure is an indication of the pumping power required to lift the fluid to the surface (Ricard et al., 2015). Assuming Ω is 1, for the standard simulation a pumping power of 0.75 MW is required (equation 6-7).

The pressure at the injection and production wells was sensitive to the flow rates and conductivity of the fractures. At flow rates of $0.10 \text{ m}^3 \text{ s}^{-1}$ and $0.40 \text{ m}^3 \text{ s}^{-1}$ pressures at the top of the

production wells were -2786 kPa and -5166 kPa. The pressure was very sensitive to fluid properties, without consideration of transient fluid properties the pumping power for a $0.20 \text{ m}^3 \text{ s}^{-1}$ flow is calculated at 2.0 MW.

6.4.3. Temperature

6.4.3.1. Steady-state temperature distribution

Using the high-temperature estimate of 125°C at the top of the Red River formation (-2966 m), the temperature in the middle of the Dawson Bay Formation (-2510 m) was 112°C . The top of the Dawson Bay formation had a temperature of 111°C and bottom 113°C . The temperatures calculated in the Duperow formation are similar to those predicted by Manz (2011a), approximately 101°C . Using the low-temperature estimate of 114°C at the top of the Red River formation, the top of the Dawson Bay formation had a temperature of 101°C and bottom 103°C (Table 6-5).

The sensitivity to the high thermal conductivity of the halite and dolomite was examined by reducing the thermal conductivity to $2.8 \text{ W m}^{-1} \text{ K}^{-1}$ from the Bakken to the top of the Red River formation. With reduced thermal conductivity, an average temperature decrease of 6°C was observed within the Dawson Bay formation and at the top of the production well. With a thermal gradient of 42°C km^{-1} , this results in a depth difference of 142 m. This indicates the halite and dolomite formations result in a 16°C km^{-1} increase in the thermal gradient. The costs associated with 142 m of drilling and completions at $\text{CAD}\$900 \text{ m}^{-1}$ is $\$127,800$ (JWN, 2017; Rose & Associates, 2016).

The produced temperature was sensitive to permeability within the fractures, but not porosity. Fracture permeability similar to the Bakken formation $8.6 \times 10^{-3} \text{ m d}^{-1}$ and a value similar to the Dawson Bay formation $3.3 \times 10^{-1} \text{ m d}^{-1}$ resulted in temperature at 30 years of 108°C and

95°C. Increased temperatures were associated with the high thermal conductivity minerals, thus they formed warm temperature anomalies. However, the temperature boundary at the top of the Red River had the greatest influence on the temperature at the top of the Prairie Evaporite. Increased formation thickness resulted in decreased temperature in the Prairie Evaporite at the same Red River temperature boundary.

Table 6-5. Temperature distribution at the top of each formation unit, based on a constant temperature of 125°C and 114°C at the top Red River formation.

Formation	Depth at Top m	Temperature °C	Temperature °C
Ground surface	0	6	6
Lodgepole	-1965	89	82
Bakken	-2096	95	87
Torquay	-2126	97	88
Birdbear	-2182	99	91
Duperow	-2214	101	92
Souris River	-2366	106	97
Dawson Bay	-2477	111	101
Prairie Evaporite	-2525	113	103
Winnipegosis	-2896	117	106
Top of Red River	-2966	125	114

Table 6-6. Power production sensitivity, temperatures at the top of the Prairie Evaporite with varying heat flow parameters.

Thermal Cond. $\text{W m}^{-1} \text{ } ^\circ\text{C}^{-1}$	Boundary Temp $^\circ\text{C}$	Thickness m	Prairie Temp $^\circ\text{C}$
3.9	126	460	111
5.1	126	460	114
2.8	126	460	106
3.9	154	460	135
3.9	98	460	86
3.9	126	534	109
3.9	126	385	113

6.4.3.2. Transient temperature distribution

Temperatures were observed at the top of the production well over a 30-year period. An injection temperature of 70°C resulted in a peak temperature at the top of the production well of

116°C, with a slow decline to a minimum temperature of 103°C at 30 years (Figure 6-2). Under the low-temperature scenario, an injection temperature of 70°C resulted in a peak temperature of 102°C.

Variations in the injected fluid temperature of 10°C had little impact on the produced temperature at the injection well. An initial injection temperature of 80°C resulted in a minimum temperature at the top of the production well of 105°C. An initial injection temperature of 60°C resulted in a minimum temperature at the top of the production well of 103°C. The distribution of temperature within the formations layers was uneven (Figure 6-3). The cool temperatures progressed into the fractures with time, with cooler temperatures generally observed in the fractures than the matrix. At the bottom of the production well, using transient fluid properties, a temperature of 112°C was observed at 30 years, compared to 105°C with constant viscosity and density.

6.4.3.3. Power Production

The ideal scenario, with a flow rate of $0.02 \text{ m}^3 \text{ s}^{-1}$, an inlet temperature of 113°C, an outlet temperature of 70°C and a pumping power of 1.0 MW resulted in a 9.3 MW gross power production, or 8.5 MW net, indicating a viable 5 MW system. In the low-temperature scenario, a produced temperature of 103°C resulted in a decrease in power production of 2.5 MW, indicating a large sensitivity to produced temperature. Reinjection temperature, or output from the power plant, was evaluated at 60 and 80°C. The power produced is sensitive to the outlet temperature, a decrease in injection temperature to 60°C resulted in an increase in power production of 1.6 MW and an increase in injection temperature to 80°C resulted in a decrease in power production of 1.8 MW. A reduction of 6°C, the thermal anomaly associated with the Prairie Evaporite, resulted in a reduction of power output of 1.5 MW. Decreasing the flow rate from $0.10 \text{ m}^3 \text{ s}^{-1}$ resulted in a

decrease in power production to 4.7 MW. Increasing the flow rate to $0.40 \text{ m}^3 \text{ s}^{-1}$ resulted in a significant increase in power production, as well as pumping power, with a net production of 16.8 MW.

Table 6-7. Power production, pumping power, and net production for various inlet and outlet temperature and flow rates in a geothermal doublet in the Williston Basin.

Flow Rate $\text{m}^3 \text{ s}^{-1}$	Inlet Temp $^{\circ}\text{C}$	Outlet Temp $^{\circ}\text{C}$	\dot{W} MW	p_p MW	net MW	
0.20	113	70	9.3	0.8	8.5	Standard Case
0.20	113	80	7.5	0.8	6.7	Less efficient plant
0.20	113	60	10.9	0.8	10.1	More efficient plant
0.20	103	70	6.8	0.8	6.0	Temp @ 30 years
0.10	113	70	4.7	0.3	4.4	Low Flow
0.40	113	70	18.8	2.0	16.8	High Flow
0.20	107	70	7.8	0.8	7.0	No anomaly

6.4.4. Geochemistry

The fluids within the targeted Williston Basin formations were all of a sodium chloride water type, with cations dominated by sodium and potassium and anions dominated by chloride (Figure 6-4). Therefore, halite was identified to be a key mineral of concern for well clogging. The mineral compositions evolved over the 30-year lifespan of the well; no steady-state was observed (Figure 6-2). Over the 30-year time-period, Br^- , Li^+ , and Sr^{2+} generally decreased, Mg^{2+} , HCO_3^- , and Ca^{2+} increased to a peak and then decreased and K^+ , Cl^- , and Na^+ are relatively constant and SO_4^{2-} generally increased (Figure 6-1). Distribution of concentration was uneven within the formation layers (Figure 6-5); this indicates that dissolution and precipitation may both be occurring within the formation. Higher concentrations were observed just beyond the end of the fractures and between the fractures.

The Na^+ and Cl^- curves are relatively constant throughout the simulation indicating that little dissolution or precipitation of NaCl is occurring within the formation. The initial increase in Mg^{2+} , HCO_3^- , and Ca^{2+} may be a result of some dissolution of the Dawson Bay formation, resulting in increased permeability and porosity, while the decrease after about 15 years is more likely a result of fluids from other formation moving into the Dawson Bay formation.

The main concern in this study was mineral precipitation within the production well. The results from the 1-D analysis indicated the potential for precipitation of aragonite, artinite, calcite, celestite, dolomite, halite, huntite, and magnesite within the system (Table 6-8). The SI values changed over time, indicating that the composition of mineral precipitation will change over time.

Fluids reflecting the composition of the Dawson Bay formation and freshwater were injected into the system. The ion concentrations at the production well were generally insensitive to the concentration of the injected fluid (Figure 6-6). The effect of transient versus constant density and viscosity on geochemistry resulted in a 7% variation in concentration at 30 years, compared to a brine injection, and a 0.04% variation at 30 days. Equilibrium values were used to calculate the mineral reactions, which may result in the overestimation of concentrations.

6.4.4.1. Lithium production

Four measurements of lithium were available for the Dawson Bay formation from the USGS produced waters database, with concentrations ranging from 5.65×10^{-3} to $1.71 \times 10^{-2} \text{ mol L}^{-1}$, with an average of $1.14 \times 10^{-2} \pm 4.70 \times 10^{-3} \text{ mol L}^{-1}$ (Blondes et al., 2017). The closest measurement was approximately 175 km southwest of the study area. Model results indicate lithium concentration will slowly decline over the lifetime of the well (Figure 6-3 “ Li^+ ”). Modeled results of Li^+ concentration ranged from $1.36 \times 10^{-2} \text{ mol L}^{-1}$ at the beginning of production to $3.16 \times 10^{-3} \text{ mol L}^{-1}$ at the end of 30 years.

Based on the modeled concentration of lithium in the Dawson Bay formation, the initial production of Li^+ at $1.36 \times 10^{-2} \text{ mol L}^{-1}$ and a flow rate of $0.2 \text{ m}^3 \text{ s}^{-1}$ would result in the production of $5.9 \times 10^5 \text{ kg y}^{-1}$. At the lowest concentration, $1.3 \times 10^5 \text{ kg y}^{-1}$ is produced. Lithium prices are currently CAD\$22,000 t^{-1} (Metalary, 2019) and are expected to stay high for the next 5 years (Schaefer, 2017). Recovery rates of 95% are expected for various lithium extraction techniques (Neupane and Wendt, 2017). Using the high production rate of $5.9 \times 10^5 \text{ kg y}^{-1}$, the value of lithium was \$13.0 million annually and the low production value was \$2.8 million.

The mass of produced lithium is sensitive to a number of the parameters in this feasibility study. Lithium concentration in the model was set at $1.16 \times 10^{-2} \text{ mol L}^{-1}$ in the Dawson Bay formation, associated with $5.1 \times 10^5 \text{ kg y}^{-1}$ production. Measured values result in a production ranging from $7.5 \times 10^5 \text{ kg y}^{-1}$ to as low as $2.5 \times 10^5 \text{ kg y}^{-1}$, resulting in an \$11.0 million annual difference in lithium market value. Production and value of lithium are directly correlated with the flow rate. Doubling the flow rate to $0.4 \text{ m}^3 \text{ s}^{-1}$ results in a doubling of production and market value.

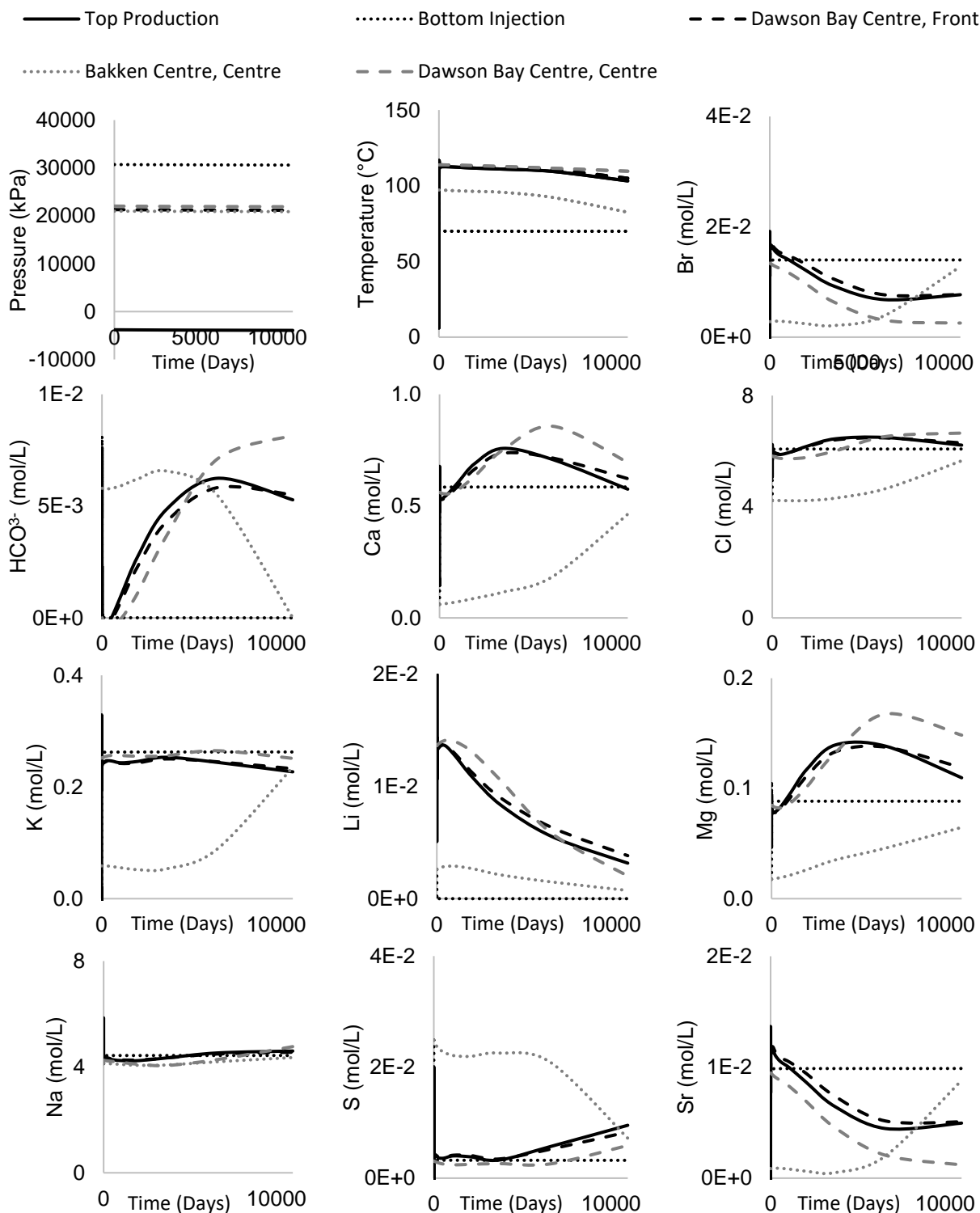


Figure 6-2. Temperature and ion distributions for a geothermal system in the Williston Basin. Centre and front refer to locations within the formation, with the first 'centre' indicating placement between the wells, the second 'centre' located in the fractures, and 'front' in line with the wells.

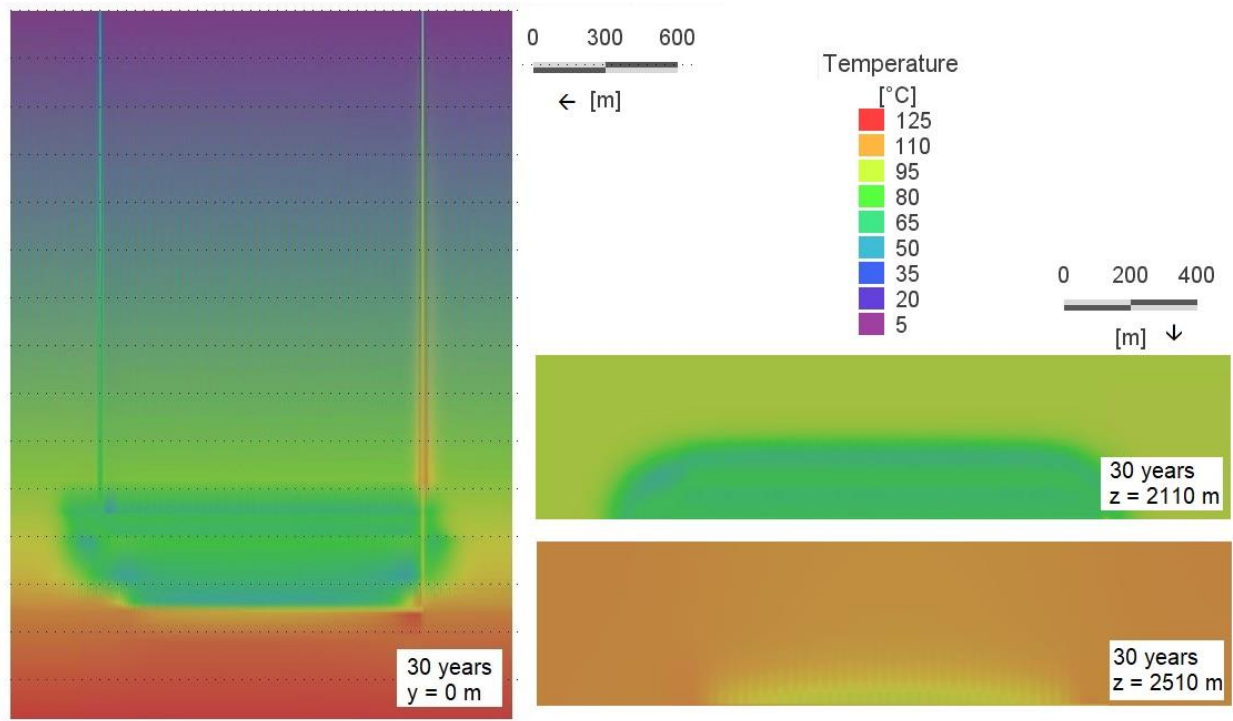


Figure 6-3. Temperature distribution within the formation following 30 years of simulation.

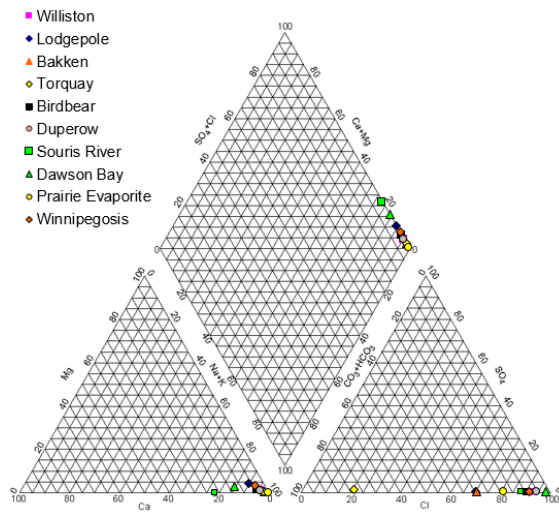


Figure 6-4. Piper plot of the composition of fluids in the Williston Basin within the targeted formations in the Mississippian and Devonian periods.

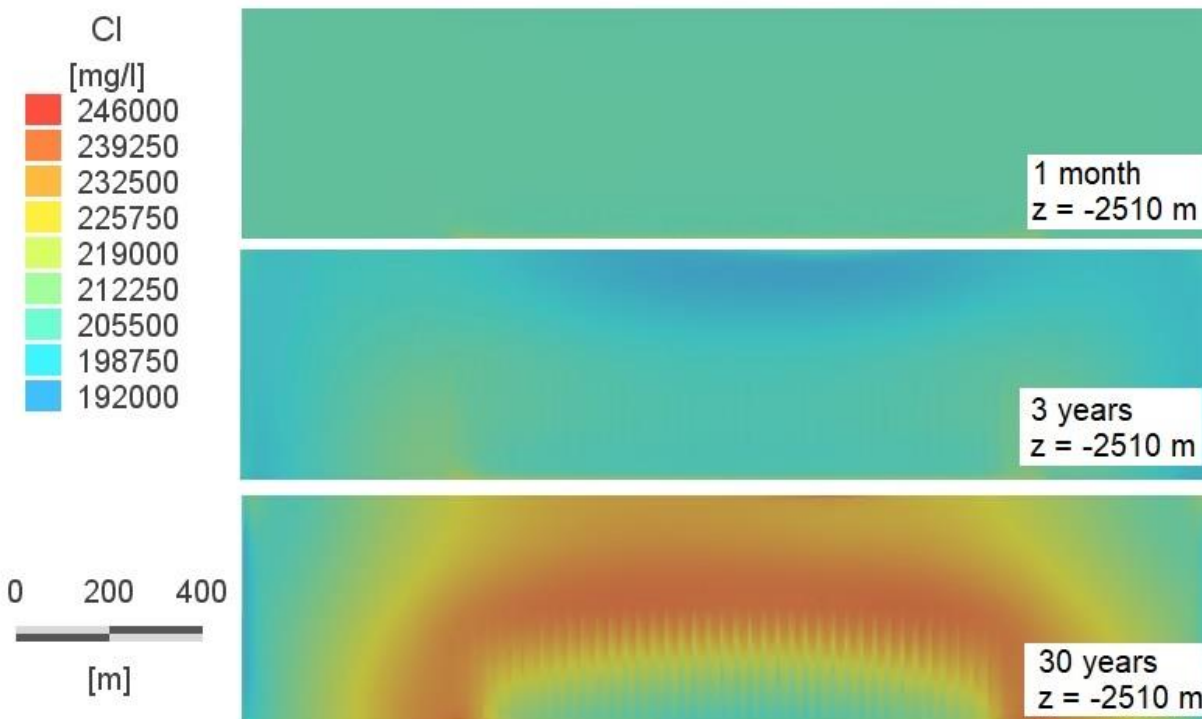


Figure 6-5. Distribution of chlorides along a horizontal slice of the Dawson Bay formation at -2510 m in a geothermal doublet.

Table 6-8. Saturation indices (SI) for minerals expected to precipitate at the top and bottom of the production well in a geothermal doublet in the Williston Basin, with the production well in the Dawson Bay formation.

Parameter		Units	1 month		3 years		30 years	
			Bottom	Top	Bottom	Top	Bottom	Top
Temp		°C	114	114	113	112	103	103
Pressure		kPa	21217	-	21195	-	21086	-
				3794		3815		3925
Aragonite	CaCO ₃	SI	n/a	n/a	2.14	2.16	3.05	3.06
Artinite	Mg ₂ CO ₃ (OH) ₂ ·3H ₂ O	SI	n/a	n/a	0.66	0.63	0.64	0.59
Calcite	CaCO ₃	SI	n/a	n/a	2.45	2.48	3.37	3.38
Celestite	SrSO ₄	SI	0.01	0.01	-0.14	-0.1	0.1	0.13
Dolomite	CaMg(CO ₃) ₂	SI	n/a	n/a	3.71	3.79	5.34	5.39
Halite	NaCl	SI	0.28	0.29	0.28	0.29	0.4	0.41
Huntite	CaMg ₃ (CO ₃) ₄	SI	n/a	n/a	7.84	7.96	10.16	10.21
Magnesite	MgCO ₃	SI	n/a	n/a	0.26	0.3	0.94	0.96

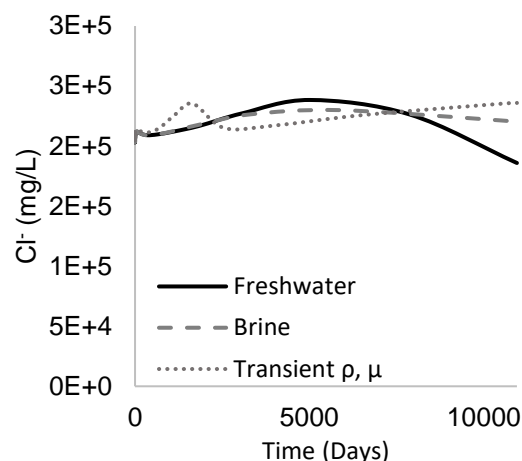


Figure 6-6. Comparison of Cl^- concentration observed at the bottom of the production well when a brine versus freshwater was injected into the system, and for transient density and viscosity.

6.5. Discussion

6.5.1. Oil and gas well conversion and reservoir suitability

Parallel, horizontal wells in the Bakken and Dawson Bay formations resulted in a temperature of 103°C at 30 years. Considering 80°C as the minimum required production temperature, the lifetime of the well can extend beyond 30 years. The use of a converted injection well from the Bakken formation indicated a feasible geothermal system. The cost savings associated with the re-use of an oil and gas well were up to 40% of drilling costs.

Reservoir quality, associated with the permeability and completed thickness was identified by Ricard et al. (2015) as an important factor in sedimentary basins, perhaps even more critical than temperature. Ricard et al. (2015) recommended a $4.9 \times 10^{-14} \text{ m}^2$ permeability thickness so that at a flow rate of $0.1 \text{ m}^3/\text{s}$, less than 1 MW of pumping power is required, allowing a net power production of 4 MW in a 5 MW system. Banks and Harris (2018) indicated that at 120°C a $0.043 \text{ m}^3/\text{s}$ flow rate could produce for viable geothermal systems in the WCSD. Banks and Harris (2018) indicated that the assessment of hydrogeological reservoir properties, such as the results presented

here could be used to determine if reservoirs could support the required flow rates. Well radius was assumed at 0.13 m², however smaller wells can significantly impact the feasible flow rates and required pumping power.

Although the natural permeability in the Bakken formation is too low, the majority of oil and gas wells in the Bakken formation in Saskatchewan are expected to be fractured with fractures extending beyond the Torquay/Three Forks formation (Davies et al., 2012). In the scenario presented here, the 1350 m completion had an estimated permeability of $2.4 \times 10^{-13} \text{ m}^2$. The estimated pumping power was 0.75 MW at a flow rate of $2.0 \text{ m}^3 \text{ s}^{-1}$, suitable for a project of this size, with the depth of pump and temperature within available technology limitations (Sanyal et al., 2007). Important in this calculation was the dependence of viscosity on temperature.

Weydt et al. (2018) indicated carbonate rocks in the Devonian formation in the Alberta Basin were a good geothermal reservoir with permeabilities ranging from 10^{-12} to 10^{-15} m^2 , and thermal conductivities ranging from 3 to $5 \text{ W m}^{-1} \text{ K}^{-1}$. Similar favourable conditions are prevalent in the Dawson Bay formation, with a permeability of $2 \times 10^{-13} \text{ m}^3$ and thermal conductivity of $3.68 \text{ W m}^{-1} \text{ K}^{-1}$, indicating favourable conditions for geothermal development (Weydt et al., 2018).

Several assumptions made in this investigation could influence the permeability and porosity of the matrix. This model assumed a nondeforming matrix. Deformation in a geothermal matrix was shown to result in changes in porosity of 0.5% at the injection well and 0.25% at the production well (Cacace and Jacquey, 2017; Jarrahi et al., 2019). Permeability and porosity in the Dawson Bay may be further complicated by the precipitation and dissolution of salt minerals during production. However, Woroniuk et al. (2018) evaluated permeability in the Dawson Bay and Souris River formations and found a weak relationship between NaCl inclusions and

permeability and suggested that reactive transport models in formations near the Prairie Evaporite do not need to couple permeability with salt content.

6.5.2. High thermal conductivity dolomite and halite formations

The Williston Basin has been a target of geothermal study and development. In 1977, the University of Regina drilled a set of injection and production wells for heating targeting the Winnipeg and Deadwood formations (Jessop and Vigrass, 1989). The wells produced high saline (110,000 ppm) water and achieved temperatures up to 74°C at 2088 m (Hutchence et al., 1986). The Winnipeg and Deadwood formations were initially targeted by the ongoing DEEP Earth Energy Production Corp. project, however, the depth was extended into the Precambrian bedrock at a depth of 3530 m, with a bottom hole temperature of 125°C (Deep Corp., 2019). Banks and Harris (2018) found temperatures of $75 \pm 12^\circ\text{C}$ at a total vertical depth of 2675 m and required depths over 4000 m to reach 120°C in the Alberta Basin in the WCSB.

The temperatures calculated in this study in the Dawson Bay formation were 103 - 112°C at a depth of 2510 m. The high thermal conductivity of the dolomite and halite resulted in a 6°C thermal anomaly. This is equivalent to 142 m depth or 16°C km^{-1} , the cost of drilling 142 m is estimated at \$127,800. Calculations indicate that this was associated with a 1.5 MW increase in power production for the same outlet temperature. Power production was sensitive to flow rate, inlet temperature, and outlet temperature. The temperatures produced in this simulation were highly dependent on the temperature calculations by Manz (2011b). It was also somewhat sensitive to the thickness of the formation, with a 75 m increase in the underlying high thermal conductivity formations resulting in a 2.5°C decrease in temperature. The outlet temperature, as well as the flow rate would be dependent on the design of the power plant.

Within the Williston Basin, the Dawson Bay formation benefits from the high thermal conductivity of the underlying halite Prairie Evaporite as well as the underlying dolomite Winnipegosis, Ashern, Interlake and Stony Mountain formations. Daniilidis and Herber (2017) recommended a minimum of 400 m thickness of salt to create thermal anomalies, here the halite is about 116 m thick and combined with the dolomite formations, the thickness is 371 m. The 6°C temperature anomaly calculated here along with the 25°C temperature anomaly calculated by Daniilidis and Herber (2017) indicate that targeting thick, high thermal conductivity formations has the potential as a geothermal reservoir.

Targeting a shallower formation may result in minimal cost savings for drilling if a horizontal well is drilled; however, a vertical well would result in cost savings. Horizontal drilling resulted in wells that are a similar total length to the well drilled to the Winnipegosis formation, which was 3530 m (Deep Corp., 2019). A vertical well to the Dawson Bay formation would cost \$2.2 million in drilling and completion, a savings of \$1.2 million over the horizontal well. The difference in targeting the region above a high thermal conductivity formation resulted in a 142 m difference, with drilling costs of \$500 m⁻¹ resulted in an estimated \$71,500 in cost savings.

6.5.3. Scale and minerals

Highly saturated brines in geothermal systems are commonly identified as an important factor after problems develop. Clark et al. (2010) indicated that 10% of geothermal power plants have a TDS greater than 200,000 mg/L, with dissolved solids dominated by sodium chloride. The most common minerals of concern in the literature are calcite and barite (Alt-Epping and Smith, 2001; Bächler and Kohl, 2005; Bozau et al., 2015; Fu et al., 2012; Wanner et al., 2017).

The Dawson Bay formation is a limestone, dolomite, and anhydrite formation. Within the Dawson Bay, fluids are generally near or at saturation with halite, with pore spaces filled with

halite (Dunn, 1982). Calculations indicate that within the formation, many of the minerals were supersaturated (Table 6-8). SIs were comparable at the bottom and top of the production well. The potential for precipitation of all saturated minerals was anticipated. The solubility of calcite and dolomite decreases with increasing temperature, so they are unlikely to precipitate within the production well. However, $\text{CO}_{2(g)}$ exsolution and pH increases can result in precipitation. Halite is highly reactive, and its solubility decreases with decreasing temperature. Therefore, precipitation was expected in the production well. Saturated halite concentrations were identified throughout the lifetime of the well, with carbonate saturation increasing over the lifetime of the well. Results indicated deposition of halite was likely to occur in the formation beyond the fractures. It is possible in the Dawson Bay formation that the halite deposited in the pore spaces will become depleted over time, resulting in lower than expected sodium and chloride levels as time progresses.

Mineral concentrations were based on a representative well located nearby. The exact concentrations would vary in an observed system, however the minerals present, and therefore minerals of concern for precipitation would likely remain the same since the fluids are assumed to be representative of the formation composition.

Chemical inhibitors can be used to prevent the formation of carbonate minerals (e.g., aragonite, artinite, calcite, dolomite, huntite, magnesite) (Alt-Epping et al., 2013). Within oil and gas wells, the management of halite deposits is considered difficult. Freshwater treatments or chemical treatment using nitrilotriacid based halite inhibitors can be used to manage halite deposits (Chen et al., 2009). The evolution of the heat exchange fluid over 30 years indicates that operators must monitor the composition of produced fluids and continually adapt the methods of scaling control. An engineered heat exchange fluid may result in reduced precipitation and dissolution (Moore and Holländer, 2015). Targeting the dolomite formation is recommended over targeting

the underlying salt formation, as exploiting the heat in the halite Prairie Evaporite formation would require hydraulic fractures, and fracture healing is possible in the halite formation. Similarly, Daniilidis and Herber (2017) recommend targeting permeable aquifers overlying salt structures. Further study into the risks of high mineral concentrations are beyond the scope of this work, however, would be required prior to system development.

6.5.4. Lithium

Understanding the geochemistry of fluids produced in geothermal systems allows for the potential of mining minerals such as lithium (Nicolas, 2017). Market value results indicate lithium production between \$3.0 and \$13.1 million annually, with lithium prices expected to stay high for the next 5 years (Schaefer, 2017). However, in addition to the market value of the metal, production costs must also be considered. Ventura et al. (2016) estimated a Li processing plant would have capital costs of \$20.5 million and annual costs of \$11.1 million. So although the market value of the Lithium is generally high, operating costs at these concentrations appear to be limiting. However, at a doubled production rate, production may be viable. The profitability of the lithium is highly dependent on local concentration and flow rate. High flow rates were more likely to produce high profits. Standalone lithium mining is generally assumed to be profitable at 1.44×10^{-2} mol/L at a depth of 1 km (Munk et al., 2016). Produced rates are generally below this value, supported by observed Dawson Bay concentrations of 1.14×10^{-2} mol L⁻¹, however, they are only 22% lower than economical rates for standalone systems.

Market value is sensitive to the lithium concentration at the location of the well and the production rate of the system. Targeting high lithium concentration in the Dawson Bay of 1.71×10^{-2} mol L⁻¹ at high production rates of $0.4 \text{ m}^3 \text{ s}^{-1}$ could result in 1.5×10^6 kg y⁻¹ production and a lithium market value \$32.9 million annually. Therefore, developers interested in a combined

geothermal and lithium production should take system design and local lithium concentrations into careful consideration.

6.5.5. Feasibility

Simulations indicate that a power plant capable of producing between 4.4 and 16.8 MW of power is possible under the given flow rates in southeastern Saskatchewan. Developing geothermal systems could help the province of Saskatchewan reduce its reliance on fossil fuels. The levelized cost of geothermal is estimated to be between USD\$54 – 159 MW-h (Clauser and Ewert, 2018; Lazard, 2015; U.S. Energy Information Administration, 2019), making it competitive with other renewable energy sources. A small power plant with low temperatures resources is generally on the higher end of the levelized costs (Clauser and Ewert, 2018). Natural gas and coal plants appear to be more cost-effective, at USD\$36 - \$71/MW-h (Stacy and Taylor, 2019), however, a carbon price of CAD\$80/tonne would render them uneconomical (Dolter and Rivers, 2018).

6.6. Conclusions

Geothermal development in southeastern Saskatchewan in the Williston Basin with the production well targeting the Dawson Bay formation and injection well targeting the Bakken formation is feasible. The Bakken formation well would require hydraulic fracturing to provide adequate permeability of 42 mD. The Bakken formation in the Williston Basin has a large number of wells appropriate for injection, which are generally already fractured. Re-entering an oil and gas well offered up to a 40% savings in the cost of drilling.

The sensitivity analysis indicated that widely varying production and temperature conditions can result in adequate flow and temperature. A flow rate of $0.20 \text{ m}^3 \text{ s}^{-1}$ with an inlet temperature of 113°C and an outlet temperature of 70°C produced 9.3 MW of power and required a 0.8 MW pumping rate. Consideration of the effects of density and viscosity with temperature

and concentration resulted in little change to concentration but did influence required pumping power due to the effect on hydraulic conductivity.

Halite and dolomite formations have high heat conductivity and are good targets for geothermal wells. Here, a 6°C thermal anomaly was associated with the halite and dolomite formations. Geothermal development should be targeted in the formations overlying the high thermal conductivity formations, since the warmest part of the formation is the top, and the overlying formation is likely to be more chemically stable with higher permeability. Within the Williston Basin, the Dawson Bay formation overlies the halite Prairie Evaporite formation and is a potential target for geothermal development. Where the Red River formation was 125°C, expected in Saskatchewan and North Dakota, a temperature of 112°C was calculated in the Dawson Bay formation and at the production well.

Geochemical modeling of the geothermal system was an excellent way to assess the geochemical stability of targeted formations. Producing from the Dawson Bay formation has the potential for aragonite, artinite, calcite, celestite, dolomite, halite, huntite, and magnesite deposition within the production well. Methods are generally available to manage the precipitation of these minerals. The availability of this data from oil and gas is an important factor in being able to complete this assessment.

Previous studies examining the co-production of lithium in the United States have excluded the Williston Basin. The results from this study estimate that at a pumping rate of 0.20 m³ s⁻¹ lithium valued at up to \$13 million could be produced. However, due to the high operational costs of extracting lithium, systems may be marginally feasible. At a pumping rate of 0.40 m³ s⁻¹, the system is more profitable, however, pumping power of 2.0 MW would be required.

The consideration of site-specific resources offered significant value added to the development of a geothermal system. The re-entry of an oil and gas well was found to be feasible with potential cost savings up to \$8 million. The targeting of high thermal conductivity formations resulted in an additional power production of 1.5 MW at the same depth. The development of lithium co-production at high concentrations and the ideal pumping rate offered the potential for \$2 million in yearly profit, however, it still may not be profitable due to initial investment costs. Numerical 3-D and 1-D geochemical models were valuable in identifying potential scale components, which can be considered in the feasibility of the system and selection of well materials.

6.7. Acknowledgments

The authors would like to acknowledge ERCO Worldwide for providing data on the composition of the Prairie Evaporite. The authors would also like to acknowledge the Vanier Canada Graduate Scholarship program for providing funding support for Kayla Moore.

Funding for this project was provided by the Natural Sciences and Engineering Research Council of Canada Vanier Canada Graduate Scholarship program and the Manitoba Graduate Scholarship Program. The funding source has no involvement in study design, collection analysis, interpretation of data or in writing the report.

6.8. References

- Alt-Epping, P., Smith, L., 2001. Computing geochemical mass transfer and water/rock ratios in submarine hydrothermal systems: implications for estimating the vigour of convection. *Geofluids*, 1(3): 163-181. DOI:10.1046/j.1468-8123.2001.00014.x
- Alt-Epping, P., Waber, H.N., Diamond, L.W., Eichinger, L., 2013. Reactive transport modeling of the geothermal system at Bad Blumau, Austria: Implications of the combined extraction of heat and CO₂. *Geothermics*, 45: 18-30. DOI:10.1016/j.geothermics.2012.08.002

- Anna, L.O., 2013. Geologic assessment of undiscovered oil and gas in the Williston Basin Province, Montana, North Dakota, and South Dakota, Assessment of Undiscovered Oil and Gas Resources of the Williston Basin Province of North Dakota, Montana, and South Dakota, 2010. United States Geological Survey, United States Department of the Interior, Reston, Virginia, pp. 56.
- Bächler, D., Kohl, T., 2005. Coupled thermal–hydraulic–chemical modelling of enhanced geothermal systems. *Geophysical Journal International*, 161(2): 533-548. DOI:10.1111/j.1365-246X.2005.02497.x
- Banks, J., Harris, N.B., 2018. Geothermal potential of Foreland Basins: A case study from the Western Canadian Sedimentary Basin. *Geothermics*, 76: 74-92. DOI: 10.1016/j.geothermics.2018.06.004
- Bear, J., 1972. Dynamics of fluids in porous media. American Elsevier Publishing Company, Inc.
- Beauheim, R.L., Domski, P.S., Roberts, R.M., 1999. Hydraulic Testing of Salado Formation Evaporites at the Waste Isolation Pilot Plant Site: Final Report, Sandia National Labs., Albuquerque, NM (US); Sandia National Labs., Livermore, CA (US).
- Bezys, R.K., McCabe, H.R., 1996. Lower to middle Paleozoic stratigraphy of southwestern Manitoba, Geological Association of Canada, Winnipeg, Manitoba.
- Blondes, M.S. et al., 2017. U.S. Geological Survey National Produced Waters Geochemical Database v2.4. In: Survey, U.S.G. (Ed.).
- Borgia, A., Pruess, K., Kneafsey, T.J., Oldenburg, C.M., Pan, L., 2012. Numerical simulation of salt precipitation in the fractures of a CO₂-enhanced geothermal system. *Geothermics*, 44: 13-22. DOI:10.1016/j.geothermics.2012.06.002
- Bozau, E., Häußler, S., van Berk, W., 2015. Hydrogeochemical modelling of corrosion effects and barite scaling in deep geothermal wells of the North German Basin using PHREEQC and PHAST. *Geothermics*, 53: 540-547. DOI: 10.1016/j.geothermics.2014.10.002
- Cacace, M., Jacquy, A.B., 2017. Flexible parallel implicit modelling of coupled thermal–hydraulic–mechanical processes in fractured rocks. *Solid Earth*, 8(5): 921-941. DOI:10.5194/se-8-921-2017
- Chen, T., Montgomerie, H., Chen, P., Vikane, O., Jackson, T., 2009. Understanding the Mechanisms of Halite Inhibition and Evaluation of Halite Scale Inhibitor by Static and Dynamic Tests, SPE International Symposium on Oilfield Chemistry. Society of Petroleum Engineers, The Woodlands. Texas, pp. 8. DOI:10.2118/121458-MS
- Christie, J., 2015. Prairie Evaporite Composition. In: Moore, K. (Ed.). ERCO Worldwide, Toronto, Ontario.
- Clark, C., Harto, C., Sullivan, J., Wang, M., 2010. Water use in the development and operation of geothermal power plants, Argonne National Laboratory (ANL).
- Clauser, C., Ewert, M., 2018. The renewables cost challenge: Levelized cost of geothermal electric energy compared to other sources of primary energy – Review and case study. *Renewable and Sustainable Energy Reviews*, 82: 3683-3693. DOI: 10.1016/j.rser.2017.10.095

- Controlled Thermal Resources, 2019. Hell's Kitchen Lithium: Secure and sustainable renewable energy solutions, The Project, El Centro, CA.
- Daniilidis, A., Herber, R., 2017. Salt intrusions providing a new geothermal exploration target for higher energy recovery at shallower depths. *Energy*, 118: 658-670. DOI:10.1016/j.energy.2016.10.094
- Davies, R.J., Mathias, S.A., Moss, J., Hustoft, S., Newport, L., 2012. Hydraulic fractures: how far can they go? *Marine and petroleum geology.*, 37(1): 1-6.
- Deep Corp., 2019. DEEP successfully completes first geothermal test well. In: Production, D.E.E. (Ed.), Our latest news. Deep Corp., Saskatoon, Canada.
- Diersch, H., 2014. FEFLOW Finite Element Modeling of Flow, Mass and Heat Transport in Porous and Fractured Media. Springer, New York.
- DiPippo, R., 2004. Second Law assessment of binary plants generating power from low-temperature geothermal fluids. *Geothermics*, 33(5): 565-586. DOI: 10.1016/j.geothermics.2003.10.003
- Dolter, B., Rivers, N., 2018. The cost of decarbonizing the Canadian electricity system. *Energy Policy*, 113: 135-148. DOI: 10.1016/j.enpol.2017.10.040
- Dunn, C.E., 1982. Geology of the Middle Devonian Dawson Bay Formation in the northern part of the Williston Basin, Williston Basin Symposium, Regina, Saskatchewan.
- Firoozy, N., 2016. Assessment of Geothermal Application for Electricity Production from the Prairie Evaporite Formation of Williston Basin in South-West Manitoba, University of Manitoba, Winnipeg, Manitoba, 165 pp.
- Firoozy, N., Holländer, H.M., 2016. Numerically derived temperature data set of Manitoba's subsurface formations GEOVancouver. Proceedings of the 69th CGS Conference, Vancouver, Canada.
- Fu, Y., van Berk, W., Schulz, H.-M., 2012. Hydrogeochemical modelling of fluid-rock interactions triggered by seawater injection into oil reservoirs: Case study Miller field (UK North Sea). *Appl Geochem*, 27(6): 1266-1277. DOI: 10.1016/j.apgeochem.2012.03.002
- Gosnold, W., Crowell, A., Nordeng, S., Mann, M., 2015. Co-Produced and Low-Temperature Geothermal Resources in the Williston Basin. *GRC Transactions*, 39: 653-660.
- Government of Canada, 2019. Canada's Action on Climate Change. In: Government of Canada (Ed.), Weather, climate and hazards. Government of Canada, Ottawa, Canada.
- Grasby, S.E. et al., 2012. Geothermal Energy Resource Potential of Canada, Geological Survey of Canada. DOI:10.4095/291488
- Gunnlaugsson, E., Ármannsson, H., Þórhallsson, S., Steingrímsson, B., 2014. Problems in geothermal operation-scaling and corrosion. In: Program, U.N.U.-G.T., LaGeo (Eds.), Short Course VI on Utilization of Low- and Medium-Enthalpy Geothermal Resources and Financial Aspects of Utilization, Santa Tecla, El Salvador.
- Harrison, S., 2014. Technologies for extracting valuable metals and compounds from geothermal fluids, California Energy Commission.
- Hartig, C.M., 2018. Porous media of the Red River Formation, Williston Basin, North Dakota: a possible Sedimentary Enhanced Geothermal System. *Int J Earth Sci*, 107(1): 103-112. DOI:10.1007/s00531-016-1398-9

- Hesshaus, A., Houben, G., Kringel, R., 2013. Halite clogging in a deep geothermal well – Geochemical and isotopic characterisation of salt origin. *Physics and Chemistry of the Earth, Parts A/B/C*, 64(0): 127-139. DOI:10.1016/j.pce.2013.06.002
- Hofmann, H. et al., 2014a. Potential for enhanced geothermal systems in low permeability limestones – stimulation strategies for the Western Malm karst (Bavaria). *Geothermics*, 51: 351-367. DOI: 10.1016/j.geothermics.2014.03.003
- Hofmann, H. et al., 2014b. Potential for enhanced geothermal systems in Alberta, Canada. *Energy*, 69: 578-591. DOI:10.1016/j.energy.2014.03.053
- Hu, K., Kohlruss, D., Yang, C., Chen, Z., 2017. Porosity and permeability evaluation for the Devonian-Mississippian Lower Middle Bakken Member in the Viewfield Pool, southeastern Saskatchewan, Geological Survey of Canada, Saskatchewan Geological Survey, Regina, Saskatchewan.
- Hutchence, K., Weston, J.H., Law, A.G., Vigrass, L.W., Jones, F.W., 1986. Modeling of a Liquid Phase Geothermal Doublet System at Regina, Saskatchewan, Canada. *Water Resources Research*, 22(10): 1469-1479. DOI:10.1029/WR022i010p01469
- Jain, C., Vogt, C., Clauser, C., 2015. Maximum Potential for Geothermal Power in Germany Based on Engineered Geothermal Systems. *Geothermal Energy*, 3(15): 1-20. DOI:10.1186/s40517-015-0033-5
- Jarrahi, M., Moore, K.R., Holländer, H.M., 2019. Comparison of solute/heat transport in fractured formations using discrete fracture and equivalent porous media modeling at the reservoir scale. *Physics and Chemistry of the Earth, Parts A/B/C*. DOI: 10.1016/j.pce.2019.08.001
- Jensen, G.K.S., 2016. Results from the 2016 field season for the Brine Sampling Project: investigating the mineral potential of brines in Saskatchewan, Saskatchewan Geological Survey.
- Jessop, A.M., Vigrass, L.W., 1989. Geothermal measurements in a deep well at Regina, Saskatchewan. *J Volcanol Geoth Res*, 37(2): 151-166. DOI: 10.1016/0377-0273(89)90067-X
- JWN, 2017. The costs to complete these Alberta oil and gas wells may surprise you. *Glacier Media Inc.*, Calgary, Canada.
- Kreis, K., Costa, A., Osadetz, K., 2006. Hydrocarbon potential of Bakken and Torquay formations, southeastern Saskatchewan. In: Gilboy, C.F., Whittaker, S.G. (Eds.), *Saskatchewan and Northern Plains Oil & Gas Symposium 2006*. Saskatchewan Geological Society Special Publication, Regina, Saskatchewan, pp. 118-137.
- Lazard, 2015. Lazard's Levelized cost of energy analysis - version 9.0.
- Limberger, J. et al., 2018. Geothermal energy in deep aquifers: A global assessment of the resource base for direct heat utilization. *Renewable and Sustainable Energy Reviews*, 82: 961-975. DOI: 10.1016/j.rser.2017.09.084
- Majorowicz, J., Grasby, S.E., 2010. Heat flow, depth–temperature variations and stored thermal energy for enhanced geothermal systems in Canada. *Journal of Geophysics and Engineering*, 7(3): 232.
- Manz, L.A., 2011a. Deep Geothermal Resources: Estimated Temperatures on Top of the Duperow Formation Kenmare 100K Sheet, North Dakota. In: Murphy, E.C., Helms,

- L.D. (Eds.), North Dakota Geothermal Maps. North Dakota Geological Survey, Bismark, ND.
- Manz, L.A., 2011b. Deep Geothermal Resources: Estimated Temperatures on Top of the Red River Formation Kenmare 100K Sheet, North Dakota. In: Murphy, E.C., Helms, L.D. (Eds.), North Dakota Geothermal Maps. North Dakota Geological Survey, Bismark, ND.
- Metalary, 2019. Lithium Price.
- Moore, K.R., Holländer, H.M., 2015. Geochemical assessment of a MgCl_2 heat transport fluid to evaluate the feasibility of using geothermal energy from saline systems, American Geophysical Union Fall Meeting, San Francisco, California.
- Moore, K.R., Holländer, H.M., 2017. Geochemical Modelling of the Dissolution of Salt Minerals and Application to Geothermal Energy, GeoOttawa 2017. Canadian Geotechnical Society, Ottawa, Canada.
- Moore, K.R., Holländer, H.M., Basri, M., Roemer, M., 2019. Application of geochemical and groundwater data to predict sinkhole formation in a gypsum formation in Manitoba, Canada. *Environmental Earth Sciences*, 78(6): 193. DOI:10.1007/s12665-019-8188-1
- Munk, L.A. et al., 2016. Lithium brines: a global perspective. *Review in Economic Geology*, 18: 339-365.
- National Energy Board, 2019. Provincial and territorial energy profiles - Saskatchewan, Energy Markets. Government of Canada, Ottawa, Canada.
- Neupane, G., Wendt, D.S., 2017. Assessment of mineral resources in geothermal brines in the us, Proceedings of the 42nd Workshop on Geothermal Reservoir Engineering, Stanford University, Stanford, CA, USA, pp. 19.
- Nicolas, M.P.B., 2017. Preliminary investigation of the potential for lithium in groundwater in sedimentary rocks in southwestern Manitoba, Manitoba Growth, Enterprise and Trade, Manitoba Geological Survey, Winnipeg, Manitoba.
- Nwachukwu, F.C., LeFever, R.D., Nordeng, S.H., Nesheim, T.O., 2018. Re-evaluating petroleum potential of Birdbear formation in McKenzie County, Williston Basin, North Dakota, AAPG Annual Convention and Exhibition, Salt Lake City, Utah.
- Palandri, J.L., Kharaka, Y.K., 2004. A compilation of rate parameters of water-mineral interaction kinetics for application to geochemical modeling, U.S. Department of the Interior, U.S Geological Survey, Menlo Park, USA.
- Palombi, D.D., 2008. Regional Hydrogeological Characterization of the Northeastern Margin in the Williston Basin, University of Alberta, Edmonton, Alberta, 196 pp.
- Parkhurst, D.L., Appelo, C., 2013. Description of input and examples for PHREEQC version 3-- A computer program for speciation, batch-reaction, one-dimensional transport, and inverse geochemical calculations. In: Survey, U.S.G. (Ed.), U.S. Geological Survey Techniques and Methods Section A, Groundwater Book 6, Modeling Techniques, Denver, Colorado, pp. 497.
- Petersen, K., Lerche, I., 1995. Quantification of thermal anomalies in sediments around salt structures. *Geothermics*, 24(2): 253-268. DOI:10.1016/0375-6505(94)00051-D
- Pitzer, K.S., 1973. Thermodynamics of electrolytes. I. Theoretical basis and general equations. *The Journal of Physical Chemistry*, 77(2): 268-277. DOI:10.1021/j100621a026

- Plummer, M.A. et al., 2016. Primary Constraints on the Design of an Enhanced Geothermal System Reservoir, 50th U.S. Rock Mechanics/Geomechanics Symposium. American Rock Mechanics Association, Houston, Texas, pp. 12.
- Ricard, L.P., Sheldon, H.A., Huddleston-Homes, C., 2015. Reservoir Quality Requirements for Geothermal Development in Deep Sedimentary Basin, Proceedings World Geothermal Congress 2015, Melbourne, Australia, pp. 1-5.
- Rose & Associates, 2016. The Current Costs for Drilling a Shale Well, Rose & Associates Oil and Gas Exploration Risk Assessment, Houston, Texas
- Rostron, B.J., Kelley, L.I., Kreis, L.K., Holmden, C., 2002. Economic potential of formation brines: Interim results from the Saskatchewan brine sampling program, Saskatchewan Geological Survey.
- Sanyal, S.K., Morrow, J.W., Butler, S.J., 2007. Net power capacity of geothermal wells versus reservoir temperature - a practical perspective, Thirty-second Workshop on Geothermal Reservoir Engineering, Stanford, California.
- Schaefer, K., 2017. Lithium Prices To Stay High To 2024—UBS. In: Bulletin, O.a.G.I. (Ed.), North Vancouver, Canada.
- Scheck-Wenderoth, M. et al., 2014. Models of heat transport in the Central European Basin System: Effective mechanisms at different scales. *Mar Petrol Geol*, 55: 315-331. DOI: 10.1016/j.marpetgeo.2014.03.009
- Schelkes, K., Vogel, P., Klinge, H., 2001. Density-dependent groundwater movement in sediments overlying salt domes - the Gorleben site example. *Phys Chem Earth Pt B*, 26(4): 361-365. DOI:10.1016/s1464-1909(01)00019-3
- Smith, S.A. et al., 2017. Relative Permeability of Williston Basin CO₂ Storage Targets. *Energy Procedia*, 114: 2957-2971. DOI:10.1016/j.egypro.2017.03.1425
- Sorey, M.L., 1978. Numerical modeling of liquid geothermal systems, US Government Printing Office, Washington, United States.
- Sproule, J.C., 1964. The Oil and Gas Prospects of the Pre-Mississippian Sedimentary Rocks of Southern Manitoba, Department of Mines and Natural Resources Manitoba, Calgary, AB.
- Stacy, T.F., Taylor, G.S., 2019. The Levelized Cost of Electricity from Existing Generation Resources, Institute for Energy Research.
- Tarcan, G., Ozen Balaban, T., Gemici, Ü., Çolak, M., Karamanderesi, İ., 2016. Geochemical assessment of mineral scaling in Kızıldere geothermal field, Turkey. *Environmental Earth Sciences*, 75: 1317. DOI:10.1007/s12665-016-6112-5
- TGI Williston Basin Working Group, 2008a. Devonian Prairie Evaporite: isopach. In: Manitoba Science, T., Energy and Mines, Survey, M.G. (Eds.), Stratigraphic Map SM2008-DPE-I.
- TGI Williston Basin Working Group, 2008b. Devonian Prairie Evaporite: structure contour. In: Manitoba Science, T., Energy and Mines, Manitoba Geological Services Branch (Eds.), Stratigraphic Map SM2008-DPE-S.
- U.S. Energy Information Administration, 2019. Cost and Performance Characteristics of New Generating Technologies, Annual Energy Outlook 2019.
- Ventura, S., Bhamidi, S., Hornbostel, M., Nagar, A., Perea, E., 2016. Selective Recovery of Metals from Geothermal Brines, SRI International, Menlo Park, CA (United States).

- Walsh, W., 2013. Geothermal resource assessment of the Clarke Lake Gas Field, Fort Nelson, British Columbia. *Bulletin of Canadian petroleum geology*, 61(3): 241-251.
- Wang, S., Yan, J., Li, F., Hu, J., Li, K., 2016. Exploitation and Utilization of Oilfield Geothermal Resources in China. *Energies*, 9(10): 798. DOI:10.3390/en9100798
- Wanner, C., Eichinger, F., Jahrfeld, T., Diamond, L.W., 2017. Unraveling the Formation of Large Amounts of Calcite Scaling in Geothermal Wells in the Bavarian Molasse Basin: A Reactive Transport Modeling Approach. *Procedia Earth and Planetary Science*, 17: 344-347. DOI: 10.1016/j.proeps.2016.12.087
- Wanner, C. et al., 2014. Reactive transport modeling of the Dixie Valley geothermal area: Insights on flow and geothermometry. *Geothermics*, 51: 130-141. DOI:10.1016/j.geothermics.2013.12.003
- Weydt, L.M., Heldmann, C.D.J., Machel, H.G., Sass, I., 2018. From oil field to geothermal reservoir: Assessment for geothermal utilization of two regionally extensive Devonian carbonate aquifers in Alberta, Canada. *Solid Earth*, 9(4): 953-983. DOI:10.5194/se-9-953-2018
- Williston Basin TGI, Unknown. Williston Basin Architecture and Hydrocarbon Potential in Eastern Saskatchewan and Western Manitoba. In: Canada, G.o., Manitoba, G.o., Saskatchewan, G.o. (Eds.), Williston Basin TGI.
- Winkler, M., 2011. Generation-4 Integrated Reservoir Modeling Report.
- Wissmeier, L., 2015. piChem - A FEFLOW Plugin for Advanced Geochemical Reactions. In: Institute, D.H. (Ed.), MIKE powered by DHI, Hørsholm, Denmark, pp. 28.
- Wissmeier, L., Barry, D.A., 2008. Reactive transport in unsaturated Soil: Comprehensive modelling of the dynamic spatial and temporal mass balance of water and chemical components. *Advances in Water Resources*, 31(5): 858-875. DOI:10.1016/j.advwatres.2008.02.003
- Wissmeier, L., Brovelli, A., Robinson, C., Stagnitti, F., Barry, D.A., 2009. Pollutant Fate and Transport in the Subsurface. In: Hanrahan, G. (Ed.), Complex Environmental Systems. ILM Publications, Thousand Oaks, USA, pp. 99-143.
- Wolff-Boenisch, D., Evans, K., 2013. Geochemical modelling of petroleum well data from the Perth Basin. Implications for potential scaling during low enthalpy geothermal exploration from a hot sedimentary aquifer. *Appl Geochem*, 37(Supplement C): 12-28. DOI:10.1016/j.apgeochem.2013.07.004
- Woroniuk, B., Tipton, K., Grasby, S.E., McIntosh, J.C., Ferguson, G., 2018. Salt dissolution and permeability in the Western Canada Sedimentary Basin. *Hydrogeol J*: 1-10. DOI:10.1007/s10040-018-1871-6
- Xia, Y., Plummer, M., Mattson, E., Podgorney, R., Ghassemi, A., 2017. Design, modeling, and evaluation of a doublet heat extraction model in enhanced geothermal systems. *Renewable Energy*, 105: 232-247. DOI:10.1016/j.renene.2016.12.064
- Yang, C., 2015. Stratigraphy and Reservoir Characterization of the Upper Devonian Duperow Formation, Southeastern Saskatchewan, Saskatchewan Geological Survey, Saskatchewan Ministry of the Environment.

7. Conclusions

The goal of this research was to explore the feasibility of developing a geothermal power plant targeting high thermal conductivity evaporite formations in the Williston Basin. Numerical THC model simulations were used to characterize the geothermal system. An important component of this scenario was the geothermal fluid composition, a common cause of technical issues. The high ionic strengths and mineral-fluid interactions expected in the geothermal simulations presented a modeling challenge. Therefore, laboratory and field studies were used to physically validate numerical codes for high ionic strength mineral-fluid interactions and resulting solute transport, and to develop modeler expertise.

Numerical simulations were done using a numerical finite element code. Transport mapping was used to provide the most stable results. Reactive transport at the high ionic strengths was calculated using the Pitzer database. Sensitive parameters were dependent on the scenario and scale so that there was not a single best approach for all subsurface fluid-mineral interaction problems. In the high fluid density contrast scenario, dispersion played an important role in the concentration distribution. In the development of sinkholes, the relationship between hydraulic conductivity and concentration was important. In the high-temperature scenario, viscosity played an important role in pressure changes. Ion concentrations were highly dependent on flow conditions so that all model settings must be carefully selected to create a representative model.

Numerical model simulations based on physical measurements in a laboratory setting were capable of simulating general flow patterns and observed concentrations associated with physical measurements from a dissolving salt dome. Of paramount importance in the development of the models were measured field data for flow and transport, including permeability, porosity,

dispersivity, and hydraulic heads. High variability was observed between replicates. Transport properties such as mineral flux rates and dispersivity along with initial conditions, caused by mineral dissolution, were key properties in calibration. Model performance was limited more by the ability to characterize transport properties in the physical system than by the modeling itself. Thus, dissolution problems should involve an approach that acknowledges uncertainty and carefully evaluates alternative parameter values.

The field-scale simulation modeled the growth of a sinkhole in a gypsum formation using equilibrium multicomponent reactive transport modeling. The model successfully predicted sinkhole growth resulting from mineral dissolution, supported by site observations. Of paramount importance in the development of the model was measured field data for flow and transport, collected using a tracer test and calibrated using numerical modeling. Cavity size at a given time was sensitive to the growth of the cavity with time, calculated based on concentrations.

This study showed that numerical models are a valuable tool in predicting mineral reactions and transport at high ionic concentrations at the laboratory and field scales. The results from field and laboratory studies indicated that one system with one result is difficult in this type of problem, due to the heterogeneity in mineral dissolution. Therefore, the range in which the system will perform successfully can be determined. However, a well-designed model with accurate flow data can be used to predict general solute movement in a mineral-fluid interaction model. These concepts directly translate to confidence in the deep geothermal model.

After validation of model application at the field scale for gypsum dissolution, modeling was extended to precipitation and dissolution of salt minerals at the depth in a geothermal reservoir. Developing geothermal wells above salt formations has the potential to reduce initial investment costs in deep sedimentary geothermal power production systems due to warm thermal anomalies.

In southeast Saskatchewan, targeting high thermal conductivity formations of halite and dolomite in the Williston Basin Devonian period resulted in produced geothermal temperatures of 113°C at depths of 2510 m. The high thermal conductivity formations resulted in a 6°C temperature anomaly, associated with 1.5 MW in power produced.

Two formation targets were considered in the simulations, first the Prairie Evaporite, a thick halite formation, and second, the overlying dolomite Dawson Bay formation. Both were assumed to be doublet systems, which produced electricity using a binary system. Oil and gas and mining data were a key component in providing permeability, temperature, and geochemical data for the Williston Basin. Previous studies were used to provide flow parameters, such as pumping rates, well spacing, and power production.

The dolomite Dawson Bay formation benefits from the high heat flow in the underlying halite Prairie Evaporite formation, as well as the dolomite Winnipegosis, Ashern, Interlake, Stonewall, and Stony Mountain formations. The Dawson Bay has a permeability of 202 mD, which, in the horizontal well design, was adequate for a geothermal system at 0.20 m³ s⁻¹. When targeting soluble formations such as dolomite, mineral precipitation in the production well was an issue due to saturated mineral conditions and changing temperature and pressure. The Dawson Bay has the potential for precipitation of aragonite, artinite, calcite, celestite, dolomite, halite, huntite, and magnesite within the production well. This data can be used by developers to investigate potential mitigation methods and piping materials.

When targeting the Prairie Evaporite, hydraulic fracturing is required to develop adequate permeability. Precipitation of halite within the production well was expected to be a concern, at a concentration of 0.52 mol L⁻¹. MgCl₂ can be used as an inhibitor in halite formations to reduce dissolution through the common-ion effect. Geochemical models of a formation based-brine with

MgCl₂ added and a pure MgCl₂-brine heat exchange fluids indicate that there are advantages to both types of fluid under fluctuating pressure and temperature in preventing mineral precipitation resulting in well clogging. Pressure controls within the production well can also be used to reduce precipitation, which may be one of the most viable options.

One of the issues with developing geothermal energy in Canada is the unfavourable economics, with a slow pay-off in investment. In addition to considering targeting thermal anomalies caused by evaporite minerals, this study also considered a number of site-specific assets, including re-entering existing oil and gas well and co-production of lithium.

A well in the Bakken formation, located 377 m above the Dawson Bay formation was shown to have good potential as an injection well. It was assumed that the oil and gas well in the Bakken formation had previously been fractured, as is likely. Without fracturing, the Bakken has a permeability of 2.24 mD. All other formation between the Dawson Bay and Bakken had permeability greater than the required 42 mD. The use of an existing well reduced or removed the cost of drilling an injection well, estimated at \$8 million, or 40% of drilling costs.

The co-production of lithium along with geothermal fluid at a flow rate of 0.20 m³ s⁻¹ is expected to be profitable at concentrations above 1.1x10⁻² mol L⁻¹, however, the cost of developing the plant must be taken into account when deciding the minimum profit margin. Observed concentrations in the Dawson Bay formation were 1.14x10⁻² ± 4.70x10⁻³ mol L⁻¹ and model results indicate concentrations in the produced fluid of 1.36x10⁻² mol L⁻¹ at the beginning of production and 3.16x10⁻³ mol L⁻¹ at the end of 30 years.

The targeting of thick, high thermal conductivity formations, such as salt formations has the potential to reduce drilling depths in deep geothermal systems, and therefore, cost.

Hydrogeochemical investigations of geothermal systems are an important tool that can be used to understand the potential for technical issues associated with geothermal fluids, such as scaling, clogging, and corrosion. The reliability of the numerical tools for mineral-fluid interactions has been proven at the laboratory and field scale. Accurate flow data were an important component in all of the geochemical scenarios. Future studies comparing produced geothermal fluids to predicted values in the Williston Basin can be used to further improve predictive capabilities. As more systems and numerical methods become validated, studies can be extended to remote areas with little data availability.

8. Outlook

Within low-enthalpy sedimentary basins thick, high thermal conductivity salt formations result in overlying warm thermal anomalies. Systems that target permeable overlying formations or systems that employ hydraulic fracturing have been shown here to be reasonable targets for geothermal systems. Thicker formations result in increased temperature anomalies (Daniilidis and Herber, 2017). Salt domes develop from gravitational and tectonic forces and can grow in diameter up to 10 km and in height from 2 to 10 km, thus have the potential to provide desirable conditions. Anticlines, or folds, occur on the scale of kilometers in size, with a vertical relief that can result in heat being conducted from a significant depth to near-surface, where it re-enters sediments near the apex (Petersen and Lerche, 1995).

Salt structures are common in sedimentary basins, including the Gulf of Mexico, the North Permian Basin in Europe, and the Iraq-Iran-Arabian Peninsula in the Middle East. Within these regions, general heat flow mapping can be used along with depth to the salt dome to identify areas that can serve as potential geothermal targets. The apex of salt anticlines should be considered as geothermal targets. The temperature anomaly will depend on the depth of the formation. Formations overlying the high thermal conductivity structures should have high permeability, adequate for a production well. However, hydraulic fracturing is also a possibility. These areas are often well characterized due to the trapping of oil and natural gas associated with salt domes, mining of salt and potash, and use as storage cavities.

Engineering geothermal heat exchange fluids can provide some reduction in the potential for scaling and clogging in geothermal systems targeting halite formations. Another option may be closed-loop geothermal system designs where no water is withdrawn from the formation, but only heat are also under development, e.g. Dai et al. (2019) and Eavor Technologies Inc. (2019).

This type of system offers another solution to scaling and clogging in geothermal systems. However, studies would be required to determine the temperature and flow requirements and potential applications.

The work in the Williston Basin demonstrated that geothermal systems are feasible, and additional resources and assets can increase profitability. Geothermal development in the Williston Basin should consider lithium concentration in the formation fluids as a potential source of additional profit, as well as the conversion of existing oil and gas wells. Following the development of a geothermal well in the Williston Basin, a comparison of produced fluids with modeled results could be used to validate numerical model results and provide further data on uncertainty, expanding on the work done here to validate subsurface mineral-fluid interaction modeling.

Geothermal technology has the potential to provide baseload power across Canada (Grasby et al., 2012). This is especially in areas with high use of fossil fuels for electricity production, such as Saskatchewan, Alberta, and Canada's north. The northern territories currently rely on diesel-fired generators for electricity. The high cost of diesel generators results in comparable leveled costs of geothermal. Further validation of numerical THC models in areas with available data, such as the Williston Basin will enable expansion to areas with limited data, with a good understanding of uncertainty. THC assessment of geothermal systems can then be applied in remote areas with limited data, such as Canada's north.

Geothermal can effectively replace fossil fuels as a source of power generation, which currently produces 18% of Canada's power (Canada Energy Regulator, 2020). A 5 MW plant produces approximately enough electricity for 5000 homes. With approximately 12.4 million households in Canada (Statistics Canada, 2020), 18% of power needs would require approximately

450 - 5 MW plants. At a cost of \$50 million per plant {Deep Corp., 2019 #1125}, the total cost would be approximately \$22.5 billion.

8.1. References

- Alkattan, M., Oelkers, E.H., Dandurand, J.-L., Schott, J., 1997a. Experimental studies of halite dissolution kinetics, 1 The effect of saturation state and the presence of trace metals. *Chem Geol*, 137(3–4): 201-219. DOI: 10.1016/S0009-2541(96)00164-7
- Alkattan, M., Oelkers, E.H., Dandurand, J.-L., Schott, J., 1997b. Experimental studies of halite dissolution kinetics: II. The effect of the presence of aqueous trace anions and $K_3Fe(CN)_6$. *Chem Geol*, 143(1–2): 17-26. DOI:10.1016/S0009-2541(97)00097-1
- ASTM International, 2000. ASTM D 2434-68 Standard Test Method for Permeability of Granular Soils. ASTM International, Conshohocken, PA.
- Blaisonneau, A., Peter-Borie, M., Gentier, S., 2016. Evolution of fracture permeability with respect to fluid/rock interactions under thermohydraulic conditions: development of experimental reactive percolation tests. *Geothermal Energy*, 4(1): 3. DOI:10.1186/s40517-016-0045-9
- Cacace, M., Jacquey, A.B., 2017. Flexible parallel implicit modelling of coupled thermal–hydraulic–mechanical processes in fractured rocks. *Solid Earth*, 8(5): 921-941. DOI:10.5194/se-8-921-2017
- Canada Energy Regulator, 2020. Provincial and Territorial Energy Profiles. Government of Canada.
- Dai, C., Li, J., Shi, Y., Zeng, L., Lei, H., 2019. An experiment on heat extraction from a deep geothermal well using a downhole coaxial open loop design. *Applied Energy*, 252: 113447. DOI:10.1016/j.apenergy.2019.113447
- Daniilidis, A., Herber, R., 2017. Salt intrusions providing a new geothermal exploration target for higher energy recovery at shallower depths. *Energy*, 118: 658-670. DOI:10.1016/j.energy.2016.10.094
- Diersch, H., 2014. FEFLOW Finite Element Modeling of Flow, Mass and Heat Transport in Porous and Fractured Media. Springer, New York.
- Diersch, H.J.G., Kolditz, O., 1998. Coupled groundwater flow and transport: 2. Thermohaline and 3D convection systems. *Advances in Water Resources*, 21(5): 401-425. DOI:10.1016/S0309-1708(97)00003-1
- Eavor Technologies Inc., 2019. Earth is our engine. In: Redfern, J. (Ed.), Canada.
- Garven, G., 1995. Continental-Scale Groundwater Flow and Geologic Processes. *Annual Review of Earth and Planetary Sciences*, 23(1): 89-117. DOI:10.1146/annurev.ea.23.050195.000513
- Grasby, S.E. et al., 2012. Geothermal Energy Resource Potential of Canada, Geological Survey of Canada, Calgary, AB. DOI:10.4095/291488
- Hassanizadeh, M.S., Leijnse, A., 1995. A non-linear theory of high-concentration-gradient dispersion in porous media. *Advances in Water Resources*, 18(4): 203-215. DOI: 10.1016/0309-1708(95)00012-8
- Jarrahi, M., Moore, K.R., Holländer, H.M., 2019. Comparison of solute/heat transport in fractured formations using discrete fracture and equivalent porous media modeling at the

- reservoir scale. *Physics and Chemistry of the Earth, Parts A/B/C*. DOI: 10.1016/j.pce.2019.08.001
- Konz, M., 2010. 2D benchmark experiments and simulations of density coupled flow problems, Universität Basel, Basel.
- NEA, OECD, 1988. International Hydrocoin project: Groundwater hydrology modelling strategies for performance assessment of nuclear waste disposal. Level 1: Code verification, Nuclear Energy Agency (NEA), Organisation for Economic Co-operation and Development (OECD), Paris.
- Petersen, K., Lerche, I., 1995. Quantification of thermal anomalies in sediments around salt structures. *Geothermics*, 24(2): 253-268. DOI:10.1016/0375-6505(94)00051-D
- Prasad, A., Simmons, C.T., 2003. Unstable density-driven flow in heterogeneous porous media: A stochastic study of the Elder [1967b] “short heater” problem. *Water Resources Research*, 39(1): SBH 4-1-SBH 4-21. DOI:10.1029/2002WR001290
- Reilly, T.E., Harbaugh, A.W., 2004. Guidelines for evaluating ground-water flow models. US Department of the Interior, US Geological Survey.
- Schincariol, R.A., Schwartz, F.W., 1990. An experimental investigation of variable density flow and mixing in homogeneous and heterogeneous media. *Water Resources Research*, 26(10): 2317-2329. DOI:10.1029/WR026i010p02317
- Scott Duncan, E.J., Lajtai, E.Z., 1993. The creep of potash salt rocks from Saskatchewan. *Geotechnical & Geological Engineering*, 11(3): 159-184. DOI:10.1007/bf00531249
- Statistics Canada, 2020. Families, households and housing. Government of Canada.
- Stiller, M., Yechieli, Y., Gavrieli, I., 2007. The rate of dissolution of halite in diluted Dead Sea brines, Ministry of National Infrastructure. Geological Survey of Israel, Jerusalem.
- Warren, J.K., 2006. *Evaporites: sediments, resources and hydrocarbons*. Springer Science & Business Media.
- Weisbrod, N., Alon-Mordish, C., Konen, E., Yechieli, Y., 2012. Dynamic dissolution of halite rock during flow of diluted saline solutions. *Geophysical Research Letters*, 39(9). DOI:10.1029/2012GL051306
- Woroniuk, B., Tipton, K., Grasby, S.E., McIntosh, J.C., Ferguson, G., 2018. Salt dissolution and permeability in the Western Canada Sedimentary Basin. *Hydrogeol J*: 1-10. DOI:10.1007/s10040-018-1871-6
- Younes, A., Ackerer, P., Mose, R., 1999. Modeling Variable Density Flow and Solute Transport in Porous Medium: 2. Re-Evaluation of the Salt Dome Flow Problem. *Transport Porous Med*, 35(3): 375-394. DOI:10.1023/a:1006504326005